



UNIVERSITATEA  
DIN BUCUREȘTI  
VIRTUTE ET SAPIENTIA



# **Rare decays in high energy interactions and performance studies on FCAL region at a linear collider**

Ph.D. Thesis

School of Doctoral Studies, Faculty of Physics, University of Bucharest

Eliza TEODORESCU

Scientific Coordinator,

Prof. Dr. Nicolae Victor ZAMFIR

- 2011 -

# Acknowledgements

*Finishing this thesis in the short period of three years was possible only with the help of a group of people with whom I've worked and who offered their help and support. I would like to offer my sincerest thanks and appreciation to them all. I would have not succeeded without you. Thank you all!*

*The list below is by no means exhaustive nor does it imply any hierarchical structure.*

*I thank Prof. Dr. Nicolae Victor Zamfir, my supervisor, for trusting me and accepting to coordinate my work.*

*I thank the honored members of the commission for investing their time into reviewing this thesis: Prof. Dr. Ștefan Antohe, the president of the commission, and the referees, Prof. Dr. Danil Căta, Dr. Cornelia Coca, Prof. Dr. Alexandru Jipa*

*I thank Dr. Cornelia Coca, my group leader, for initiating me into the wonderful world of Particle Physics, for all the educative discussions and all the sensible advices and suggestions.*

*I thank Dr. Raluca Anca Muresan, my group leader, for all the constructive critics, all the fruitful discussions and all the encouragement and support.*

*I thank Dr. Ioan Ursu for his support and encouragement and for making it possible for me to continue working in the LHCb collaboration.*

*I thank Dr. Wolfgang Lohmann and Dr. Konrad Elsener for giving me the great opportunity to work in their groups, for their trust in me and for all their encouragement. It has been an honor working with you!*

*I thank Andrey Sapronov, Andre Philippe Sailer and Alexandra Popescu for all their patience in listening to my stupid questions and actually finding answers to them. Thank you guys!*

*I thank all the people in the FCal Collaboration. It has always been a pleasure participating in FCal Meetings because of all the fine people in this group.*

*I thank Vanya Belyaev, Olivier Deschamps, Fatima Soomro, Daria Savrina for spending their time in making me understand the LHCb software and the intricacies of Radiative Decays and for all their very instructive talks. Thank you all very much!*

*I want to thank to my very special friends for all their support and encouragement, I could have never done it without you: Ana, Alexandra, Dana, Mihai, Valentina. You are all very dear to me!*

*I thank my mother, my father and my brother for being who they are and always being there for me.*

*And last but never least, I thank my husband, Max, for all the patience, support and understanding. I hope I can be there for you as you were for me.*

# Abstract

The main subjects of this thesis involve studies on rare radiative decays using data collected with the LHCb detector at LHC (Large Hadron Collider) and performance studies on detector components at the ILD (International Large Detector) detector concept proposed for a future  $e^+e^-$  linear collider, ILC (International Linear Collider) and CLIC (Compact Linear Collider).

Using  $88 \text{ pb}^{-1}$  of data collected with the LHCb detector, two rare radiative decay modes have been studied,  $B_d \rightarrow K^* \gamma$  and  $B_s \rightarrow \phi \gamma$ . The selection strategy is presented and a study is being performed in order to improve the selection efficiency for the two radiative decays.

Precise measurements on the  $B_d \rightarrow K^* \gamma$  decay are crucial for the detector calibration and also because this particular channel will be used as control channel for measurements on other radiative decays. For this decay, a study is performed on simulated data in order to determine possible sources of background which can complicate the analysis of the  $B_d \rightarrow K^* \gamma$  radiative decay as well as a study on the proper-time acceptance function for this channel.

The second part of the thesis presents simulation studies on detector components placed in the Very Forward Region of the ILD detector concept proposed for a future  $e^+e^-$  linear collider: BeamCal (beam calorimeter) at ILC and QD0 (final focus quadrupole magnet) at CLIC.

The electromagnetic and neutron shower shape in BeamCal has been investigated and the radiation levels have been estimated for one year of operation at ILC accelerator, as well as bunch-by-bunch fluctuations of energy depositions, using two different simulation algorithms.

A detailed but simplified model of QD0 was implemented in the general software framework used for the simulation of the ILD detector concept at CLIC. With this model the electromagnetic and neutron doses in different components of QD0 were estimated.

# Contents

<b>1. Introduction.....</b>	<b>6</b>
1.1 Author's point of view.....	6
1.2 Elementary Particles and Symmetries in Particles Physics.....	7
1.3 CP symmetry violation – history.....	10
1.4 Standard Model parametrization of the CKM matrix.....	12
1.5 CKM elements.....	19
1.5.1 <i>Magnitudes</i> .....	19
1.5.2 <i>CKM phases</i> .....	21
1.6 Main contributions and outline of the thesis.....	22
1.7 Published papers.....	25
<b>2. LHC Accelerator and detectors.....</b>	<b>28</b>
2.1 Introduction.....	28
2.2 Large Hadron Collider (LHC).....	29
2.3 LHCb detector.....	32
2.3.1 <i>Introduction</i> .....	32
2.3.2 <i>VELO System</i> .....	33
2.3.3 <i>Magnet</i> .....	34
2.3.4 <i>RICH</i> .....	35
2.3.5 <i>Tracking System: Inner Tracker + Trigger Tracker</i> .....	37
2.3.6 <i>Outer Tracker</i> .....	39
2.3.7 <i>Calorimeters</i> .....	40
2.3.8 <i>Muon System</i> .....	41
2.3.9 <i>Trigger System</i> .....	43
<b>3. Software details.....</b>	<b>45</b>
3.1 Introduction.....	45
3.2. Event Generator.....	46
3.3 Detector simulation.....	47
3.4 Track reconstruction.....	48
3.4 Particle identification.....	50
<b>4. Radiative decays at LCHb.....</b>	<b>53</b>
4.1 Motivation for studying radiative decays at LHCb.....	53
4.2 Searches of signal peaks for $B_d \rightarrow K^* \gamma$ and $B_s \rightarrow \phi \gamma$ in data collected with LHCb detector at $\sqrt{s} = 7$ TeV.....	54
4.3 Conclusions.....	74
<b>5. Background studies for <math>B_d \rightarrow K^* \gamma</math>.....</b>	<b>75</b>
5.1 Background studies on simulated data.....	75
5.2 Conclusions.....	90
<b>6. Lifetime acceptance for <math>B_d \rightarrow K^* \gamma</math>.....</b>	<b>91</b>
6.1 Strategy and results.....	91
6.2 Conclusions.....	106

<b>7. Introduction to ILC and CLIC.....</b>	<b>108</b>
7.1. Physics at the ILC and CLIC.....	109
7.2 General overview on the ILC and CLIC.....	110
7.3 Detector concepts at ILC and CLIC.....	114
7.3.1 <i>Introduction and general overview</i> .....	114
7.3.2 <i>Challenges on detector construction</i> .....	115
7.3.3 <i>The ILD concept</i> .....	116
7.3.3 <i>Very forward region</i> .....	117
7.3.4 <i>BeamCal detector</i> .....	119
<b>8. Software details.....</b>	<b>121</b>
8.1 Introduction.....	121
8.2. Event generator: GuineaPig.....	121
8.3. Detector simulation: BeCaS and Mokka.....	123
<b>9. BeamCal studies.....</b>	<b>126</b>
9.1 Introduction.....	126
9.2 BeamCal results in Becas and Mokka.....	127
9.2.1 <i>Electromagnetic shower</i> .....	127
9.2.2 <i>Neutron shower</i> .....	132
9.2.3 <i>The effect of different magnetic fields on backgrounds in BeamCal...</i>	134
9.3 Conclusions.....	138
<b>10. QD0 at CLIC.....</b>	<b>139</b>
10.1 Introduction.....	139
10.2 Very Forward Region at CLIC_ILD.....	139
10.3 Motivation for study and simulation details.....	141
10.4 Electromagnetic Dose on QD0 from Incoherent Pairs.....	143
10.5 Neutrons from Incoherent Pairs.....	145
10.6 Conclusions.....	147
<b>11 Summary and Conclusions.....</b>	<b>148</b>
<b>References.....</b>	<b>152</b>
<b>Appendix 1.....</b>	<b>158</b>
<b>Appendix 2.....</b>	<b>164</b>
<b>Appendix 3.....</b>	<b>166</b>

# 1. Introduction

## 1.1 Author's point of view

“Cogito ergo sum” – “I think therefore I am” is the conclusion of the father of modern philosophy, René Decartes in his 1637's “Discourse on the Method” [1]. Besides his insights in matters of spiritual self and human concieneness, his legacy as a scientist is also most notable. He introduced the Cartesian coordinate system, offering the possibility of representing algebraic ecuations as geometrical shapes, thus entwining the abstract with the intuitive. This ultimately led to analysis.

Although it is considered that mathematics is the universal language, the first recorded history events were transmitted through drawings; pictures on the walls of the caves. This is the form of communication which persisted through time, and even nowadays, when trying to understand and describe phenomena which define our surrounding reality we try to give them a graphical representation, to give them a shape. The shape seems to be the solid evidence that something exists which deserves our attention. As soon as this is established, there comes the instinctive need to answer the what's, the how's and the why's. We have come a long way in understanding our world, what we see, how most things work and how we evolved but we still seem to have trouble finding an answer when asking ourseves why we are here, why our world is as it is, why do we have the ability to even ask these questions and to what end. We can choose to try and find answers either by hypothesizing based on each personal experieces, which in my point of view, is the poetical-phylosopher way that only provides us with subjective interpretations, or, the scientific way; we have the facts and we do our best to put them all togheter and build the bigger picture. The problem here is that we do not have all the pieces of this great puzzle which we call our Universe but, this is exactly what makes everything more thrilling, it is up to each of us to contribute to solving this great mistery by finding even the smallest of the missing pieces and adding it to the puzzle.

Things become even more exciting when we go beyond the visible limit, deep into the fabric of our world, deeper into the unknown. As microscopic scale phenomena were being discovered, it became obvious that physics lows as we knew them could not describe what we were beginning to see. New concepts were introduced and new theories were developed, the mathematical apparatus became more and more complex which allowed the analysis and understanding of increasingly complex phenomena. The technological progress experienced a

constant growing as well, and this offered the possibility to imagine and build sophisticated experiments to put under a microscope the unseen world. Even today, what we do is to try and give a form to the unknown and then interpret it.

## 1.2 Elementary Particles and Symmetries in Particles Physics

The idea of indivisible units shaping up into more complex configurations to build our world has been postulated more than two thousands years ago. Throughout history, it has been asiduously tried to identify these units. At first, the atom was thought to be the smallest matter component. Only during the 19<sup>th</sup> and 20<sup>th</sup> century this belief has been proved wrong, not only does the atom has a sub-structure, a nucleus surrounded by electrons, but the nucleus has a sub-structure of its own, protons and neutrons and more than that, they too are subdivided into even smaller parts, the quarks. Nowadays, the quarks together with leptons, a category of particles of which the best known representative is the electron, are considered the most elementary particles.

Now that we know them, and theories have been perfected to describe their properties and interactions, we want to understand where they come from, what mechanism made possible their existence and why was matter favored over anti-matter. Theory tells us that all this happened very close to the moment of the Universe's creation. Today, with the help of the very powerful accelerating machines which have been built, we are able to recreate the conditions of the very early Universe and this may allow us to find answers to these questions.

Elementary particles are those constituents of matter which do not have any known substructure, at the actual level of knowledge ( $10^{-18}$ - $10^{-19}$  m). The elementary particles are either particles which are effectively matter components or those who mediate the interactions between them.

Classified by one of their intrinsic characteristic, the spin (the rotation of a particle around its axis), the matter components are fermions (charged particles with semi-integer spin). They interact with each other by exchanging bosons, characterized by integer spin. Quarks and leptons are at the moment the most elementary particles; they do not have any known internal structure. At today's level of knowledge, there are four fundamental forces which describe the interactions between matter components: the strong interaction, the weak interaction,

electromagnetism and gravitation. Particles composed of quarks can interact through all types of known interactions while leptons cannot interact through the strong interaction.

The known leptons are the electron,  $e^-$ , the muon,  $\mu^-$  and the tau,  $\tau^-$ , with an electric charge  $Q=-1$  (in units of  $e$ ) and the corresponding neutrinos:  $\nu_e$ ,  $\nu_\mu$  and  $\nu_\tau$ , respectively, with  $Q=0$ . Quarks are distinguishable through *flavor*, e.g.  $u$ ,  $d$ ,  $s$ ,  $c$ ,  $b$ ,  $t$  (with  $Q=2/3, -1/3, -1/3, 2/3, -1/3$  and  $2/3$ , respectively) and *color*. They cannot exist by themselves; they exist only in combinations of colors which result in a colorless state. [2]

The exchange bosons are specific to each of the fundamental interactions: the photon is the mediator of the electromagnetic interaction, 8 gluons represent the exchange quanta for the strong interaction between quarks and the three bosons of the weak interaction are  $W^\pm$  and  $Z$ . [2]

Fermions can be structured into three families of particles with identical properties, except for the mass, as follows [2]:

$$\text{First family: } \begin{pmatrix} \nu_e \\ e^- \end{pmatrix}_L, e^-_R, \begin{pmatrix} u \\ d \end{pmatrix}_L, u_R, d_R$$

$$\text{Second family: } \begin{pmatrix} \nu_\mu \\ \mu^- \end{pmatrix}_L, \mu^-_R, \begin{pmatrix} c \\ s \end{pmatrix}_L, c_R, s_R$$

$$\text{Third family: } \begin{pmatrix} \nu_\tau \\ \tau^- \end{pmatrix}_L, \tau^-_R, \begin{pmatrix} t \\ b \end{pmatrix}_L, t_R, b_R$$

Plus all their antiparticles (Figure 1.1)

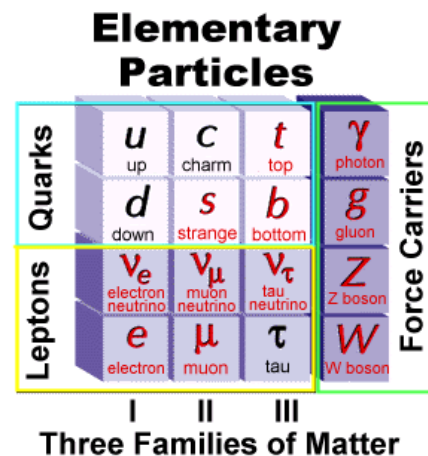


Figure 1.1 Quarks and leptons families

Particle Physics is largely described through symmetries. A symmetry  $S$  exists if the physical system under investigation is invariant to the transformation produced by  $S$  [3].

There are discrete and continuous symmetries.

1. *Discrete symmetries*: the parameters characteristic to this type of symmetries can have only discrete values: parity ( $P$ ), charge conjugation ( $C$ ) and time reversal ( $T$ ). [3]

- *Parity (P)* space coordinates inversion, (x, y, z) → (-x, -y, -z) and all internal quantum numbers
- *Charge conjugation (C)* reverses the electric charge (Q → -Q) and all internal quantum numbers
- *Time reversal (T)* t transforms into -t, it affects also the momentum and angular momentum (Figure 1.2)

Quantity		<i>P</i>	<i>C</i>	<i>T</i>
Space vector	<b>x</b>	- <b>x</b>	<b>x</b>	<b>x</b>
Time	<i>t</i>	<i>t</i>	<i>t</i>	- <i>t</i>
Momentum	<b>p</b>	- <b>p</b>	<b>p</b>	- <b>p</b>
Spin	<b>s</b>	<b>s</b>	<b>s</b>	- <b>s</b>
Electrical field	<b>E</b>	- <b>E</b>	- <b>E</b>	<b>E</b>
Magnetic field	<b>B</b>	<b>B</b>	- <b>B</b>	- <b>B</b>

Figure 1.2 Types of symmetries

All experimental observations indicate a deep symmetry in nature where the combination of all three discrete transformations cannot be broken. These observations are subsumed into the “*CPT Theorem*” which states that all interactions must be invariant to the global transformation which is the sum of the three discrete transformations, *C*, *P* and *T*. [4]

Electromagnetic and strong interactions are invariant to individual *C*, *P* and *T* transformations while weak interactions can break *P* and *C* symmetries or their *CP* combination, but never the time reversal symmetry. [5]

2. *Continuous symmetries*: continuous values for the involved parameters, e.g. rotation  $R(\theta)$ , where the angle  $\theta$  can take continuous values.

They are subdivided into two classes:

- Symmetries in space-time (act simultaneously on space and time): translations, rotations
- Internal symmetries: act on internal quantum numbers: isospin symmetry. They transform one particle into another particle with different quantum numbers but with the same mass and they are classified as *global* (transformation parameters do not depend on space-time coordinates) and *local or gauge* (transformation parameters depend on space-time coordinates) symmetries. Gravity has gauge symmetry; we can measure the gravitational potential energy anywhere in the Universe and the difference between the potential energies of a body measured in two different space points is always the same. [5]

Global symmetries are summarized by Noether’s theorem: any differentiable symmetry of a physical system has a corresponding conservation law. [6]

Quantum field theories based on gauge symmetries are known as Gauge Theories. Quantum Electrodynamics (QED) is based on  $U(1)_{em}$  group, Quantum Chromodynamics (QCD) on  $SU(3)_C$  group and Electroweak Theory on the combined  $SU(2)_L \times U(1)_Y$  group. The

Standard Model of Elementary Particles envelops all gauge theories describing the fundamental interactions:  $SU(3)_c \times SU(2)_L \times U(1)_Y$ . [4]

In 1973 the discovery of Neutral Currents was the first clear indication that the Standard Model (SM) gives a correct interpretation of the electromagnetic interaction. This allowed the first estimation of the masses of the weak interaction bosons, W and Z. Other interesting characteristics of SM are quark mixing and CP violation. After the experimental evidence of  $d - s$  mixing, the existence of the **charm** ( $c$ ) quark has been theorized, as the partner for the **strange** ( $s$ ) quark in weak interactions. Charm quark has been discovered in 1974 through the  $J/\Psi$  particle, the  $c\bar{c}$  bound state. The discovery of  $\tau$  and  $\nu_\tau$  leptons and the **beauty** ( $b$ ) quark confirmed the scenario of three families of quarks. This was completed in 1994 when the **top** ( $t$ ) quark was discovered. Quark mixing in the hypothesis of three generations of quarks is described by the Cabibbo-Kobayashi-Maskawa (CKM) matrix which incorporates the phase necessary to describe the CP violation in Standard Model. [7]

In 1964, Cronin, Fitch et al. observed experimentally for the first time the CP violation in weak decays, the effect being quite small,  $\sim 0.2$ . [8]

### 1.3 CP symmetry violation - history

In 1954, M. Gell-Man talks about some heavy bosons,  $\theta^0$ , which decay into a  $\pi^+\pi^-$  pair. Studying charge conjugation invariance he shows that  $\theta^0$  must be considered a mix of particles with different lifetimes, each lifetime having its own characteristic decay modes. These heavy bosons are in fact  $K^0$  and anti- $K^0$ . [9]

Kaons are the lightest strange particles, thus their decay implies the violation of strangeness. This quantum number is conserved by strong interaction; consequently, the kaon decay is a pure weak interaction phenomenon.

In time, a  $K^0$  initial state evolves into a mixture of  $K^0$  and  $\overline{K}^0$  states. The evolution in time of this system is determined by solving the time dependant Schrodinger equation, where the Hamiltonian,  $\mathcal{H}$ , is a diagonal matrix. If the CP symmetry is taken into account,  $\mathcal{H}$  is no longer diagonal so the  $K^0$  and  $\overline{K}^0$  states are no longer eigen functions for  $\mathcal{H}$  but their sum ( $K_1$ ) and their difference ( $K_2$ ) are. These new states have different lifetimes and they are their own antiparticles but, one state is even with respect to CP symmetry while the other is odd. [9]

Studies on the decay modes of these particles have shown that weak decays break the CP symmetry but the effect is very small,  $\sim 0.2\%$ . A new law of physics has to be constructed to account for this small effect thus, two new states,  $K_S$  and  $K_L$ , are introduced, which are rotated by a small angle with respect to  $K_1$  si  $K_2$  (Figure 1.3)[9]

$$\begin{aligned} |K_L\rangle &= |K_2\rangle + \varepsilon |K_1\rangle \\ |K_S\rangle &= |K_1\rangle + \varepsilon |K_2\rangle \end{aligned}, \quad |\varepsilon| \ll 1 \quad (\text{Eq. 1.1})$$

$$\text{Where } |\varepsilon| = \left| \frac{A(K_L \rightarrow \pi^+ \pi^-)}{A(K_S \rightarrow \pi^+ \pi^-)} \right| \quad (\text{Eq. 1.2})$$

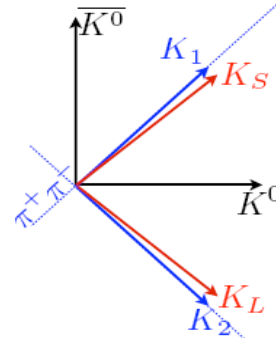


Figure 1.3 Representation of states in K system

Experimentally, a value different from 0 was found for  $\varepsilon$ ,  $(.282 \pm 0.017) \times 10^{-3}$ . If the CP symmetry would not be broken in Nature,  $\varepsilon$  would be 0 and  $K_L$  could not decay into two pions. In reality,  $K_L$  actually decays more often into three pions, thus the longer lifetime found experimentally.[9]

Three types of quarks were known in the '60s. The interaction between them was being modeled similarly to the interaction between leptons but this scenario led to a very short lifetime for the neutron and strange particles. It was concluded that the weak interaction coupling is systematically different for particular processes. Nicola Cabibbo introduced the idea that, for the d quark in weak interactions, the weak eigen state,  $d'$  is different from the mass eigen state, d.  $d'$  seen by the exchange boson W is in fact a super-position of d and s states.[10]

If a  $d'$  state exists, based on the same reasoning, there is also an  $s'$  state, as depicted in Figure 1.4. If this is true,  $d'$  and  $s'$  can be expressed as rotated states of d and s, (Eq. 1.3) [10]:

$$\begin{pmatrix} d' \\ s' \end{pmatrix} = \begin{pmatrix} \cos \theta_C & \sin \theta_C \\ -\sin \theta_C & \cos \theta_C \end{pmatrix} \begin{pmatrix} d \\ s \end{pmatrix} \quad (\text{Eq. 1.3})$$

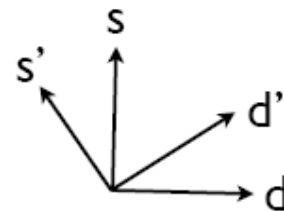


Figure 1.4.  $d'$  and  $s'$  states

Then, if  $s'$  exists, similarly to the  $d$  quark, why would there not be an  $u$ -type partner for it:  $\begin{pmatrix} u \\ d' \end{pmatrix}_L, \begin{pmatrix} c \\ s' \end{pmatrix}_L$  [r]. This is how the existence of the  $c$  quark has been theoretically predicted.

In 1972, when trying to describe the CP violation, Kobayashi and Maskawa demonstrate that the weak interaction cannot be realistically modeled based on a four field configuration, as proposed by Glashow, Iliopoulos and Maiani in 1970 [11]. They propose a sextuplet of fields to explain the CP violation:

$$\begin{pmatrix} \cos \theta_1 & -\sin \theta_1 \cos \theta_3 & -\sin \theta_1 \sin \theta_3 \\ \sin \theta_1 \cos \theta_2 & \cos \theta_1 \cos \theta_2 \cos \theta_3 - \sin \theta_2 \sin \theta_3 e^{i\delta} & \cos \theta_1 \cos \theta_2 \sin \theta_3 + \sin \theta_2 \cos \theta_3 e^{i\delta} \\ \sin \theta_1 \sin \theta_2 & \cos \theta_1 \sin \theta_2 \cos \theta_3 + \cos \theta_2 \sin \theta_3 e^{i\delta} & \cos \theta_1 \sin \theta_2 \sin \theta_3 - \cos \theta_2 \sin \theta_3 e^{i\delta} \end{pmatrix} \quad (\text{Eq. 1.4})$$

CP violation effects can be obtained due to the interference between different currents components. Thus, this model predicts three generations of quarks [12]:

$$\begin{pmatrix} u \\ d' \end{pmatrix}_L, \begin{pmatrix} c \\ s' \end{pmatrix}_L, \begin{pmatrix} t \\ b' \end{pmatrix}_L \quad \text{with} \quad \begin{pmatrix} d' \\ s' \\ b' \end{pmatrix} = V_{CKM} \begin{pmatrix} d \\ s \\ b \end{pmatrix} \quad (\text{Eq. 1.5})$$

$V_{CKM}$  is the Cabibbo-Kobayashi-Maskawa (CKM) matrix, it is a  $3 \times 3$  unitarity matrix introduced to describe the strength of the flavor changing weak interactions between the three generations of quarks. Basically, it expresses the difference between free and weakly interacting quarks.[2]

$$\begin{bmatrix} V_{ud} & V_{us} & V_{ub} \\ V_{cd} & V_{cs} & V_{cb} \\ V_{td} & V_{ts} & V_{tb} \end{bmatrix} \begin{bmatrix} |d\rangle \\ |s\rangle \\ |b\rangle \end{bmatrix} = \begin{bmatrix} |d'\rangle \\ |s'\rangle \\ |b'\rangle \end{bmatrix} \quad (\text{Eq. 1.6})$$

$V_{CKM}$  must be unitary, e.g.  $t$  can decay in a  $b$ ,  $s$  or  $d$  quark, meaning  $|V_{td}|^2 + |V_{ts}|^2 + |V_{tb}|^2 = 1$ . An  $N \times N$  matrix has  $2N^2$  parameters. There are  $N^2 - 2N + 1$  physical parameters out of which  $N(N-1)/2$  are rotation angles. Thus, for  $N=3$  there are 4 parameters: 3 rotation angles and an irreducible complex phase. [7]

## 1.4. Standard Model parametrization of the CKM matrix

This parametrization is based on the three Euler rotations and starts from three orthogonal and normalized vectors:  $|d\rangle$ ,  $|s\rangle$  and  $|b\rangle$ . [4]

First, a rotation by an angle  $\theta_{12}$  around vector  $|b\rangle$  is applied:

$$\begin{aligned} |d\rangle' &= \cos \theta_{12} |d\rangle + \sin \theta_{12} |s\rangle, \\ |s\rangle' &= -\sin \theta_{12} |d\rangle + \cos \theta_{12} |s\rangle, \\ |b\rangle' &= |b\rangle \end{aligned} \quad (\text{Eq. 1.7})$$

If  $\cos \theta_{12} = c_{12}$  and  $\sin \theta_{12} = s_{12}$ , the matrix form can be written as [4]:

$$\begin{pmatrix} |d\rangle' \\ |s\rangle' \\ |b\rangle' \end{pmatrix} = \begin{pmatrix} c_{12} & s_{12} & 0 \\ -s_{12} & c_{12} & 0 \\ 0 & 0 & 1 \end{pmatrix} \times \begin{pmatrix} |d\rangle \\ |s\rangle \\ |b\rangle \end{pmatrix} \quad \text{where } |D\rangle' = \begin{pmatrix} |d\rangle' \\ |s\rangle' \\ |b\rangle' \end{pmatrix} \quad \text{and } |D\rangle = \begin{pmatrix} |d\rangle \\ |s\rangle \\ |b\rangle \end{pmatrix} \quad (\text{Eq. 1.8})$$

A rotation by an angle  $\theta_{13}$  around  $|s\rangle'$  is applied next. The  $\delta$  phase which does not conserve the CP symmetry is also introduced at this stage [4]:

$$\begin{aligned} |d\rangle'' &= c_{13} |d\rangle' + s_{13} e^{-i\delta} |b\rangle', \\ |s\rangle'' &= |s\rangle', \\ |b\rangle'' &= -s_{13} e^{i\delta} |d\rangle' + c_{13} |b\rangle' \end{aligned} \quad (\text{Eq. 1.9})$$

And the matrix form:

$$|D\rangle'' = V'' |D\rangle' \quad \text{where } V'' = \begin{pmatrix} c_{13} & 0 & s_{13} e^{-i\delta} \\ 0 & 1 & 0 \\ -s_{13} e^{i\delta} & 0 & c_{13} \end{pmatrix} \quad (\text{Eq. 1.10})$$

The last rotation is around vector  $|d\rangle''$  with the angle  $\theta_{23}$ :

$$\begin{aligned} |d\rangle''' &= |d\rangle'', \\ |s\rangle''' &= c_{23} |s\rangle'' + s_{23} |b\rangle'', \\ |b\rangle''' &= -s_{23} |s\rangle'' + c_{23} |b\rangle'' \end{aligned} \quad (\text{Eq. 1.11})$$

$$\text{Thus: } |D\rangle''' = V''' |D\rangle'' \quad \text{and } V''' = \begin{pmatrix} 1 & 0 & 0 \\ 0 & c_{23} & s_{23} \\ 0 & -s_{23} & c_{23} \end{pmatrix} \quad (\text{Eq. 1.12})$$

In summary,  $|D\rangle''' = V |D\rangle$  with  $V = V''' V'' V'$  where  $V$  is the unitary matrix and the general 3x3 matrix form is [4]:

$$V = \begin{pmatrix} 1 & 0 & 0 \\ 0 & c_{23} & s_{23} \\ 0 & -s_{23} & c_{23} \end{pmatrix} \begin{pmatrix} c_{13} & 0 & s_{13}e^{-i\delta} \\ 0 & 1 & 0 \\ -s_{13}e^{i\delta} & 0 & c_{13} \end{pmatrix} \begin{pmatrix} c_{12} & s_{12} & 0 \\ -s_{12} & c_{12} & 0 \\ 0 & 0 & 1 \end{pmatrix} \quad (\text{Eq. 1.13})$$

$$\text{or: } V = \begin{pmatrix} c_{12}c_{13} & s_{12}c_{13} & s_{13}e^{-i\delta} \\ -s_{12}c_{23} - c_{12}s_{23}s_{13}e^{i\delta} & c_{12}c_{23} - s_{12}s_{23}s_{13}e^{i\delta} & s_{23}c_{13} \\ s_{12}s_{23} - c_{12}c_{23}s_{13}e^{i\delta} & -c_{12}s_{23} - s_{12}c_{23}s_{13}e^{i\delta} & c_{23}c_{13} \end{pmatrix} \quad (\text{Eq. 1.14})$$

The standard parametrization of the CKM matrix was proposed by Chau si Keung and it is the product of three complex rotation matrices and a phase corresponding to CP violation,  $\delta$ . The rotations are represented by the Euler angles and describe the mixing angles between the three generations of quarks. [4]

The angles  $\theta_{ij}$  can be chosen such that they are in the first quadrant so  $s_{ij}, c_{ij} \geq 0$ . Experimental measurements indicated that  $s_{13} \ll s_{23} \ll s_{12} \ll 1$ . The use of this hierarchy is very advantageous in Wolfenstein parametrization. [13]

Wolfenstein starts from the CKM matrix which, in the Standard Model, it describes the quark mixing in weak interaction current [4]:

$$V_{CKM} = \begin{pmatrix} V_{ud} & V_{us} & V_{ub} \\ V_{cd} & V_{cs} & V_{cb} \\ V_{td} & V_{ts} & V_{tb} \end{pmatrix} \quad (\text{Eq. 1.15})$$

$V_{ij}$  describes the transition amplitude between  $i$  and  $j$  quarks and  $V_{ij}^*$  the transition amplitude between  $i$  and  $j$  anti-quarks. Basically, the CKM matrix gives the probability of a quark  $q$  to decay into a quark  $q'$ . This transition probability is proportional to  $|V_{qq'}|^2$ . [5]

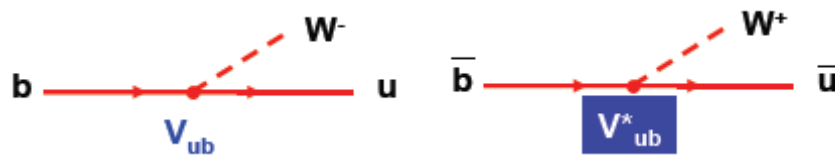


Figure 1.5 Examples of weak decays, where  $V_{ub}$  is the coupling

The irreducible  $\delta$  phase results in the  $V_{ub}^* \neq V_{ub}$  identity, which suggests that matter and antimatter behave different, consequently CP violation exists. [3]

Matrix elements are determined from ratios of decay rates. For example,  $|V_{ud}|$  is extracted by comparing the decay rate of neutrons to the decay rate of muons. Their ratio is proportional to  $|V_{ud}|^2$ . It was found that  $|V_{ud}| = 0.9735 \pm 0.0008$  which is approximately 1. [4]

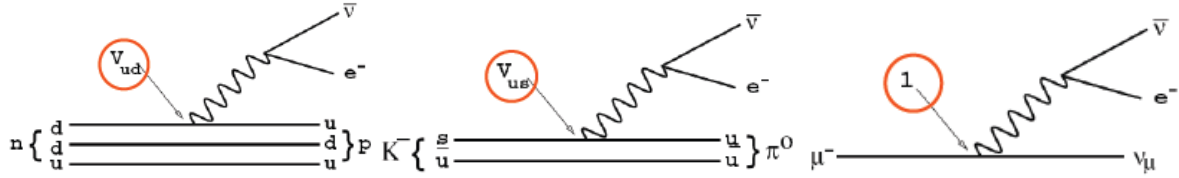


Figure 1.6 Feynmann diagrams describing neutron, kaon and muon decays

Analogous,  $|V_{us}|$  is determined by comparing the semileptonic decay rate of  $K^-$  with the decay rate of the muon which results in  $|V_{us}| = 0.2196 \pm 0.0023$ . This value is denoted  $\lambda$ . Measurements on lifetimes of B particles,  $\tau_B$ , indicate that  $V_{cb} \approx 0.06$  which suggests proportionality to  $\lambda^2$  rather than  $\lambda$ . A new parameter, A, is introduced such that  $V_{cb} = A\lambda^2$  with  $A \approx 5/4$ . The other terms of the CKM matrix are proportional to  $\lambda^3$ . The unitarity condition allows for the following choice of terms [4]:

$$V = \begin{pmatrix} 1 - \frac{1}{2}\lambda^2 & \lambda & \lambda^3 A(\rho - i\eta) \\ -\lambda & 1 - \frac{1}{2}\lambda^2 & A\lambda^2 \\ \lambda^3 A(1 - \rho - i\eta) & -A\lambda^2 & 1 \end{pmatrix} \quad (\text{Eq. 1.16})$$

where two new parameters have been introduced,  $\rho$  and  $\eta$ . For the CKM matrix parametrization, Wolfenstein [13] uses the following notations:

$$\begin{aligned} \lambda &= s_1 \\ A\lambda^2 &= (s_2^2 + s_3^2 + 2s_2s_3\cos\delta)^{1/2} \\ A^2\lambda^4\eta &= s_2s_3\sin\delta \\ A\lambda^2(\rho^2 + \eta^2)^{1/2} &= s_3, \text{ or } A\lambda^2[(1-\rho)^2 + \eta^2]^{1/2} = s_3 \end{aligned} \quad (\text{Eq. 1.17})$$

Only three of the above equations are independent. It was decided that the phase responsible for CP asymmetry would be introduced only through  $\lambda^3$  terms.

As  $\lambda$  and A were known with satisfactory precision, work was being done to find new empirical constraints on  $\rho$  and  $\eta$  parameters. The only significant constraint is given by the ratio between  $b \rightarrow u$  and  $b \rightarrow c$  transitions which is  $|V_{ub}/V_{cb}| < 0.2$  or  $\rho^2 + \eta^2 < 1$ .

This information leads to:

$$s_{12} = \lambda = \frac{|V_{us}|}{\sqrt{|V_{ud}|^2 + |V_{us}|^2}}, \quad s_{23} = A\lambda^2 = \lambda \left| \frac{V_{cb}}{V_{us}} \right|, \quad (\text{Eq. 1.18})$$

$$s_{13}e^{i\delta} = A\lambda^3(\bar{\rho} + i\bar{\eta}) = V_{ub}^* = \frac{A\lambda^3(\bar{\rho} + i\bar{\eta})\sqrt{1 - A^2\lambda^4}}{\sqrt{1 - \lambda^2[1 - A^2\lambda^4(\bar{\rho} + i\bar{\eta})]}}$$

This parametrization makes sure that the term  $\bar{\rho} + i\bar{\eta} = -(V_{ud}V_{ub}^*)/(V_{cd}V_{cb}^*)$  is independent on the phase and that the CKM matrix, expressed in terms of  $\lambda$ ,  $A$ ,  $\bar{\rho}$  and  $\bar{\eta}$  is unitary in all powers of  $\lambda$ . [4]

The four parameters used in the calculations, are known with different precision,  $\lambda$  is known within 0.5%,  $A$  within 2%,  $\rho$  between 15 to 20% and  $\eta$  up to 5%. CKM elements are fundamental parameters of the Standard Model, consequently, their precise determination is mandatory. The CKM unitarity condition,  $VV^\dagger = V^\dagger V = 1$  can be expressed as 9 relations of the type  $\sum_{k=1}^n V_{ik}V_{jk}^* = \delta_{ij}$  which can be represented as triangles in the complex plane [7]:

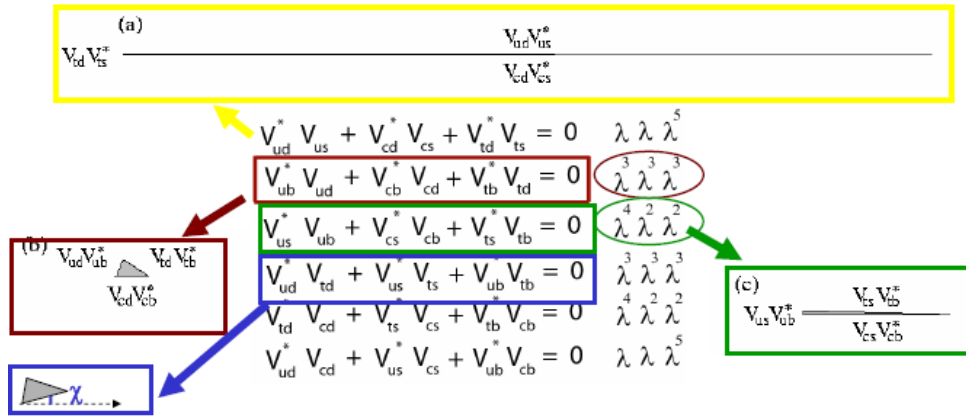


Figure 1.6 Unitarity triangles

$B_d$  triangle, represented in Figure 1.7 is given by  $V_{ub}^*V_{ud} + V_{cb}^*V_{cd} + V_{tb}^*V_{td} = 0$ . If all terms are normalized to  $V_{cd}V_{cb}^*$ ,

$$\frac{V_{ud}V_{ub}^*}{V_{cd}V_{cb}^*} + \frac{V_{cd}V_{cb}^*}{V_{cd}V_{cb}^*} + \frac{V_{td}V_{tb}^*}{V_{cd}V_{cb}^*} = 0 \quad (\text{Eq. 1.19})$$

the triangle will be aligned on the real axis, as shown in Figure 1.8. The area allowed in the  $\rho - \eta$  plane can be easily determined through this unitarity triangle (UT).

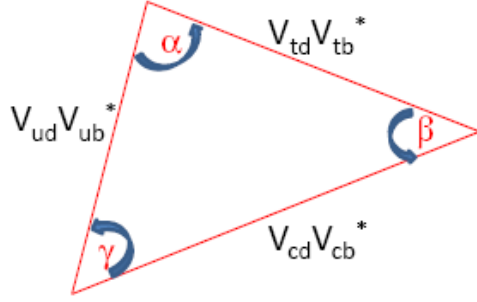


Figure 1.7  $B_d$  triangle

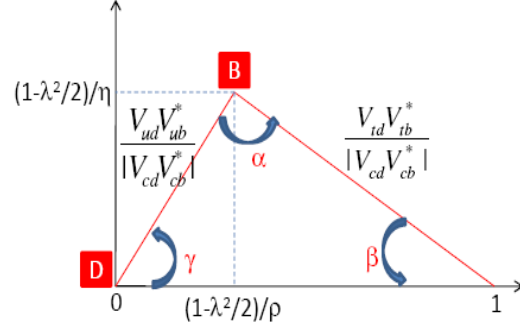


Figure 1.8 Unitarity triangle aligned on the real axis

The apex of the triangle is given by Eq. 1.20 and depicted in Figure 1.8:

$$\bar{\rho} + i\bar{\eta} = -\frac{V_{ud}V_{ub}^*}{V_{cd}V_{cb}^*} \Rightarrow \rho + i\eta = \frac{\sqrt{1-A^2\lambda^4}(\bar{\rho} + i\bar{\eta})}{\sqrt{1-\lambda^2}[1-A^2\lambda^4(\bar{\rho} + i\bar{\eta})]} \quad (\text{Eq. 1.20})$$

where  $\bar{\rho}$  and  $\bar{\eta}$  can be expressed as Taylor series of  $\rho$  and  $\eta$ :

$$\bar{\rho} = \rho - \frac{1}{2}\rho\lambda^2 + \dots \quad \text{and} \quad \bar{\eta} = \eta - \frac{1}{2}\eta\lambda^2 + \dots \quad (\text{Eq. 1.21})$$

Thus,  $R_u$  and  $R_t$  sides are [13]:

$$R_u = \left| \frac{V_{ud}V_{ub}^*}{V_{cd}V_{cb}^*} \right| = \sqrt{\rho^2 + \eta^2} \quad \text{and} \quad R_t = \left| \frac{V_{td}V_{tb}^*}{V_{cd}V_{cb}^*} \right| = \sqrt{(1-\rho)^2 + \eta^2} \quad (\text{Eq. 1.22})$$

The sides of the un-scaled triangle are calculated in the following relations:

$$\begin{aligned} V_{td}V_{tb}^* &= A\lambda^3(1-\rho-i\eta) + A\lambda^5(\rho+i\eta) \\ V_{ud}V_{ub}^* &= A\lambda^3(\rho+i\eta)\lambda(1-\lambda^2/2) \\ V_{cd}V_{cb}^* &= -A\lambda^3 \end{aligned} \quad (\text{Eq. 1.23})$$

which give  $\text{Re}\left(\frac{V_{ud}V_{ub}^*}{|V_{cd}V_{cb}^*|}\right) = \rho\left(1 - \frac{\lambda^2}{2}\right)$  and  $\text{Im}\left(\frac{V_{ud}V_{ub}^*}{|V_{cd}V_{cb}^*|}\right) = \eta\left(1 - \frac{\lambda^2}{2}\right)$ . The angles of

the triangle are extracted in a similar fashion, Figure 1.8, and expressed in Eq. 1.24 to 1.26:

$$\beta = \arg\left(\frac{V_{td}V_{tb}^*}{|V_{cd}V_{cb}^*|}\right) = \text{arctg}\left(\frac{(1-\lambda^2/2)\eta}{1-(1-\lambda^2/2)\rho}\right) \quad (\text{Eq. 1.24})$$

$$\gamma = \arg\left(\frac{V_{ud}V_{ub}^*}{|V_{cd}V_{cb}^*|}\right) = \text{arctg}\left(\frac{\eta}{\rho}\right) \quad (\text{Eq. 1.25})$$

$$\alpha + \beta + \gamma = \pi \quad (\text{Eq. 1.26})$$

The CKM phase in Standard Parametrization is given by  $\delta = \gamma + A^2 \lambda^4 \eta + O(\lambda^6)$ . And the relations between the angles and the  $\rho$  and  $\eta$  coordinates are calculated in Eq. 1.27:

$$\begin{aligned} \cos \gamma &= \bar{\rho} / R_u, \quad \sin \gamma = \bar{\eta} / R_u \\ \cos \beta &= (1 - \bar{\rho}) / R_t, \quad \sin \beta = \bar{\eta} / R_t \end{aligned} \quad (\text{Eq. 1.27})$$

Also, as depicted in Figure 8, the BD side can be expressed as:

$$\overline{BD} = \left| \frac{V_{ud} V_{ub}^*}{V_{cd} V_{cb}^*} \right| = \sqrt{\bar{\rho}^2 + \bar{\eta}^2} = \left( 1 - \frac{\lambda^2}{2} \right) \frac{1}{\lambda} \left| \frac{V_{ub}}{V_{cb}} \right| \quad (\text{Eq. 1.28})$$

Eq. 1.28 contains the limits on the allowed interval where the apex of the unitrity triangle can be found in the  $(\rho, \eta)$  plane. This constrain is a circle with a radius equal to BD, Figure 1.10 a) [14]. Another very precise constrain in the  $(\rho, \eta)$  plane is given by the mass difference in  $B_s$  and  $B_d$  systems,  $\Delta m_d$  and  $\Delta m_s$ . Both  $\Delta m_d$  and  $\Delta m_d / \Delta m_s$  are proportional to  $(1 - \bar{\rho})^2 + \bar{\eta}^2$ , which is the equation of a circle with the origin in  $(1,0)$  in the  $(\rho, \eta)$  plane as shown in Figure 1.10 b) and c). [14]

Figure 1.10 depicts all constrains on the sides of the unitarity triangles and they are accessible through measurements on decay or mixing rates. Other constrains extracted from measurements on CP asymmetries concern the angles of the triangles and they are shown in Figure 1.11. [15]

The angles  $\beta$  and  $\gamma = \delta$  are directly related to  $V_{td}$  and  $V_{ub}$  CKM matrix elements through the following relations:

$$V_{td} = |V_{td}| e^{-i\beta} \quad \text{and} \quad V_{ub} = |V_{ub}| e^{-i\gamma} \quad (\text{Eq. 1.29})$$

Thus, the unitarity condition can be rewritten as in Eq. 1.30:

$$R_u e^{i\gamma} + R_t e^{-i\beta} = 1 \quad (\text{Eq. 1.30})$$

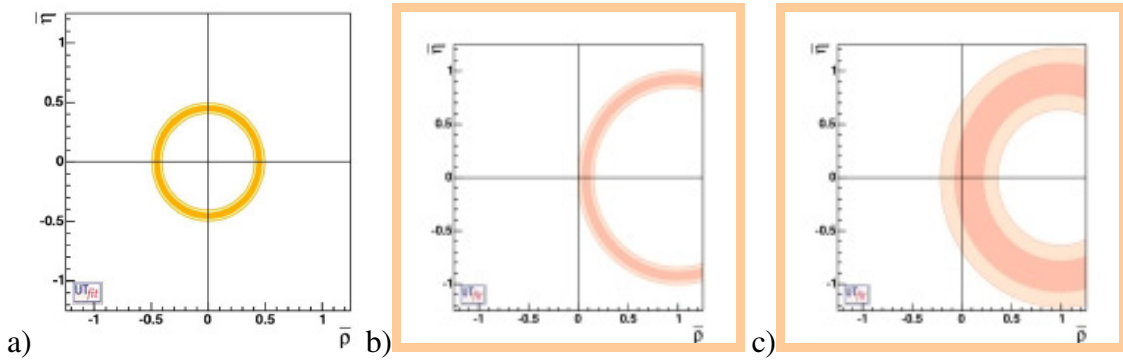


Figure 1.10 Constrains given by a)  $V_{ub}/V_{cb}$  b)  $\Delta m_s$  and c)  $\Delta m_d$  [14]

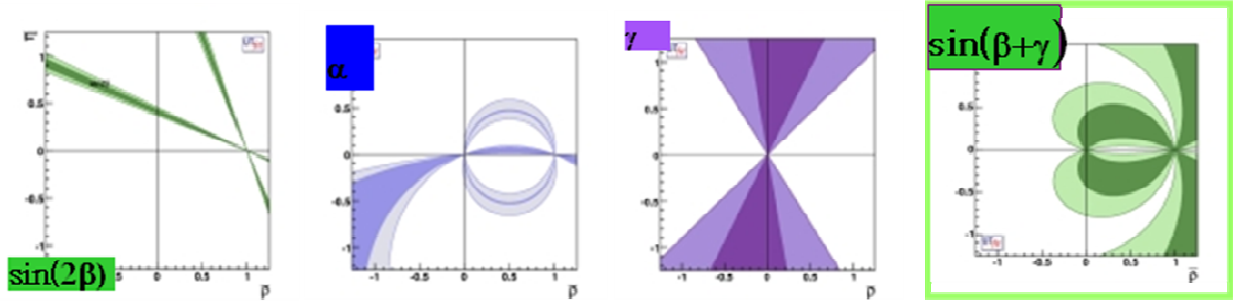


Figure 1.11 Constrains due to determinations on the angles of the unitarity triangles [15]

All constraints given by the unitarity condition of the CKM matrix with three generations of quarks reduce noticeably the allowed intervals for some of the CKM elements. [16]. They are all represented in Figure 1.12 [17]

$$\Delta m_d, \Delta m_s, V_{ub}, V_{cb}, \delta_K + \cos 2\beta + \beta + \alpha + \gamma + 2\beta + \gamma$$

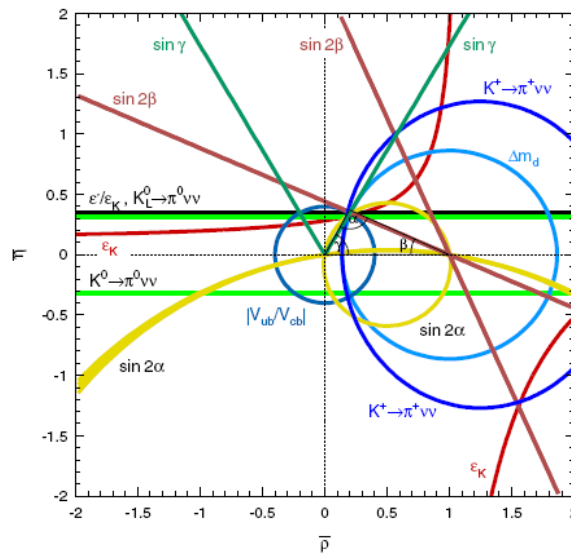


Fig. 1.12 Schematic representation of all CKM constrains in the complex plane [17]

## 1.5 CKM elements

### 1.5.1. Magnitudes

Matrix elements are usually determined from ratios of decay rates. As mentioned before,  $|V_{ud}|$  and  $|V_{us}|$  are extracted by comparing the decay rate of neutrons or  $K^-$ , respectively, to the decay rate of muons. It was determined that  $|V_{ud}| = 0.9735 \pm 0.0008$  and  $|V_{us}| = 0.2196 \pm 0.0023$ . [18]

$|V_{cd}| = 0.230 \pm 0.011$  [18] is calculated from semi-leptonic decays of charmed particles.

The difference between the ratio  $\frac{2 \text{ muons production}}{1 \text{ muon production}}$  in neutrino and anti-neutrino beams is proportional to the product between  $|V_{ud}|^2$  and the branching fraction of semi-leptonic charmed mesons decay,  $B_\mu = 0.0873 \pm 0.0052$ .

Measurements on  $|V_{cs}|$  have been performed at LEP-2 in *on-shell* (decays where the classical equations of motions are considered) decays of  $W^\pm$ . The direct measurement of  $|V_{cs}|$  is possible in semi-leptonic decays of  $D$  meson or leptonic decays of  $D_s$  meson. Based on theoretical calculations of form factors found in  $D \rightarrow K\ell\nu$  and  $D \rightarrow \pi\ell\nu$  decays allowed a theoretical prediction of  $|V_{cs}| = 0.957 \pm 0.017_{\text{exp}} \pm 0.093_{\text{teor}}$ . [18]

$|V_{cb}| = 0.0402 \pm 0.0019$  is determined from the ratio between the decay rate of  $B^0 \rightarrow D^{*-} l^+ \nu$  and the decay rate of muon. For the calculation of  $V_{ub}$  the decay rates of  $B^0 \rightarrow D^{*-} l^+ \nu$  and  $B^0 \rightarrow \pi^- l^+ \nu$  channels are compared. The ratio between the two decays is proportional to  $(V_{ub}/V_{cb})^2$ . Inclusive decays of the type  $B \rightarrow X_u \ell \bar{\nu}$  are also taken into consideration for the evaluation of  $V_{ub}$  but high backgrounds due to  $B \rightarrow X_c \ell \bar{\nu}$  decays introduce large errors on these measurements. A mean value for  $V_{ub}$  obtained from both inclusive and exclusive channels is  $|V_{ub}| = (4.31 \pm 0.30) \times 10^{-3}$ . [18]

$|V_{td}|$  and  $|V_{ts}|$  cannot be determined from measurements involving the top quark, consequently,  $B - \bar{B}$  oscillations mediated by box diagrams or rare decays in K and B channels mediated by loop diagrams are envisaged. Considering  $|V_{tb}| = 1$  it was found that  $|V_{td}| = (7.4 \pm 0.8) \times 10^{-3}$ . DØ si CDF experiments have established new theoretical constrains on  $|V_{td}|/|V_{ts}| = 0.208^{+0.008}_{+0.006}$ . Using the identity  $V_{cb}V_{cs}^* \approx -V_{tb}V_{ts}^*$  it is found that  $|V_{ts}| = (40.6 \pm 2.7) \times 10^{-3}$ . [18]

Direct measurements on  $|V_{tb}|$  from top quark decays take into account the branching fractions:

$$R = B(t \rightarrow Wb)/B(t \rightarrow Wq) = |V_{tb}|^2 / \sum_q |V_{tq}|^2 = |V_{tb}|^2, \text{ where } q = b, s, d. \quad (\text{Eq. 1.31})$$

CDF [19] and DØ [20] studies on Tevatron data collected during the second run indicate  $R = 1.12_{-0.23}^{+0.27}$  and  $R = 1.03_{-0.17}^{+0.19}$ , respectively. This results establish a lower limit on  $V_{tb}$ ,  $|V_{tb}| > 0.78$ . New constrains from the electroweak sector indicate  $|V_{tb}| = 0.77_{-0.24}^{+0.18}$ . [18]

## 1.5.2 CKM phases

CP violation (CPV) is related to the phases of the CKM matrix elements, thus, measurements on CPV observables can be exploited in order to find constrains on the angles of the unitarity CKM triangles and on the  $\bar{\rho}$ ,  $\bar{\eta}$  parameters. There is direct and indirect CP violation. The transition amplitude in indirect CPV alters the total strangeness, before and after the decay, by two units, ( $\Delta S=2$ ). Direct CPV refers to decays where  $\Delta S=1$  and allows the decay of an *odd* initial state into an *even* final state, and vice-versa. [21]

CPV in  $K \rightarrow \pi\pi$  decays is directly related to the ratio  $\varepsilon'/\varepsilon$ , where  $\varepsilon = \frac{A(K_L \rightarrow (\pi\pi)_{I=0})}{A(K_S \rightarrow (\pi\pi)_{I=0})}$  is a very precise measure of the *indirect* CPV while the *direct* CPV

implies the interference of at least two amplitudes with different phases thus, it is expressed by  $\varepsilon'$ :

$$\varepsilon' = \frac{1}{\sqrt{2}} \left[ \frac{A(K_L \rightarrow (\pi\pi)_{I=2})}{A(K_S \rightarrow (\pi\pi)_{I=0})} - \varepsilon \cdot \omega \right] \quad \text{with} \quad \omega = \frac{A(K_S \rightarrow (\pi\pi)_{I=2})}{A(K_S \rightarrow (\pi\pi)_{I=0})} \quad (\text{Eq. 1.32})$$

Measurements on  $\varepsilon'$  allow a qualitative test on the CKM mechanism. A value different from 0 is a clear evidence of the direct CP violation. It was found that  $\text{Re}(\varepsilon'/\varepsilon) = (1.67 \pm 0.23) \times 10^{-3}$ . [21]

***β or φ<sub>1</sub>***

CPV measurements in B decays provide direct information on the angles of the unitarity triangles. Time dependent CP asymmetry in decays of B mesons into a common final state,  $f$ , for  $B^0$  and  $\bar{B}^0$  is given by [18]:

$$\mathcal{A}_f = \frac{\Gamma(\bar{B}^0(t) \rightarrow f) - \Gamma(B^0(t) \rightarrow f)}{\Gamma(\bar{B}^0(t) \rightarrow f) + \Gamma(B^0(t) \rightarrow f)} = S_f \sin(\Delta m t) - C_f (\cos \Delta m t) \quad (\text{Eq. 1.33})$$

$$\text{where } S_f = \frac{2 \text{Im} \lambda_f}{1 + |\lambda_f|^2}, \quad C_f = \frac{1 - |\lambda_f|^2}{1 + |\lambda_f|^2}, \quad \lambda_f = \frac{q}{p} \frac{\bar{A}_f}{A_f} \quad (\text{Eq. 1.34})$$

The ratio  $q/p$  describes the  $B^0 - \bar{B}^0$  mixing and is approximately equal to  $V_{tb}^* V_{td} / V_{tb} V_{td}^* = e^{-2i\beta + O(\lambda^4)}$ .  $A_f$  ( $\bar{A}_f$ ) is the decay amplitude of  $B^0 \rightarrow f$  ( $\bar{B}^0 \rightarrow f$ ).

If  $f$  is a CPV eigen-state then  $|A_f| = |\bar{A}_f|$ ,  $C_f = 0$  and  $S_f = \sin(\arg \lambda_f) = \eta_f \sin 2\phi$  where  $\eta_f$  is the eigen-value of the eigen-state  $f$  and  $2\phi$  is the phase difference between the two decay modes  $B^0 \rightarrow f$  and  $B^0 \rightarrow \bar{B}^0 \rightarrow f$ .  $b \rightarrow c\bar{c}s$  transitions which result in CPV eigen-states allow the determination of  $S_f = -\eta_f \sin 2\beta$ . BABAR and Belle performed precise measurements on  $\sin 2\beta$  and found  $\sin 2\beta = 0.687 \pm 0.032$ . [18]

### **$\alpha$ or $\phi_2$**

$\alpha$  is the angle between  $V_{ib}^*V_{td}$  and  $V_{ub}^*V_{ud}$ , as a consequence,  $\sin 2\alpha$  can only be extracted from time dependent CP asymmetries in  $b \rightarrow u\bar{u}d$  decays. Up until today,  $\alpha$  has been measured in  $B \rightarrow \pi\pi$ ,  $\rho\pi$  and  $\rho\rho$  decays. Measurements on  $B \rightarrow \pi\pi$  decays provide only some large intervals where  $\alpha$  could be found,  $0^\circ < \alpha < 17^\circ$  and  $73^\circ < \alpha < 180^\circ$ . A rough estimation of this angle is given by  $B \rightarrow \rho\rho$  decay,  $(96 \pm 13)^\circ$  while BABAR determined  $\alpha = (113_{-17}^{+27} \pm 6)^\circ$  from  $B \rightarrow \rho\pi$  decays. Based on all measurements, a mean value of  $\alpha = (99_{-8}^{+13})^\circ$  is accepted. [18]

### **$\gamma$ or $\phi_3$**

$\gamma$  does not depend on those CKM matrix elements related to the top quark, as a result, this angle can be directly estimated from tree B decays, with no contribution from beyond Standard Model physics. Belle and BABAR determined  $\gamma$  to be  $\gamma = 68_{-15}^{+14} \pm 13 \pm 11^\circ$  and  $\gamma = 68 \pm 28 \pm 13 \pm 11^\circ$ , respectively. The accepted mean value for  $\gamma$  is  $\gamma = 68_{-12}^{+15}^\circ$ . [18]

## **1.6 Main contributions and outline of the thesis**

In the context of particles physics, this thesis concentrates on testing the performance of LHCb [22] detector at LHC (Larg Hadron Collider) [23] in what concerns rare radiative decays and in optimizing software tools for the simulation of detector components in the Very Forward Region, FCal (Forward Calorimetry) [24], of a detector concept proposed for a future linear collider, ILC (International Liniar Collider) [25] and CLIC (Compact Liniar Collider) [26].

The thesis consists of two parts. The first part presents results obtained on real data collected with the LCHb experiment as well as studies on Monte Carlo simulated data regarding

background sources for radiative decays. The second part concentrates on developing and optimizing the proper simulation tools needed for studies at a detector for a future linear collider.

At LHCb, using the amount of data collected throughout 2010 accelerator run and a part of the data collected in 2011, the main goal is to demonstrate the capability of the LHCb detector of efficiently detecting rare radiative decays in B-sector. The investigation focuses on two representative radiative channels,  $B_d \rightarrow K^* \gamma$  and  $B_s \rightarrow \phi \gamma$ . For these two channels, a common selection is envisaged, and it is expected that the ratio of the signal yield for the two channels is stable with respect to the applied selection criteria. Further on, the variable  $\xi = \frac{S}{\sqrt{S+B}}$  is calculated which is a measure of how much signal is selected with respect to the background. The selection is optimal when  $\xi$  is maximal thus the distribution of this variable as a function of the selection cuts applied for discriminating the signals of interest is investigated and the optimal values for the selection cuts are determined.

Then, using simulated data, an investigation of possible background for the  $B_d \rightarrow K^* \gamma$  is performed and possible background sources are determined. Also, a study on the proper time acceptance for the  $B_d \rightarrow K^* \gamma$  decay is done. The studies on this decay channels are crucial for the calibration of the detector and moreover, this particular radiative decay will be used as control channel for other radiative decays.

The use of simulated data is very advantageous as the user can access information which is not available in real data. The simulation process evolves in a few steps. First, events are generated. These events are then sent through an accurate detector simulation and the interactions in the detector material are described in as much detail as possible. Next, the response of the detector is simulated (a process called digitization) and the reconstruction of events is applied on the output provided by the digitization step. The advantage is that the reconstructed events can ultimately be compared with the generated ones and the reconstruction efficiency can be determined and optimized at any time.

On this premise, at ILC and CLIC, the optimization of the simulation software which is being developed for a detector at a future linear collider is performed and the radiation levels are estimated in some of the detector components.

BeamCal at ILC is one of the detector components which have been investigated. The results concerning BeamCal are presented in this thesis. The simulation of BeamCal has been done using two different software algorithms and background levels (electromagnetic and neutron

showers) have been estimated and compared in the two cases. As all detector concepts proposed for ILC and CLIC are placed inside a solenoidal magnetic field, a study on the effect of different magnetic fields configurations on BeamCal background levels has also been performed.

QD0 at CLIC, the final quadrupolar magnet of the Beam Delivery system which transports and de-magnifies the beams is the second detector component investigated in this study. QD0 is important because, although it is basically an accelerator component, it is placed inside the experiment, in the area closest to the beam-pipe, where the Very Forward Region of the detector is located. Consequently, its design can affect the radiation dose in the other inner detector components, especially BeamCal which is placed right in front of QD0. At ILC, QD0 has a simple cylindrical design and it has been demonstrated [27] that the effect on backgrounds induced in BeamCal is negligible. On the other hand, at CLIC, previous studies based on beamtests and simulation results have shown that the best performance can be obtained using a combination of permanent and warm electromagnet which lead to the proposal of a complex eight-shaped design for QD0. The performance of such a complex shape can be more easily affected and damaged by the high radiation doses generated in the Very Forward Region and moreover, it can negatively affect backgrounds in other inner detector components. For these reasons, a simplified but detailed model of QD0 has been implemented in the simulation algorithm for a detector concept at CLIC and radiation doses have been estimated.

The thesis is structured in 11 chapters. Chapter 1 gives a short overview of Particle Physics at today's level of understanding. Chapters 2 to 6 are related to the results obtained at the LCHb experiment, the LHC accelerator and LCHb detector are briefly described in Chapter 2 and details about the software algorithms are given in Chapter 3. Chapter 4 describes the motivation for studying radiative decays and theoretical aspects on this subject as well as author's results obtained on experimental data collected with the LHCb detector. Chapter 5 and 6 present author's results on background and lifetime acceptance studies when using simulated data at the LHCb experiment.

Chapters 7 to 10 are related to the ILC and CLIC results. A comparison between the two future accelerators and details about the detectors and software algorithms proposed for these colliders are given in Chapters 7 and 8. Author's results on BeamCal at ILC and QD0 at CLIC are reported in Chapters 9 and 10, respectively.

Chapter 11 summarizes the main conclusions.

## 1.7 Published papers

Results presented in this thesis are published in the following ISI journals:

1. FCAL collaboration, **E. Teodorescu**, et al (58 authors), *Forward Instrumentation for ILC Detectors* JINST 5 P12002, 2010
2. C. Coca, W. Lohmann, M. Orlandea, A. Saponov, **E. Teodorescu**, *Expected electromagnetic and neutron doses for the BeamCal at ILD*, Rom. J. Phys., vol 55, no. 7-8, (2010)687-707
3. **E. Teodorescu**, *A look into the effect of supplementary magnetic fields on background levels in BeamCal at ILC*, Proceedings of the 18<sup>th</sup> FCAL Collaboration Workshop, 2011, ISBN: 978-973-0-11117-0, pag 70-74
4. **E. Teodorescu** on behalf of the LHCb collaboration, *Rare Decays at LCHb*, 2011, LHCb-Poster-2011-181, to be published at the SLAC eConf system in the Proceedings of the 6<sup>th</sup> edition of Physics at LHC conference
4. poster prepared by **E. Teodorescu** on behalf of the LHCb collaboration, *Radiative Decays at LCHb*, 2011, LHCb-Poster-2011-189, to be published at the SLAC eConf system in the Proceedings of the 5<sup>th</sup> edition of HEP-Mad conference

Contributions which are directly related to the work of the author inside the LCHb experiment and FCal (Forward Calorimetry) Collaboration at ILC and CLIC, such as monitoring and recording real data with the LHCb detector or optimization studies on simulation algorithms for detectors proposed at ILC and CLIC, are reflected in the following list of papers, published in ISI journals or e-print archives:

1. C. Coca, M. Orlandea, L. Dumitru, **E. Teodorescu**, *High-Performance Computing System for High Energy Physics*, Rom.J. Phys., vol 56, no. 3-4, (2011)359-365
2. ILC Collaboration, **E. Teodorescu** et al., *ILC Reference Design Report: Volume 1- EXECUTIVE SUMMARY*, e-Print: arXiv:0712.1950 [physics.acc-ph]
3. ILC Collaboration, **E. Teodorescu** et al., *International Linear Collider Reference Design Report Volume 2: PHYSICS AT THE ILC, Sep 2007*, e-Print: arXiv:0709.1893 [hep-ph]
4. ILC Collaboration, **E. Teodorescu** et al., *International Linear Collider Reference Design Report Volume 3: ACCELERATOR, Sep 2007*, e-Print: arXiv:0712.2361 [physics.acc-ph]
5. ILC Collaboration, **E. Teodorescu** et al., *ILC Reference Design Report Volume 4 – DETECTORS*, arXiv:0712.2356 [physics.ins-det]
6. ILC/ILD collaboration: **E. Teodorescu** et. al., *International Large Detector Letter of Intent ILD-LoI*, <http://www.ilcild.org/documents/ild-letter-of-intent/LOI.pdf/view>, 2009

7. LHCb Collaboration, **E. Teodoroescu** et al., *Measurement of  $\sigma(pp \rightarrow b \text{ anti-}b X)$  at  $\sqrt{s} = 7 \text{ TeV}$  in the forward region* Phys.Lett.B694(2010)209-216
8. LHCb Collaboration, **E. Teodoroescu** et al., *Prompt  $K_{\text{short}}$  production in  $pp$  collisions at  $\sqrt{s} = 0.9 \text{ TeV}$* , Phys.Lett.B693 (2010)69-80
9. LHCb Collaboration, **E. Teodoroescu** et al., *"First observation of  $B_s^0 \rightarrow D_{s2}^{*+} X \mu \nu$  decays"*, Physics Letters B 698 (2011) 14-20, [arXiv:1102.0348 \[hep-ex\]](https://arxiv.org/abs/1102.0348).)
10. LHCb Collaboration, **E. Teodoroescu** et al., *First observation of  $B_s^0 \rightarrow J/\psi f_0(980)$  decays*, Physics Letters B 698 (2011) 115-122. (Preprint CERN-PH-EP-2011-011, [arXiv:1102.0206 \[hep-ex\]](https://arxiv.org/abs/1102.0206).)
11. LHCb Collaboration, **E. Teodoroescu** et al., *Measurement of  $J/\psi$  production in  $pp$  collisions at  $\sqrt{s} = 7 \text{ TeV}$* , Eur. Phys. J. C 71 (2011) 1645 **LHCB-JPSI-007 (2011-02-28)** (Preprint CERN-PH-EP-2011-018, [arXiv:1103.0423 \[hep-ex\]](https://arxiv.org/abs/1103.0423).)
12. LHCb Collaboration, **E. Teodoroescu** et al., *Search for the rare decays  $B_s^0 \rightarrow \mu^+ \mu^-$  and  $B^0 \rightarrow \mu^+ \mu^-$* , Physics Letters B 699 (2011) 330-340, [arXiv:1103.2465 \[hep-ex\]](https://arxiv.org/abs/1103.2465).)
13. LHCb Collaboration, **E. Teodoroescu** et al., *Determination of  $f_s/f_d$  for 7 TeV  $pp$  collisions and a measurement of the branching fraction of the decay  $B^0 \rightarrow D^- K^+$* , [arXiv:1106.4435](https://arxiv.org/abs/1106.4435); CERN-PH-EP-2011-075; LHCB-PAPER-2011-006, **LHCB-B2DH-005 (2011-05-19)**
14. LHCb Collaboration, **E. Teodoroescu** et al., *Measurement of  $V_0$  production ratios in  $pp$  collisions at  $\sqrt{s} = 0.9$  and  $7 \text{ TeV}$* , CERN-PH-EP-2011-082; [arXiv:1107.0882](https://arxiv.org/abs/1107.0882)
15. LHCb Collaboration, **E. Teodoroescu** et al., *Measurement of the inclusive  $\phi$  cross-section in  $pp$  collisions at  $\sqrt{s} = 7 \text{ TeV}$* , [arXiv:1107.3935](https://arxiv.org/abs/1107.3935); CERN-PH-EP-2011-106
16. LHCb Collaboration, **E. Teodoroescu** et al., *Observation of  $J/\psi$  pair production in  $pp$  collisions at  $\sqrt{s} = 7 \text{ TeV}$* , CERN-PH-EP-2011-135

In direct connection with the subject of this thesis there are also papers published in extenso in conference Proceedings, numerous oral talks and posters presented at International Workshops and Collaboration Meetings and analysis notes published at CERN Document Server (CDS) database:

### Talks

1. **E. Teodoroescu**, *Energy spectra and particle distributions in BeamCal at ILC*, FCAL Collaboration Meeting, May 6-7, 2008, Krakow, Poland, <http://www-zeuthen.desy.de/ILC/fcal/>
2. **E. Teodoroescu**, *"BeamCal simulations with BeCas - Doses and bunch by bunch fluctuations in BeamCal at the ILC"*, FCAL Collaboration Meeting, Berlin-Zeuthen, Germany, 29-30 June 2009, <http://www-zeuthen.desy.de/ILC/fcal/>
3. **E. Teodoroescu**, *"Background Simulations in BeamCal at the ILC"*, Proceedings: Trans-European School of High Energy Physics, Zakopane, Poland, July 7-15, 2009, <http://events.lal.in2p3.fr/TESchool09/TESchool09-proceedings.pdf>

4. **E. Teodorescu**, *QD0@CLIC: Implementation of QD0 in Mokka*, FCAL Collaboration Meeting, Cracow, April 2010, <http://www-zeuthen.desy.de/ILC/fcal/>
5. **E. Teodorescu**, *Mokka simulation studies on the Very Forward Detector components at CLIC and ILC*, Workshop: “High Precision measurements of luminosity at future linear colliders and polarization of lepton beams”, 3-5 October 2010, Tel Aviv, Israel, <http://www-zeuthen.desy.de/ILC/fcal/>
6. **E. Teodorescu**, *Radiation Dose to the QD0 Quadrupole in the CLIC Interaction Region*, CLIC Machine Detector Interface WG, November 5<sup>th</sup> 2010, (<http://indico.cern.ch/conferenceDisplay.py?confId=109217>)
7. **E. Teodorescu**, *A look into the effect of supplementary magnetic fields on background levels in BeamCal at ILC*, FCAL Collaboration Workshop May 30 – June 1, 2011, Predeal, Romania, [http://www.nipne.ro/fcal\\_2011/docs/Proceedings\\_FCAL\\_RO\\_2011.pdf](http://www.nipne.ro/fcal_2011/docs/Proceedings_FCAL_RO_2011.pdf)

*Private sessions: Rare Decays Group at LHCb*

8. **E. Teodorescu**, *Lifetime acceptance and background studies for  $B_d \rightarrow K^* \gamma$* , LHCb Rare Decay Group Meeting, March 30, 2011
9. **E. Teodorescu**, *Background and stability check in  $B_d \rightarrow K^* \gamma$  and  $B_s \rightarrow \phi \gamma$* , LHCb Rare Decay Group Meeting, July 27, 2011

#### Posters

1. **E. Teodorescu**, A. Sailer, K. Elsener, C. Coca, “*QD0@CLIC: Implementation of QD0 in Mokka*”, Student Poster Session at European School of High Energy Physics, Raseborg, Finland, June 30-July 3 2010, <http://physicschool.web.cern.ch/PhysicSchool/ESHEP/ESHEP2010/default.html>
2. **E. Teodorescu** on behalf of LHCb Collaboration, *Rare Decays at LHCb*, Physics at LHC, Perugia, Italia, 6-11 June, 2011, Poster-2011-181, <http://cdsweb.cern.ch/collection/Posters?ln=en>
3. **E. Teodorescu** on behalf of LHCb Collaboration, *Radiative Decays at LHCb*, Physics at LHC, Perugia, Italia, 6-11 June, 2011, Poster-2011-189, <http://cdsweb.cern.ch/collection/Posters?ln=en>

#### CERN Analysis Notes

1. **E. Teodorescu**, A. Sailer, *Radiation Dose to the QD0 Quadrupole in the CLIC Interaction Region*, LCD Note, LCD-2010-013, <https://edms.cern.ch/document/1099226/1>
2. LHCb Collaboration, *Measurement of the ratio of branching fractions  $\mathcal{B}(B^0 \rightarrow K^{*0} \gamma) / \mathcal{B}(B_s^0 \rightarrow \phi \gamma)$  with the LHCb experiment at  $\sqrt{s} = 7 \text{ TeV}$*  LHCb-CONF-2011-055- by contributing to the preparation of the analysis note CERN-LHCb-ANA-2011-064 of the Radiative Decays Group where I am an author

## 2. LHC Accelerator and detectors

### 2.1 Introduction

The Standard Model [2] of particle physics is one of the most successful theories capable of describing in great detail the world as we see it. But, although the Standard Model provides satisfactory answers about what the constituents of matter are and how they interact it is not able to elucidate why everything which surrounds us is as we see and understand it.

History has proven that everytime we perfected our “microscopes” to peek at the unseen world of elementary particles, discoveries well beyond our expectations have been possible. In this physics field our microscopes are powerful acceletators which can collide particles over a very wide range of energies transporting us further back in time and closer to the moment considered to be the birting time of the Universe. The Large Hadron Collider, LHC [23], is, as stated in its name, the largest accelerator ever built to test our teorethical asspumnptions and to expand our knowledge on a few appetizing subjects like the evidence of the Higgs particle, dark matter and dark energy, extra dimensions, matter-antimatter disproportion or supersymmetry.

There are four large experiments at LHC [23], Atlas [29], Alice [30], CMS [31] and LHCb [22], which have been carefully designed to approach many of the intricacies of these very interesting topics.

The ATLAS and CMS experiments will try and confirm a hypothesis born in 1964 regarding the last undiscovered ingredient of the Standard Model, the Higgs boson [30]. Thorough the Higgs mechanism [31], the Standard Model [2] offers an attractive theoretical prediction on how particles acquire mass. Even if the Higgs boson is discovered, the experiments at the LHC will only be able to find its signature. The study of Higgs properties makes the object of the physics program proposed by the future liniar electron-positron colliders, the International Linear Collider, ILC [25], and the Compact Linear Collider, CLIC [26], which are briefly described in the second section of this thesis and simulation studies regarding one of the detector concepts proposed for these accelerators are presented.

There is strong evidence that only about 4% of the Universe is made of matter. The rest is referred to as dark matter and dark energy and, again, ATLAS and CMS propose a way to test their existence by searching for supersymmetric particles which are believed to be the constituents of dark matter and dark energy. [31]

Another question mark drawn by Mother Nature related to the abundance of matter over antimatter in the Universe. Our theory indicates that equal amounts of matter and antimatter should have been produced through a “Big Bang”-like theory. The evidence is clear that we live in a Universe predominantly made of matter. It is the task of the LHCb experiment to observe and study any differences in the behavior of matter with respect to antimatter. [31]

The closer we get to the time when the Big Bang took place, the more interesting and different the state of the matter we encounter. Evidence has indicated that in the very few milliseconds after the Big Bang matter as we know it today could not have existed, instead, a very hot and dense mixture of quarks and gluons was created. LHC will be able to recreate those conditions while the ALICE experiment will have the possibility to investigate the properties of the quark-gluon plasma. [31]

There is also the matter of extra-dimensions. They are very difficult to detect so all detectors will have to combine the knowledge they are privy to and further study this aspect. [31]

## 2.2 Large Hadron Collider (LHC)

The Large Hadron Collider is a circular high energy proton-proton accelerator with a circumference of 27 km at a depth of 50 to 175 m underground situated at the border between Swiss and France in the old tunnel excavated for the Large Electron Positron collider, LEP [32]. In the little space of time since it has first registered a proton-proton collision, the largest and most powerful particle accelerator already recorded several world records. In November 2009 LHC reached the highest accelerating energy ever achieved. It accelerated protons at 1.18 TeV per beam compared to Tevatron’s [33] collider previous world record of 0.98 TeV.

A few months later, in March 2010 the energy per beam was successfully increased even higher at 3.5 TeV, then towards the end of the year LHC accelerated for the first time heavy-ions which permitted the first direct observation of the jet quenching phenomenon.

Just one year later, in April 2011, the highest luminosity (the measure of the number of collisions which take place) ever reached was recorded,  $\mathcal{L} = 4.67 \times 10^{32} \text{ cm}^{-2} \text{ s}^{-1}$  as compared

to the previous record held by the Tevatron,  $\mathcal{L} = 4.024 \times 10^{32} \text{cm}^{-2} \text{s}^{-1}$ . As the luminosity increases, the probability of particle collisions grows also, and for studies related to rare processes this is a great advantage, as a term of comparison, at the present luminosity it takes only 12 hours to record the amount of data recorded during the whole 2010 LHC run. [34]

At LHCb, approximately  $35 \text{pb}^{-1}$  worth of data has been recorded during the 2010 LHC run and about  $88 \text{pb}^{-1}$  by the beginning of May 2011. [22]

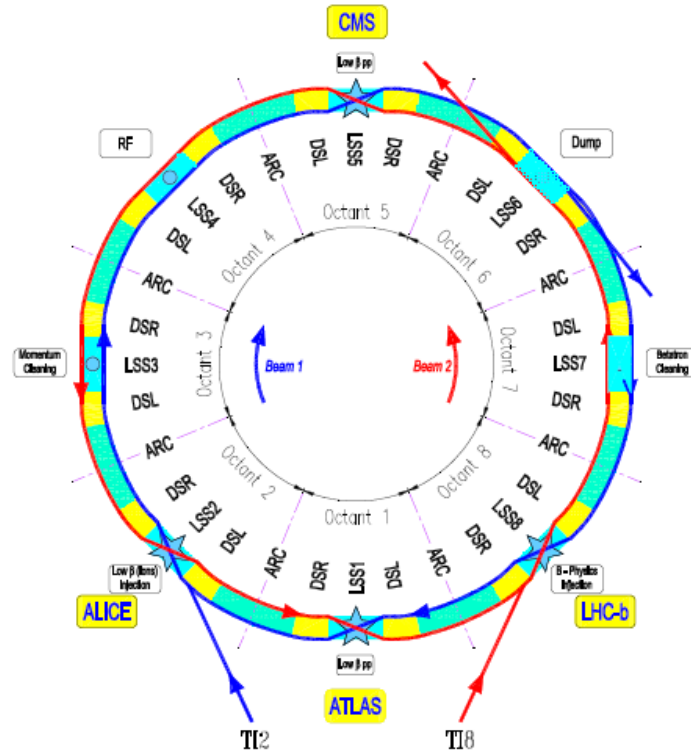


Figure 2.2.1 The LHC layout

LHC collides a clockwise rotating beam, Beam 1, with a counter-clockwise beam, Beam 2, of either protons or heavy-ions, as depicted in Figure 2.2.1. The milestone center-of-mass energy of 14 TeV is expected to be reached at LHC and a peak luminosity of  $\mathcal{L} = 10^{34} \text{cm}^{-2} \text{s}^{-1}$  (for the ATLAS and CMS experiments) where:

$$\mathcal{L} = \frac{N_b^2 n_b f_{rev} \gamma}{4\pi \epsilon_n \beta^3} F \quad \text{Eq. 2.2.1}$$

With  $N_b$  = number of particles per bunch,  $n_b$  = number of bunches per beam (which at LHC is 2808 with a nominal bunch spacing of 25 ns),  $f_{rev}$  = revolution frequency,  $\gamma$ =relativistic

gamma factor,  $\epsilon_n$  = normalized transverse beam emittance,  $\beta^*$  = beta function at the collision point and  $F$  = geometric luminosity reduction factor due to the crossing angle at the interaction point, IP. [35]

The high luminosities proposed at the LHC exclude the proton-antiproton option adopted by Tevatron where a single magnet and vacuum system is sufficient. Two proton beams, as used at LHC, require separate magnetic fields and vacuum systems with an overlap of approximately 130 m through a common beam pipe in the vicinity of IP where the four experiments are located. The LEP tunnel does not allow the installation of two separate rings of magnets thus an innovative magnet design has been perfected for the LHC: there are two sets of coils and beam channels hosted by a single mechanical frame and cryostat. The integrated dipole field along the storage ring determines the peak beam energy, consequently, the designed 7 TeV energy per beam can be obtained by using superconducting magnets able to generate dipole magnetic fields of 8.33 T. [36]

LHC is subdivided into eight arc and straight sections coupled by dispersion suppressors which take care of adapting the LHC orbit to the LEP tunnel. The arc cells are composed of a cryostat, a short straight section and three dipole magnets while for the straight sections, quadrupole magnets are being used. The two high luminosity experiments are located on two diametrically opposed straight sections, ATLAS at point 1 and CMS at point 5. Point 2, where ALICE is inserted, and Point 8, hosting LHCb, contain also the injection systems for Beam 1 and Beam 2. The two beams intersect only in these four points. There is also a beam dump region, located at point 6, where the two beams are being extracted from the accelerator, either at the end of the run or in case of emergency, using a complex combination of magnets.[35]

Passing through vacuum and magnetic fields generated by superconducting magnets cooled by a colossal cryogenics system, the beams are stored into the main rings for 10 to 20 hours and brought into collision in the four interaction points where the experimental detectors are placed. The proton beams are being injected into LHC at 450 GeV from the Super Proton Synchrotron, SPS. [36]

The detailed description of LHC does not make the object of this thesis but I find it important to stress out that this machine is one of the most complex and innovative structures ever build by man.

## 2.3 LHCb detector

### 2.3.1 Introduction

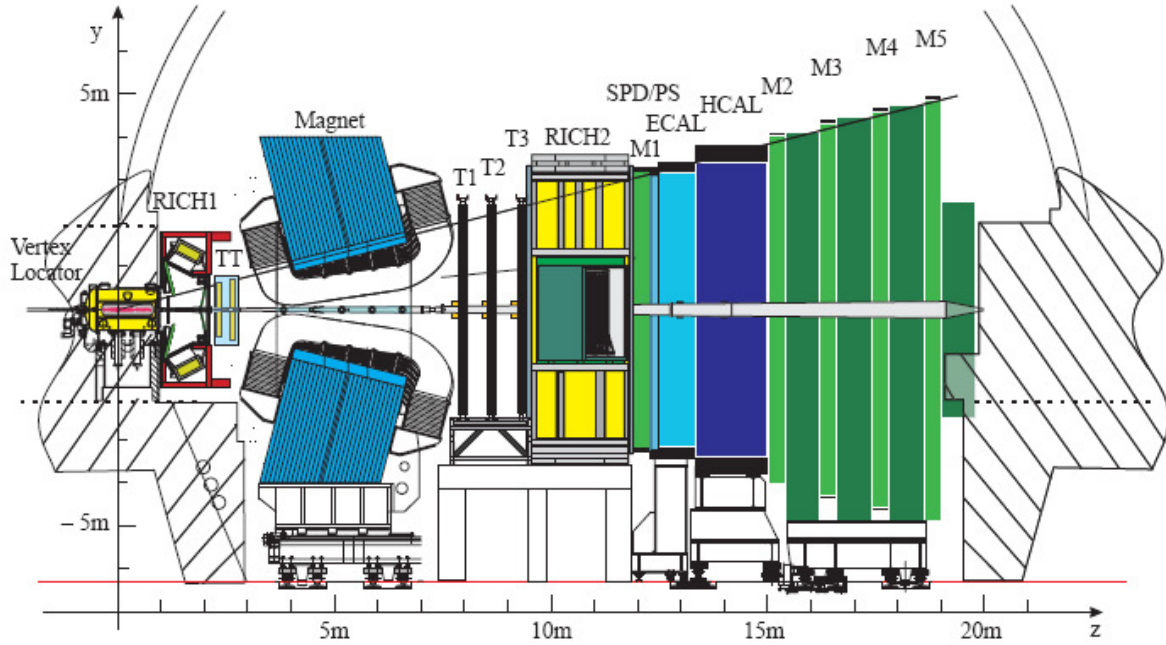


Figure 3.2.1 LHCb detector: Vertex Locator (VELO), the dipole magnet, the two RICH detectors, the Tracking system (TT, T1-T3), the Scintillating Pad Detector (SPD), the Preshower (PS), the Electromagnetic (ECAL) and Hadronic (HCAL) calorimeters and the Muon stations (M1-M5)

LHCb experiment [22], sketched in Figure 3.2.1, is designed to analyze CP violation and rare decays of B-mesons and b-baryons, to improve the Standard Model determinations on CKM parameters and to explore the full potential of physics beyond the Standard Model. If new physics manifests itself, studying CP asymmetries in B-meson decays may help to explain why the universe is predominately made of matter rather than antimatter. [37]

In this regard, LHCb combines good decay time resolution, to resolve  $B_s$  oscillations, mass resolution, to efficiently suppress the background, excellent particle identification, for  $\pi$ -K separation and an efficient trigger system for the study of many B-decay topologies. [r]  $\pi$ -K separation in a variety of final states is mandatory for the physics interest of the experiment, mainly, precise CPV measurements are possible in many important decay channels only if hadron identification is acquired. [38]

As  $b\bar{b}$  pairs at LHC are produced at small angles with respect to the beam axis the LHCb detector has been conceived as a single-arm forward spectrometer. It is composed of Vertex Locator, Tracking System, RICH detectors, Calorimeter System (Preshower, ECAL, HCAL)

and Muon system which are described briefly in the following. The detector acceptance extends to 300 mrad in the horizontal plane (x,z) and up to 250 mrad in the vertical plane (y,z). The inner acceptance is determined by the 10 mrad cone-shaped beam-pipe. [39]

Up to now, with more than 90% efficiency of data taking and at a measured cross-section of  $\sigma_{bb} = 284 \times 10^6 \text{ pb}$ , LHCb recorded  $\sim 37 \text{ pb}^{-1}$  in 2010 and  $\sim 50 \text{ pb}^{-1}$  in 2011 at  $\sqrt{s}=7$  TeV, a total amount of  $88 \text{ pb}^{-1}$ . [22]

### **2.3.2 VELO System**

One of the fundamental requirements in particle reconstruction is the determination of their production and decay vertices. The task of performing precise measurements on the track coordinates in the area near the interaction region is acquired by the **VE**rtex **LO**cator (VELO) detector. The precise determination of these coordinates allow the reconstruction of production and decay vertices, used for the calculation of the decay lifetimes, as well as measurements on the impact parameters of particles used to tag their flavor. Information from VELO is also used as input to the high level trigger. [40]

The VELO is designed as an assembly of silicon stations along the beam direction. Precise measurements are possible only if the whole angular acceptance is covered by sensitive detectors which register hits. To acquire this performance the sensors would have to reach into the area required by the LHC during injection, consequently, they have to be retractable. [40]

One of the distinctive characteristics of b-hadron decays is that the secondary (or decay) vertex is displaced with respect to the primary vertex. Then, B-hadrons with all their decay products inside the spectrometer acceptance are usually produced with polar angles smaller than 200 mrad thus the decay products do not point towards the primary vertex (the projection of the impact parameter of the decay products to the primary vertex in the rz-plane is large). This fact was exploited for the design of the VELO sensors, they are a combination of strips with constant radius for the (r,z)-track reconstruction and radial-strip sensors having a stereo angle of (10-20 degrees) for (r, $\phi$ )-track reconstruction. They have a circular shape instrumented with azimuthal and quasiradial strips for (r, $\phi$ )-measurements and cover 182 degrees. The inner radius of the sensitive area is 8 mm and the outer radius is 42 mm. A schematic view of a sensor is depicted in Figure 3.2.2 a) and b). Each sensor is divided into an inner and an outer region for a constant occupancy in the two regions. They are flipped from station to station and the strips are tilted with a stereo angle different for the inner and outer

regions. The strips in R-sensor are segmented into 4 or two azimuthal sections corresponding to the inner and outer regions respectively. This gives the possibility to determine the primary vertex coordinates with the R-sensors alone. [40]

Simulation and experimental studies have shown that n-strip detectors on n-bulk material (n-on-n) with AC coupling and polysilicon biasing are the best choice. The lifetime of such a sensor in the LHCb environment is expected to be around 3 years. [40]

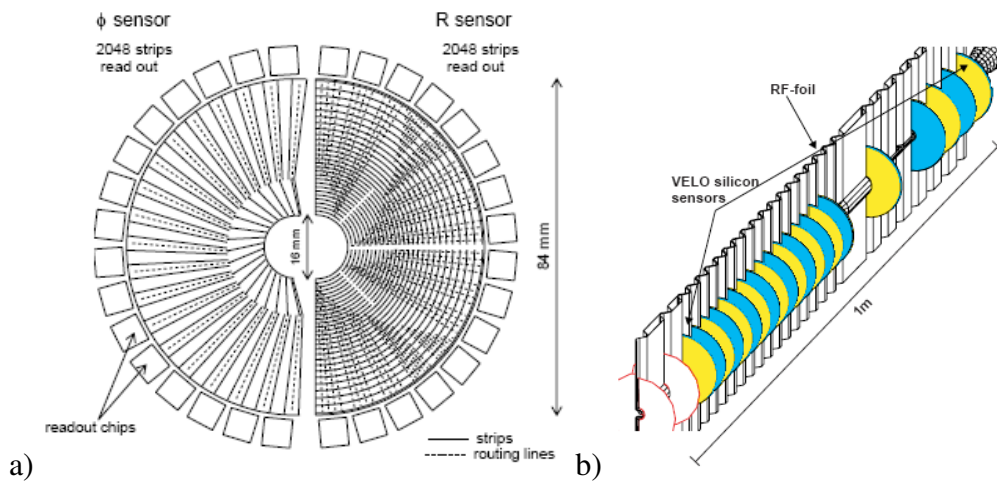


Figure 3.2.2 a) VELO sensor b) Vertex Locator [40]

### 2.3.3 Magnet

A comparative study between two magnet technologies has been performed in order to determine the optimal choice in terms of costs and performance: the option involving a warm magnet and the option of a superconducting magnet. It was concluded that a warm magnet by far exceeds the performances of a superconducting magnet as it rapid ramping-up of the field, synchronous to the ramping-up of LHC magnets together with regular field inversions. The schematic view of the design of the warm magnet is given in Figure 3.2.3. The magnet reaches a bending power of 4 Tm (integrated from  $z = 0$  to  $z = 10$  m). Two trapezoidal coils bent at  $45^\circ$  on the two transverse sides, are placed inside an iron yoke. The magnet is shaped such that it follows the detector acceptance. [41]

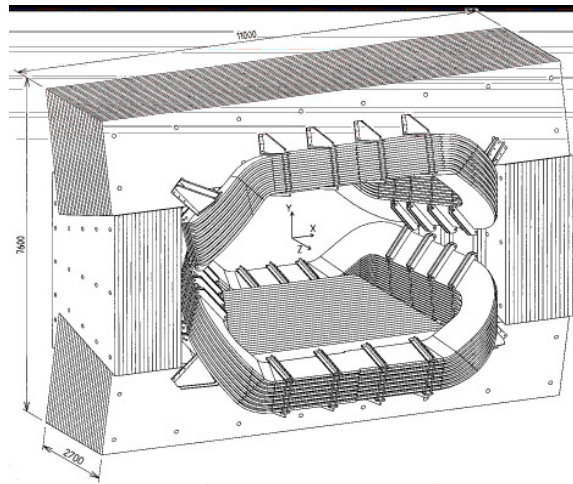


Figure 3.2.3 LHCb Magnet [41]

### 2.3.4 RICH

Particle identification, PID, over a large range of momentum is of utmost importance for the physics topics proposed at LHCb. This is achieved by detecting the ring images of Cherenkov light produced by the passing of charged particles through different radiators. Cherenkov light appears when a high energetic charged particle passes through a medium at a speed higher than the speed of light in that specific medium polarizing the molecules of the medium along its path. The molecules rapidly revert to their fundamental state by emitting photons. The photons are emitted as cone-like shapes along the path of the charged particle, the sizes of the cones providing reliable information about the particle which passed through the medium. The collection of these photons is acquired through photodetector systems. The task of particle identification at LHCb is accomplished by the two RICH detectors (**R**ing **I**maging **C**herenkov), RICH1 and RICH2. The PID system can also offer valuable information regarding electron and muon identification. For heavier particles it can improve the momentum determination. [42]

Three radiators with different refraction indexes are needed to cover the whole momentum range expected at LHCb (1-150 GeV/c), silica aerogel for low momentum tracks, C4F10 for intermediate momenta and gaseous CF4 for high momentum tracks.

RICH1 is placed in front of the dipole magnet of the LHCb spectrometer but close to the interaction region in order to reduce the photodetection area and to register those particles which would otherwise be scattered outside the acceptance by the magnet. It consists in a mixture of aerogel (5 cm thick layer) and an 85 cm long barrel of radiator C4F10 gas covering

the full outer acceptance of LHCb detector (300 mrad in the horizontal (x,z) plane and 250 in the vertical (y,z) plane). Spherical mirrors positioned at an angle, with respect to the beam axis, focus the Cherenkov light into images outside the LHCb acceptance so that the material of the photodetectors which collect the light will not affect the tracking procedure. The positioning of the mirrors cumulated with the angular acceptance lead to a necessary volume of 2.4x2.4x1 m<sup>3</sup>. A schematic view of RICH1 is given in Figure 3.2.4 a). The aerogel layer provides positive kaon-identification above 2 GeV/c and  $\pi$ -K separation up to 10 GeV/c while the C4F10 gas goes up to 50 GeV/c. [42]

For the analysis of high momentum tracks which pass through the magnet another Cherenkov CF<sub>4</sub>-based gaseous detector, RICH2, is situated downstream with respect to the magnet. It covers 120 mrad in the horizontal plane and 100 mrad in the vertical plane and its purpose is to separate pions from kaons beyond 100 GeV/c.

Again the photodetectors must be placed outside LHCb acceptance which results in a 7x7x2 m<sup>3</sup> chamber. The schematic view of RICH2 is given in Figure 3.2.4 b). In order to reduce the total length of the detector, the image reflected by the spherical mirrors is reflected once more on a flat secondary mirror towards the plane of the photodetectors.

The inner acceptances are determined by the cone-shaped beam-pipe and correspond to 25 mrad in RICH1 and 15 mrad in RICH2.

Both detectors are situated in areas with low magnetic fields to avoid significant curving of the tracks. A total area of ~2.6 m<sup>2</sup> is required with an effective granularity of the detectors of ~2.5mmx2.5 mm.

The main goal of the RICH system at LHCb is to insure particle identification over a large range of momenta, from 1 to 150 GeV/c. Even reconstruction in RICH is based on information provided by the tracking systems. Tracks are reconstructed using a Kalman filter to fit hits identified in RICH and spatial coordinates provided by VELO.

The hits in RICH are distributed as elliptical shapes which depending on the angle of the track are more or less distorted. Instead of attempting to fit these ellipses, another method is pursued to significantly simplify the procedure. The emission Cherenkov angles ( $\theta_C$ ,  $\varphi_C$ ) corresponding to each hit are reconstructed considering that this hit comes from a given track. Hits coming from a certain track have the same Cherenkov polar angle,  $\theta_C$  and a uniformly distributed azimuthal angle,  $\varphi_C$ . [42]

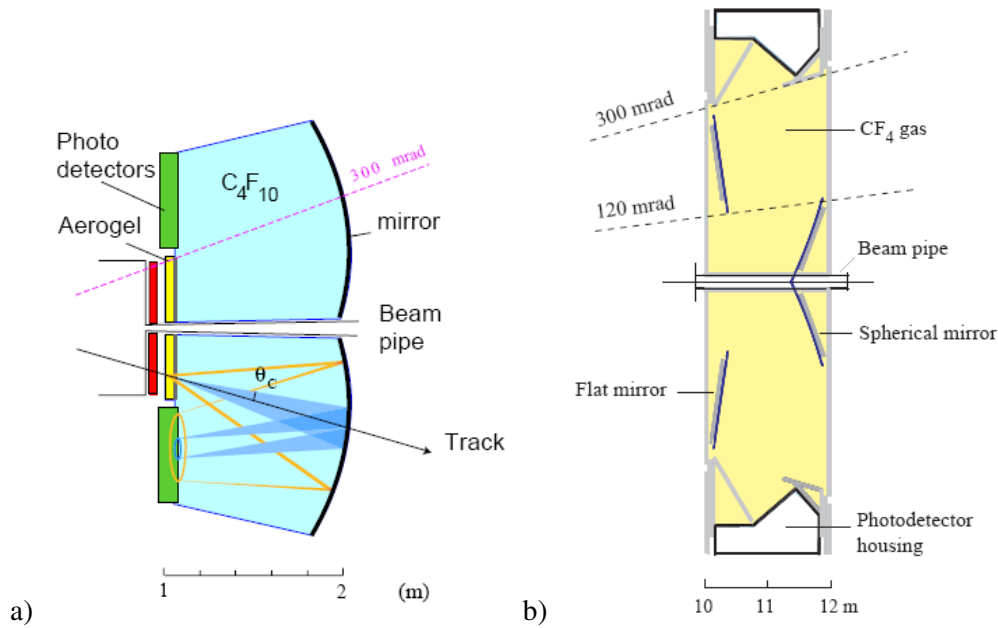


Figure 3.2.4 a)RICH1, b) RICH2 [42]

### 2.3.5 Tracking System: Inner Tracker + Trigger Tracker

The tracking system is required to perform three important tasks. First, it has to find charged particles between the vertex detector and calorimeters and measure their momentum. Second, it has to provide precise measurements on the direction of the tracks which is used as input to the particle identification algorithm. And third, to realize to make the connection between measurements provided by the vertex detector and calorimeter and muon systems.

The precise measurement of invariant mass of  $B$  candidates and signal-background separation is acquired if the momentum resolution is excellent. The momentum resolution is affected by multiple scatterings thus an important criterion in designing the detectors is the minimization of the material budget. On the other hand, a moderate hit spatial resolution of about  $\sim 70$  microns is acceptable. Another issue which has to be considered is the radiation damage which affects both the sensitive detectors and front-end electronics. Ionization radiation doses of  $\sim 1$ Mrad and neutron fluences equivalent to neutrons of 1 MeV of  $9 \times 10^{12}$   $\text{cm}^{-2}$  are expected over 10 years of operation at the nominal luminosity,  $L = 2 \times 10^{32}$   $\text{cm}^{-2} \text{ s}^{-1}$ . These are moderate doses for modern silicon detectors. [43]

The main tracking system at LHCb consists in 4 planar tracking stations: the Trigger Tracker, TT, placed between RICH1 and the magnet and three stations, T1-T3, between the magnet and RICH2. Two different technologies have been developed for T1-T3 stations. The

outer region of these stations, The Outer Tracker (OT), is covered by drift chambers composed of straw-tubes. For the inner region closest to the beam-pipe, where particle densities are highest, another approach must be engaged. [43]

The higher particle densities found in the region closest to the beam-pipe impose more stringent requirements on the capabilities of the detectors needed to cover this area. For this reason, the Inner Tracker (IT), consists in micro-strip silicon detectors which are highly granular and provide lower occupancies (the probability that in a certain event a certain strip is being hit) than the straw tubes, needed for better reconstruction efficiency. provide faster response and read-out times. The IT is displayed as a 120 cm wide and 40 cm high cross around the beam-pipe. The TT station, 140 cm wide and 120 cm high, is also an assembly of micro-strip silicon detectors. [43]

The TT station serves two purposes: the reconstruction of low momentum tracks which are strongly curved in the magnetic field and taken out of the acceptance before reaching the T1-T3 stations and second, the HLT1 uses the information provided by TT to assign low momentum to tracks characterized by high impact parameters. As T1-T3, TT consists in four sandwich detection layers; the outer layers have vertical strips while the two layers in between have pads rotated by  $\pm 5$  degrees with respect to the vertical.

The Inner Tracker consists in 3 tracking stations, T1-T3. Each station consists in 4 independent chambers displayed cross-shaped around the beam-pipe. Each chamber is an assembly of four detector layers with vertical or almost vertical strips, similar to the TT station. The IT covers only 1.3% of the sensitive area of a station but 20% of the charged particles produced close to the interaction point pass through the IT. For each track the entry and exit coordinates are registered for each detector they pass through, together with the time-of-flight with respect to the interaction point. A hit is recorded if a signal larger than 6000 e- is accumulated on one single strip. A simple clusterization algorithm is engaged to search for consecutive strips which have registered hits.

A schematic view of T1-T3 stations is given in Figure 3.2.5 a). The Inner Tracker unrotated and rotated strip layers are represented in Figure 3.2.5 b). [43]

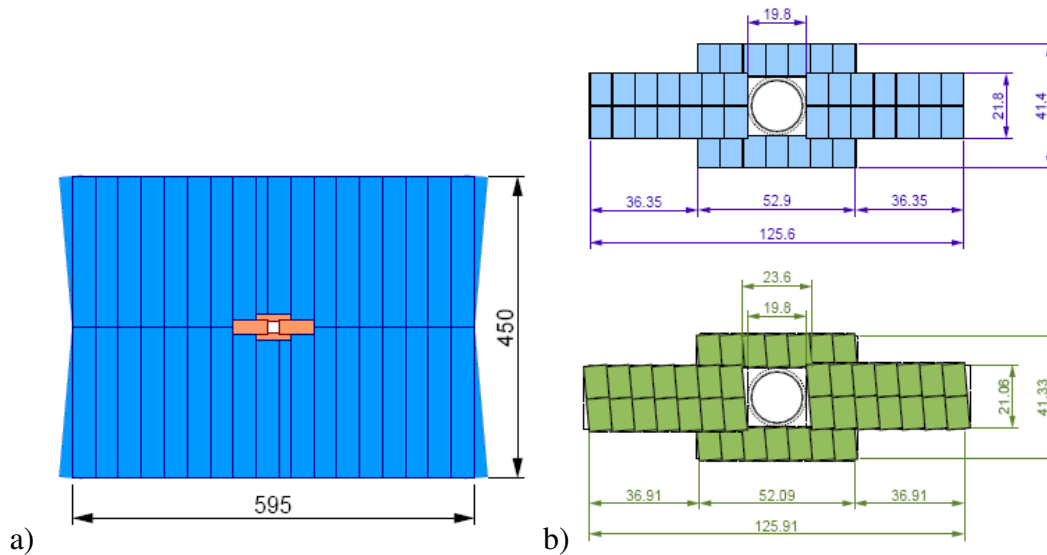


Figure 3.2.5 a) T1-T3, b) IT [43]

### 2.3.6 Outer Tracker

The tracking system array is geometrically displayed in such a manner as to maximize the upstream tracking, track segments are searched furthest away from the interaction point and track particles back through the magnet to the vertex detector. Fast algorithms have to be able to assign momentum information to tracks as feedback to the high level triggers. As a consequence, the z position of the tracking stations has been chosen based on simulation studies concerning the maximization of reconstruction efficiency and momentum resolution. Great effort is being invested in performing precision measurements in the bending plane, x-z (tracks are deviated by the magnetic field only in the horizontal plane). Drift cells with vertical wires, X planes, measure exclusively track coordinates in the bending plane, as a consequence, these planes are placed at the extremities for a fast identification of the tracks in the x-z plane. The U and V planes, consisting in wires rotated by  $\pm 5$  degree angle with respect to the vertical, are placed between the X planes. Each plane of a station is assembled from individual modules. Each module consists in two staggering layers of straw tubes which results in a total of 8 detection layers per station as there are 4 layers per chamber of the IT. These modules are independent structures which offers them mechanical rigidity and hermeticity. [44]

The drift gas choosing was done considering the maximization of the drift velocity. A mixture of Ar/CF<sub>4</sub>/CO<sub>2</sub> placed inside casings of carbon doped polymers (not metal as the CF<sub>4</sub> molecules can contaminate the gas with fluorine through recombination with the metal)

has been found to meet this crucial requirement. With a proper mixture of gases the resolution of drift coordinates can be kept under 200 microns. [44]

### **2.3.7 Calorimeters**

The calorimeter system reconstructs high transverse energy hadrons, electrons and photons. This information is supplied to the trigger which takes a decision at 4 ms after the interaction. Positive identification of electrons is crucial for flavor tagging in semileptonic decays. Also, some physics studies of B decays require efficient  $\pi^0$  and prompt photons reconstruction which the calorimeter system is able to provide. [45]

The calorimeter system consists in the scintillator pad detector, SPD, the pre-shower, PS, the electromagnetic calorimeter, ECAL, and the hadronic calorimeter, HCAL. The SPD was introduced later in the design of the calorimeter system with the purpose of signaling the presence of charged particles.

Aside from particle identification of hadrons, electrons and photons, the calorimeters also have to provide their energies and positions. Another demanding requirement is the ability to separate prompt photons or  $\pi^0$  in order to allow the reconstruction of B-decays with prompt  $\gamma$  or  $\pi^0$  in the final states, e.g. radiative decays. [45]

Because it has been demonstrated that the trigger efficiency has a weak dependency on the outer detector limits, the outer acceptance for the calorimeters is 300 mrad in the horizontal plane and 250 mrad in the vertical plane. Background is highest in the innermost regions, thus to avoid radiation damage and occupancy problems a central hole of 30 mrad around the beam-pipe is included in the design. Towards the outer regions of the calorimeters the background is two orders of magnitude lower, consequently, variable lateral segmentation is adopted. ECAL is sub-divided into three zones corresponding to the cell-sizes. The innermost cell sizes are close to the Moliere radius, so that an isolated shower is fully contained in 4 cells. The hadronic shower dimensions cumulated with the performance requirements of the hadron trigger led to larger cells for the HCAL and a sub-division into two zones only. [45]

The technologies adopted for ECAL and HCAL are determined by the stringent energy resolution requirement. The energy resolution is a crucial parameter in the mass resolution of B-decays containing a prompt  $\gamma$  or  $\pi^0$ . For this reason, a sampling calorimeter,

which meets the trigger requirements, the new “shashlik” technology, has been adopted as it has been shown that it provides energies resolutions of approx. 10%. ECAL is a sandwich of 2 mm thick lead sheets and 4 mm thick scintillator plates. This performance is overtaken only by crystal detectors but the costs are way beyond LHCb resources. Light collection is achieved by careful design of wavelength shifting (WLS) fibers.

For HCAL layers of 16 mm iron alternate with 4 mm scintillator tiles. The readout is also accomplished by WLS fibers. In this case the sensor and absorber plates are parallel to the beam.

Similarly to the ECAL and HCAL, scintillators have been adopted for the SPD and PS also. These two detectors are two detection planes with a thickness of 15 mm. The SPD is placed before a 12 mm lead wall and the PS immediately after it. Because of this design, a minimum ionizing particle produces around 25 photoelectrons which allow a clean separation between electron and photon showers. In these cases, only one WLS fiber is needed to collect the scintillation light.

For all four detectors the scintillation light is transmitted to a phototube by wavelength shifting fibers. Because SPD and PS require one fiber each, the two fibers can be read on multianode photomultipliers as opposed to ECAL and HCAL which require a phototube each because of the larger number of fiber bunches. [45]

Digitization sensitivity must cover a wide range of energies, from 10 MeV for low energy  $\pi^0$  and up to 200 GeV for the most energetic electrons and photons.

### **2.3.8 Muon System**

Many B decays sensitive to CP violation have muons in the final states. Also, muons provide flavor tagging in semi-leptonic b decays for of accompanying neutral B mesons in the initial states. Rare decays studies with muons in the final state are also very important as they may reveal new physics beyond the Standard Model. Consequently, muon identification and triggering are a crucial requirement of the LHCb detector.

There are five muon tracking stations interspersed with shields to attenuate hadrons, electrons and photons. For a muon to initiate the trigger it must hit all 5 muon stations. The muon’s transverse momentum is calculated based on hits from the first two stations. There is a correlation between the polar angle of the particles and the momentum, high momentum tracks tend to be closer to the beam axis. [46]

Offline muon identification is also required from the muon system. Muons reconstructed in the tracking stations with momenta down to 3 GeV/c must be correctly identified with more than 90% efficiency in order to keep the pion misidentification probability lower than 1.5%. High efficiency for muon identification is required for tagging as well as clean reconstruction of B decays having muons in the final states.

The five muon stations are displayed as follows: at 12.1 m from the interaction point the first station, M1, is placed in front of the calorimeter preshower and it provides measurements on the transverse momentum of muon tracks. The other 4 stations cover depths from 15.2 m (M2) up to 18.8 m (M5). Between the stations, there is a muon shield which consists in the electromagnetic and hadronic calorimeter and three iron filters. [46]

Similar to the tracking system, the muon system covers an angular acceptance from 20 (16) mrad to 306 (258) mrad in the bending (non-bending) plane. As the highest particle fluxes are closest to the beam-pipe, in the innermost regions, each muon station is subdivided into four regions with different granularity (logical-pad dimensions) as depicted in Figure 3.2.6. Pads in consequent regions have areas twice the area of the pads corresponding to the previous region.

The choosing of the technologies employed for the muon stations was done considering background rates, performance studies results, ageing conditions, background rates and last but not least cost, risk and resources. It was decided that 52 % of the total area will be covered by Multi Wire Proportional Chambers (MWPC) and the rest of 48% corresponding to the outer regions (R3 and R4) of M4 and M5 should be instrumented with Resistive Plate Chambers (RPC). [46]

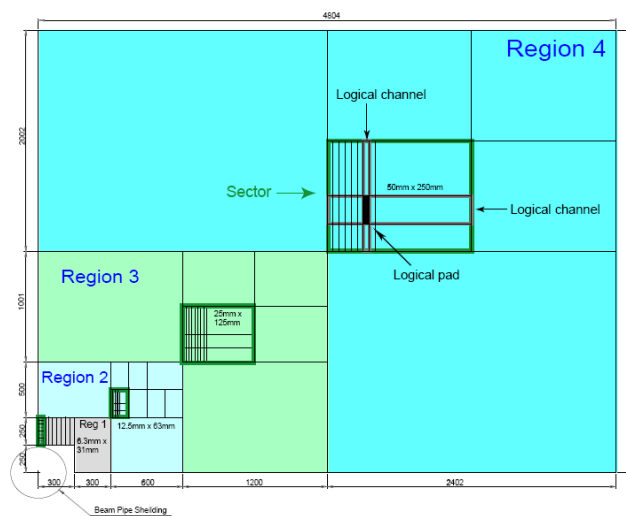


Figure 3.2.6 A Muon station [46]

### 2.3.9 Trigger System

LHCb is designed to operate at a much lower luminosity than the maximum luminosity of LHC. At  $\mathcal{L}=2\times 10^{32} \text{ cm}^{-2}\text{s}^{-1}$  the radiation damage can more easily be dealt with and the number of interactions per crossing is dominated by single interactions which simplify considerably the triggering and reconstruction procedures. An interaction is considered visible if it produces at least two charged particles with sufficient hits in the VELO and T1-T3 to allow them to be reconstructible. The role of the trigger system is to reduce the rate of crossings with visible interactions from 10 MHz (which corresponds to the low luminosity) to a few hundred Hz, the rate at which events are written to storage. Three trigger levels are required to perform this task: Level-0 trigger, which is a hardware trigger implemented into the electronics, and the High Level Trigger (HLT), subdivided into HLT1 and HLT2, both being software triggers ran on a computer processor farm. [47]

Level-0 trigger, executed in full custom electronics uses the data provided by the muon system, SPD, PS, ECAL and HCAL to trigger on muons, hadrons,  $e$ ,  $\gamma$  and  $\pi^0$  with the largest transverse energy, the charged particle multiplicity and the total energy. Information from the Pile-Up system is also used to recognize multiple interactions per crossing. HLT1 uses the information from Based on Level-0 and adding the information from VELO, TT and, if necessary, from T1-T3 and M2-M4 the HLT1 reduces the rate to 40 kHz. HLT2 makes a decision based on all data in the event except data from RICH to reduce the output rate down to 200 Hz. A schematic view of the triggering process is given in Figure 3.2.7. [47]

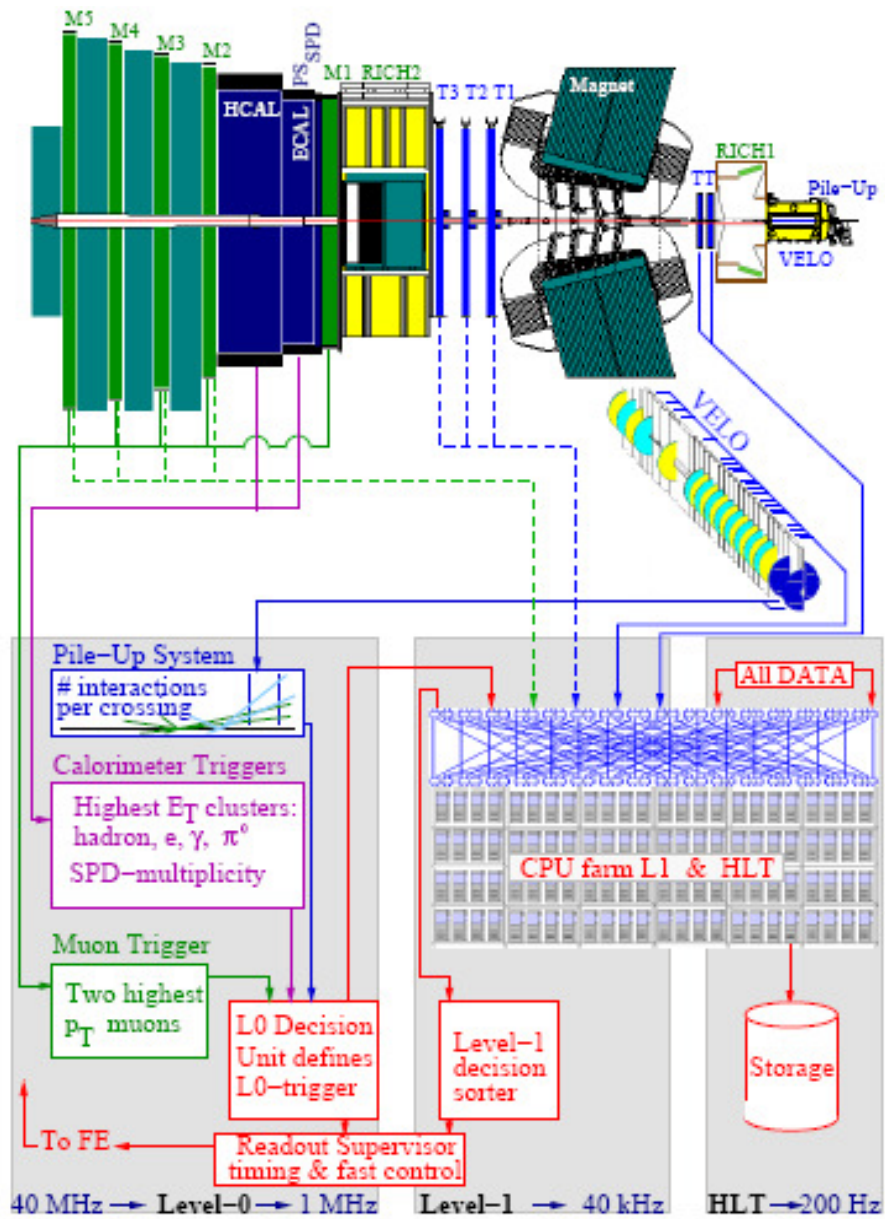


Figure 3.2.7 Trigger System Layout [47]

# 3 Software details

## 3.1 Introduction

Any proposed future experiment is based upon either concrete facts or best assumptions when addresses new aspects in research and development. The concrete facts are the knowledge and experience gained through experiments performed up to the time of the proposal while the assumptions are based on simulating the answer which is most likely to obtain according to untested theories up to that moment. The *best* assumptions come from imagining every hypothetical scenario and trying to sum up all the knowledge we gain from them.

The new era of modern physics in which we find ourselves came not only with more and more exotic theories but, to accommodate and test these new theories the experiments became more and more complex. In parallel, the simulation of as many aspects as possible of such experiments became exceedingly difficult. Simple programming routines can no longer satisfactory describe the hypotheses of complex experiments, consequently, dedicated algorithms must be developed to accurately describe specific tasks.

For example, a great amount of effort and resources is being invested in creating generators of events which would reproduce with high accuracy the experimental observations and, most importantly, to be able to predict what could be happen beyond the technological limits of the moment. The final result of an Event Generator algorithm mimics what happens during a collision at an accelerator. In real life, our eyes into this collision or interaction point are the detectors. For trustworthy simulation results it is imperative that the detector setup as well as its response is as close to the reality as possible.

The advantage in using simulation algorithms is that at every step we know exactly what we are dealing with, e.g. what particles pass through the detector, their spatial coordinates, their momenta and energies, etc. In reality, the only information our detector provides us with are pulse shapes and amplitudes, electrical currents and so on. A relevant comparison between the simulated and real data can be performed only when the simulation provides also this type of signals and this is accomplished through a procedure which is called digitization (the simulation of the detector response).

Next, we find ourselves in the situation where we have the detector response and we have to interpret it. We need to reconstruct and identify whatever passed through our detector.

This is acquired through complex particle reconstruction and particle identification algorithms. The optimization of such algorithms is based upon the information we started the simulation with, we know what we sent through the detector before the digitization so we tune our reconstruction until it matches this input. Reconstruction algorithms are created in such a way so that they can be applied indiscriminately both on real and simulated data.

In the end, efficient selection procedures must be optimized to separate the interesting signatures from the unwanted background. At this step a deep understanding of the physics involved in the process is required.

What still needs to be noted is that for each of the simulation steps many algorithms are being developed, tested and compared and that each real experiment requires specific algorithms to perform the tasks described above.

The LHCb experiment makes no exception to the rule; special algorithms have been developed to simulate the event generation, particle tracking through the detector, the detector response, trigger decision response, event reconstruction which includes track and particle identification and offline selection of specific final states. [49]

## 3.2. Event Generator

Minimum bias (non-singular diffractive events) proton-proton interactions at a center of mass energy of 14 TeV are generated with PYHTIA 6.2 [48] with the option of including hard QCD processes, simple diffraction, double diffraction and elastic scattering. Other event samples are obtained by constraining this large sample of minimum bias events, e.g. inclusive  $b\bar{b}$  sample is obtained by requiring that each event has at least one b or  $\bar{b}$  event. [49]

A number of Monte Carlo samples has been generated to test the reconstruction performance and trigger and selection efficiency at LHCb.

Specific signal samples of B decays as well as other B-hadron decays which constitute background for these decays have been generated. A sample of 20 million  $b\bar{b}$  inclusive events has been simulated to estimate the combinatorial background in offline selections. Two special background samples have been created for prompt  $J/\psi$  produced in the primary vertex and decay into either a  $\mu^+\mu^-$  or  $e^+e^-$  pair. A large sample of 30 million minimum-bias events has been generated for trigger studies. For this sample there is no generator level cut but for all other samples the polar angle of the generated particles is required to be less than 400

mrad, meaning that all particles are produced within the geometrical acceptance of the detector. After this cut is applied the selection efficiency is 34.7% for the signal samples and 43.2% for the inclusive  $b\bar{b}$  sample. [49]

### 3.3 Detector simulation

The simulation of the detector experimental setup and the interaction of the generated particles with the material of the detector is done with the Geant3 [50] toolkit. The goal is to simulate in as much detail as possible all detector components, besides the sensitive areas, this includes passive materials as well, such as beam pipe, frames, mechanical supports or shields. The passing of particles through the detector is recorded by Geant3 as spatial coordinates of the particle in each detection plane, the energy deposition in the respective layer and the time of flight of the particle with respect to the time of the primary interaction.

This information is used further to generate the digitized raw data and combined with experimental data, provided by prototype testing, the efficiencies and resolutions characteristic to individual sub-detector are estimated.

For example, the tracking detector response can be divided into two categories: the response of the silicon detectors (VELO, TT, IT) and straw detector response (OT). [49]

#### *Silicon detectors response*

The number of electron-hole pairs corresponding to the energy deposition in silicon is distributed along the track. The charge corresponding to each segment of a track is collected on readout strips which generate a hit if the collected signal is higher than a threshold. The effective efficiency of detecting a particle passing through silicon layers is higher than 99% for VELO and between 97.5% and 98% for TT and IT. [49]

#### *Straw detector response*

The path length of a particle passing through the straw detector is calculated based on the distance of closest approach of the track with respect to the wire. If a hit is registered the response of the detector is generated based on the relation:

$$t_{\text{TDC}} = t_{\text{bunch}} + t_{\text{tof}} + t_{\text{drift}} + t_{\text{delay}}$$

where  $t_{\text{bunch}}$  is the bunch time (-50, -25, 0, 25 ns),  $t_{\text{tof}}$  is the time-of-flight of the track passing through the straw,  $t_{\text{drift}}$  is the drift time in the cell and  $t_{\text{delay}}$  is the time it takes for the signal to propagate through the wire. [49]

## 3.4 Track reconstruction

Track reconstruction can be done separately in the vertex region and in the tracking systems. Hits provided by VELO, TT, IT and OT are combined in order to reconstruct particle tracks all the way from the VELO to the calorimeters. Aside from the possible final products of B mesons and barions decays, the reconstruction program tries to find all tracks in an event which give enough hits in the detectors. [49]

The reconstruction strategy starts by searching track “seeds where the best “seeding” regions are VELO and T stations as they are placed in areas with low magnetic field which allows searches of almost straight track segments. VELO seeds are reconstructed as straight lines based on  $(r,\varphi)$  coordinated of the VELO clusters and offer an initial track without information about its momentum. T seeds are reconstructed using clusters provided by the IT and hits provided by OT. In this region, although the magnetic field is small it is not negligible thus T seeds are parabolas. Consequently, the estimation of the momentum is possible either based on the curvature of the parabola or considering that the track comes from the nominal interaction point. The input for the tracking pattern recognition is the simulated detector response of the tracking system.

For the understanding of the reconstruction procedure described in the following, the introduction of a few LHCb specific terms related to tracks is needed. Trajectories generated inside the spectrometer have been subdivided in the following categories:

- Long tracks – traverse the whole tracking system, from VELO to T stations. They represent the most important set of tracks used in the reconstruction of B-hadrons.
- Upstream tracks – traverse only VELO and TT (not the T1-T3 stations). They have low momentum and do not reach the magnet but pass through RICH1 where they can generate Cherenkov [51] photons. Consequently, they are used to understand the background in RICH.
- Downstream tracks – traverse only the TT and T1-T3 stations. They are the decay products of  $K_s^0$  and  $\Lambda$ .
- VELO tracks – measured only by VELO. They are usually tracks produced at large angles or backward tracks used for primary vertex reconstruction.

- T tracks – measured only in the T stations. They are usually produced in secondary interactions and can be used for the global pattern recognition in RICH2. [49]

The track reconstruction is accomplished by applying the following steps:

The search of long tracks – the matching between a VELO seed with each the T-stations hits is attempted. The combination between a VELO seed and one T-station hit determines the momentum of the track candidate, thus the trajectory along the measurement planes. Then, hits around this trajectory are searched in other stations (including TT). When enough hits have been found the track is reconstructed. 90% of the long tracks are reconstructed in this manner.

When this procedure has been performed for all VELO seeds the T-station hits are excluded and another search is employed to find T-seeds. This way, another 5% of the long tracks can be reconstructed by extrapolation of the T-seeds into the VELO region and requiring that the position and the slope of the track candidate match a VELO seed.

When this procedure is finish also, all VELO and T seeds are excluded before searching for other types of tracks.

Upstream and downstream track search - two different algorithms try matching the remaining seeds in VELO and T-station with TT clusters.

VELO and T track search – VELO and T seeds remaining after the procedures described above have been performed are stored as VELO tracks without momentum information or as T tracks with badly measured momentum. [49]

When all tracks have been found, they are refitted with a Kalman filter [52]. A preliminary initial state is given by the pattern recognition algorithms. The Kalman filter starts with the most downstream measurement position and goes upstream updating the state vector,  $(x, y, dx/dz, dy/dz, Q/p)$ , at each measurement plane. The fit retrieves from the geometry database the inactive material layers in order to estimate any trajectory kinks due to multiple scattering in the absorber material and also performs a correction for the energy loss,  $dE/dx$ . Once it reaches the most upstream measurement, the fit restarts from this point towards the back of the detector in order to update downstream state vectors with information from all measurements. The quality of the reconstruction is determined by the  $\chi^2$  of the fit. In the end, the Kalman Filter method is equivalent to a fit of the “Least Square Method” type.

A VELO or T seed is considered a successfully reconstructed track if more than 70% of the corresponding hits originate from one single Monte Carlo particle, an upstream or downstream track must have additionally a correctly assigned TT track and a long track must have all VELO and T track segments correctly identified. This way, tracks coming from the vertex region and passing through the seeding region are identified with 95% efficiency.

After this fit, a track is characterized by the state vectors specified at the given  $z$  position in the experiment. [49]

### 3.5 Particle identification

The two RICH, the calorimeter system and the muon detector provide the particle identification at LHCb.

Among common types of charged particles which can be detected ( $e$ ,  $\mu$ ,  $\pi$ ,  $K$ ,  $p$ ) the electrons are mainly identified by the calorimeter system,  $m$  with the Muon system and hadrons with the RICH detectors, although RICH can also improve lepton identification so as a result, a combination of information provided by all detectors is pursued. Neutral electromagnetic particles ( $\gamma$ ,  $\pi^0$ ) are also identified by the calorimeter system where  $\pi^0 \rightarrow \gamma\gamma$  can either be resolved into two separate photons or as one merged cluster. Finally,  $K_s^0$  is reconstructed through its decay  $K_s^0 \rightarrow \pi^+\pi^-$ . [49]

#### *a) Reconstruction in RICH detectors*

RICH particle identification algorithms start from a known value of the angle of a track with respect to the beam axis as it passes through the PID detectors. This angle is reconstructed with a precision of  $\sim 1.2$  mrad in RICH1 and 0.6 in RICH2. The PID algorithm of RICH1 takes as input long, upstream and downstream tracks while the RICH2 algorithm considers long, downstream and T tracks.

In RICH, a hypothetical pixel pattern which is expected for a given mass is used as a gauge. Then, all the pixel patterns which record hits during interaction are compared with this hypothesis and a likelihood function is determined. After all track mass-hypotheses are assigned, they are all being varied until this global likelihood is maximized, thus optimally controlling the background of photons coming from neighboring tracks. For the discrimination of pions from kaons, the ratio between the kaon and pion hypotheses is estimated; in log-likelihood, this ratio is transformed into a difference:

$$\Delta \ln \mathcal{L} (K\pi) = \ln \mathcal{L}(K) - \ln \mathcal{L} (\pi) = \ln [\mathcal{L} (K)/\mathcal{L}(\pi)] \quad \text{Eq. 3.2.1}$$

This function tends to have positive values for kaons and negative values for pions which is very helpful in terms of “ $\pi$ -K separation significance” defined as:

$$N_s = \sqrt{2|\Delta \ln \mathcal{L}|} \quad \text{Eq. 3.2.2}$$

By applying a cut on  $\Delta \ln \mathcal{L} (K\pi)$ , used for the separation of pion from kaons, the mis-identification rate of pions can be largely reduced. There is also a risk in this scenario; the kaon identification efficiency is also diminished. [49]

***b) Lepton identification (electrons, muons)***

Lepton identification is performed by the Muon and Calorimeter Systems. RICH system also provides useful information about the distinction between leptons and hadrons. [49]

***c) Muon identification***

Muon identification starts with well reconstructed tracks having momenta larger than 3 GeV/c which are being extrapolated to the Muon stations. Around such an identified extrapolation point a field of interest is defined (FOI) where hits are searched in the Muon detector. A track is considered a muon candidate when hits have been found inside corresponding FOIs into a minimum of three muon stations. [49]

***d) Electron identification***

The electromagnetic calorimeter plays the most important role in the process of electron identification. The procedure of identifying electrons consists in a matching between the momentum of the track and the energy of the charged cluster in ECAL as well as a matching between the corrected position of the cluster baricenter and the extrapolated impact parameter (IP) of the track. The  $\chi^2$  of this global fit procedure represents the major ECAL estimator,  $\chi^2_e$ . A similar estimator is defined for the photons,  $\chi^2_\gamma$ , and detailed at the photon identification section. Considering this estimator, charged clusters are defined as those clusters which verify the relation  $\chi^2_\gamma < 49$ .

Improvement in electron identification is acquired by using the energy deposited in the Preshower detector as well as the energy deposited along the track inside HCAL. The final result is a combination of data provided by the calorimeter system and RICH and MUON systems. [49]

### *e) Photon Identification*

ECAL is responsible for the reconstruction and identification of photons also. “Cellular Automaton” algorithm searches for clusters in ECAL and performs a matching of the clusters against all reconstructed tracks. Based on position of the impact parameter of the track on the face of ECAL and the position of the cluster’s baricenter a matching estimator,  $\chi^2_\gamma$ , between the cluster and the track is constructed. The distribution of the minimum values of  $\chi^2_\gamma$  for all clusters shows a peak at small values of  $\chi^2_\gamma$  which is due to charged tracks. Clusters characterized by  $\chi^2_\gamma > 4$  are considered photon candidates. The evaluation of the corrections which must be applied to the photon energy and position is done based on the transversal and longitudinal shower shape. Also, hits registered in the SPD detector are taken into consideration for the photon reconstruction. Moreover, a cut on the energy deposited in the Prehower can enhance the purity of the sample both for converted and un-converted photons. [49]

### *f) $\pi^0$ reconstruction*

There are two categories of reconstructible  $\pi^0$ , merged  $\pi^0$  and resolved  $\pi^0$ . At transverse momenta,  $P_T$ , lower than 3 GeV/c, the  $\pi^0$  are reconstructed from a clearly resolved pair of photons which constitute the final products of  $\pi^0$  decay, while at higher  $P_T$  the two photons cannot be spatially separated within the limit of ECAL granularity, as such only one merged cluster is visible. This is a merged  $\pi^0$ . [49]

#### *Resolved $\pi^0$*

Photon candidates having  $P_T > 200 \text{ MeV}/c$  are paired in order to reconstruct the resolved  $\pi^0$ . The two photons can either both reach the calorimeter or one of them may convert before the calorimeter leaving a signal into the SPD. [49]

#### *Merged $\pi^0$*

To account for this situation, an algorithm has been developed in order to separate two photons potentially merged into a single cluster. The energy deposited in each cell of the cluster is assigned to two virtual sub-clusters following an iterative procedure which is based on the expected transversal shower shape of a single photon. Then, each of the two sub-clusters is reconstructed as coming from an individual photon. [49]

# 4. Radiative decays at LHCb

## 4.1 Motivation for studying radiative decays at LHCb

Radiative decays of b hadrons caused by  $b \rightarrow s$  transition are one of the manifestations of the flavour-changing neutral current process. Theoretically, these decays are described through one-loop processes involved in penguin diagrams (Figure 4.1.1), which give the lowest contribution to the amplitude of these transitions. [37]

In quantum field theory, these loops can host heavier degrees of freedom which can be markers of new physics processes, consequently, the study of radiative decays offers the possibility to observe the manifestation of the Physics beyond the Standard Model, if it exists. [71]

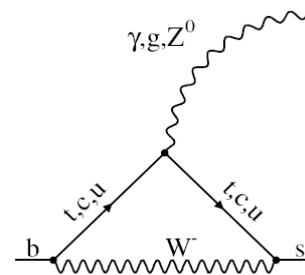


Figure 4.1.1 Penguin diagram for  $b \rightarrow s$  transitions

Most of the physics aspects of radiative decays are well understood theoretically. Through SM calculations, a large number of observables can be theoretically estimated. Deviations from the SM predictions on the decay rates, CP and isospin asymmetries or angular distributions, are a clear proof of the existence of NP, therefore precise measurements on these observables are mandatory. [58]

Theoretical predictions for some of the exclusive  $B \rightarrow V\gamma$  (where V is a vector meson) decays are presented in Table 4.1.1 [53]. Two of the benchmark channels for radiative decays are  $B^0 \rightarrow K^{*0}\gamma$  and  $B_s^0 \rightarrow \phi\gamma$ . In the following chapters, studies concerning these two decay modes at LHCb will be presented.

Decay Mode	Branching ratio
$B^+ \rightarrow K^{*+}\gamma$	$(4.6 \pm 1.4) \times 10^{-5}$
$B^0 \rightarrow K^{*0}\gamma$	$(4.3 \pm 1.4) \times 10^{-5}$
$B_s^0 \rightarrow \phi\gamma$	$(4.3 \pm 1.4) \times 10^{-5}$

Table 4.1.1 Theoretical branching fractions for exclusive  $B \rightarrow V\gamma$  decays

Even in theory, the branching ratios of radiative decays is known with quite a large uncertainty due to the poor knowledge of the hadronic form-factor which contributes with  $\sim 25\%$  to the total predicted uncertainty. Since the error is already dominated by theory, precise experimental measurements on branching ratios do not represent the main goal in the

radiative decays field, thus another perspective is envisaged to extract relevant information by studying radiative decays: CP asymmetries, time-dependent rates, angular distributions, isospin asymmetries and so on. [54]

The polarization of emitted photons in radiative decays is particularly interesting as the  $\bar{B}_s(B_s)$  meson decays predominantly into a left (right)-handed photon. Standard Model predicts almost 100% polarization of the photon, in the SM only the left-handed components of the external fermions couple to the W boson. The amplitude ratio, representing the fraction of “wrong” helicity photons  $\mathcal{A}_R/\mathcal{A}_L$  is proportional to the mass ratio  $m_s/m_b$ ,  $\mathcal{A}_R$  ( $\mathcal{A}_L$ ) represents the amplitude for the emission of left (right) handed photons in the  $b \rightarrow s_L \gamma_L$  ( $b \rightarrow s_R \gamma_R$ ) decays. But, there are a few theoretical models, either SM extensions or non-SM, which allow or don't suppress the right-handed over the left handed photons. The admixture of photons with the “wrong” polarization may be rather large in some of the beyond SM models. [54]

Therefore, the experimental challenge is to measure the amplitude ratio  $\left| \frac{\mathcal{A}(B \rightarrow \phi \gamma_R)}{\mathcal{A}(B \rightarrow \phi \gamma_L)} \right|$  where  $\phi$  represents a hadronic final state. There is no direct experimental method to measure the photon polarization but there are a few indirect strategies. One approach is to study the time evolution of  $B_s^0 \rightarrow \phi^{CP} \gamma$  decays, where  $\phi^{CP}$  is a CP-eigenstate. The time dependent decay width can be parameterized as:

$$\Gamma_{B \rightarrow \phi^{CP} \gamma}(t) \sim \cosh \frac{\Delta \Gamma t}{2} - \mathcal{A}^\Delta \sinh \frac{\Delta \Gamma t}{2} + \mathcal{C} \cos \Delta m t - \mathcal{S} \sin \Delta m t \quad \text{Eq. 4.1.1}$$

$$\Gamma_{\bar{B} \rightarrow \phi^{CP} \gamma}(t) \sim \cosh \frac{\Delta \Gamma t}{2} - \mathcal{A}^\Delta \sinh \frac{\Delta \Gamma t}{2} - \mathcal{C} \cos \Delta m t + \mathcal{S} \sin \Delta m t \quad \text{Eq. 4.1.2}$$

In SM,  $\mathcal{C}=0$ , thus the measurement of  $\mathcal{A}^\Delta$  and  $\mathcal{S}$  directly determines the “wrong”-polarized photon fraction. For the  $B_s$  system,  $\Delta \Gamma_s$  is not negligible thus  $\mathcal{A}^\Delta \approx \sin 2\psi$  where [37]:

$$\tan \psi \equiv \left| \frac{\mathcal{A}(\bar{B}_s \rightarrow \phi^{CP} \gamma_R)}{\mathcal{A}(\bar{B}_s \rightarrow \phi^{CP} \gamma_L)} \right| \quad \text{Eq. 4.2.3}$$

## 4.2 Searches of signal peaks for $B_d \rightarrow K^* \gamma$ and $B_s \rightarrow \phi \gamma$ in data collected with LHCb detector at $\sqrt{s} = 7$ TeV

The experimental challenge in radiative decays studies is to measure the photon polarization through the amplitude ratio  $\left| \frac{\mathcal{A}(B \rightarrow \phi \gamma_R)}{\mathcal{A}(B \rightarrow \phi \gamma_L)} \right|$  where  $\phi$  represents a hadronic final state. In particular the study of  $B_s^0 \rightarrow \phi^{CP} \gamma$  decays, where  $\phi^{CP}$  is a CP-eigenstate, offers one

possibility to reach this goal. But prior to this investigation, this rare radiative decay mode has to be disentangled from the large backgrounds which complicate its analysis. As the kinematic description of  $B_s \rightarrow \phi \gamma$  is very similar to  $B_d \rightarrow K^* \gamma$ , a common selection is envisaged where  $B_d \rightarrow K^* \gamma$  will serve as control channel for  $B_s \rightarrow \phi \gamma$ . Moreover, the  $B_d \rightarrow K^* \gamma$  channel has been thoroughly investigated by prior experiments thus its study at LHCb is very advantageous for detector calibration. [37]

The branching ratio of the  $B_d \rightarrow K^* \gamma$  decay mode, observed more than ten years ago by CLEO [55] then updated by Babar [56] and Belle [57], is the earliest proof of the flavour-changing neutral current processes and it is precisely known with a branching fraction  $\mathcal{B}(B_d \rightarrow K^* \gamma) = (43.3 \pm 1.5) \times 10^{-6}$ . Obtaining the same (or a more precise) measured value at LHCb will be crucial as this decay will be used as normalization channel for other radiative decays. The penguin  $B_s \rightarrow \phi \gamma$  decay has been observed by Belle [57], using a sample of  $24 \text{ fb}^{-1}$  at  $\Upsilon(5S)$ , but the precision reached is rather poor,  $\mathcal{B}(B_s \rightarrow \phi \gamma) = 57^{+22}_{-19} \times 10^{-6}$ .

As described in the previous chapter, the study of the  $b \rightarrow s \gamma$  and  $b \rightarrow d \gamma$  radiative transitions in neutral B meson decays is exceedingly interesting as contributions to the decay amplitude can come from the one-loop process involved in penguin diagrams. These transitions can be very sensitive to New Physics (or Physics Beyond Standard Model), their properties being particularly sensitive to the presence of new heavy particles that may propagate virtually within the loops. [54]

The purpose of the studies presented in this chapter is to demonstrate that the rare radiative decay modes  $B_d \rightarrow K^* \gamma$  and  $B_s \rightarrow \phi \gamma$ , can already be put in evidence with the limited statistics collected with the LHCb detector up to the beginning of May 2011, a total amount of  $88 \text{ pb}^{-1}$  of data. Starting from the official LHCb selection, optimized on simulated data, it will be shown that the two benchmark channels can be seen with this statistics. Then the selection criteria are being tuned on real data with the purpose of optimizing the signal to background ratio for these channels and an improved set of selection cuts is obtained. The tuning procedure and the improved set of selection cuts are presented in detail in this chapter and the results are compared with the official LHCb results.

To summarize, a list of interesting measurements with radiative decays of b hadrons includes [37]:

1. measurement of the photon polarisation and  $CP$ -violation parameters  $C$  and  $S$  in the decay  $B_s^0 \rightarrow \phi \gamma$

2. measurement of the photon polarisation in the decays of polarised beauty baryons  $\Lambda_b \rightarrow \Lambda^0 \gamma$  and  $\Lambda_b \rightarrow (\Lambda^* \rightarrow pK^-) \gamma$
3. measurement of the photon polarisation in the decay  $B^+ \rightarrow \phi K^+ \gamma$
4. measurement of direct  $CP$ -violation in the decay  $B^0 \rightarrow K^{*0} \gamma$
5. precise measurement of the ratio of branching fractions for  $B_s^0 \rightarrow \phi \gamma$  and  $B^0 \rightarrow K^{*0} \gamma$  decays.

Calorimeter calibration, the implementation of the High Level Trigger (HLT),  $\pi^0/\gamma$  separation at high transverse energy and the determination of proper time acceptance function from data are mandatory prerequisites for the successful study of radiative decays.

Simulation studies have shown that already with  $2 \text{ fb}^{-1}$  recorded with LHCb at the nominal conditions of operation ( $L=2 \times 10^{32} \text{ cm}^{-2} \text{ s}^{-1}$ ) the determination of photon polarization in  $B_s \rightarrow \phi \gamma$  should be accomplished with a precision of 0.22 as well as the determination of the direct  $CP$  asymmetry in  $B_d \rightarrow K^* \gamma$  which can be done with a precision of 1%. Also based on MC studies, it has been shown [59][60][61] that a 3% miscalibration of ECAL is equivalent to 20% increase in signal width which translates into an effective 20% increase of the combinatorial background in the signal region, Figure 4.2.1. [37]

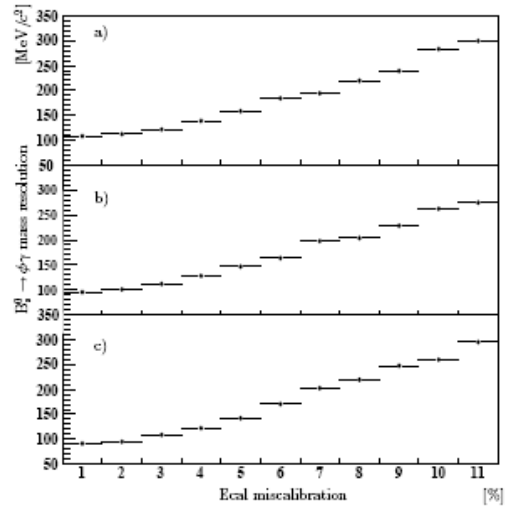


Figure 4.2.1  $B_s^0 \rightarrow \phi \gamma$  mass resolution versus ECAL miscalibration [37]

Valuable information can be extracted about the ECAL miscalibration from the  $B_d \rightarrow K^* \gamma$  signal peak. From the *position* of the mass peak we can estimate the global miscalibration factor for energetic photons while the reconstructed mass *width* contains information about the channel to channel calorimeter miscalibration. Using cosmic and early 2010 data, the LHCb calorimeter has been calibrated at the 2% level. [62]

The calibration procedure involved three stages:

1. Calibration at the ~10% level using cosmic rays (during detector commissioning, 2007-2008)
2. Calibration at the 4-5% level using an 'energy flow' method to level out the channel response

3. Calibration at the 2% level using an iterative procedure based on a limited  $\pi^0$  sample. This technique does not rely on information from the other subdetectors (is tracking independent) and is based on the direct relation between the energy shift of the photon and the shift of the visible position of  $\pi^0$  peak. [37]

In the near future, as soon as a larger  $\pi^0$  sample will be collected, it is expected that the miscalibration factor will be lowered to 1% level. [62]

The efficient selection of  $B$ -meson events is acquired through a *high performance trigger* [47]. A more detailed description of the trigger system is found in Chapter 2.3.9.

Here, it is worth mentioning that based on particles with large transverse momentum and displaced secondary vertices the LHCb trigger system will select the small fraction of interesting events (from the large number of  $bb$  and other  $pp$  inelastic events) which will be written to storage for further offline analysis.

The following study is based on real data collected at LHC with the LHCb detector which amount to  $\sim 88 \text{ pb}^{-1}$  at a center of mass energy of  $\sqrt{s}=7 \text{ TeV}$ , in proton-proton collisions.  $37.5 \text{ pb}^{-1}$  have been recorded in 2010 and  $50.5 \text{ pb}^{-1}$  during 2011. A schematic representation of the data flow is given in Figure 4.2.2.



Figure 4.2.2 Data flow at LHCb

For 2010 data all trigger lines had (Table 4.2.1):

*relaxed* cuts in first  $4 \text{ pb}^{-1}$   
*very hard* cuts in  $5.4 \text{ pb}^{-1}$   
*'intermediate'* cuts in  $28.6 \text{ pb}^{-1}$

2010 $\mathcal{L}_{int}$	L0 $\gamma$ cut	Hlt1 depend on	Hlt2 depends on
$4 \text{ pb}^{-1}$	2.4-2.8 GeV	L0 $\gamma$ OR L0e	none
$5.4 \text{ pb}^{-1}$	4.4 GeV	NO Radiative lines	none
$28.6 \text{ pb}^{-1}$	3.2 GeV	Hlt1TrackPhotonLine	Hlt1TrackPhotonLine

Table 4.2.1 Trigger lines for radiative decays for 2010 data at LHCb

Figure 4.2.2 shows the steps engaged for recording data up to the final stage of offline analysis. First, the relevant events must trigger the hardware L0 trigger, then HLT1 has to confirm this decision and finally the confirmed event goes through HLT2. After passing the relevant triggers (radiative decays will be triggered mainly due to the presence of a high energy photon [63]) the remaining data go through a so called stripping process which is called “Stripping line”. For each exclusive decay channel, the stripping line represents a collection of

specific kinematical cuts which are designed to efficiently select the desired decay and keep the background within reasonable limits. Radiative stripping runs on the output of the entire HLT2.

Ultimately, the offline selection is applied. The event selection criteria have been tuned on simulated data samples to maximize the ratio  $\xi = \frac{S}{\sqrt{S+B}}$ . These sets of cuts represented the official offline selection criteria accepted by the LHCb collaboration prior to accumulating a significant collection of real data on which these cuts could be optimized. Both the official offline and the stripping selections are summarized in Table 4.2.2. The official invariant mass peaks for the two benchmark channels for radiative decays,  $B^0 \rightarrow K^{*0} \gamma$  and  $B_s^0 \rightarrow \phi \gamma$ , published by the LHCb collaboration are presented in Figure 4.2.3 [63] [64] as a reference for the results presented in this thesis.

Cut	Old official offline		Stripping Cuts	
	$B^0 \rightarrow K^{*0} \gamma$	$B_s^0 \rightarrow \phi \gamma$	$B^0 \rightarrow K^{*0} \gamma$	$B_s^0 \rightarrow \phi \gamma$
$K, \pi$ minimum $IP\chi^2$	>25	>25	>10	>10
$K, \pi$ track $\chi^2/dof$	none	none	<10 (HLT2)	<10 (HLT2)
$K, \pi$ $PT$	none	none		
$K \Delta \log \mathcal{L}(K-\pi)$	>3	>3		
$K \Delta \log \mathcal{L}(K-p)$	>5	none		
$\pi \Delta \log \mathcal{L}(K-\pi)$	<5	none		
$K^*/\phi \Delta_{Mass}$	<100 MeV	<10 MeV	<100 MeV	15 MeV
$K^*/\phi$ vertex $\chi^2$	<9	<9	<15	<15
$\gamma_{PT}$	>2.8 GeV	>2.8 GeV	>2.6 GeV	>2.6 GeV
$B_d/B_s$ minimum $IP\chi^2$	<9	<9	<15	<15
$B_d/B_s$ direction angle	<8 mrad	<10 mrad	<20 mrad	<20 mrad
$ \cos(B_d/B_s \text{ helicity}) $	<0.8	<0.8		

Table 4.2.2 Offline and stripping selection for the two benchmark channels for radiative decays,  $B^0 \rightarrow K^{*0} \gamma$  and  $B_s^0 \rightarrow \phi \gamma$  [64][66]

Because of the small decay rates together with large backgrounds from different sources, the reconstruction of the radiative decay modes at LHCb is very challenging. The most dangerous source of background is the combinatorial background coming from  $b\bar{b}$  events because such events include both primary and secondary vertices and they are characterized by large multiplicities for charged and neutral particles. The background produced by minimum-bias events can be high as well but it is reduced at trigger level. Another important background source for these two particular decays is due to hadronic B decays with neutral pions in the final state,  $B_d \rightarrow K^* \pi^0$ , and decay rates comparable with those characteristic to the decays under study. This background could be kept under control through the  $\pi^0/\gamma$  separation algorithm which takes into account the shape of the shower distribution. [37]

In detail, the offline selection strategy develops as follows: first, the separation of pions from kaons is engaged. This is accomplished in RICH detectors by comparing the expected pattern from a given set of mass hypotheses for the reconstructed tracks passing through the detectors with the observed pixel pattern and determining a likelihood. Then, the mass-hypotheses assigned to the tracks are varied such that the likelihood is maximized. A charged track is considered a pion candidate if  $\Delta \log \mathcal{L}_{\pi K} = \log (\mathcal{P}(\pi)/\mathcal{P}(K)) < 5$  and it is a kaon candidate if  $\Delta \log \mathcal{L}_{K\pi} > 3$  and  $\Delta \log \mathcal{L}_{Kp} > 5$ . [49]

The tracks coming from primary interactions are eliminated through a cut on the significance of the track impact parameter (IP, the distance of closest approach to the reconstructed primary vertex),  $(\chi_{IP}^2 = (IP/\sigma_{IP})^2)$ , with respect to all reconstructed primary vertices,  $\chi_{IP}^2 > 25$ . Significance larger than  $4-5\sigma$  basically implies that primary tracks will not be associated with any reconstructed secondary vertex. [66][67][68]

After the separation of pions from kaons, two relevant tracks are combined to form the  $K^*$  and  $\phi$  vector meson candidates and an unconstrained vertex fit,  $K^*/\phi$  vertex  $\chi^2 < 9$  is applied. The  $K/\pi$  separation together with the mass constraint for the  $K^*$  and  $\phi$  are the only differences involved in the reconstruction of the two decay channels,  $B_d \rightarrow K^* \gamma$  and  $B_s \rightarrow \phi \gamma$ . Because the combined mass of two kaons is very close to the  $\phi$  vector meson mass, very little energy is transferred as kinetic energy, thus the two resulting kaons are close together in space. This is not the case for the  $K-\pi$  pair; as their combined masses are not as close to the  $K^*$  mass, more kinetic energy can be transferred to the two particles. As a consequence, the mass window for  $K-\pi$  combinations is 100 MeV around the  $K^*$  nominal mass and 10 MeV for the  $K-K$  pairs in reconstructing the  $\phi$  meson. [66][67][68]

Next,  $K^*(\phi)$  candidates are combined with a photon candidate. A photon is defined as a cluster in the electromagnetic calorimeter which cannot be associated with any charged track. Low energy photons are rejected through a cut on the photon transverse energy,  $E_T > 2.8$  GeV.

Because of the very short lifetime of  $K^*(\phi)$ , the decay vertex of  $K^*(\phi)$  is basically the decay vertex of the B candidate. The production vertex of B is chosen as the primary vertex with the smallest B impact parameter,  $\chi_{IP}^2 < 9$ . [66][67][68]

Additional selection cuts are applied to eliminate as much background as possible. This is done by exploiting the general properties of beauty production in proton-proton

collisions. Due to the large mass of B mesons, the secondary particles produced during their decays are strongly deviated in transversal plane, which translates into large transverse momenta for secondary particles,  $P_T(K,\pi) > 500 \text{ MeV}$ . Also, the long lifetime of B mesons results in the spatial isolation of the B decay vertex, thus the probability of reconstructing particles coming from the primary interaction is much smaller. [66][67][68]

Combinatorial background is suppressed by constraining the angle between the B momentum vector and B flight direction (distance between production and decay vertices). Because of the heavy B mass, B-mesons are produced on a very forward direction so they are very little deviated in the transversal plane, consequently, this angle,  $\theta_B$ , should be very close to 0. As such, it is chosen to be smaller than 8 mrad for  $B_d$  and smaller than 10 mrad for  $B_s$ . [66][67][68]

Decays of the type  $B_d \rightarrow K^* \pi^0$  and  $B_s \rightarrow \phi \pi^0$  represent a very dangerous source of background due to possible energetic neutral pions,  $\pi^0$ , in the final states which can be identified as single photons. To suppress the correlated background from decays with  $\pi^0$  in final states another property of radiative decays is taken into account:  $K^*(\phi)$  are produced with different polarizations for signal and background. In this regard, the helicity angle,  $\theta_H$ , is defined as the angle between the direction of one of the daughters of the vector meson,  $K^*(\phi)$ , and the reconstructed B direction, in the reference system of the  $K^*(\phi)$  meson. This angle is distributed as a  $\sin^2 \theta$  function for the signal, as a  $\cos^2 \theta$  for the correlated background and has a flat distribution for the combinatorial background.  $K^*$  helicity for  $B_d \rightarrow K^* \pi^0$  is 0 and  $\pm 1$  for  $B_d \rightarrow K^* \gamma$ . The cut on the helicity angle has been optimized to  $\cos \theta_H > 0$  [66][67][68]. Significant reduction of the background level is accomplished through additional cuts, such as cuts on the B transverse momentum, on the track multiplicity or on the confidence level for the photon,  $\gamma_{CL}$  [64][65]. These cuts have been tuned directly on the data taken during the 2010 accelerator run and they are presented in Table 5.1.3.

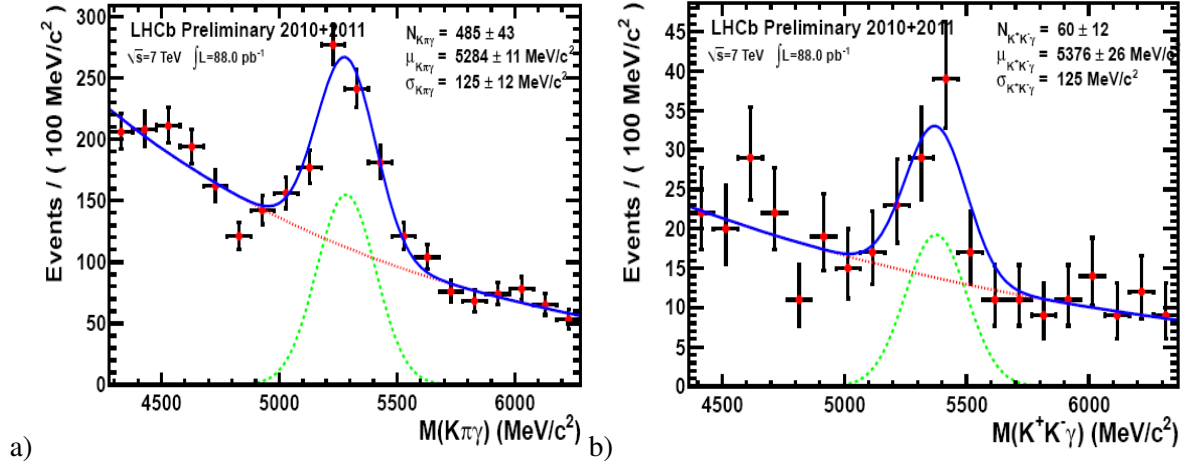


Figure 4.2.3 Invariant mass peaks for the two benchmark radiative decays channels, a)  $B^0 \rightarrow K^{*0} \gamma$  and b)  $B_s^0 \rightarrow \phi \gamma$  [69]

Figure 4.2.3 a) and b) show the invariant mass peaks for  $B^0 \rightarrow K^{*0} \gamma$  and  $B_s^0 \rightarrow \phi \gamma$  respectively. They represent the official approved invariant mass peaks for  $B_d$  and  $B_s$  mesons, reconstructed through radiative modes  $K^* \gamma$  and  $\phi \gamma$  respectively. The event selection described above was applied on the stripped candidates. The plots show that with  $88 \text{ pb}^{-1}$  of integrated luminosity we collected  $(6.1 \pm 0.7) B_d \rightarrow K^* \gamma$  candidates/ $\text{pb}^{-1}$  and  $(0.6 \pm 0.2) B_s \rightarrow \phi \gamma$  candidates/ $\text{pb}^{-1}$  [r]. Based on the 2010/2011 preliminary results, it is expected to collect a sample of  $\sim 6000$   $B_d \rightarrow K^* \gamma$  events and  $\sim 600$   $B_s \rightarrow \phi \gamma$  events by the end of 2011, when a data set of  $\sim 1 \text{ fb}^{-1}$  will be recorded. It is also expected that this statistics will allow the determination of the ratio of  $B_d \rightarrow K^* \gamma$  and  $B_s \rightarrow \phi \gamma$  branching fractions. These results have been presented at the *P@LHC Physics at LHC* international conference, Perugia, 2011, by the author of this thesis, on behalf of the LHCb collaboration [64] and at the *HEP-Mad 5<sup>th</sup> High-Energy Physics Conference*, Madagascar, 2011, [65] where the poster prepared by the author of this thesis has been presented.

In the following, an improvement of the selection strategy for these two radiative channels is presented. The new selection is checked and tuned directly on the real data collected with the LHCb detector up until the beginning of May 2011.

As the kinematics of  $B_d \rightarrow K^* \gamma$  and  $B_s \rightarrow \phi \gamma$  is very similar, the ratio between the number of signal events in the two mass peaks should be approximately constant when applying the common selection on the two respective stripping candidates.

The strategy involved consists in applying all the selection criteria while loosening one of the cuts down to the stripping value, when available, or zero when not, then gradually increase this cut up to a value for which enough candidates pass the selection to observe a mass peak.

After each change, the number of selected events in the  $B_d \rightarrow K^* \gamma$  and  $B_s \rightarrow \phi \gamma$  mass peaks is compared and the stability of their ratio is checked, represented in Figure 4.2.4 a) to i), left plots. The limited statistics does not allow for this study to be performed in bins of any of the variables which are being constrained, thus, only lower (or upper, when necessary) limits are chosen for the variable involved, e.g.  $\gamma_{P_T} > 2600$ ,  $\gamma_{P_T} > 2800$ ,  $\gamma_{P_T} > 3000$  etc., and not ( $\gamma_{P_T} > 2600$  and  $\gamma_{P_T} < 2800$ ). Such a procedure was envisaged in the frame of the LHCb collaboration.

After the ratio check, the same procedure is applied for the comparison of the number of signal events in the  $B_d \rightarrow K^* \gamma$  mass peak to the number of background events which pass the selection, shown in Figure 4.2.4, a) to i), middle plots, the red and blue dots respectively. This comparison allows the calculation of the ratio,  $\xi = \frac{S}{\sqrt{S+B}}$ , for the  $B_d \rightarrow K^* \gamma$  channel.  $\xi$  is represented in Figure 4.2.4, a) to i), right plots. The optimal values of the selection cuts are extracted from these results by identifying the maximum of  $\xi$  distribution.

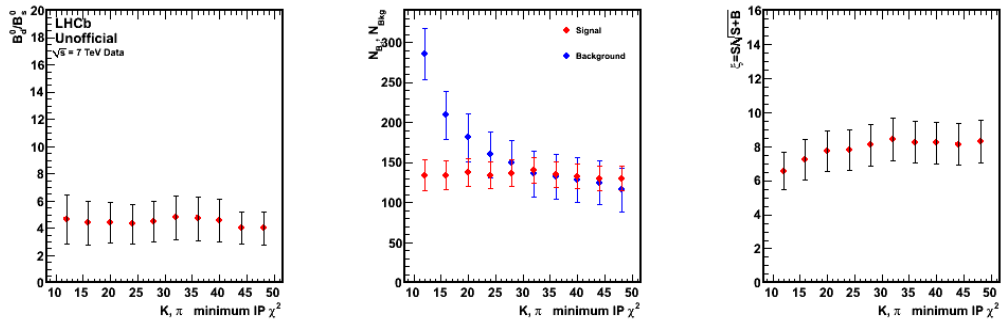
The selection tuning (the optimization of the cuts), as described above, is being done on the 2010 data set (Figures 5.2.4 a) to i)), the optimal values for the selection cuts being extracted from this study, then, the optimized selection is applied on 2010+2011 data set, and the stability of the ratio of signal yields in the two mass peaks is verified again. The results are presented in Appendix 3 and they show, as expected, that the ratio is stable within errors for the 2010+2011 as well.

Inside the LHCb collaboration, it has been discussed that the cut on the transverse momentum of B meson together with the selection of the best tracks should be removed. In the following, it will be demonstrated that both of these cuts remove important amounts of background and most importantly, the cut on the B-meson transverse momentum not only removes the background, but also reduces the structures present in the low and high mass sidebands, the mass intervals 4400-5000 MeV/c<sup>2</sup> and 5600-6400 MeV/c<sup>2</sup>, respectively. Consequently, in parallel, the scenario implying the removal of the cut on the transverse momentum of the B particle is investigated and represented in Figure 5.2.4 a') to i'). The plots clearly indicate background reduction when the cut on the transverse momentum of  $B_d$  ( $B_{P_T}$ ) is applied. Figure 5.2.4 f) shows that the optimal cut on  $B_{P_T}$  is around 4 GeV. A similar study has been performed for the hypothesis of removing the cut on "Best Tracks". This cut also removes large amounts of background; the results upon which this conclusion is based are presented in Appendix 1.

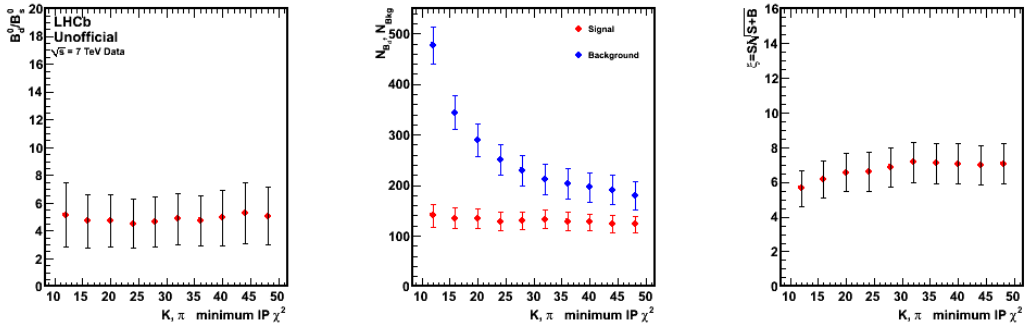
Along with the background removal, the cut on  $B_{PT}$  also reduces significantly the structures present in the distribution of the background. To support this affirmation, the invariant mass distribution of  $B_d \rightarrow K^* \gamma$  has been investigated for different cut values of  $B_{PT}$ . Three cases are presented in Appendix 2,  $B_{PT} > 0$ ,  $B_{PT} > 2000$  MeV (official value) and  $B_{PT} > 3500$  MeV (optimal value extracted from the present study) in the hypothesis where all offline cuts are applied while the cut on  $\gamma_{PT}$  is being varied from 2600 MeV (the stripping cut) to 4000 MeV.

The ratio check for the  $K^*/\phi$  mass window cannot be performed as there is a large difference between the mass windows for the two daughter particles involved in the decays. The mass window for  $K^*$  is up to 100 MeV while for the  $\phi$  it is set to 15 MeV in the stripping cuts.

K,  $\pi$  minimum IP a) all cuts applied, a')  $B_{PT}$  removed

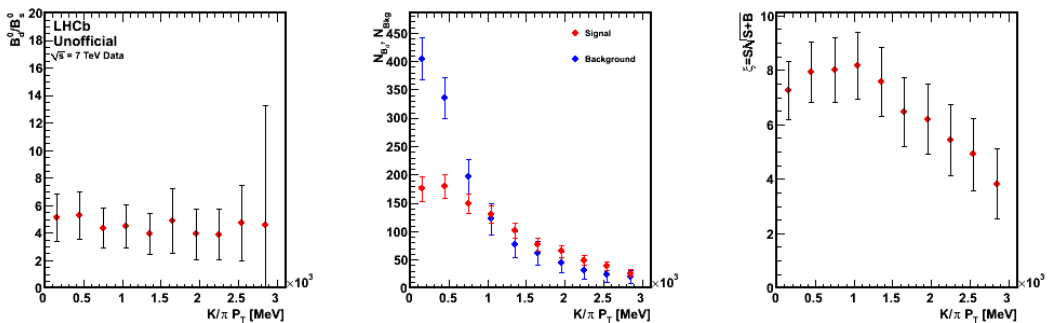


a)

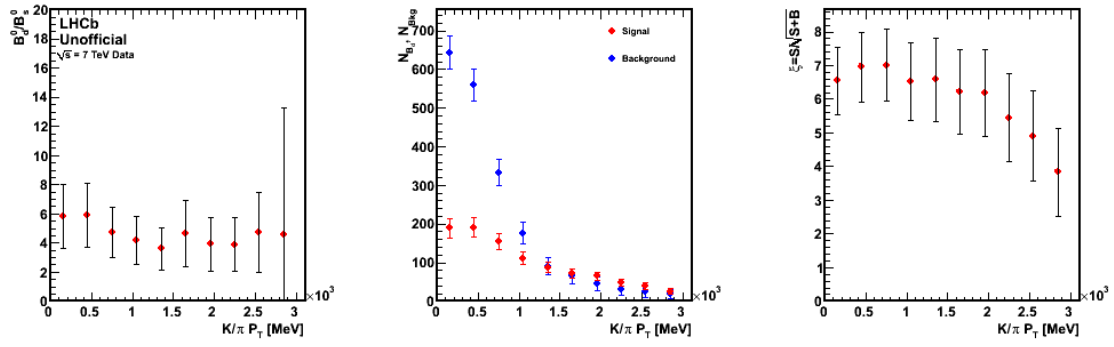


a')

K,  $\pi$   $P_T$  b) all cuts applied, b')  $B_{PT}$  removed

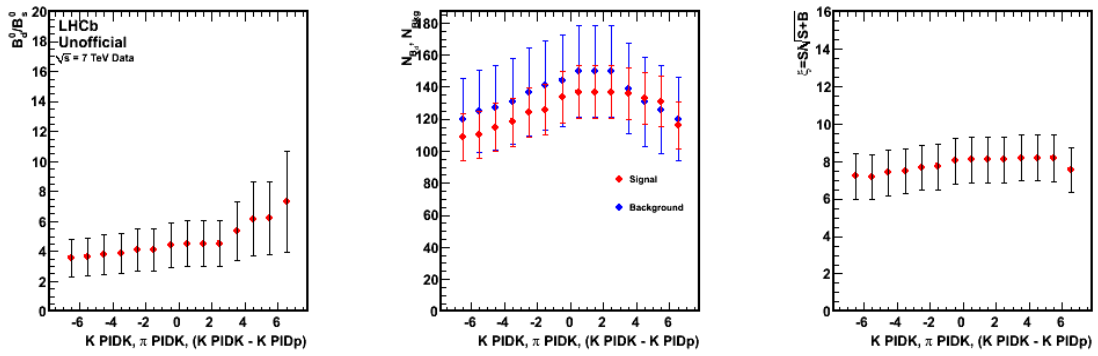


b)

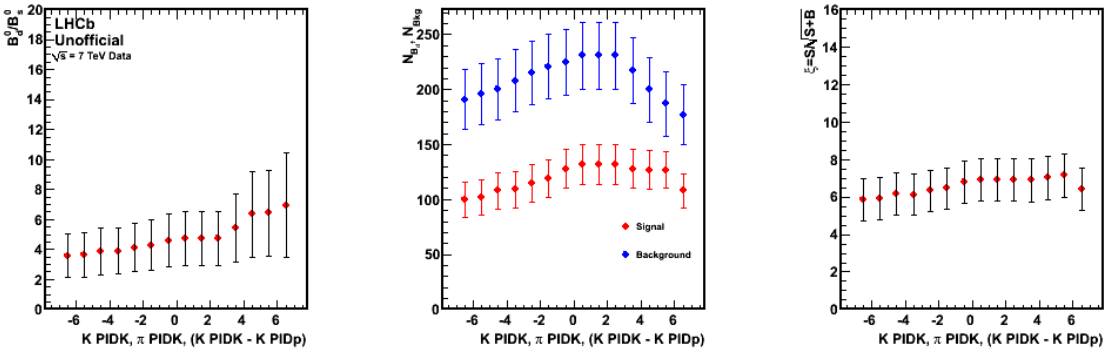


b)

$K$  PIDK,  $\pi$  PIDK,  $K$  PIDK -  $K$  PIDp c) all cuts applied, c')  $B P_T$  removed

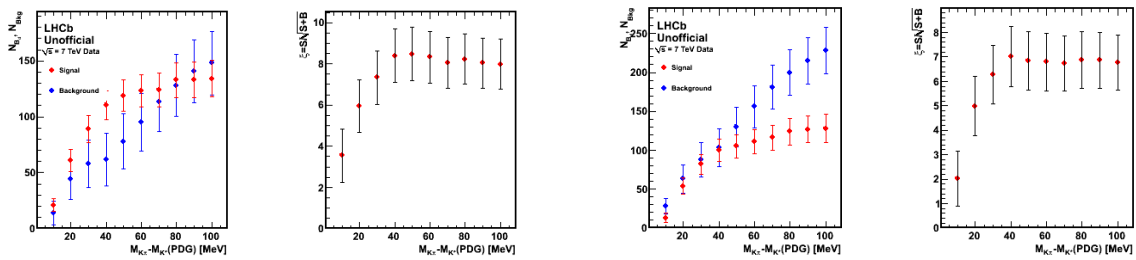


c)



c')

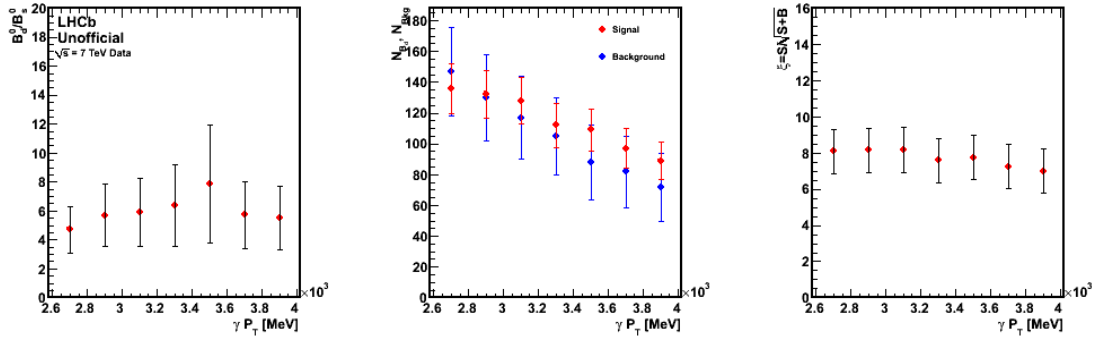
$K^*$  mass window around the nominal PDG value, d) all cuts applied, d')  $B P_T$  removed



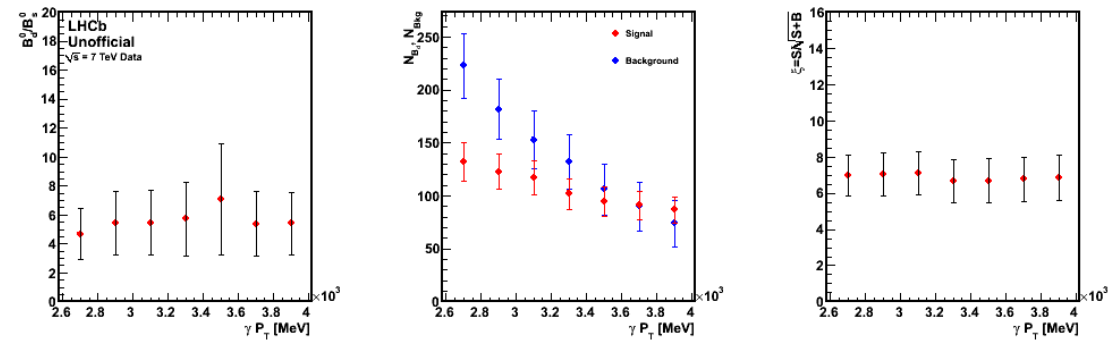
d)

d')

$\gamma P_T$  e) all cuts applied, e')  $B P_T$  removed

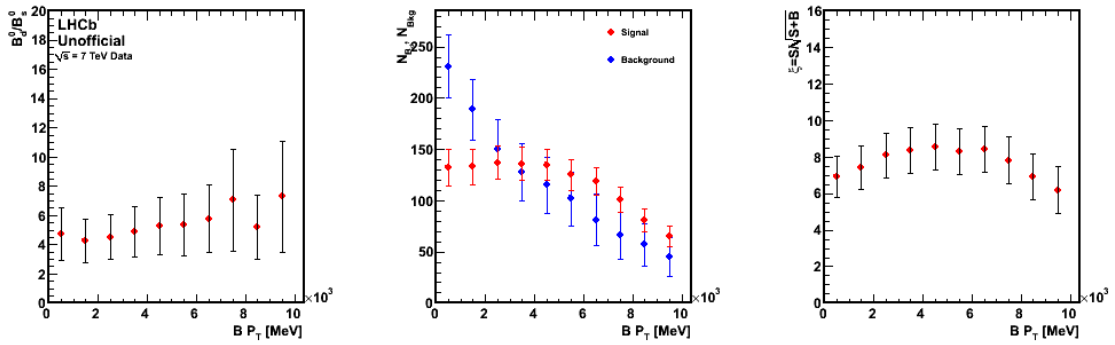


e)



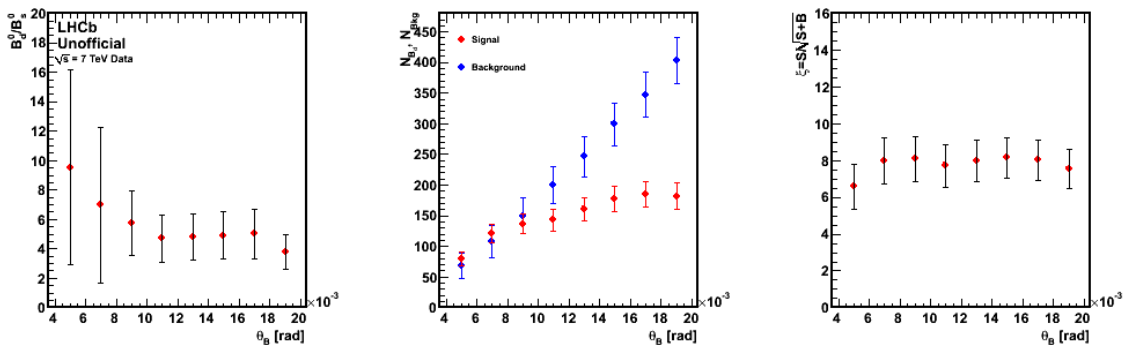
e')

$B P_T$  f) all cuts applied

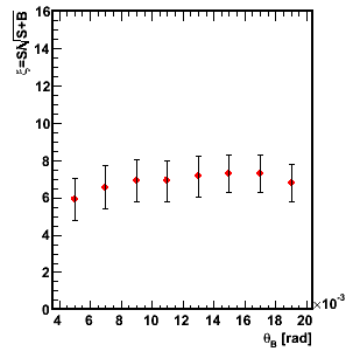
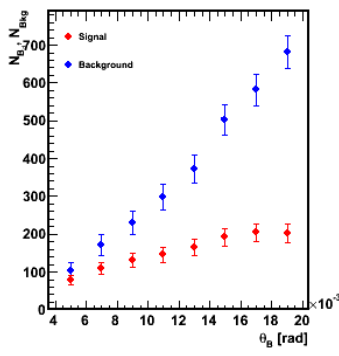
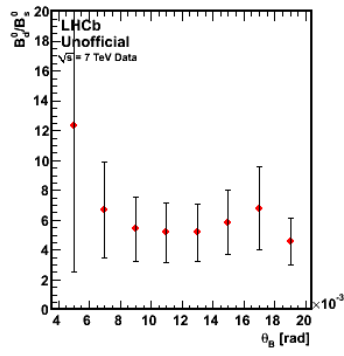


f)

B direction angle, g) all cuts applied, g')  $B P_T$  removed

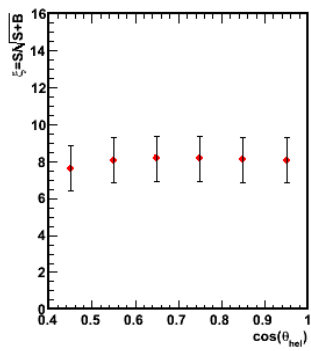
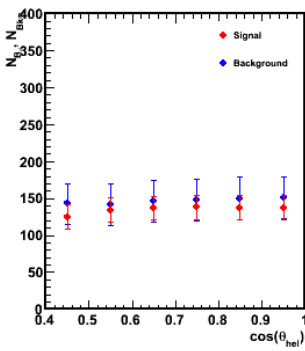
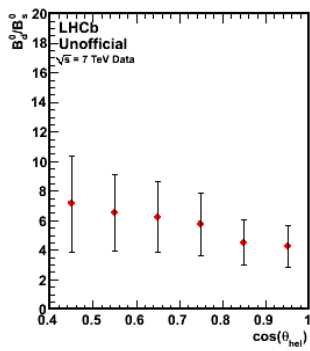


g)

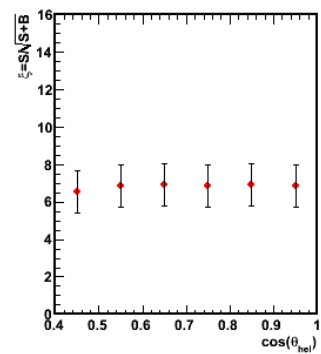
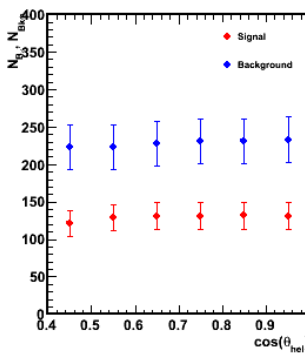
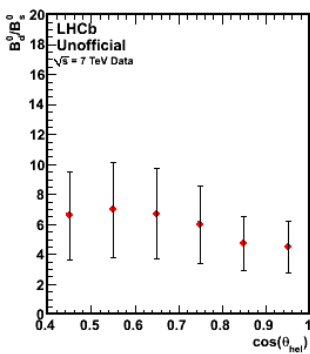


g')

B helicity angle, h) all cuts applied, h') B P<sub>T</sub> removed

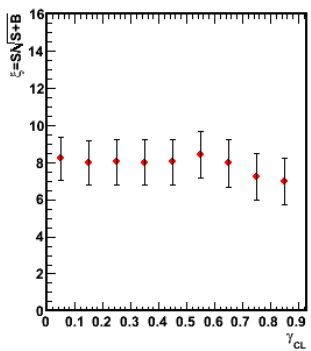
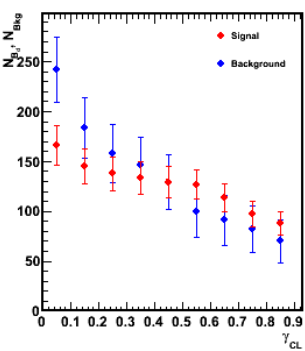
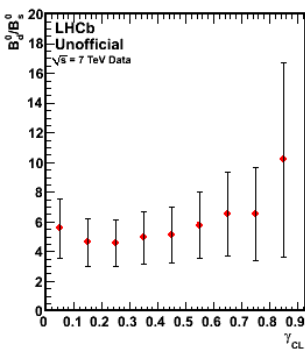


h)

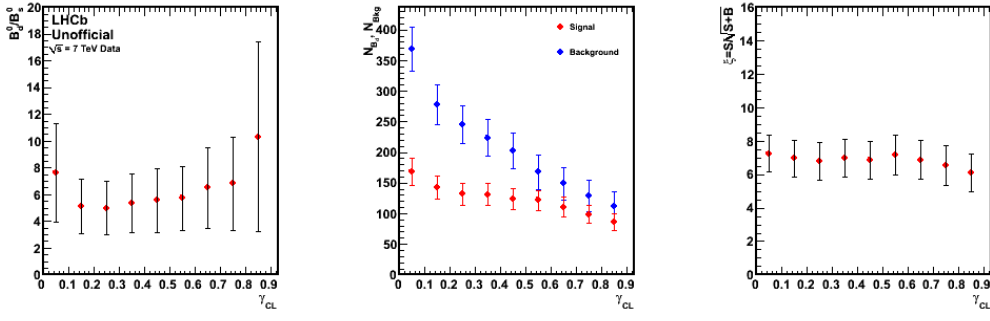


h')

$\gamma$  CL, i) all cuts applied, i') B P<sub>T</sub> removed



i)



i)

Figure 4.2.4 Stability check of the ratio  $\mathcal{R} = \mathcal{N}(B_d \rightarrow K^* \gamma) / \mathcal{N}(B_s \rightarrow \phi \gamma)$  for 2010 data (left-hand plots), the number of signal and background events for the  $B_d \rightarrow K^* \gamma$  channel (middle plots) and the calculation of  $\xi = \frac{S}{\sqrt{S+B}}$  (right-hand plots) when varying the following cuts a)  $K, \pi$  minimal IP  $\chi^2$  b)  $K, \pi$  transverse momentum, c)  $K$   $P_{IDK}$ ,  $\pi$   $P_{IDK}$ , ( $K$   $P_{IDK}$ -  $K$   $P_{IDp}$ ), d)  $K^*$  mass window, e) photon transverse momentum, f)  $B_d$  transverse momentum, g) direction angle,  $\theta_B$ , h) helicity angle and i) photon confidence level, when all the other offline cuts are applied at their nominal values presented in Table 4.2.2. The figures labeled with prime letters represent the same variables in the case where the  $B_{PT}$  cut is removed

For the consistency of the fits on the two mass peaks, the study presented in Figure 4.2.4, has been performed at a fixed standard deviation,  $\sigma$ , of the Gaussian functions used for the mass fits. This figure shows that the  $B_d/B_s$  ratio remains stable within errors with respect to each of the selection cuts and clearly a cut on the transverse momentum of B is very efficient in removing background events.

However, the hypothesis of the standard deviation as a free parameter of the fit has also been studied and the results are presented in the following. The official selection criteria have been applied on the 2010+2011 data, while varying one of the cuts. The impact of the removal of the  $B_{PT}$  cut on the  $\sigma$  distribution has also been studied. Three options have been pursued, Option I, the  $B_{PT}$  cut is removed from the selection, Option II,  $B_{PT} > 2$  GeV, and Option III,  $B_{PT} > 3.5$  GeV. The results are shown in Figure 4.2.5 a) to d) for the standard deviation of the  $B_d \rightarrow K^* \gamma$  mass peak when  $B_{PT}$ ,  $K$  and  $\pi$  minimal IP  $\chi^2$ ,  $K^*$  mass window and the helicity angle are being varied. The distributions for the rest of the selection cuts are given in Appendix 1. At the same time, the standard deviation of the  $B_s \rightarrow \phi \gamma$  mass peak has been plotted but the limited statistics of the  $B_s \rightarrow \phi \gamma$  sample gives rise to large uncertainties; a few examples are presented in Appendix 1.

The plots shown in Figure 4.2.5 a) to d) indicate a dependence of  $\sigma$  on the  $B_{PT}$  cut. The mass width increases steadily up to a cut on  $B_{PT}$  of about 3.5 GeV after which it remains constant within errors up to values as high as 10 GeV. Coupled with the results shown in Appendix 2 (the invariant mass distribution of  $B_d \rightarrow K^* \gamma$  for different cut values of  $B_{PT}$  while the  $\gamma_{PT}$  cut is being varied) there is strong evidence that when removing the cut on  $B_{PT}$ , the background shape is not well approximated by an exponential function and the invariant mass peak is not correctly fitted by a Gaussian function, as demonstrated in Figure A.2.1 a) to g) left

plots (Appendix 2). Consequently, the signal yield estimated from the fit is not accurate when low momentum B candidates are removed. Thus, a cut on  $B_{PT}$  is mandatory for a reliable description of the background which strongly affects the signal yield extraction reliability.

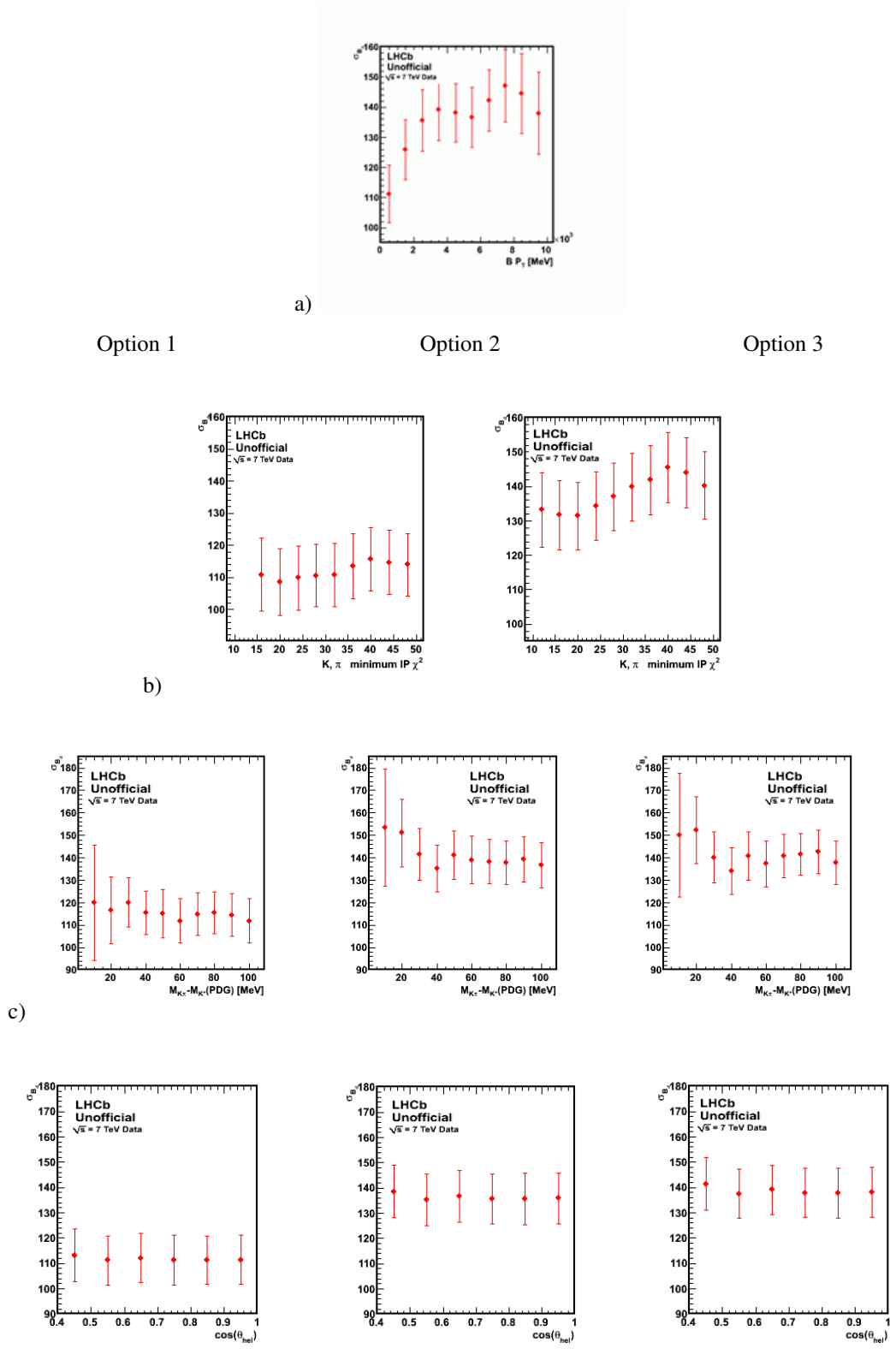


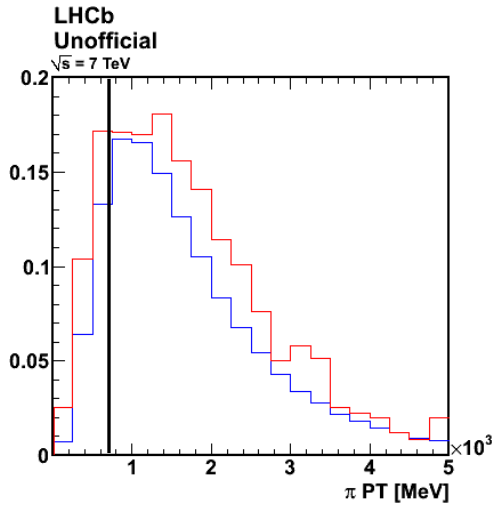
Figure 4.2.5 The distribution of the standard deviation of  $B_d \rightarrow K^* \gamma$  mass peak when different selection cuts are varied a)  $B_{PT}$ , b)  $K, \pi$  minimal  $IP \chi^2$ , c)  $K^*$  mass window, d) the helicity angle, in three different scenarios: Option I, the  $B_{PT}$  cut is removed from the selection, Option II,  $B_{PT} > 2$  GeV, and Option III,  $B_{PT} > 3.5$  GeV

The procedure undertaken above was performed with the purpose of optimizing the selection criteria on a larger sample of real data. The optimization consists in maximizing the signal to background ratio, or more precisely, the  $\xi$  ratio,  $\xi = \frac{S}{\sqrt{S+B}}$ . By analyzing  $\xi$  distribution, shown in Figure 4.2.4 a) to i), right plots, a new tuned set of selection criteria has been determined for  $B_d \rightarrow K^* \gamma$  and  $B_s \rightarrow \phi \gamma$  decay channels and it is presented in the following. The optimized cuts are summarized in Table 4.2.4, third column, and compared to the “old” official selection criteria tuned on Monte Carlo simulated data (first column) [67] and to the official offline selection criteria tuned on 2010 real data, second column [69], which have been approved by the LHCb collaboration and used to produce the official invariant mass plots for the two decay channels,  $B_d \rightarrow K^* \gamma$  and  $B_s \rightarrow \phi \gamma$ .

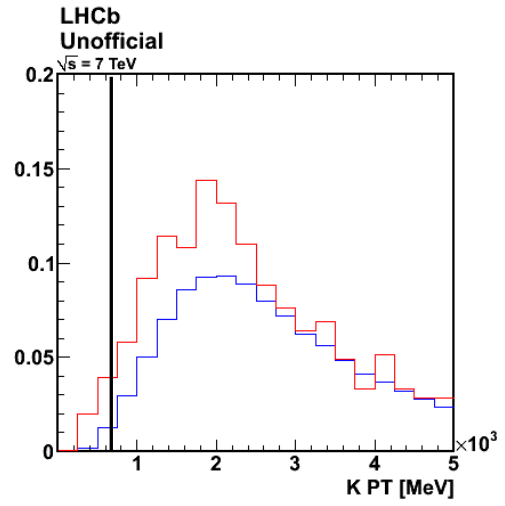
Cut	Old offline cuts (tuned on MC)		Official offline cuts (tuned on 37/pb)		New Tuned Cuts (tuned on 88/pb)	
	$B^0 \rightarrow K^{*0} \gamma$	$B_s^0 \rightarrow \phi \gamma$	$B^0 \rightarrow K^{*0} \gamma$	$B^0 \rightarrow \phi \gamma$	$B^0 \rightarrow K^{*0} \gamma$	$B_s^0 \rightarrow \phi \gamma$
$K, \pi$ minimum $IP\chi^2$	>25	25	>25	25	>36	>36
$K, \pi P_T$			750	750	750	750
$K \Delta \log \mathcal{L}(K-\pi)$	>3	>3	>5	>5	>3	>3
$K \Delta \log \mathcal{L}(K-p)$	>5	-	>2	>2	>3	>3
$\pi \Delta \log \mathcal{L}(K-\pi)$	<5	-	<0	-	<-3	-
$K^*/\phi \Delta_{Mass}$	<100 MeV	<10 MeV	<100 MeV	<10 MeV	<60 MeV	<10 MeV
$K^*/\phi$ vertex $\chi^2$	<9	<9	<9	<9	<9	<9
$\gamma_{PT}$	>2.8 GeV	>2.8 GeV	>2.5 GeV	>2.5 GeV	>2.6 GeV	>2.6 GeV
$B_d/B_s$ minimum $IP\chi^2$	<9	<9	<9	<9	<9	<9
$B_d/B_s$ direction angle	<8 mrad	<10 mrad	<20 mrad	<20 mrad	<8 mrad	<10 mrad
$ \cos(B_d/B_s \text{ helicity}) $	<0.8	<0.8	<0.8	<0.8	<0.8	<0.8
$B_d/B_s P_T$			>2 GeV	>2 GeV	>3.5 GeV	>3.5 GeV
BestTracks			<250	<250		
$\gamma_{CL}$			>0.25	>0.25	0.3	0.3

Table 4.2.4 Comparison between the official selection and the author’s selection

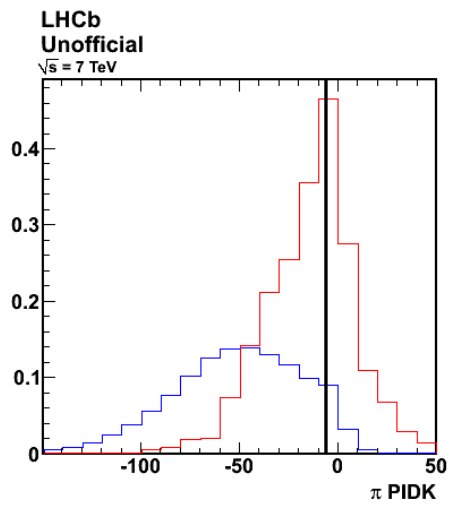
The effect of the selection cuts is better understood when studying the distribution of each of the variables which are being constrained. Figure 4.2.6 a) to l) shows the distribution of the cut variables when all the offline cuts are applied except for the cut which is being plotted for the  $B_d \rightarrow K^* \gamma$  channel. The red lines in Figure 4.2.6 a) to l) correspond to real data and they are being compared to the Monte Carlo simulated data using the  $B_d \rightarrow K^* \gamma$  signal sample, the blue lines. The black markers indicate the cut values summarized in Table 4.2.4, third column. Overall, there is good agreement between real data and simulation in what concerns the  $B_d \rightarrow K^* \gamma$  candidates passing the offline selection, the differences come from the fact that in the simulated sample there are only signal events while for the data background events are also present.



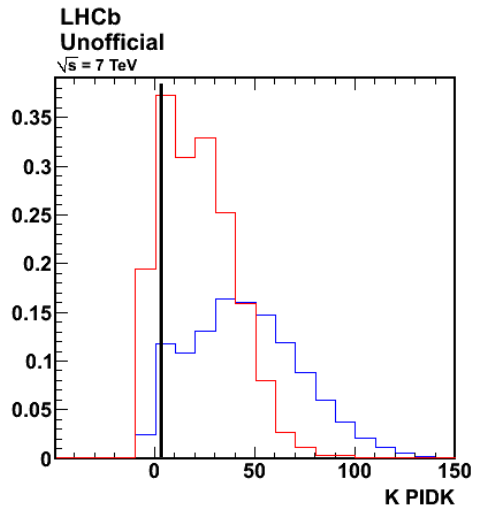
a)



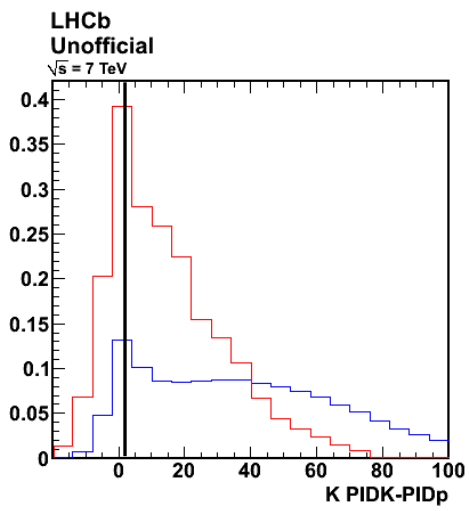
b)



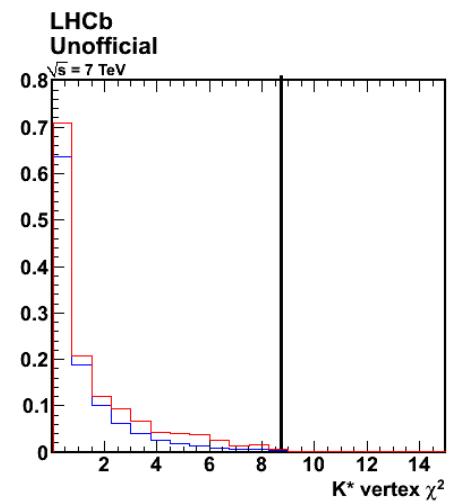
c)



d)



e)



f)

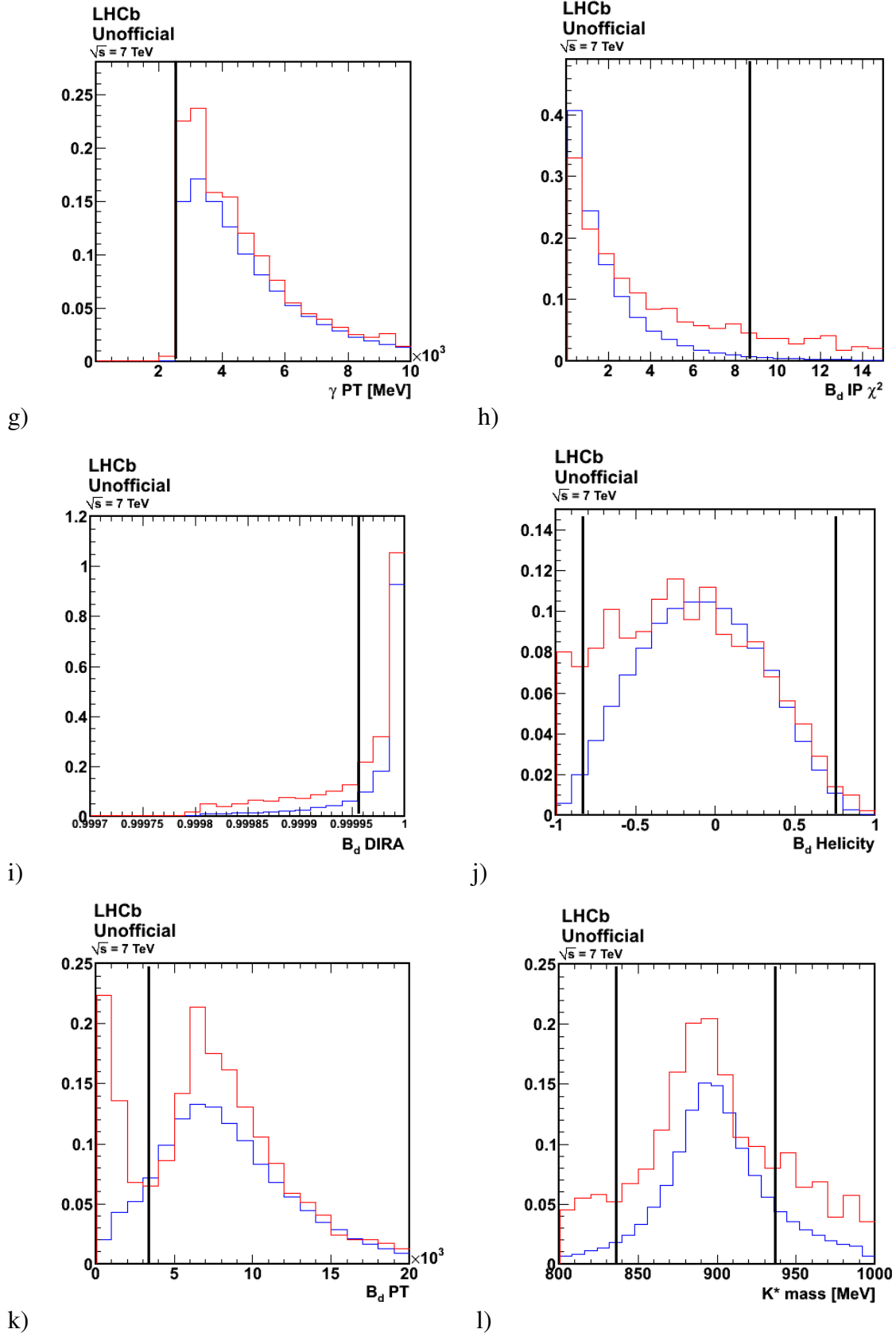


Figure 4.2.6 Distribution of cut variables while all new selection cuts are applied except for the cut shown in the respective distribution: a)  $\pi$   $P_T$ , b)  $K$   $P_T$  c)  $\pi$  PIDK d)  $K$  PIDK e)  $K$  PIDK-PIDp f)  $K^*$  vertex  $\chi^2$  g)  $\gamma$   $P_T$  h)  $B_d$  IP  $\chi^2$  i)  $B_d$  direction angle j)  $B_d$  helicity k)  $B_d$   $P_T$  and l)  $K^*$  mass. The blue line corresponds to  $B_d \rightarrow K^* \gamma$  Monte Carlo sample, the red line corresponds to real data and the black vertical lines indicate the values of the new offline selection cuts summarized in Table 4.2.4.

Figure 4.2.8 shows the reconstructed invariant mass distribution for  $B_d \rightarrow K^* \gamma$  and  $B_s \rightarrow \phi \gamma$  decay channels when the optimized set of selection cuts is applied on the candidates passing the stripping selection. The figure demonstrates that the new selection improves the signal to background ratio by significantly removing background events. Compared to Figure 4.2.7, showing the invariant mass peaks for  $B_d \rightarrow K^* \gamma$  and  $B_s \rightarrow \phi \gamma$  channels using the official selection cuts, the new cuts reduce the signal yield by only 15% for  $B_d \rightarrow K^* \gamma$  and 24% for  $B_s \rightarrow \phi \gamma$  while the background is reduced up to 85% for  $B_d \rightarrow K^* \gamma$  and up to 63% for  $B_s \rightarrow \phi \gamma$ . This is not the only advantage of the new selection cuts. When the new cuts are applied the background shape can be well fitted by an exponential function which results in a reliable extraction of the signal yield, as opposed to the official selection cuts where there were obvious structures in the background shape at low and high mass [69]. An additional selection of the best tracks found in the detector, Figure 4.2.9, seems to remove even more of the background but as the background is reduced by another 5% for  $B_d \rightarrow K^* \gamma$ , the signal yield is reduced in equal proportion so its use is rather obsolete.

Thus, the new tuned criteria select the  $B_d \rightarrow K^* \gamma$  channel with a signal to background ratio  $S/B=1.39 \pm 0.17$  and  $B_s \rightarrow \phi \gamma$  with  $S/B=1.15 \pm 0.32$ .

A new stability check of the  $B_d$  to  $B_s$  signal ratio was performed for the new tuned selection cuts. The results are shown in Figure 4.2.10 and they prove that the  $B_d/B_s$  ratio is stable with respect to the new selection.

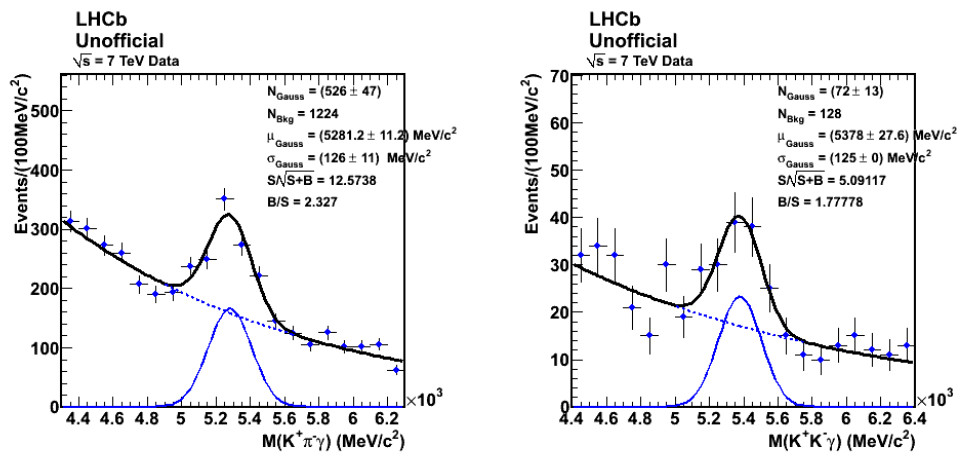


Figure 4.2.7 Invariant mass peaks for  $B_d \rightarrow K^* \gamma$  and  $B_s \rightarrow \phi \gamma$  channels using the official selection cuts approved by the LHCb collaboration and used to produce the official plots for these two channels, shown in Figure 4.2.3

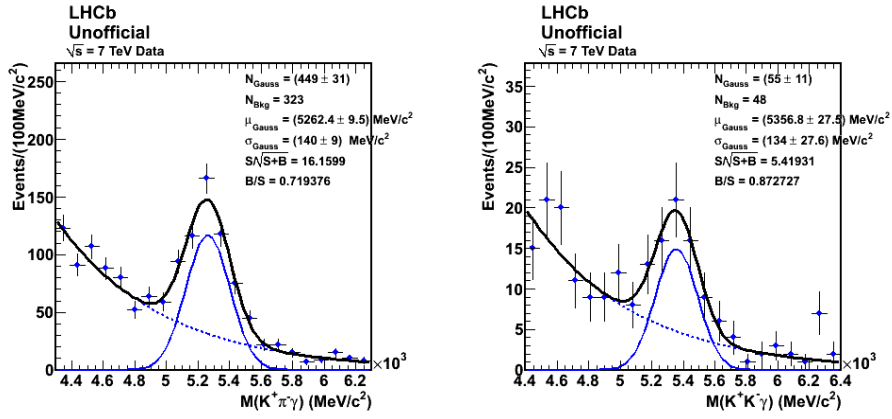


Figure 4.2.8 Invariant mass peaks  $B_d \rightarrow K^* \gamma$  and  $B_s \rightarrow \phi \gamma$  channels using the new tuned set of cuts summarized in Table 4.2.4, third column

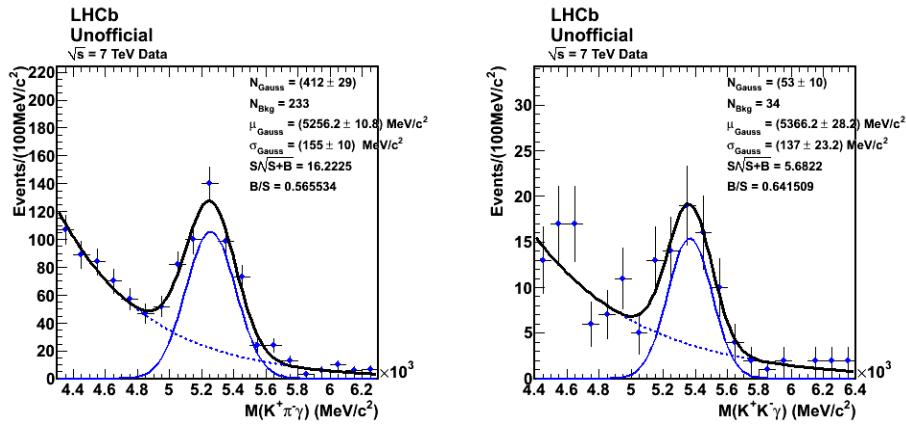


Figure 4.2.9 Invariant mass peaks  $B_d \rightarrow K^* \gamma$  and  $B_s \rightarrow \phi \gamma$  channels using the new tuned set of cuts summarized in Table 4.2.4, third column to which the selection of best tracks is added (BestTracks<250)

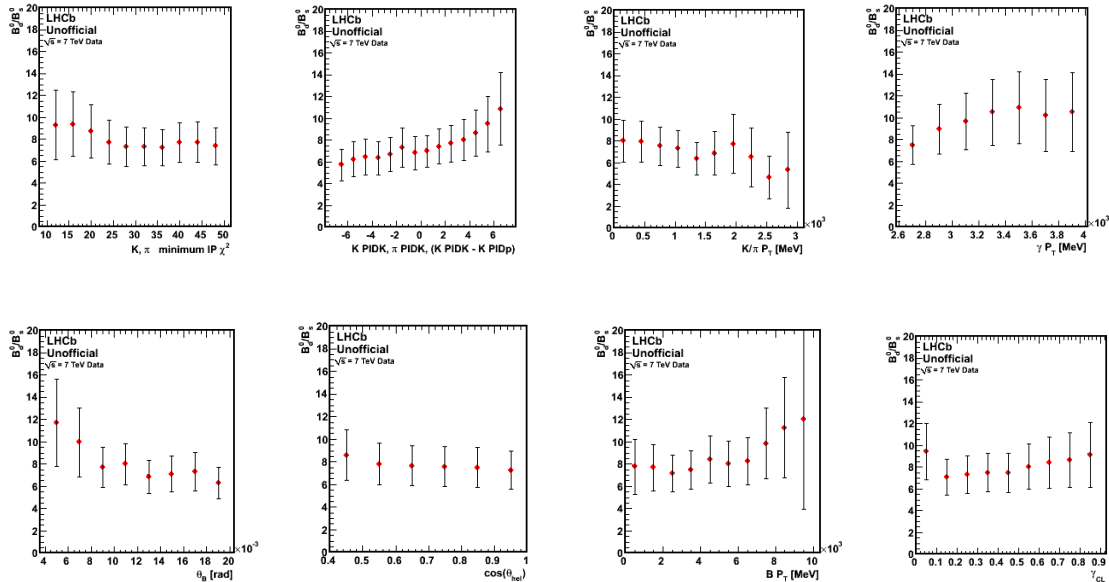


Figure 4.2.10 Stability check of the ratio  $\mathcal{R} = \mathcal{N}(B_d \rightarrow K^* \gamma) / \mathcal{N}(B_s \rightarrow \phi \gamma)$  for 2010+2011 data, using the new selection cuts, when varying the following cuts:  $K, \pi$  minimal IP  $\chi^2$ ,  $K$   $PIDK$ ,  $\pi$   $PIDK$ ,  $(K$   $PIDK - K$   $PIDp)$ ,  $K, \pi$  transverse momentum, photon transverse momentum, direction angle,  $\theta_B$ , helicity angle,  $B_d$  transverse momentum, and photon confidence level, when all the other offline cuts are applied at their nominal values presented in Table 4.2.4, third column.

## 4.3 Conclusions

In this chapter it has been demonstrated that with the  $88 \text{ pb}^{-1}$  of data collected during the 2010 run and partially in 2011 radiative decays peaks are visible at LCHb. The selection strategy proposed for two representative radiative decays,  $B_d \rightarrow K^* \gamma$  and  $B_s \rightarrow \phi \gamma$ , has been described and distributions of the variables on which selection cuts are applied in real data were compared to the distributions of the same variables in simulated data. It is shown that, overall, there is a good agreement between data and simulation, the differences coming from the fact that while in simulation only signal events were included, in real data some background is also present.

Next, the ratio between the signal yields in the two radiative channels has been checked and it has been proved that this ratio is stable within errors with respect to the selection criteria applied. Also, a cut on the transverse momentum of B meson is found to be very efficient in reducing the background level as well as the peaking structures observed in the left and right mass sideband.

The dependence of signal and background yields on each of the selection cuts was studied in two cases, when a cut on  $B_{P_T}$  is not applied and when  $B_{P_T} > 2 \text{ GeV}$ . This study further confirmed the importance of the  $B_{P_T}$  cut and it allowed the calculation of  $\xi = \frac{S}{\sqrt{S+B}}$  which is a measure of how well the signal is discriminated from the background. The goal is to find the cut values which maximize this variable. Based on  $\xi$  distribution as a function of each variable on which a cut is applied, a new set of selection criteria has been optimized to select with increased efficiency the two radiative decays  $B_d \rightarrow K^* \gamma$  and  $B_s \rightarrow \phi \gamma$ . It was found that the new tuned criteria select the  $B_d \rightarrow K^* \gamma$  channel with a signal to background ratio  $S/B = 1.39 \pm 0.17$  and  $B_s \rightarrow \phi \gamma$  with  $S/B = 1.15 \pm 0.32$ .

# 5. Background studies for $B_d \rightarrow K^* \gamma$

## 5.1 Background studies on simulated data

The understanding of background is a crucial prerequisite in any particle physics analysis, but it is especially important for the study of decays with very small branching ratios ( $\mathcal{B}$ ) where the analysis requires a sample as clean as can possibly be obtained. This is the case of the very rare decay  $B_d \rightarrow K^* \gamma$  which has a  $\mathcal{B} = 4.3 \times 10^{-5}$  [70].

Prior to looking at real data, a study of the composition of the background can be performed on Monte Carlo samples. For these samples, the event generator provides all details about the simulated decays which cannot be accessed when looking directly at real data. This is an advantage that can be used to the purpose of making an estimation of what is to be expected as background for different decay channels and provide the tools for eliminating this background.

The reconstruction of decay channels is affected by different uncertainties introduced at different steps in the reconstruction process. For example, the track reconstruction algorithm identifies tracks, with limited precision, by putting together hits in the detector, the particle identification algorithms assign particles to these tracks with a certain amount of accuracy and event reconstruction algorithms combine these particles in order to recreate a specific decay, also with a certain amount of accuracy. Mis-reconstruction of events can come from bad reconstructed tracks, bad matching between tracks and particles or combinations of daughters coming from different decays. At event generator level, we know with 100% certainty which decays have been simulated and this is the advantage which is being explored when working with Monte Carlo data; we can determine the true generated decay to which each of the reconstructed decays has been matched. [72]

In the following I will report on the method used for determining the possible sources of background for the  $B_d \rightarrow K^* \gamma$  decay and I will show how much of this background can be removed by the offline selection, summarized in Table 4.2.2, first column.

Data flow at LHCb follows a few steps before the final offline analysis is applied. First, the relevant events must trigger the hardware L0 trigger, then, they must be confirmed by the high level triggers, HLT1 and HLT2, which are software triggers [47]. After passing

the relevant triggers (radiative decays will be triggered mainly due to the presence of a high energy photon) the remaining data go through a so called stripping process which is called “Stripping line”. For each exclusive decay channel, the stripping line represents a collection of specific kinematical cuts which are designed to efficiently select the desired decay and keep the background within reasonable limits. Radiative stripping runs on the output of the entire HLT2. Ultimately, the offline selection is engaged [73]. The stripping selection cuts for the radiative stream are also summarized in Table 4.2.2.

In detail, the offline selection strategy is described in Chapter 4.2.2 of this thesis.

The first step in determining the background sources is to apply the  $B_d \rightarrow K^* \gamma$  selection on a large sample of inclusive  $b\bar{b}$  pairs. This sample contains about 20 million generated  $b\bar{b}$  events and it has been created primarily for studies regarding combinatorial backgrounds. For this sample, a selection cut is applied at the generator level to select only particles which are produced inside the detector angular acceptance, the requirement being that the polar angle  $\theta < 400$  mrad. This selection criterion has a selection efficiency of 43% thus the initial sample, before the acceptance constraint, contains  $\sim 46.5$  million  $b\bar{b}$  events [74].

After applying the offline and stripping selection for the  $B_d \rightarrow K^* \gamma$  radiative decay, summarized in Table 4.2.2, on the inclusive  $b\bar{b}$  sample, 23 candidates pass this selection as reconstructed  $B_d \rightarrow K^* \gamma$  decays, shown in Figure 5.1. The fact that the data sample contains simulated events, offers the possibility to access information regarding all decays which have been generated and more than that, tools have been developed to provide details on the correctness of matching between generated and reconstructed events. Consequently, for each reconstructed event, the user can determine the true generated decay or the true generated particle to which a certain reconstructed track has been matched to. This is called “Monte Carlo Truth/True” information [75] and from here on it will be referred to as “MCTruth”.

This advantage is explored in the following study to determine how many of the 23 reconstructed  $B_d \rightarrow K^* \gamma$  events passing the offline selection (Table 4.2.2) are true  $B_d \rightarrow K^* \gamma$  decays. This is done by comparing each reconstructed event with the corresponding generated event provided by the event generator.

A first look at the MCTruth information shows that only 6 events are true  $B_d$  particles, the green line in Figure 5.1, in other six cases the  $B_d$  has actually been matched to a track corresponding to a  $B^+$  particle, the blue dashed line, and eleven times the  $B_d \rightarrow K^* \gamma$  decay has

been reconstructed from random combinations of tracks which satisfied the kinematical constraints, the red dashed line.

A next step is to look at all the daughters of all the selected candidates and establish if they are true daughters or if they are other particles which have been misidentified as a  $K^*$ ,  $\gamma$ ,  $K$  and  $\pi$  daughters or granddaughters resulted in the  $B_d \rightarrow K^* \gamma$  decay.

The information related to the identity of all the daughters is summarized in Figure 5.2. The red dots correspond to the selected candidates as seen in a double mass representation: the reconstructed  $K^*$  mass window (100 MeV around the nominal mass of  $K^*$ ) vs. reconstructed  $B_d$  mass in a mass interval ranging from 4200 to 6300 MeV. Figure 5.2 shows that within these mass limits there are 4  $B_d \rightarrow K^* \gamma$  events where all daughters are matched to true  $K^*$ ,  $\gamma$ ,  $K$  and  $\pi$ , thus there are 4 true  $B_d \rightarrow K^* \gamma$  events. In 4 other cases, although all daughters are true daughters, the mother is a true  $B^+$ , in 10 cases the  $K^*$  is a real  $D^0$ ,  $D^{+/-}$ ,  $B^0$  or a strange resonance like  $X_{su}$ ,  $X_{sd}$  and in three cases the pion is a true electron or muon and the photon is a true electron.

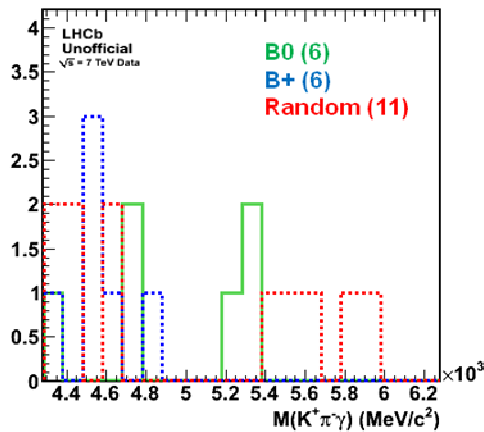


Figure 5.1  $B_d \rightarrow K^* \gamma$  reconstructed events after all offline selection cuts have been applied on the inclusive  $b\bar{b}$  sample, the reconstructed events matched to: true  $B_d$  are shown in green, to true  $B^+$ , in blue and random combinations in red

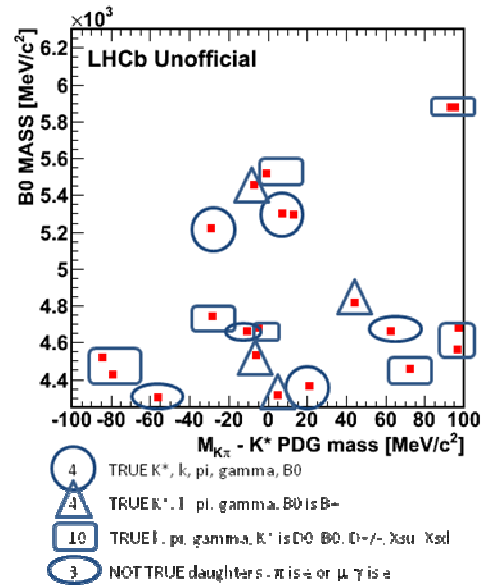


Figure 5.2  $K^*$  mass window vs.  $B_d$  mass, identification of the real daughters involved in the  $B_d \rightarrow K^* \gamma$  decay

More information about the nature of the background, such as finding out where all the reconstructed particles come from, can be obtained by looking at the true mothers and grandmothers of all the particles involved in the reconstructed decays. This information is summarized in Table 5.1. The first column represents the true mothers (Mo), grandmothers

(GD) and, when needed, the great-grandmothers (GGD) corresponding to each of the particles involved in the  $B_d \rightarrow K^*(K^+\pi^-)\gamma$  decay. Based on this information possible background channels for  $B_d \rightarrow K^*\gamma$  can be identified; they are detailed on the second column of Table 5.1. However, this hierarchical information does not provide the complete decay tree, even if all predecessors can be determined for a certain daughter, it is not enough to determine whether two daughters come from a common mother or whether there is any connection between the mothers.

A solution is to access the MCTruth information provided by the event generator and print the full decay tree in order to follow step by step the matching between the reconstructed and the corresponding generated decay. This operation is performed for all the 23 reconstructed  $B_d \rightarrow K^*\gamma$  candidates which remain after the offline selection applied on the  $b\bar{b}$  inclusive sample in order to evaluate all possible background sources for this specific decay channel. The generated decays corresponding to each of the  $B_d \rightarrow K^*\gamma$  reconstructed candidates are summarized on the third column of Table 5.1.

By combining all the information described above it is possible to identify not only the specific detailed decay channels which can interfere with the analysis of  $B_d \rightarrow K^*\gamma$  but also the nature of the background sources. The information summarized in Table 5.1 indicates that one of these background sources is the erroneous reconstruction of a  $K^*$  particle. The  $K^*$  is matched to a track which in reality is another particle most often decaying into a pair of charged K and  $\pi$ , or a group of particles which include a  $K$ - $\pi$  pair. There is also the risk that the charged daughters, K and  $\pi$ , are matched to other particles altogether, such as electrons or muons.

Another non-negligible source of background is the combination of a random photon, coming from other B- or  $\pi^0$ -decays, with a  $K^*$  to form a  $B_d \rightarrow K^*\gamma$  event. Moreover, completely random K,  $\pi$  and  $\gamma$ , coming from different decays, can be combined to form  $K^*$  and  $B_d$  particles. This is referred to as “combinatorial background”.

Mother & Grandmother (Mo&GD) Information	Predicted decay based on Mo&GD information	MCTruth decays
<b>Real B<sub>d</sub> K* γ</b>		
K* from B <sup>0</sup> , GD=0 γ Mo=B <sup>0</sup> , GD=0 K Mo=K*, GD=B <sup>0</sup> π Mo=K*, GD=B <sup>0</sup>	B <sup>0</sup> K <sup>*0</sup> +γ K+π	B <sup>0</sup> + K*(892) <sup>0</sup>   K <sup>+</sup> p   π <sup>-</sup> e <sup>+</sup> + ... + γ
K* Mo=B <sup>0</sup> , GD=B <sup>*0</sup> γ Mo=B <sup>0</sup> , GD=B <sup>*0</sup> K Mo=K*, GD=B <sup>0</sup> , GGD=B <sup>*0</sup> π Mo=K*, GD=B <sup>0</sup> , GGD=B <sup>*0</sup>	B <sup>*0</sup> B <sup>0</sup> K <sup>*0</sup> +γ K+π	B <sup>0</sup> + K*(892) <sup>0</sup>   K <sup>+</sup>   π <sup>-</sup> + γ  B <sup>0</sup> + D <sup>-0</sup>   a <sub>1</sub> (1260) <sup>-</sup> ρ(770) <sup>0</sup> π <sup>-</sup>   K <sup>+</sup> e <sup>-</sup> + π <sup>-</sup> + π <sup>+</sup>
K* Mo=B <sup>0</sup> , GD=0 γ Mo=B <sup>0</sup> , GD=0 K Mo=K*, GD=B <sup>0</sup> π Mo=K*, GD=B <sup>0</sup>	B <sup>0</sup> K <sup>*0</sup> +γ K+π	B <sup>0</sup> + K*(892) <sup>0</sup>   K <sup>+</sup>   π <sup>-</sup> + γ  B <sup>-</sup> + D <sup>0</sup>   K <sup>-</sup>   π <sup>0</sup> γ   e <sup>+</sup>   ν <sub>e</sub> + τ <sup>-</sup> π <sup>-</sup> π <sup>0</sup> ( γ ) ν <sub>τ</sub> + ν <sub>τ</sub> ~
B id is B <sup>-0</sup> , from 0 K* Mo=D <sup>0</sup> , GD=B <sup>-0</sup> γ Mo=π <sup>0</sup> , GD=B <sup>0</sup> GGD=0 K Mo=K <sup>-</sup> , GD=D <sup>0</sup> π Mo=K <sup>-</sup> , GD=D <sup>0</sup>	B <sup>-0</sup> D <sup>0</sup> +... K <sup>*0</sup> +... K+π B <sup>0</sup> π <sup>0</sup> +... γ+...	B <sup>-0</sup> + D <sup>0</sup>   K*(892) <sup>-0</sup> K <sup>-</sup> π <sup>+</sup>   ρ(770) <sup>0</sup> π <sup>+</sup> π <sup>-</sup> + π <sup>0</sup> γ ( e <sup>+</sup> e <sup>-</sup> ) γ  B <sup>0</sup> + Ω <sub>c</sub> <sup>0</sup>   X <sub>i</sub> <sup>*0</sup> π <sup>0</sup> X <sub>i</sub> <sup>0</sup>   K <sup>*0</sup> K <sub>L</sub> <sup>0</sup> + K <sup>+</sup> π <sup>0</sup> ( γ ) π <sup>+</sup> p K <sub>L</sub> <sup>0</sup> + p~ e <sup>-</sup>
<b>B D<sup>0</sup>, D* something + random photon</b>		
γ is e+ K* Mo=B <sup>0</sup> , GD=B <sup>*0</sup> , GGD=0 γ Mo=0, GD=0 K Mo=K*, GD=B <sup>0</sup> π Mo=K*, GD=B <sup>0</sup> , GGD=B <sup>*0</sup>	B <sup>*0</sup> B <sup>0</sup> + something K* + something K π <b>+ random photon</b>	B <sup>-0</sup> + D <sub>2</sub> (2460) <sup>+</sup>   D <sup>0</sup> K <sub>L</sub> <sup>0</sup> π <sup>0</sup> π <sup>0</sup>   π <sup>+</sup> e <sup>-</sup> + K <sup>-</sup> + K*(892) <sup>0</sup> K <sup>+</sup> π <sup>-</sup>  B <sub>s</sub> <sup>0</sup> + D <sub>s</sub> <sup>*-</sup>   D <sub>s</sub> <sup>-</sup> φ(1020) μ <sup>-</sup> ν <sub>μ</sub> ~   γ e <sup>+</sup> e <sup>-</sup> + e <sup>+</sup> 2e <sup>-</sup> 4γ + ν <sub>e</sub>
K* is D <sup>-0</sup> K* Mo=B <sup>+/-</sup> , GD=B <sup>+/-</sup> γ Mo=π <sup>0</sup> , GD=0	B <sup>*+/-</sup> B <sup>+/-</sup> +something D <sup>0</sup> +something K ρ	B <sup>+</sup> + D <sup>-0</sup>   K <sup>+</sup> μ <sup>+</sup>   ρ <sup>-</sup> π <sup>0</sup> π <sup>-</sup>

<p>K Mo=D<sup>0(-)</sup>, GD=B<sup>+/-</sup>  <math>\pi</math> Mo=<math>\rho</math>, GD=D<sup>0(-)</sup></p>	<p><math>\pi + \dots</math>  <math>\pi^0 \quad \gamma \dots</math></p> <p><b>Random photon</b> coming from a <math>\pi^0</math>. The <math>\pi^0</math> comes from the decay of a <math>D^*</math> coming from another B decay  <u><math>K^*</math> is wrongly matched to a <math>D^0</math></u></p>	<p><math> \pi^0 \quad \gamma\gamma</math>  <math>+ K^+</math>  <math>+ K^*(892)^{\sim 0}</math>  <math> K^- \pi^+</math></p> <p><math>B^- + D^*(2007)^0</math>  <math> \pi^0 \quad \gamma\gamma</math>  <math> D^0 \quad \rho^- \pi^+</math>  <math>+ \mu^- + \nu_{\mu}^{\sim}</math></p>
<p>B id is 0, from from 0  <math>K^*</math> from <math>D^{*0}(2007)</math>, GD=B<sup>-</sup>  <math>\gamma</math> from <math>\pi^0</math>, GD=0, GGD=0  <math>K</math> Mo=<math>D^0</math>, GD=<math>D^{*0}(2007)</math>,GGD=B<sup>-</sup>  <math>\pi</math> Mo=<math>D^0</math>, GD=<math>D^{*0}(2007)</math>,GGD=B<sup>-</sup></p>	<p><math>B^- D^{*0}(2007)+\dots</math>  <math>D^0+\text{something}</math>  <math>K+\pi</math>  <math>\pi \quad \gamma+\dots</math></p> <p><b>Random photon</b> coming from a <math>\pi</math>, from another B decay  <u><math>K^*</math> is wrongly matched to a <math>D^0</math></u></p>	<p><math>B^- + D^{*0}(2007)^0</math>  <math> \pi^0 \quad \gamma\gamma</math>  <math> D^0 \quad K^- \pi^+ \pi^0</math>  <math>+ \tau^-</math>  <math>+ \nu_{\tau}^{\sim}</math></p> <p><math>B_s^0 + D_s^{*+}</math>  <math> D_s^+ \quad \phi(1020)^+ \rho(770)^+</math>  <math> \gamma \quad e^+ e^-</math>  <math>+ \tau^- \quad \pi^- \pi^0(\gamma\gamma) \nu_{\tau}</math>  <math>+ \nu_{\tau}^{\sim}</math></p>
<p>B id is 0  <math>K^*</math> Mo=<math>K^*(1430)</math>, GD=B<sup>0</sup>  <math>\gamma</math> Mo=<math>\pi^0</math>, GD=<math>\rho(770)^{+/-}</math>, GGD=0  <math>K</math> Mo=<math>K^*</math>, GD=<math>K^{*0}(1430)</math>  <math>\pi</math> Mo=<math>K^*</math>, GD=<math>K^{*0}(1430)</math></p>	<p><math>B^0 \quad K^{*0}_2(1430) + \text{something}</math>  <math>K^* + \text{something}</math>  <math>K \pi</math>  <math>\rho(770)^{+/-} \quad \pi^0 \quad \gamma \dots</math></p> <p><b>Photon comes from a <math>\pi</math></b>, which comes from a <math>\rho(770)^+</math>  In the reconstruction, we miss the step with the higher <math>K^*</math></p>	<p><math>B^{\sim 0} + \pi^-</math>  <math> n(\quad n) n \pi^-(\quad \pi^0) \pi^0(\quad \gamma\gamma)</math>  <math>+ K^*_2(1430)^{\sim 0}</math>  <math> K^*(892)^{\sim 0} \quad K^- \pi^+</math>  <math> \pi^+</math>  <math> \pi^-</math>  <math>+ D^*(2010)^+</math>  <math> D^0 \quad K^*(892)^{\sim 0} \rho(770)^0</math>  <math> \pi^+ (\pi^+ \pi^0 \pi^- \rho)</math></p> <p><math>B^+ + \rho(770)^+</math>  <math> \pi^0 \quad \gamma\gamma</math>  <math> \pi^+</math>  <math>+ D^{\sim 0}</math>  <math> \omega(782) \quad \pi^0 \pi^- \pi^+</math>  <math> K_L^0 \quad K_S^0</math></p>
<p>B is B<sup>+</sup>, K<sup>*</sup> is D<sup>-0</sup>  <math>K^*</math> Mo=<math>D^*(2007)^0</math>, GD=B<sup>+/-</sup>  <math>\gamma</math> Mo=<math>\pi^0</math>, GD=<math>\rho(770)^{+/-}</math>, GD=B<sup>+/-</sup>  <math>K</math> Mo=<math>D^{0(-)}</math>, GD=<math>D^{*0}(2007)</math>  <math>\pi</math> Mo=<math>D^{0(-)}</math>, GD=<math>D^{*0}(2007)</math></p>	<p><math>B^{+/-} D^{*0}(2007) \rho(770)^+</math>  <math>\pi^0 \quad \gamma + \dots</math>  <math>D^0+\text{something}</math>  <math>K \pi</math>  <math>\pi</math> was a real <math>\pi^0</math> or e- coming from <math>D^0</math>  <u><math>K^*</math> is wrongly matched to a <math>D^0</math></u>  <b>Photon comes from a <math>\pi</math></b>, which comes from a <math>\rho(770)^+</math></p>	<p><math>B^+ + D^*(2007)^{\sim 0}</math>  <math> \pi^0 \quad \gamma\gamma</math>  <math> D^{\sim 0} \quad K^+ \pi^0 e^- \nu_e^{\sim}</math>  <math>+ \rho(770)^+</math>  <math> \pi^0 \quad \gamma\gamma</math>  <math> \pi^+</math></p>
<p><math>K^*</math> is D<sup>+/-</sup>  <math>K^*</math> Mo=B<sup>0</sup>, GD=B<sup>*0</sup>, GGD=0  <math>\gamma</math> Mo=<math>\pi^0</math>, GD=<math>\rho(770)^+</math>, GGD=B<sup>0</sup>  <math>K</math> Mo=<math>D^{+/-}</math>, GD= B<sup>0</sup>, GGD=B<sup>*0</sup>  <math>\pi</math> Mo=<math>D^{+/-}</math>, GD= B<sup>0</sup>, GGD=B<sup>*0</sup></p>	<p><math>B^{*0} B^0 + \text{something}</math>  <math>\rho(770)^{+/-} + D^{+/-}</math>  <math>\pi^0 \quad K \pi</math>  <math>\gamma \dots</math></p> <p><b>Photon comes from a <math>\pi</math></b>, which comes from a <math>\rho(770)^+</math></p>	<p><math>B^0 + D^*(2460)^-</math>  <math> D^*(2010)^- \quad D^{\sim 0} \pi^-</math>  <math> \pi^0 \quad \gamma\gamma</math>  <math>+ \pi^0 \quad \gamma\gamma</math>  <math>+ \pi^+ \quad e^- e^-</math>  <math>+ \pi^0 \quad \gamma(e^+ e^-) \gamma</math>  <math>+ \eta \quad \gamma(e^+ e^-) \gamma</math></p> <p><math>B^{\sim 0} + \rho(770)^-</math>  <math> \pi^0 \quad \gamma\gamma</math></p>

		$  \pi^- e^-$ $+ D^+ K^- \pi^+ (5n 5\pi^+ 3\pi^0 3\pi^-) \pi^+$
<p>B id is <math>B^-</math>, from <math>B^{*-}</math>  <math>K^* Mo=B^-</math>, <math>GD=B^{*-}</math>  <math>\gamma Mo=\pi^0</math>, <math>GD=\rho(770)^-</math>, <math>GGD=B^-</math>  <math>K Mo=D^0</math>, <math>GD=B^-</math> <math>GGD=B^{*-}</math>  <math>\pi Mo=D^0</math>, <math>GD=B^-</math>, <math>GGD=B^{*-}</math></p>	<p><math>B^{*-} B^- \dots</math>  <math>\rho(770)^{+/-} + D^0</math>  <math>\pi^0 K + \pi</math>  <math>\gamma</math></p> <p><math>K^*</math> is wrongly matched to a <math>D^0</math>,  there are 4 events of this type  <b>Photon comes from a <math>\pi</math></b>, which  comes from a <math>\rho(770)^+</math>, there are 4  cases when <math>\gamma</math> comes from  <math>\rho(770)^{+/-} \pi^0 \gamma \dots</math> and it is  associated to either a D or higher  <math>K^*</math>. We find 3 events of the type  <math>B^{(+/-, 0)} \rho(770)^{+/-} D^{(*, +/-, 0)}</math></p>	<p><math>B^- + \rho(770)^-</math>  <math>  \pi^0 ( \gamma \gamma ) \pi^-</math>  <math>+ D^0 K^- \mu^+ ( e^- e^- e^- ) \nu_\mu</math></p> <p><math>B^0 + D^*(2010)^+</math>  <math>  \pi^0 \gamma \gamma</math>  <math>  D^+ K^- \pi^+ \pi^+</math>  <math>+ D_{s1}(2460)^-</math>  <math>  D_s^{*-} D_s^- \gamma</math>  <math>  \pi^0 \gamma \gamma</math></p>
<b>B <math>X_{su}</math>, <math>X_{sd}</math> + something</b>		
<p>B is <math>B^+</math>, <math>K^*</math> is <math>X_{su}</math>  <math>K^* Mo=B^{+/-}</math>, <math>GD=0</math>  <math>\gamma Mo=B^{+/-}</math>, <math>GD=0</math>  <math>K Mo=X_{su}</math>, <math>GD=B^{+/-}</math>  <math>\pi Mo=\eta</math>, <math>GD=X_{su}</math></p>	<p><math>B^{+/-} \gamma X_{su}</math>  <math>\eta + K</math>  <math>\pi + \dots</math></p> <p><math>K^*</math> is miss-identified as <math>X_{su}</math>  Some of the daughters were  matched to the decay of <math>B^+</math> but B  was associated to another head  particle, a <math>B^{-0}</math></p>	<p><math>B^+ + X_{su}</math>  <math>  \eta \pi^0 \pi^- \pi^+</math>  <math>  K^+</math>  <math>+ \gamma</math></p> <p><math>B^{-0} + D_{-1}(H)^+</math>  <math>  D^*(2007)0 \pi^0 D^0</math>  <math>  \pi^+</math>  <math>+ n</math>  <math>+ \Delta^-</math></p>
<p>B is <math>B^+</math>  <math>K^* Mo=X_{su}</math>, <math>GD=B^{+/-}</math>, <math>GGD=B^{*+/-}</math>  <math>\gamma Mo=B^{+/-}</math>, <math>GD=B^{*+/-}</math>  <math>K Mo=K^*</math>, <math>GD=X_{su}</math>  <math>\pi Mo=K^*</math>, <math>GD=X_{su}</math></p>	<p><math>B^{*+/-} B^{+/-} + \dots</math>  <math>\frac{X_{su} + \gamma}{K^* + \text{something}}</math>  <math>K \pi</math></p>	<p><math>B^- + X_{su} \sim</math>  <math>  \pi^0 \gamma \gamma</math>  <math>  K^{*0} K \pi^+</math>  <math>  \pi^- \dots</math>  <math>+ \gamma \dots</math></p> <p><math>B^+ + \pi^+</math>  <math>  e^- + \dots</math>  <math>+ \Sigma_c^-</math>  <math>  \pi^0 \gamma \gamma</math>  <math>  \Lambda_c^- (\pi^-, \rho(770)^-, \pi^+, n^-)</math>  <math>+ \Delta^+</math>  <math>  \pi^0 \gamma \gamma</math>  <math>  p^+ 3\pi^0, 2K_s^0, 2p^+</math></p>
<p>B is <math>B^{+/-}</math>, <math>K^*</math> is <math>X_{su}</math>  <math>K^* Mo=B^{+/-}</math>, <math>GD=B^{*+/-}</math>, <math>GGD=0</math>  <math>\gamma Mo=B^{+/-}</math>, <math>GD=B^{*+/-}</math>  <math>K Mo=X_{su}</math>, <math>GD=B^{+/-}</math>, <math>GGD=B^{*+/-}</math>  <math>\pi Mo=\rho(770)^0</math>, <math>GD=X_{su}</math></p>	<p><math>B^{*+/-} B^{+/-} + \text{something}</math>  <math>\frac{\gamma + X_{su}}{K + \rho(770)^0} + \dots</math>  <math>\pi + \dots</math></p> <p>Daughters are all matched to a  charged B decay but the mother  particle is matched to a neutral B  which is <math>B_s^0</math></p>	<p><math>B_s^0 + D_s^-</math>  <math>  f_0(980) \pi^+ \pi^-</math>  <math>  \pi^- e^-</math>  <math>+ \dots \rightarrow a_2(1320)^+</math>  <math>  \eta 3\pi^0</math>  <math>  \pi^+ e^-</math>  <math>+ \pi^-</math>  <math>+ \pi^+ \dots p</math>  <math>+ \pi^0 \gamma ( e^+ e^- ) \gamma ( e^+ e^- )</math></p> <p><math>B^- + X_{su} \sim</math>  <math>  \rho(770)^0 \pi^+ \pi^-</math>  <math>  K^- e^- \dots</math>  <math>+ \gamma e^+ e^-</math></p>

<p>B is B<sup>+</sup>  K* Mo=X<sub>su</sub>, GD=B<sup>+/-</sup>, GGD=0  γ Mo=B<sup>+/-</sup>, GD=0  K Mo=K*, GD=X<sub>su</sub>  π Mo=K*, GD=X<sub>su</sub></p>	<p>B<sup>+/-</sup> <math>\frac{X_{su}\gamma}{K^*} + \dots</math>  K π</p> <p>We find 4 decays of the type B<sup>+/-</sup> <math>\frac{X_{su}\gamma}{K^*}</math>! This is comparable to the number of signal channels, which is expected to be the leading channel for the rare decay domain</p>	<p>B<sup>-</sup> + Xsu<sup>~</sup>    K*(892)<sup>~0</sup> K<sup>-</sup> π<sup>-</sup>    π<sup>-</sup> (3π<sup>-</sup> 2p 2n 2π<sup>+</sup> π<sup>0</sup>)  + γ( ... ( e<sup>-</sup>) + ... ( e<sup>-</sup>))</p> <p>B<sup>0</sup> + D*(2010)<sup>-</sup>    π<sup>0</sup> γγ    D<sup>-</sup> φ(1020)<sup>+</sup> π<sup>-</sup> π<sup>0</sup>  + D*(2007)<sup>0</sup>    π<sup>0</sup> γγ    D<sup>0</sup> K<sub>1</sub>(1270)<sup>~0</sup> π<sup>0</sup>  + K<sup>+</sup> μ<sup>+</sup> ν<sub>μ</sub></p>
<p>K* is X<sub>sd</sub>  B ID is B<sup>0</sup>, from B*<sup>+</sup> from 0  K* Mo=B<sup>-0</sup>, GD=B*<sup>0</sup>  γ Mo=B<sup>-0</sup>, GD=B*<sup>0</sup>, GGD=B<sup>+</sup>  K Mo=anti-X<sub>sd</sub>, GD=B<sup>-0</sup>  π Mo=ρ(770)<sup>+</sup>, GD=X<sub>sd</sub><sup>~</sup>, GGD=B<sup>-0</sup></p>	<p>B<sup>+</sup> B*<sup>0</sup>+...  B<sup>-0</sup>  <math>\frac{\gamma + X_{sd}}{K + \rho(770)^+}</math>  π  X<sub>sd</sub> is miss-identified as K*</p>	<p>B<sup>-0</sup> + Xsd<sup>~</sup>    ρ(770)<sup>+</sup> π<sup>0</sup> π<sup>+</sup>    K<sup>-</sup>  + γ</p>
<b>Random Combinations</b>		
<p>B id is 0, from 0  K* Mo=B*<sup>0</sup>, GD= 0  γ Mo=π<sup>0</sup>, GD=ρ(770)<sup>+</sup>, GGD=0  K Mo=D<sup>0</sup>, GD=D*<sup>0</sup>(2007)  π Mo=ρ(770)<sup>0</sup>, GD=B<sup>0</sup></p>	<p>Random Combinations, tracks are matched to particles coming from two different decays, <u>K* matched to a D*<sup>0</sup>(2007)</u></p>	<p>B<sup>0</sup> + K<sup>+</sup>  + D*(2007)<sup>0</sup>    D<sup>0</sup> a<sub>1</sub>(1260)<sup>+</sup> K<sup>-</sup>    γ e<sup>+</sup>e<sup>-</sup>  + ρ(770)<sup>0</sup> π<sup>+</sup> π<sup>-</sup>  + D<sup>-</sup> a<sub>1</sub>(1260)<sup>-</sup>( ρ(770)<sup>-</sup> π<sup>0</sup>) K<sub>L</sub><sup>0</sup></p> <p>B<sub>s</sub><sup>~0</sup> + D*<sup>-</sup>    K<sup>-0</sup> K<sub>S</sub><sup>0</sup>    D<sup>-</sup> K<sup>0</sup> e<sup>-</sup> ν<sub>e</sub><sup>~</sup>  + ρ(770)<sup>+</sup> π<sup>0</sup> γγ π<sup>+</sup>  + π<sup>-</sup>  + π<sup>+</sup> π<sup>+</sup> π<sup>-</sup>( μ<sup>-</sup> ν<sub>μ</sub><sup>~</sup>) ρπ<sup>+</sup>( π<sup>+</sup> π<sup>0</sup>) π<sup>-</sup></p> <p>π<sup>0</sup>( γγ) π<sup>+</sup> π<sup>0</sup>( γγ) n( Si28) π<sup>0</sup>( γγ)</p>
<p>K* is D0  K* Mo=0, GD=0  γ Mo=η, GD=η', GGD=0  K Mo=0, GD= 0  π Mo=η, GD= D<sup>0</sup>, GGD=B<sup>0</sup></p>	<p>η' η + ... γ  B<sup>0</sup> D<sup>0</sup> + ... η + ... π + ...  random K* and K</p> <p>Tracks are combined from two decays, <u>K* is wrongly matched to a D<sup>0</sup></u></p>	<p>B<sup>-0</sup> + π<sup>+</sup>  + D<sup>-0</sup> K<sup>+</sup> π<sup>-</sup> η<sup>-</sup> π<sup>0</sup> π<sup>-</sup> π<sup>+</sup>  + K<sup>-</sup> ...</p> <p>B<sup>0</sup> + D<sup>-</sup>    K<sub>1</sub>(1400)<sup>0</sup> K*(892)<sup>+</sup> π<sup>-</sup>    π<sup>-</sup> e<sup>-</sup>  + D*(2007)<sup>0</sup> D<sup>0</sup>( K<sup>-</sup> π<sup>+</sup> π<sup>0</sup>) γ  + K<sup>+</sup></p>
<p>B id is 0, from 0  K* Mo=0, GD=0  γ Mo=π<sup>0</sup>, GD= ω(782), GGD=0  K Mo=0, GD=0  π Mo=K<sub>1</sub>(1270)<sup>0</sup>, GD=0</p>	<p>Random Combinations</p>	<p>B<sup>0</sup> + D<sup>+</sup>    D<sub>s</sub><sup>+</sup> η<sup>+</sup> e<sup>+</sup> ν<sub>e</sub>    γ  + D*(2010)<sup>-</sup>    π<sup>0</sup> γγ    D<sup>-</sup> a<sub>1</sub>(1260)<sup>-</sup> K<sub>S</sub><sup>0</sup></p> <p>B<sup>-</sup> + D*(2007)<sup>0</sup>    π<sup>0</sup> γγ    D<sup>0</sup> a<sub>1</sub>(1260)<sup>+</sup> K<sup>-</sup>  + D<sup>-</sup> K<sup>+</sup> π<sup>-</sup> π<sup>-</sup>( e<sup>-</sup>)  + K*(892)<sup>~0</sup>    K<sup>-</sup> π<sup>+</sup></p>
<p>B id is 0  K* Mo=string, GD=B<sup>+/-</sup></p>	<p>Random Combinations</p>	<p>B<sup>0</sup> + D*(2010)<sup>-</sup></p>

GGD=B <sup>*+/-</sup> γ Mo=π <sup>0</sup> , GD=0 K Mo=K <sup>*</sup> , GD=string π Mo=K <sup>*</sup> , GD=string		π <sup>0</sup> e <sup>+</sup> e <sup>-</sup> γ   D <sup>-</sup> K <sub>S</sub> <sup>0</sup> π <sup>-</sup> π <sup>0</sup> + π <sup>+</sup> + ρ(770) <sup>+</sup> π <sup>0</sup> ( γγ) π <sup>+</sup> + ρ(770) <sup>-</sup> π <sup>0</sup> ( γγ) π <sup>-</sup> B <sup>-</sup> + string   ρ(770) <sup>-</sup> π <sup>0</sup> π <sup>-</sup>   K <sup>*</sup> (892) <sup>~0</sup> K <sup>-</sup> π <sup>+</sup>   K <sup>*</sup> (892) <sup>-</sup> π <sup>0</sup> K <sup>-</sup>   K <sup>+</sup>
(K <sup>*</sup> , B <sup>0</sup> ) TRUEID=0 K <sup>*</sup> Mo=0, GD=0 γ Mo=π <sup>0</sup> , GD=ρ(770) <sup>+/-</sup> , GGD=B <sup>0</sup> K Mo=D <sup>+/-</sup> , GD=B <sup>0</sup> , GGD=B <sup>*0</sup> π Mo=K <sup>*</sup> , GD=D <sup>0</sup>	Random combinations	B <sup>0</sup> + ρ(770) <sup>+</sup>   π <sup>0</sup> γγ   π <sup>+</sup> e <sup>-</sup> e <sup>-</sup> ... + D <sup>-</sup> K <sup>+</sup> π <sup>-</sup> π <sup>-</sup> μ <sup>-</sup> +ν <sub>μ</sub> <sup>~</sup> B <sup>-</sup> + D <sup>*</sup> (2007) <sup>0</sup>   π <sup>0</sup> γγ   D <sup>0</sup> K <sup>*</sup> (892) <sup>-</sup> ρ(770) <sup>+</sup> + τ <sup>-</sup>   π <sup>-</sup> ( e <sup>-</sup> e <sup>-</sup> ) π <sup>-</sup> π <sup>+</sup> ν <sub>τ</sub> + ν <sub>τ</sub> <sup>~</sup>

Table 5.1 Possible background channels which can affect the reconstruction and selection of  $B_d \rightarrow K^* \gamma$

Table 5.1 summarizes the 23 *reconstructed*  $B_d \rightarrow K^* \gamma$  candidates with all the true mothers, grandmothers and great-grandmothers together with the corresponding true generated decays, which remain after the offline selection applied on the  $b\bar{b}$  inclusive sample.

The information about the true mothers and grandmothers shows that out of 23 reconstructed candidates, only 4 events are real  $B_d \rightarrow K^* \gamma$ . The MCTruth information, available for each of these events, shows that only 3 of them are true generated  $B_d \rightarrow K^* \gamma$  decays, in one of the 4 true events, the  $K^*$  and  $\gamma$  are not the direct products of a B decay, they come from a  $D^0$  particle. The true decay is  $\underline{B^0 \rightarrow D^0(K^*(\rightarrow K\pi)\rho^0(\pi^+\pi^-))\underline{D^0}(\rightarrow \gamma\gamma(\rightarrow e^+e^-))}$  so, the reconstruction algorithm loses the converted photon and the neutral particles ( $\rho^0$  and  $D^0$ ) and sees only the  $K^*$  and the unconverted photon (from  $\pi^0$ ) as coming from the decay of a  $B^0$ .

An important source of combinatorial background is the miss-reconstruction of  $K^*$ : the case when strange ( $X_{su}$ ,  $X_{sd}$ ) or charm ( $D^0$ ,  $D^{+/-}$ ,  $D^*$ ) resonances are incorrectly identified as  $K^*$ . There are 7 events where  $K^*$  is matched to a true  $D^0$  or  $D^{+/-}$ . In these cases, the photon is coming either from a random  $\pi^0$  (3 cases), or from a  $\pi^0$  coming from a  $\rho$  meson (4 cases,  $\rho(770)^{+/-} \rightarrow \pi^0 \gamma \dots$ ), where  $\rho$  has the same B mother as the D resonance. In 4 events  $K^*$  is matched to an  $X_{su}$  and once to an  $X_{sd}$ . Thus, events of the type  $B_d \rightarrow X_{su} \gamma$  happen with the same frequency as the signal we want to study,  $B_d \rightarrow K^* \gamma$ .

These types of background can be reduced by narrowing the mass window for the vector meson  $K^*$ , e.g. down to  $50 \text{ MeV}/c^2$  around the  $K^*$  nominal mass.

Also, there is the possibility that the  $K^*$  is matched to a true  $K^*$  but  $\gamma$  is a random photon, or, the case when the  $K^*$  comes from a higher  $K^*$ , such as  $K_2^*(1430)^0$ , and  $\gamma$  comes from the decay of  $\rho$  meson. There are 7 events where  $\gamma$  is matched to a random photon and  $K^*$  is either a true  $K^*$ , a higher  $K^*$  or a true D meson (charged or neutral). In 3 of these cases the photon comes from a  $B_s$  mother.

Another source of background consists in random combinations of particles which survive the kinematical constraints in the reconstruction process of  $B_d$  and can also be matched to the particles involved in a  $B_d \rightarrow K^* \gamma$  decay. There are 5 events where completely random particles are combined to reconstruct a  $B_d$ . There are also two cases where one of the charged daughters ( $K$  or  $\pi$ ) comes from the primary vertex and two cases where  $\pi$  is a real muon or electron.

Random combinations of particles, charged particles coming from the primary vertex or particle mis-identification can be controlled by tightening the constraints on both charged and neutral particle identification, as well as asking that the vector meson vertex is well isolated so that the charged daughters do not point towards the interaction region.

Also, a cut on the  $B_d$  transverse momentum is efficient in removing low momentum background. A summary of possible background decay channels which may complicate the analysis of the  $B_d \rightarrow K^* \gamma$  decay is given in Table 5.2. This table shows that most background channels involve charmed or strange resonances which are being misidentified as the vector meson,  $K^*$ , and random combinations of tracks coming from two or more different decays.

<b>Summary of the possible background channels detailed in Table 3</b>	
$B^0 \rightarrow D^0 \pi^0$	
$B^0 \rightarrow D_s^*(2460)^+ K^*(892)^0 K^-$	
$B^0 \rightarrow (D^*(2010)^+ D^0 \pi^+) (K_2^*(1430)^0 K^* \pi^+ \pi^-) \pi^-$	
$B^0 \rightarrow X_{sd} \gamma$	
$B^+ \rightarrow X_{su} \gamma$	
$B^+ \rightarrow D^0 K^*(892)^0 K^+$	
$B^- \rightarrow (D^*(2007)^0 D^0 \pi^0) \tau^- \sim \nu_\tau$	
$B^+ \rightarrow D^*(2007)^0 \rho(770)^+$	
$B^- \rightarrow D^0 \rho(770)^-$	
<b>Random combinations (particles matched to daughters coming from different decays):</b>	
$B^0 \rightarrow D^*(2007)^0 \rho(770)^0 D^- K^+$	
$B^0 \rightarrow D^0 \pi^+ \pi^- + B^0 D^*(2007)^0 D^- K^+$	
$B^0 \rightarrow D_s^- D^*(2010)^- + B^+ (D^*(2007)^0 D^0 \pi^0) K^*(892)^0 D^-$	
$B^0 \rightarrow D^- \rho(770)^+ + B^- (D^*(2007)^0 D^0 \pi^0) \tau^- \sim \nu_\tau$	
$B^0 \rightarrow D^*(2010)^- \pi^+ \rho(770)^+ \rho(770)^- + B^- \text{ string } \rho(770)^- K^+ K^*(892)^0 K^+$	

Table 5.2 Summary of the possible background channels detailed in Table 5.1

After the identification of possible background sources, Tables 5.1 and 5.2, which can affect the analysis, a check is performed on how efficient the official offline selection is in removing the unwanted background. In order to benefit of more significant statistics, the  $B_d \rightarrow K^* \gamma$  reconstruction and offline selection is applied on simulated *signal samples* corresponding to some of the background channels identified and listed in Table 5.2, in order to determine how many of the these background events pass the offline selection.

As seen in Table 5.1 decays where a  $B_d$  or  $B_u$  particle decays into a  $D^{+/-}$ ,  $D^0$ ,  $D^*$  plus other particles, with a  $K$ - $\pi$  pair in the final state, are more than often involved in the reconstruction of the  $B_d \rightarrow K^* \gamma$  decay. On this premise, background channels which occur through a charmed resonance are investigated. Then, to understand how much background comes from combinations with at least one particle coming from the primary vertex, the offline selection is tested on channels such  $B_d \rightarrow D^- \pi^+$  or  $B_d \rightarrow D^- K^+$  or  $B_u \rightarrow D^0 \pi^+$  or  $B_u \rightarrow D^0 K^+$ .

As there is also the possibility that photons or pions can be misidentified as electrons decay channels with electrons in the final state are also tested, e.g.  $B_d \rightarrow K^{*0} ee$ . In the same context, there is also the possibility that a correctly identified charged daughter is coming from another particle than the  $K^*$ ; for this, signal samples such as:  $B_d \rightarrow D^{*0} (\rightarrow D^0 (\rightarrow K \pi) \gamma) K^{*0} (\rightarrow K \pi)$ ,  $B_d \rightarrow D^{*0} (\rightarrow D^0 (\rightarrow K \pi) \pi^0) K^{*0} (\rightarrow K \pi)$  are studied.

To test the offline selection efficiency in removing background coming from events with merged neutral pions ( $\pi^0$ ) and “bad” photons, channels with photons in intermediate states or  $\pi^0$  in final states are very interesting to study as there is a high risk that such a photon is randomly reconstructed as the photon coming from the B particle in  $B_d \rightarrow K^* \gamma$  decay. Possible signal channel candidates are:  $B_d \rightarrow D^{*0} (\rightarrow D^0 (\rightarrow K \pi) \pi^0) K^{*0} (\rightarrow K \pi)$  or  $B_d \rightarrow D^0 K^* (\rightarrow K \pi \pi^0)$ .

A list of the signal samples, identified as possible background for  $B_d \rightarrow K^* \gamma$ , used to test the offline selection efficiency for this channel, together with the size of these Monte Carlo samples, is given in Table 5.3.

<b>Signal Samples used for background studies</b>	<b>Number of generated events</b>
$B_d \rightarrow D^- \pi^+ / K^+$	~1million
$B_d \rightarrow D^{*0} K^{*0}, D^0 \gamma, K \pi$	~0.5 million
$B_d \rightarrow D^{*0} K^{*0}, D^0 \pi^0, K \pi$	~0.5 million
$B_d \rightarrow D^0 K^*, K \pi \pi^0$	~0.5 million
$B_d \rightarrow D^{*0} X, K \pi$ (inclusive $D^{*0}$ production)	~0.5 million
$B_d \rightarrow K^{*0} ee$	~1.2 million
$B_u \rightarrow D^0 K, K \pi$	~1.5 million
$B_u \rightarrow D^0 \pi, K \pi$	~1 million

Table 5.3 Signal samples used as background for  $B_d \rightarrow K^* \gamma$

In order to understand the effect of the  $B_d \rightarrow K^* \gamma$  offline selection (Table 4.2.2) on the decay channels identified as background for  $B_d \rightarrow K^* \gamma$  (Table 5.3), and to benefit of higher statistics, the reconstruction procedure for  $B_d \rightarrow K^* \gamma$  is performed on the signal samples corresponding to these possible background channels and then  $B_d \rightarrow K^* \gamma$  stripping and offline selections are applied on the reconstructed  $B_d \rightarrow K^* \gamma$  candidates.

The number of events remaining after the stripping and offline cuts are given in double mass representations of the  $B_d$  candidate mass (in the mass interval 4200-6300  $\text{MeV}/c^2$ ) versus the mass of the  $K^*$  candidates reconstructed in a mass window of 100 MeV around the nominal  $K^*$  mass (895.94  $\text{MeV}[r]$ ), “ $M_{K\pi-K^*}$  PDG mass”, Figures 5.3 to 5.9. The procedure is applied for each of the background channels listen in Table 5.3. The events remaining after the stripping cuts are shown in Figures 5.3 to 5.9, a) then, three different sets of offline cuts are independently applied on these samples: the “old” official cuts, tuned on *Monte Carlo data* and summarized in Table 4.2.2, and two new sets of cuts tuned on *real data*, given in Table 4.2.4, the “new” official offline selection cuts, tuned on the 37  $\text{pb}^{-1}$  collected during 2010 run of LHC and approved by the LHCb collaboration (Table 4.2.4, third column), and a new set of cuts tuned on the 2010 and 2011 real data, 88  $\text{pb}^{-1}$ , collected with the LHCb detector designed to improve the signal to background ratio for this channel (Table 4.2.4, forth column), Figures 5.3 to 5.9, b), c) and d) respectively.

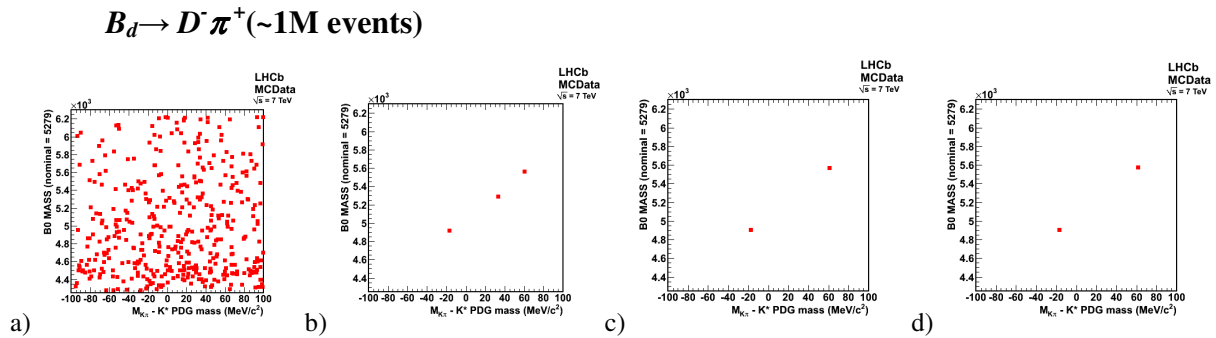


Figure 5.3 Double mass representation of the selected  $B_d \rightarrow K^* \gamma$  candidates using the  $B_d \rightarrow D^- \pi^+$  signal sample a) after the stripping selection b) after the old official offline selection cuts, c) after the new official offline selection cuts, d) after the new tuned offline selection cuts

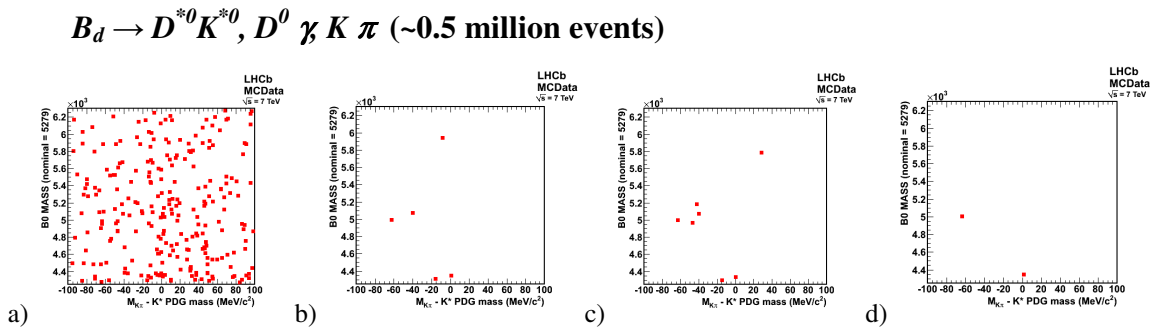


Figure 5.4 Double mass representation of the selected  $B_d \rightarrow K^* \gamma$  candidates using the  $B_d \rightarrow D^{*0}(D^0) \gamma K^*(K\pi)$  signal sample a) after the stripping selection b) after the old official offline selection cuts, c) after the new official offline selection cuts, d) after the new tuned offline selection cuts

$B_d \rightarrow D^{*0} K^0, D^0 \pi^0, K \pi$  (~0.5 million events)

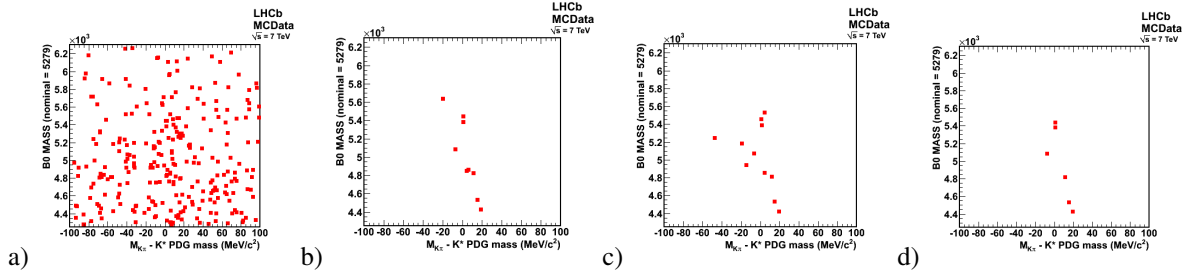


Figure 5.5 Double mass representation of the selected  $B_d \rightarrow K^* \gamma$  candidates using the  $B_d \rightarrow D^{*0} (D^0 \pi^0) K^{*0} (K \pi)$  signal sample a) after the stripping selection b) after the old official offline selection cuts, c) after the new official offline selection cuts, d) after the new tuned offline selection cuts

$B_d \rightarrow D^0 K^*, K \pi \pi^0$  (~0.5 million events)

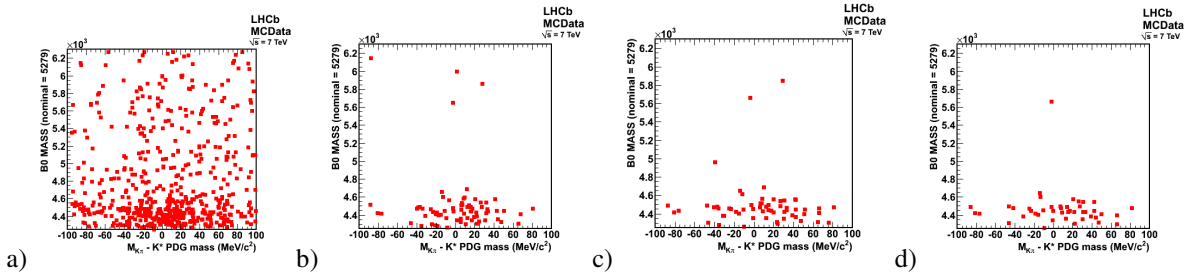


Figure 5.6 Double mass representation of the selected  $B_d \rightarrow K^* \gamma$  candidates using the  $B_d \rightarrow D^0 K^*, K \pi \pi^0$  signal sample a) after the stripping selection b) after the old official offline selection cuts, c) after the new official offline selection cuts, d) after the new tuned offline selection cuts

$B_d \rightarrow K^{*0} ee$  (~1.2 million events)

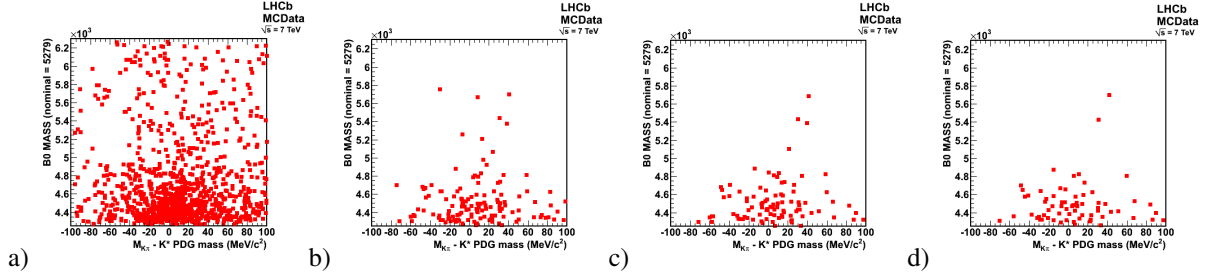


Figure 5.7 Double mass representation of the selected  $B_d \rightarrow K^* \gamma$  candidates using the  $B_d \rightarrow K^{*0} ee$  signal sample a) after the stripping selection b) after the old official offline selection cuts, c) after the new official offline selection cuts, d) after the new tuned offline selection cuts

$B_d \rightarrow D^{*0} X, K \pi$  (~0.5 million events) and  $B_u \rightarrow D^0 K, K \pi$  (~1.5 million events)

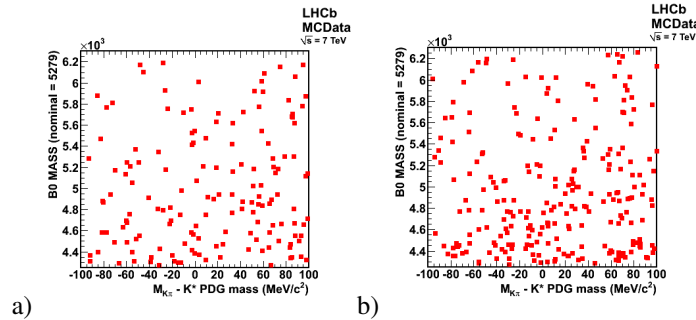


Figure 5.8 Double mass representation of the selected  $B_d \rightarrow K^* \gamma$  candidates using the  $B_d \rightarrow D^{*0} X, K \pi$  signal sample (left) and  $B_u \rightarrow D^0 K, K \pi$  (right) after the stripping selection, in both cases no candidates remain after any of the offline selection

$B_u \rightarrow D^0 \pi K \pi$  (~1 million events)

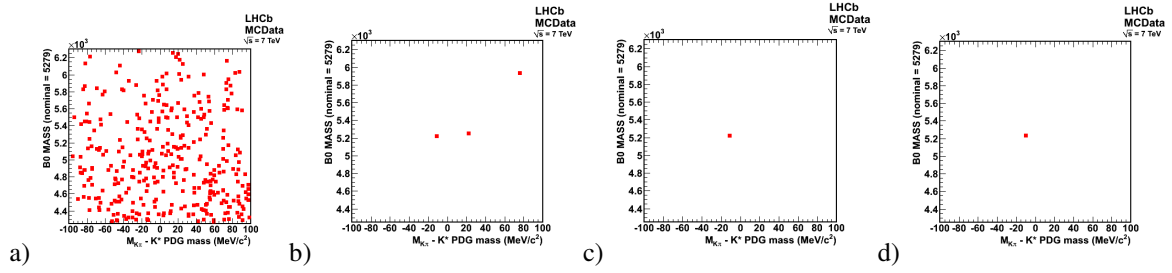


Figure 5.9 Double mass representation of the selected  $B_d \rightarrow K^* \gamma$  candidates using the  $B_u \rightarrow D^0 \pi, K \pi$  signal sample (left) and  $B_u \rightarrow D^0 K, K \pi$  (right) a) after the stripping selection b) after the old official offline selection cuts, c) after the new official offline selection cuts, d) after the new tuned offline selection cuts

Figures 5.3 to 5.9 indicate that the offline selection for  $B_d \rightarrow K^* \gamma$  is efficient in removing the background coming from some of the identified background channels but there are cases where large background remains in the low  $B_d$  mass region, e.g.  $B_d \rightarrow D^0 K^*$  with  $(K \pi \pi^0)$  in the final state, and  $B_d \rightarrow K^{*0} e e$ , where much of the background comes from the fact that an electron is misidentified as a photon. There are also cases where most or all of the background events are removed already by the cuts on daughter particles (charged and neutral), e.g.  $B_d \rightarrow D^{*0} X, K \pi$  and  $B_u \rightarrow D^0 \pi, K \pi$ .

For the two cases,  $B_d \rightarrow D^0 K^*, K \pi \pi^0$  and  $B_d \rightarrow K^{*0} e e$ , where a peaking structure of the background is observed at low  $B_d$  mass, the  $B_d \rightarrow K^* \gamma$  invariant mass reconstructed in these channels is fitted with a simple Gaussian function in order to determine the position and width of the structure. The results are shown in Figure 5.10. The plots show that these background channels might produce a peaking structure in the  $B_d \rightarrow K^* \gamma$  low mass sideband at around 4450  $\text{MeV}/c^2$ . The width of the structure is different for the two samples, however, the contamination due to  $B_d \rightarrow K^{*0} e e$  can be neglected because of the small branching ratio of this channel,  $\mathcal{B}(B_d \rightarrow K^{*0} e e) = 1.03 \times 10^{-7}$  [14]. Knowing the branching ratios and the number of generated events for  $B_d \rightarrow K^{*0} e e$  and  $B_d \rightarrow K^* \gamma$  signal samples and combining this knowledge with the information provided by Figure 5.10, b) the background fraction induced by this channel can be estimated. This decay contributes with less than 0.01% to the number of events being reconstructed as  $B_d \rightarrow K^* \gamma$ .

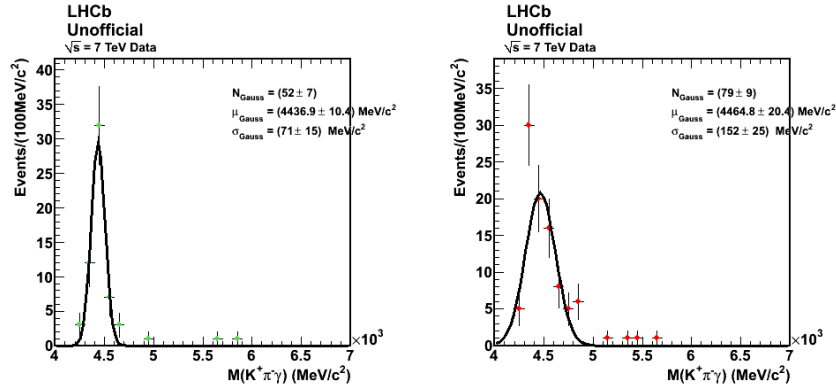


Figure 5.10 Fit of  $B_d \rightarrow K^* \gamma$  invariant mass reconstructed in  $B_d \rightarrow D^0 K^*$ ,  $K \pi \pi^0$  (left) and  $B_d \rightarrow K^{*0} ee$  (right) signal samples

The new offline selection as well as the new tuned selection, summarized in Table 4.2.4, are also tested on the inclusive  $b\bar{b}$  sample. The invariant mass of the reconstructed  $B_d \rightarrow K^* \gamma$  events after applying these selections is represented in Figure 5.11, a) and b) respectively, the green line shows reconstructed  $B_d$  events which are being matched to true  $B_d$  particles, the blue line indicates reconstructed  $B_d$  events badly matched to true  $B^+$  and the red line represents reconstructed  $B_d$  events matched to random combinations of particles. Both plots show that the new selections are more efficient in removing bad-reconstructed events, especially the new tuned selection which reduces random combinations of particles by a factor 10.

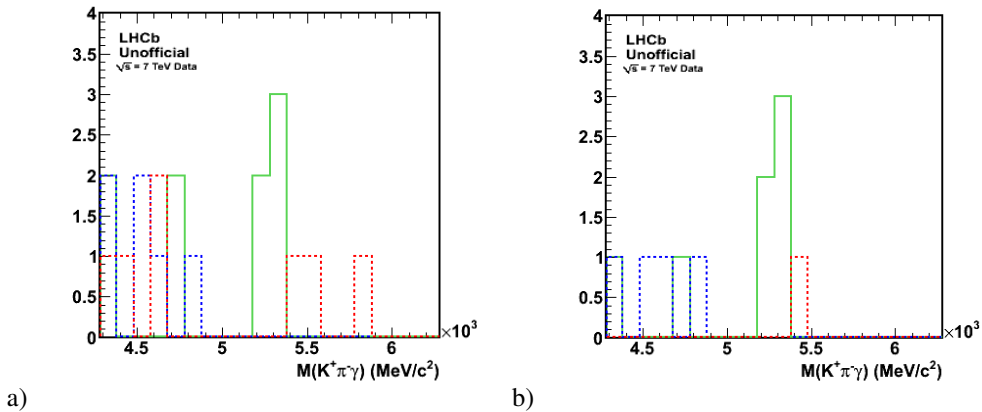


Figure 5.11  $B_d \rightarrow K^* \gamma$  reconstructed events after a) the “new” offline selection cuts b) the new tuned offline selection cuts have been applied on the inclusive  $b\bar{b}$  sample, the reconstructed events matched to: true  $B_d$  are shown in green, to true  $B^+$ , in blue and random combinations in red

## 5.2 Conclusions

In this chapter the method used to determine possible sources of background which can complicate the analysis of the  $B_d \rightarrow K^* \gamma$  radiative decay was described.

It has been shown that possible background sources which can affect the offline analysis of the  $B_d \rightarrow K^* \gamma$  decay are the mis-identification of the charged daughters or charged daughters coming from the primary vertex, the erroneous reconstruction of the vector meson,  $K^*$ , the combination of the  $K^*$  with a random photon coming from a  $\pi^0$  or another B-decay or completely random  $K$ ,  $\pi$  and  $\gamma$ , coming from different decays, being combined to form the  $B_d$  candidate. This is called “combinatorial background”.

Different sets of offline selection criteria corresponding to  $B_d \rightarrow K^* \gamma$  have been described and tested on several Monte Carlo signal samples identified as potential background for this radiative decay and it has been proved that the new set of offline cuts tuned on the 2010 real data collected with the LHCb detector is up to a factor 10 more efficient in reducing background coming from random combinations of particles.

Other specific types of background can be controlled by narrowing the mass window for the vector meson,  $K^*$ , or by tightening the constraints on both charged and neutral particle identification criterion, or on the vector meson vertex isolation, so that the charged daughters do not point towards the interaction region. Also, a cut on the  $B_d$  transverse momentum is efficient in removing low momentum background.

Results contributed to the CERN note LHCb-ANA-2011-064, LHCb-CONF-2011-055

# 6. Lifetime acceptance for $B_d \rightarrow K^* \gamma$

## 6.1 Strategy and results

The lifetime of a particle, together with the mass, is an important measurement which can be achieved in a particle physics experiment.  $B_d$  lifetime is well known in literature from CLEO [55], BaBar [56] and Belle [57] experiments thus, attempting such a measurement at LHCb would allow checking the calibration of the detector. Moreover, understanding the lifetime acceptance for the  $B_d \rightarrow K^* \gamma$  channel, defined as the efficiency of selection as a function of proper time, is crucial as this function is well known theoretically for  $B_d$  and can be used as control signal for  $B_s$ .

In this chapter, the behavior of the lifetime acceptance function for  $B_d \rightarrow K^* \gamma$  channel is described when the LHCb official offline cuts are applied one by one. The goal is to investigate which of the cuts has the strongest impact on the distribution of the acceptance function in two scenarios: first, the case when the pre-selection consists in the stripping selection used for the real data, Table 4.2.2 (right columns), this case should be a good approximation of what is expected to be seen in experimental data, and it will be further referred to as the “Stripping Case”, and second, the case when prior to any offline selection all the reconstructed daughters involved in the decay are matched to the true generated particles,  $K^*$ ,  $\gamma$ ,  $K$ ,  $\pi$ , the “MCMatch” case. To fulfill algorithm requirements, very loose cuts are applied on the mass window (the difference between the reconstructed mass and the PDG [70] nominal mass) for the reconstructed mothers,  $\Delta M(K^*, B_d) = 2000 \text{ MeV}/c^2$ , and on the transverse momentum of the photon,  $\gamma_{p_T} > 1000 \text{ MeV}/c$ . It is important to stress out the difference between the two scenarios, in the first case, the acceptance function is determined for those *reconstructed* events which pass the stripping selection and afterwards are matched to true events while in the second case events are truth matched to the true *generated events* before the selection.

In parallel, the lifetime distribution for  $B_d \rightarrow K^* \gamma$  is determined. Each decay is characterized by a decay time which, in simulation, is calculated using Eq. 6.1.1. This method is used to calculate the true  $\tau$ ; the exact value of the flight distance,  $d_{\text{TRUE}}$ , the exact mass,  $M_{\text{TRUE}}$ , and momentum,  $P_{\text{TRUE}}$ , are known from MCTruth information.

$$\tau_{TRUE} = \frac{M_{TRUE} * (\overline{d_{TRUE}} * \overline{P_{TRUE}})}{P_{TRUE}^2} \quad \text{Eq. 6.1.1}$$

For the reconstructed  $\tau$ , a more elaborate and more precise method is used; an intuitive depiction of the method is given in Figure 6.1.1 and Eq. 6.1.2. It uses the pointing constraint to find the best position of B vertex and momentum (within errors). Given the PV (production vertex) and SV (decay vertex), with the associated errors, and the flight direction of B (the momentum), the decay vertex coordinates are varied within the limits of its errors until the angle between the momentum and the flight direction is minimum [76].

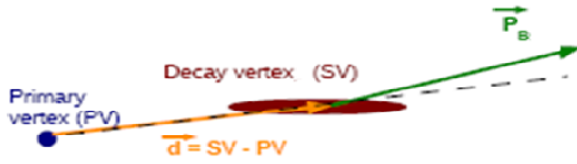


Figure 6.1.1 Lifetime calculation method

$$\tau_{REC} = \frac{M \times \vec{P} \cdot (SV - PV)}{|\vec{P}|^2}$$

Eq. 6.1.2 Reconstructed  $\tau$ , M=mass, P=momentum, SV=secondary vertex, PV=production vertex

In the ideal case of a perfect detector the lifetime distribution is described by an exponential function which has as an exponent the inverse of the lifetime,  $\tau$ , of the particle  $e^{-t/\tau}$ . In reality, each measurement of the decay time,  $t$ , is affected by the finite resolution of the detector so the distribution of the measured lifetime is described by the convolution between a Gaussian and an exponential function. In the following, using simulated data, the lifetime acceptance function and lifetime distribution are studied in the two cases mentioned above while applying the offline selection cuts one by one. It is shown that there are cases when the lifetime distribution is well described by a simple exponential function, but there are a few selection cuts which affect the lifetime reconstruction.

Figure 6.1.2 shows the lifetime distribution and lifetime acceptance for the reconstructed  $\tau$  (red line) and true  $\tau$  (green line), in the Stripping Case scenario (only the stripping selection cuts are applied). The lifetime acceptance is defined as the ratio between the reconstructed proper time distribution and the nominal exponential,  $e^{-t/\tau}$ . In the ideal detector this ratio should be a flat distribution. As seen in Figure 6.1.2 b), the true  $\tau$  acceptance function, in green, rises steeply at small lifetimes then reaches a flat plateau, as expected, but there is a non zero slope for the acceptance function for  $\tau_{REC}$ . The behavior seen at small lifetimes is reflected in the lifetime distribution in Figure 6.1.2 a) where there is a comparison between the reconstructed  $\tau$ , true  $\tau$  (red and green, respectively) and the expected

nominal exponential distributions (black line). The picture clearly indicates the deviation of the reconstructed  $\tau$  distribution from the expected exponential.

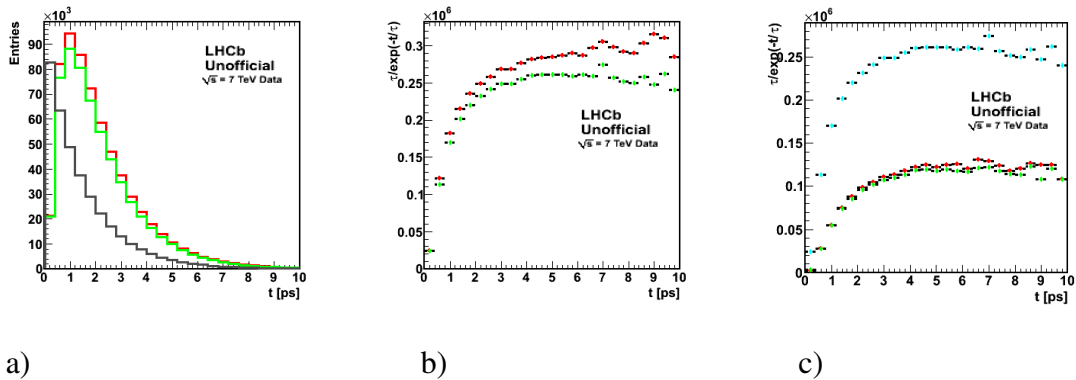


Figure 6.1.2 **Stripping** Case, a) lifetime distribution, comparison between reconstructed (red) and true (green)  $\tau$  and the nominal exponential (black) after all stripping cuts are applied b) lifetime acceptance function for reconstructed (red) and true (green)  $\tau$  after all stripping cuts are applied c) lifetime acceptance function, comparison between reconstructed (red) and true (green)  $\tau$  after all offline cuts are applied and true tau before offline selection (blue)

Then, in Figure 6.1.2 c), the reconstructed  $\tau$  and true  $\tau$  acceptance functions (red and green, respectively) after all offline selection cuts are applied, are compared to the true  $\tau$  acceptance function when none of the offline selection cuts are applied (blue line). The plot indicates the reduction of the non-zero slope after the offline selection. Also, the number of candidates which pass the selection is reduced to less than half which indicates that half of the candidates were in fact bad-reconstructed background events. The same comparison is performed for the “MCTruth” case in order to determine if the same effect is observed on the generated events.

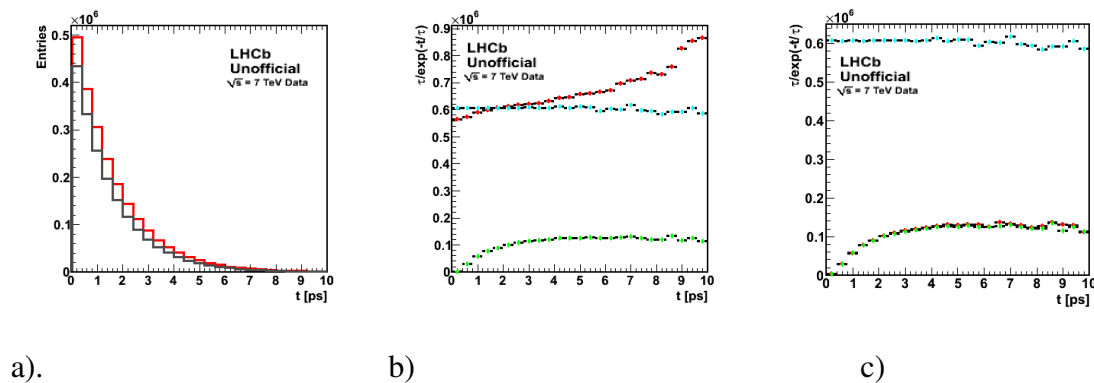


Figure 6.1.3 **MCMATCH** Case, a)  $\tau$  distribution, no selection cuts applied, comparison between nominal exponential function in black and reconstructed  $\tau$  distribution in red b)  $\tau$  acceptance function, no offline cuts applied, comparison between reconstructed (red) and true (blue) tau before any offline cuts are applied and true tau after all cuts, in green c) lifetime acceptance, all offline cuts applied, comparison reconstructed (red) and true (green) tau after all cuts are applied and true tau before any cuts (blue)

Figure 6.1.3 shows the lifetime distribution and lifetime acceptance in the “MCMatch” scenario. Figure 6.1.3 a) shows that before any offline selection is applied, the reconstructed  $\tau$  (red line) has an exponential behavior when compared to the nominal exponential (black line) but in Figure 6.1.3 b) the same non-zero slope for the reconstructed  $\tau$  acceptance function distribution (red line) is observed while the true  $\tau$  acceptance function (blue line) has the expected flat distribution. After the offline selection is applied, pictured in Figure 6.1.3 c), both the reconstructed and the true  $\tau$  acceptance functions have a similar behavior which proves that the offline selection applied on the reconstructed candidates efficiently removes bad-reconstructed background events and keeps true signal events. Compared to the true  $\tau$  acceptance function, when no selection is performed, the flat blue line in Figure 6.1.3 c), the same picture shows that the offline selection cuts away events with small lifetimes and reduces the global number of events by a factor 6.

In the following, the effect of the offline selection cuts on the lifetime acceptance function distribution is shown. This is done by studying the behavior of the acceptance function when each of the offline official selection cuts is applied one by one. The results are shown in Figures 6.1.4 to 6.1.26. In each plot, the reconstructed  $\tau$  acceptance function (or lifetime distribution) after the respective offline cut is applied is compared to the true  $\tau$  acceptance function (or lifetime distribution) after the same cut is applied and both these distributions (the red and green distributions) are then compared to the true  $\tau$  acceptance function (or lifetime distribution) before any selection cuts are applied (the blue line).

It is shown that the cuts on “ $\gamma_{P_T}$ ” (photon transverse momentum) and “ $\Delta B_d$ ” (difference between the reconstructed mass and the nominal PDG mass of  $B_d$ ) reduce the slope of the acceptance function distribution to almost zero. For this reason, the acceptance function distribution is studied either for each of the individual cuts or combined with these two cuts.

### **$\gamma_{P_T} > 2.8 \text{ GeV}/c$**

The lifetime acceptance function and the lifetime distribution when the cut on the transverse momentum of the photon,  $\gamma_{P_T} > 2.8 \text{ GeV}$  is applied are represented in Figure 6.1.4, for the MCMatch case, and Figure 6.1.5, for the Stripping case.

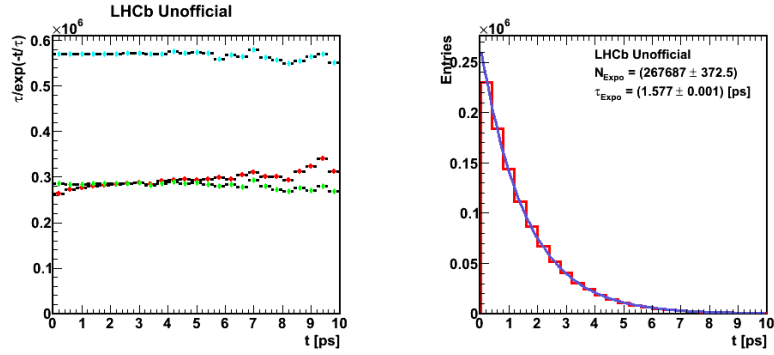


Figure 6.1.4  $\gamma_{P_T} > 2.8 \text{ GeV}/c$  (**MCMATCH**) a) comparison between reconstructed (red) and true (green)  $\tau$  acceptance function after the  $\gamma_{P_T} > 2.8 \text{ GeV}/c$  cut and true  $\tau$  acceptance function before the cut (blue) b)  $\tau$  distribution fitted with a simple exponential

Figure 6.1.4 a) shows that this cut alone reduces the positive slope of the acceptance function distribution to  $\sim 12\%$  and it removes about half of the candidates. Consequently, this cut is vital in removing background photons with low energies which obviously represent one of the sources of the unexpected behavior of the lifetime acceptance function. In this case the lifetime distribution can be fitted with a simple exponential function, Figure 6.1.4 b), which gives  $\tau = 1.577 \pm 0.001 \text{ ps}$ ; the nominal lifetime accepted in the literature is  $1.525 \pm 0.009 \text{ ps}$ . [70]

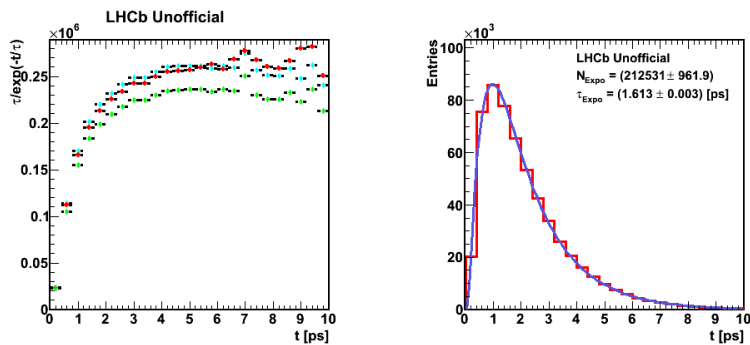


Figure 6.1.5  $\gamma_{P_T} > 2.8 \text{ GeV}/c$  (**Stripping case**) a) lifetime acceptance function, comparison between reconstructed (red) and true (green)  $\tau$  after the  $\gamma_{P_T} > 2.8 \text{ GeV}/c$  cut and true  $\tau$  before the cut (blue) b) lifetime distribution fitted with exponential+gauss

In the Stripping case the lifetime distribution cannot be fitted with a simple exponential function, as shown in Figure 6.1.5 b). The fit function is a convolution between an exponential and a gaussian which results in a value for  $B_d$  lifetime of  $\tau = 1.613 \pm 0.003 \text{ ps}$ . In the Stripping case also, the cut on the transverse momentum of the photon reduces the positive slope of the acceptance function distribution to the expected flat plateau, Figure 6.1.5 a).

### $B_d \Delta Mass$ (MCMatch)

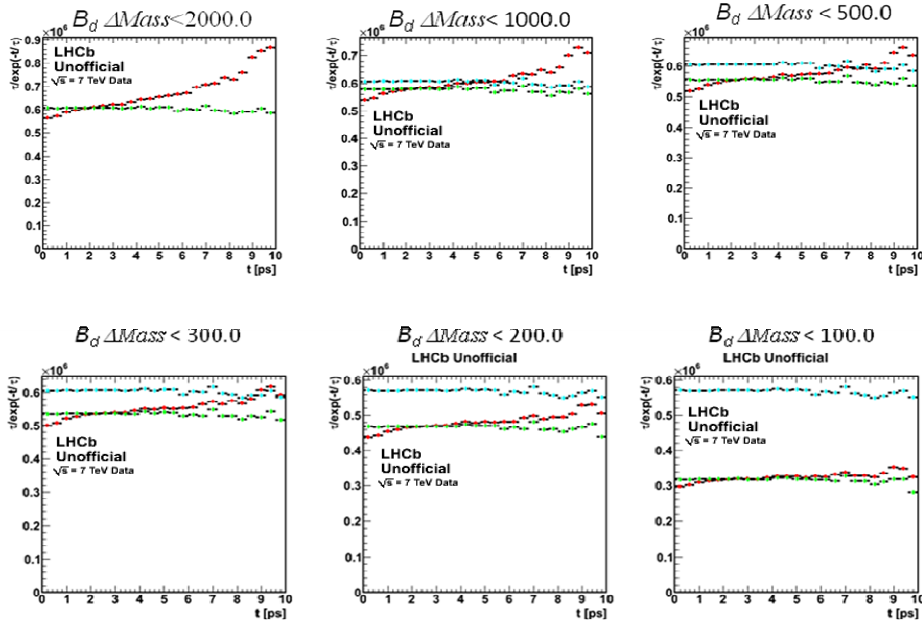


Figure 6.1.6 Comparison between reconstructed (red) and true (green)  $\tau$  after the  $B_d \Delta Mass$  (MCMatch) cut and true  $\tau$  before the cut (blue)

The sequence of plots in Figure 6.1.6 shows how the slope of the reconstructed  $\tau$  acceptance distribution (for the MCMatch case) is lowered to almost 0 only by narrowing the mass window for the  $B_d$  candidates from 20 standard deviations ( $\sigma$ ) to  $1\sigma$ . The global number of candidates is also reduced to about half. Clearly, a cut on the mass window for the reconstructed  $B_d$  candidates must be set in the offline selection, but as it is shown in Figure 6.1.6, a narrower mass window is needed in order to improve the lifetime measurement.

This fact is proved further in Figure 6.1.7, where the reconstructed  $\tau$  acceptance function is represented for the *Stripping case* and where it is shown that a mass window of  $1000 \text{ MeV}/c^2$  has no effect on the slope of the lifetime distribution but the slope is reduced to 0 when we lower the mass window to  $1\sigma$ .

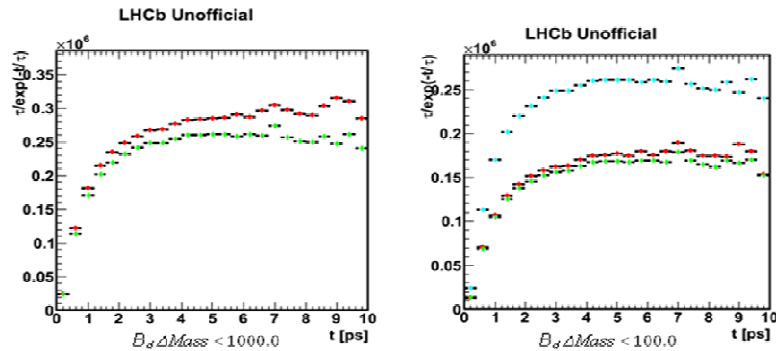


Figure 6.1.7 Stripping selection a)  $B_d \Delta Mass < 1000 \text{ MeV}/c^2$ , b)  $B_d \Delta Mass < 100 \text{ MeV}/c^2$

In Figures 6.1.8 to 6.1.26 the effect of the remaining offline selection cuts (Table 4.2.2) on the lifetime acceptance and lifetime distribution is represented. For each cut, first the MCMATCH case (with the individual cut effect followed by the effects of the combination of the individual cut and the cuts on  $\gamma_{P_T}$  and  $B_d \Delta Mass$ ) is shown, then the same is done for the Stripping case.

Figures 6.1.8 to 6.1.26 show that the rest of the cuts reduce more or less the non-zero slope of the lifetime acceptance function distribution but not as much as the cuts on the transverse momentum of the photon and on the  $B_d$  mass window. It is shown that some of the cuts induce other effects as well, e.g. steeper or smoother rising of the acceptance function distribution at small lifetimes, namely the cut on the minimal impact parameter  $\chi^2$  of  $K$  and  $\pi$  and the cut on  $B$  direction angle, or even a negative slope in the distribution of the true  $\tau$  acceptance function, such as the cut on  $B^0 \text{ min IP } \chi^2$ .

***K,  $\pi$  minimal IP  $\chi^2 > 25$***

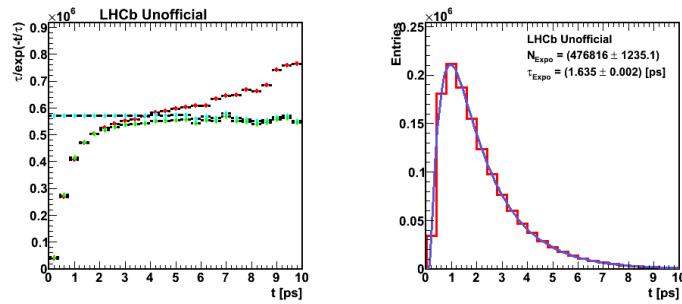


Figure 6.1.8 *MCMATCH case + K,  $\pi$  min IP  $\chi^2 > 25$* , these cuts remove candidates with small lifetimes, but do not reduce the slope of the acceptance function, lifetime distribution fitted with exponential+gauss

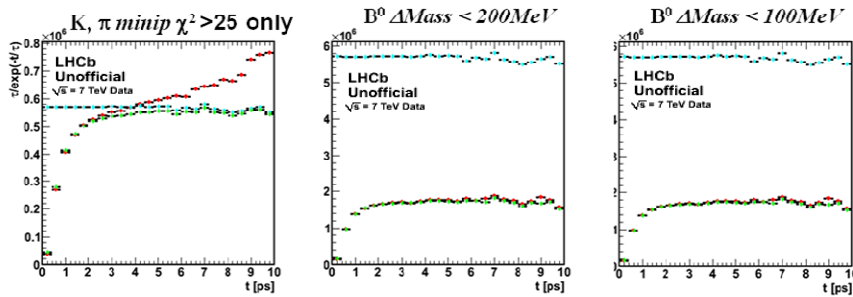


Figure 6.1.9 *MCMATCH case + K,  $\pi$  min IP  $\chi^2 > 25$  &&  $\gamma_{P_T} > 2.8 \text{ GeV}/c$  &&  $B^0 \Delta Mass (< 200 \text{ MeV}/c^2$  and  $< 100 \text{ MeV}/c^2$ )*, this combination of cuts reduces the slope to almost 0 and the number of candidates is reduced to about a third

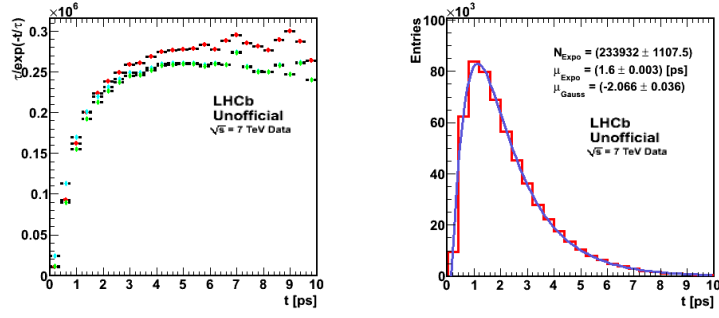


Figure 6.1.10 *Stripping case+K, pi min IP  $\chi^2 > 25$* , there is a reduction of the slope for  $\tau_{\text{REC}}$ , lifetime distribution fit with exponential+gauss,  $\tau = 1.6 \pm 0.003$  ps

**$K^+PIDK > 3$  &  $\pi^-PIDK < 5$**

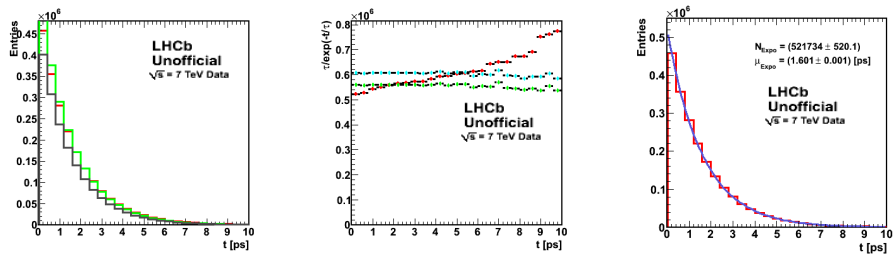


Figure 6.1.11 *MCMATCH case+K<sup>+</sup>PIDK>3 & pi<sup>-</sup>PIDK<5*, these cuts do not reduce the slope, lifetime distribution can be fitted with a simple exponential function,  $\tau = 1.601 \pm 0.001$  ps

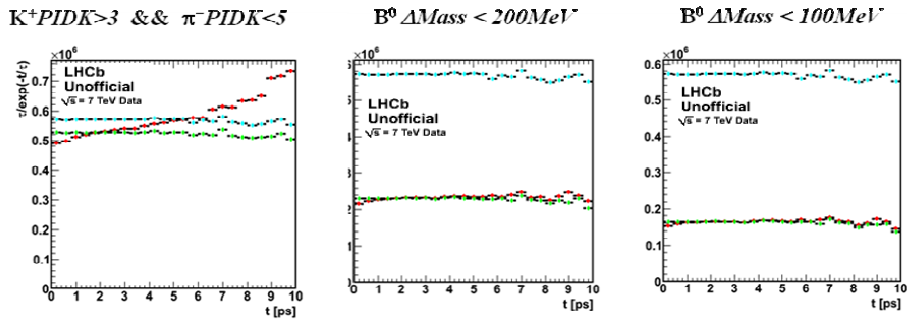


Figure 6.1.12 *MCMATCH case+(K<sup>+</sup>PIDK>3 & pi<sup>-</sup>PIDK<5) & gamma<sub>P\_T</sub>>2.8GeV/c & B<sup>0</sup> Delta Mass as before*, this combination of cuts reduces the slope to almost 0 and the number of candidates is reduced to about a third

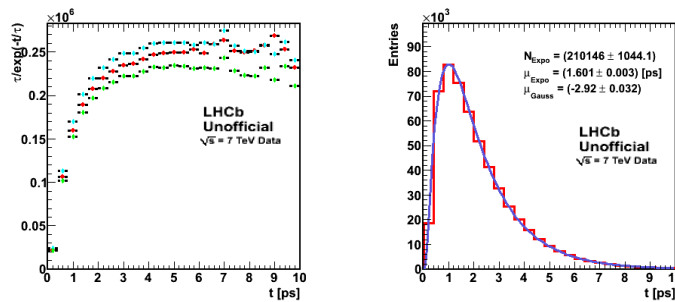


Figure 6.1.13 *Stripping case+K<sup>+</sup>PIDK>3 & pi<sup>-</sup>PIDK<5*, we observe a reduction of the slope, lifetime fit with exponential+gauss,  $\tau = 1.601 \pm 0.003$  ps

### $K^+PIDK - PIDp > 5$

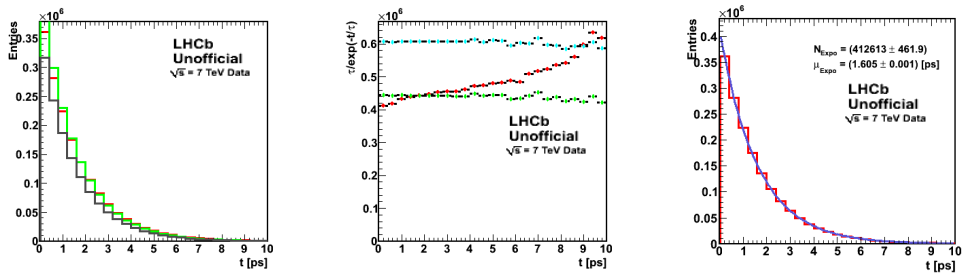


Figure 6.1.14 *MCMatch case*+ $K^+PIDK - PIDp > 5$ , this cut reduces the slope by  $\sim 30\%$  and cuts away around 30% of the candidates with low lifetimes, lifetime distribution can be fitted with abn exponential,  $\tau = 1.605 \pm 0.001$  ps

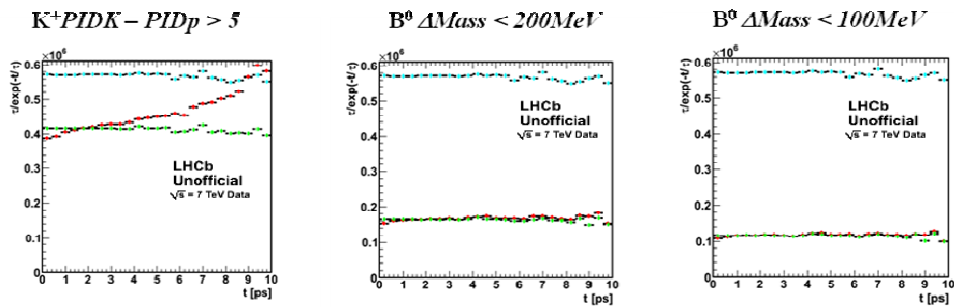


Figure 6.1.15 *MCMatch case*+ $K^+PIDK - PIDp > 5$  &&  $\gamma_{P_T} > 2.8 GeV/c$  &&  $B^0 \Delta Mass$ , again, this combination of cuts reduces the slope (to almost 0) along with the number of candidates

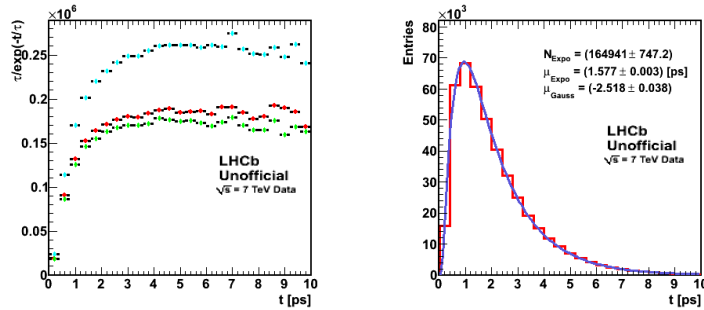


Figure 6.1.16 *Stripping case*+ $K^+PIDK - PIDp > 5$ ,  $\tau_{REC}$  acceptance slope is reduced to 0, the number of candidates also reduced to almost half, lifetime fit with exponential+gauss,  $\tau = 1.577 \pm 0.003$  ps

### $K^* \Delta Mass < 100 MeV/c^2$

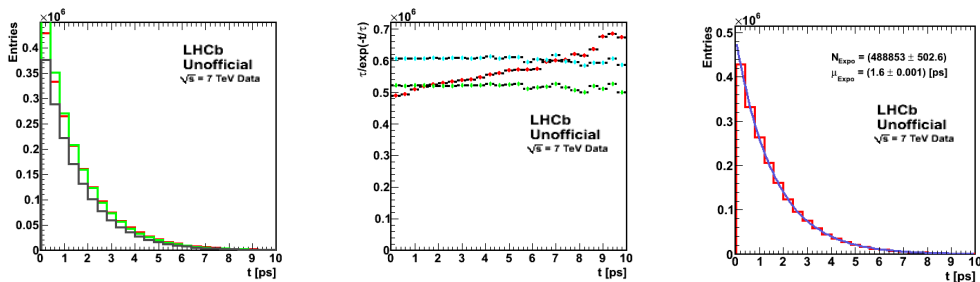


Figure 6.1.17 *MCMatch case*+ $K^* \Delta Mass < 100 MeV$ , there is a small reduction of the acceptance slope but this cut does not remove as many candidates in the small lifetimes region, lifetime distribution can be fitted with a simple exponential function,  $\tau = 1.6 \pm 0.001$  ps

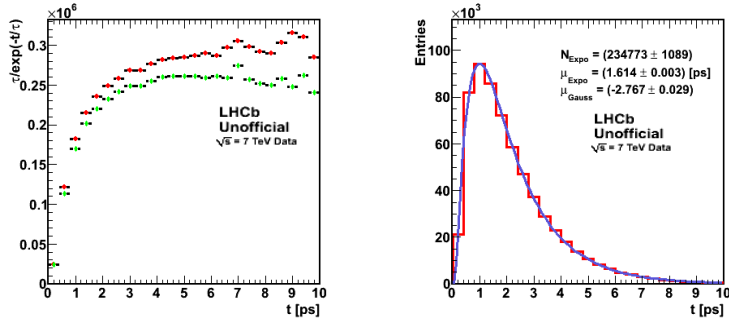


Figure 6.1.18 *Stripping case*+ $K^* \Delta Mass < 100 MeV/c^2$ , this cut does not affect the distributions  $K^* \text{ vertex } \chi^2 < 9$

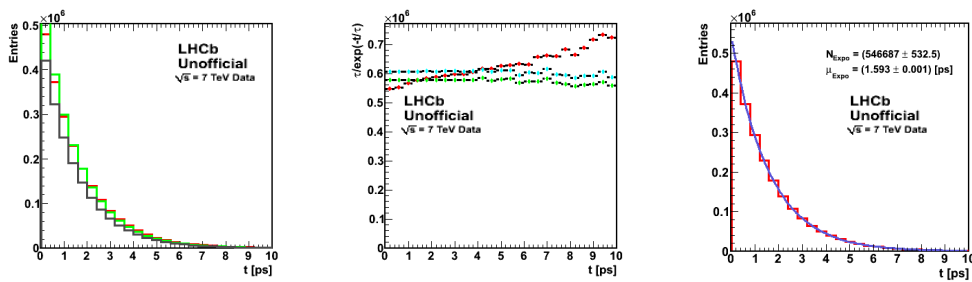


Figure 6.1.19 *MCMATCH case*+ $K^* \text{ vertex } \chi^2 < 9$ , this cut also reduces the slope by  $\sim 30\%$  but it does not remove the candidates with small lifetimes, lifetime distribution can be fitted with a simple exponential function,  $\tau = 1.593 \pm 0.001$  ps

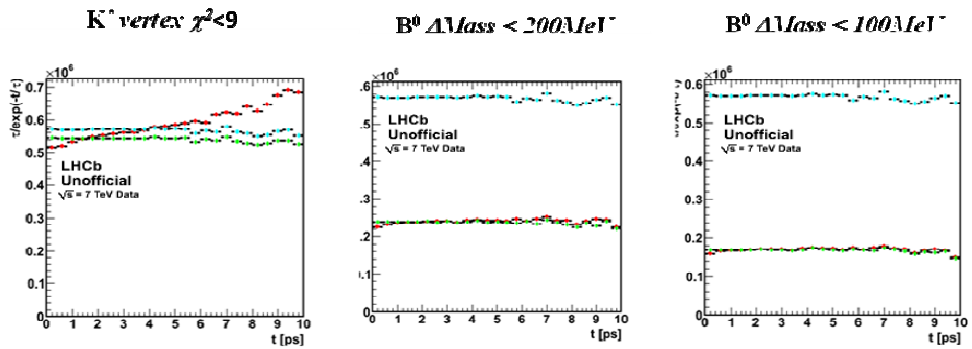


Figure 6.1.20 *MCMATCH case*+ $K^* \text{ vertex } \chi^2 < 9$  &&  $\gamma_{P_T} > 2.8 GeV/c$  &&  $B^0 \Delta Mass$ , this combination of cuts reduces the slope to almost 0 along with the number of candidates

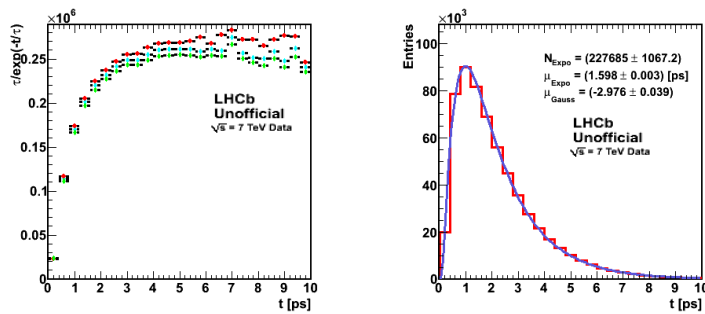


Figure 6.1.21 *Stripping case*+ $K^* \text{ vertex } \chi^2 < 9$ , there is a clear reduction of the non-zero slope of the acceptance function distribution, lifetime fit with exponential+gauss,  $\tau = 1.598 \pm 0.003$  ps

$B^0 \text{ min IP } \chi^2 < 9$

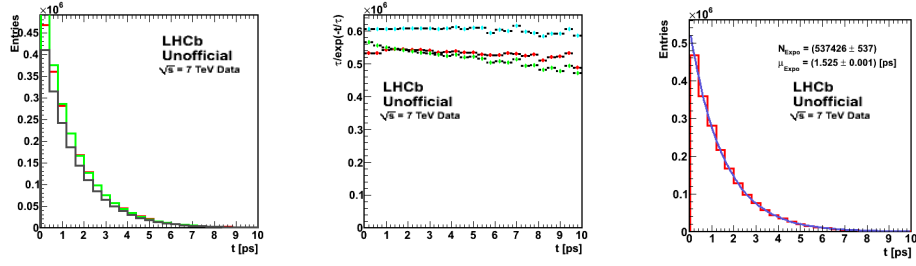


Figure 6.1.22 *MCMATCH case*+ $B^0 \text{ min IP } \chi^2 < 9$ , this cut alone reduces the slope for the reconstructed  $\tau$  acceptance to almost 0 and it keeps almost all of the candidates. Instead, for the true  $\tau$ , this cut induces a negative slope to the distribution, lifetime distribution can be fitted with a simple exponential function,  $\tau=1.525\pm 0.001$  ps (the PDG [70] value)

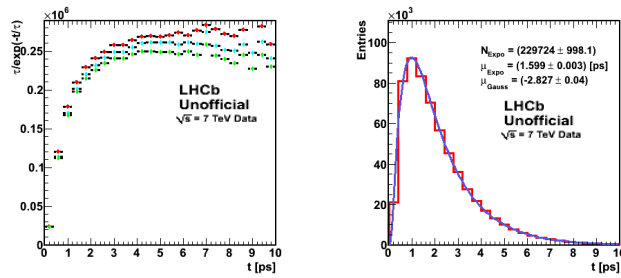


Figure 6.1.23 *Stripping case*+ $B^0 \text{ min IP } \chi^2 < 9$ , there is clear reduction of the non-zero slope of the acceptance function distribution, lifetime fit with exponential+gauss,  $\tau = 1.599\pm 0.003$  ps

$B^0 \text{ direction angle } \theta_B < 8 \text{ mrad}$

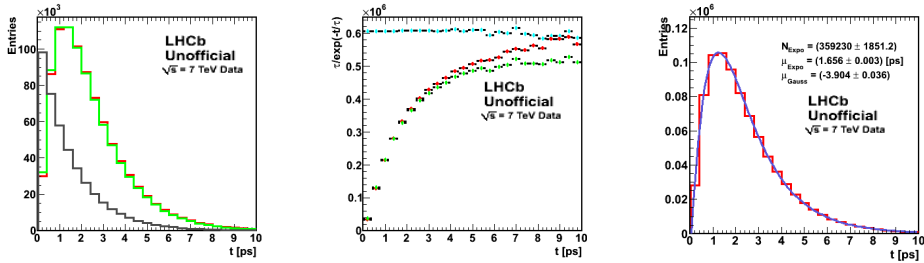


Figure 6.1.24 *MCMATCH case*+ $\theta_B < 8 \text{ mrad}$ , this cut produces a similar behavior both for the reconstructed  $\tau$  and true  $\tau$  acceptance functions at small lifetimes: the rise of the distribution is smoother, lifetime distribution cannot be fitted with a simple exponential function, fit with exponential+gauss,  $\tau = 1.656\pm 0.003$  ps

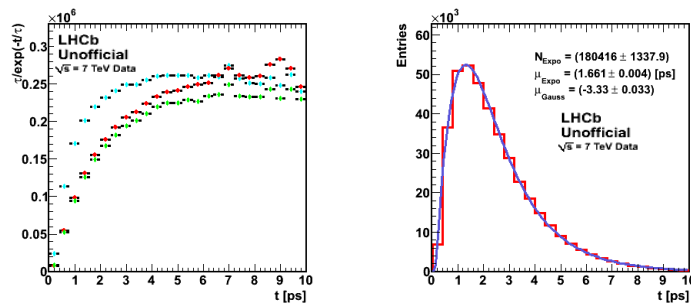


Figure 6.1.25 *Stripping case*+ $\theta_B < 8 \text{ mrad}$ , the same smooth rise to the plateau is observed but the rise is not as steep as for the true  $\tau$  acceptance function distribution before the cut is applied

$|\cos(\theta_H)|, \theta_H=B^0$  helicity angle

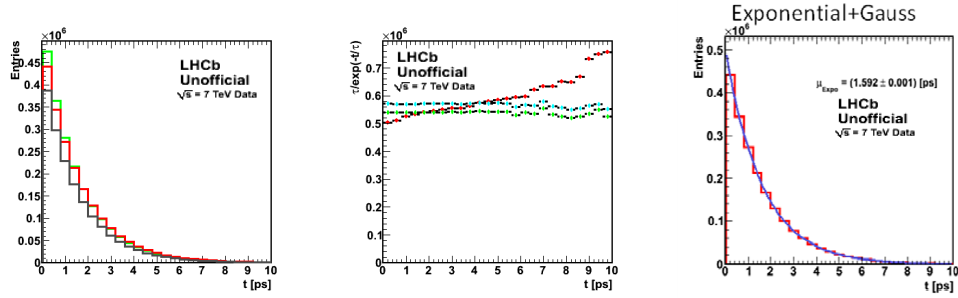


Figure 6.1.26 *MCMATCH case*  $+|\cos(\theta_H)| < 0.8$ , this cut does not change the distribution noticeably, lifetime distribution can be fitted with a simple exponential but here the fit is done with exponential+gauss,  $\tau = 1.592 \pm 0.001$  ps

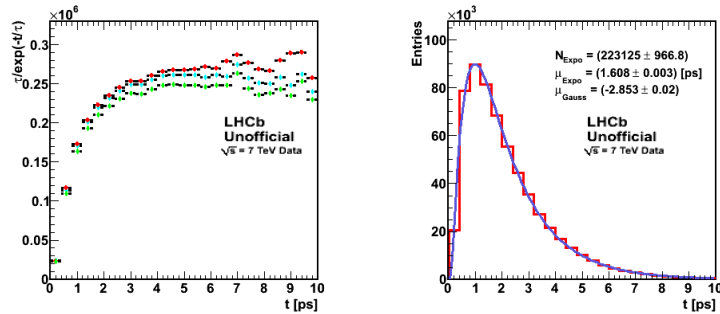


Figure 6.1.26 *Stripping case*  $+|\cos(\theta_H)| < 0.8$ , there is a small reduction of the acceptance slope

The evaluation of the B meson true lifetime is done according to Eq. 6.1.1. This equation shows that the correct determination of B lifetime depends on the precise reconstruction of B-meson mass,  $M$ , B-meson flight distance,  $d$ , and B-meson momentum,  $P$ . The effect of the reconstruction of each of these variables on the lifetime measurement can be studied by re-calculating the reconstructed  $\tau$  according to Eq. 6.1.1 and replacing the true  $M$ ,  $d$  and  $P$  with their reconstructed values. The difference  $\tau_{\text{REC}} - \tau_{\text{TRUE}}$  is expected to have a Gaussian distribution centered around 0.

The difference  $\tau_{\text{REC}} - \tau_{\text{TRUE}}$  is represented in Figure 6.1.27 a), b) and c) in three cases: Figure 6.1.27 a) none of the offline selection cuts are applied, Figure 6.1.27 b) all the offline selection cuts are applied but the  $B^0$  mass window is  $1000 \text{ MeV}/c^2$  and Figure 6.1.27 c) all the offline selection cuts are applied but the  $B^0$  mass window is  $100 \text{ MeV}/c^2$ .

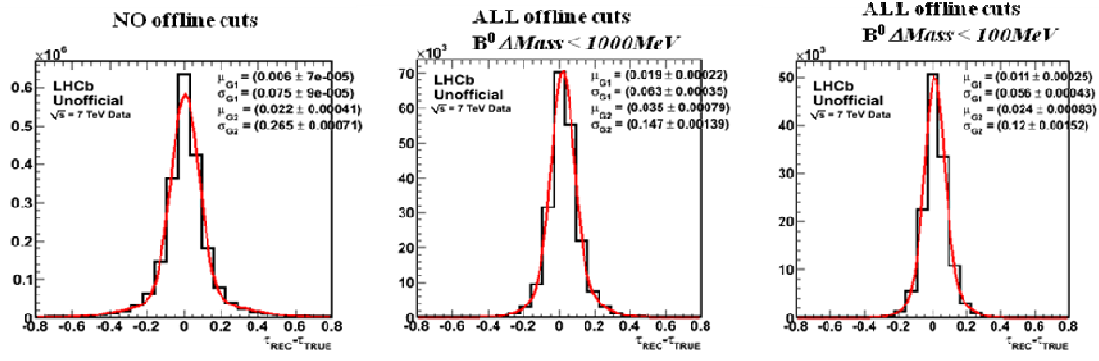


Figure 6.1.27 Double gaussian fit on the difference  $\tau_{REC}-\tau_{TRUE}$ , a) no offline cuts, b) all offline cuts and  $B^0 \Delta Mass < 1000 \text{ MeV}/c^2$ , c)  $B^0 \Delta Mass < 100 \text{ MeV}/c^2$

The distributions in Figure 6.1.27 are best fitted with the sum of two Gaussian functions. In all cases, each of the two Gaussians show a shift of the mean value towards positive values which means that the difference between the reconstructed and true  $\tau$  is asymmetrical with respect to 0. To understand which of the variables in Eq. 6.1.1 is responsible for this bias, the  $B^0$  lifetime is re-calculated in two cases:

- 1) keep the true mass ( $M$ ) and momentum ( $P$ ) and use the reconstructed distance between the production and decay vertexes ( $d$ ):

$$\tau_{REC} = \frac{M_{TRUE} * (\overline{d_{REC}} * \overline{P_{TRUE}})}{P_{TRUE}^2} \quad \text{Eq. 6.1.3}$$

- 2) keep true  $d$  and use the reconstructed  $M$  and  $P$ :

$$\tau_{REC} = \frac{M_{REC} * (\overline{d_{TRUE}} * \overline{P_{REC}})}{P_{REC}^2} \quad \text{Eq. 6.1.4}$$

Using these new equations the difference  $\tau_{REC}-\tau_{TRUE}$  is re-evaluated both for MCMATCH and Stripping cases. The results are represented in Figures 6.1.28 to 6.1.31, A) MCMATCH case, B) Stripping case.

#### A) MCMATCH case

- 1) First, the reconstructed  $\tau$  is calculated by considering the *reconstructed distance* between the production and decay vertices of the  $B^0$  and the *true mass and momentum* of  $B_d$ . The difference  $\tau_{REC}-\tau_{TRUE}$  is represented in Figure 6.1.28 a), b) and c) in three cases: a) none of the offline selection cuts are applied, b) all offline cuts are applied and the mass window is  $1000 \text{ MeV}/c^2$ , and c) all offline cuts are applied and the mass window is  $100 \text{ MeV}/c^2$ .

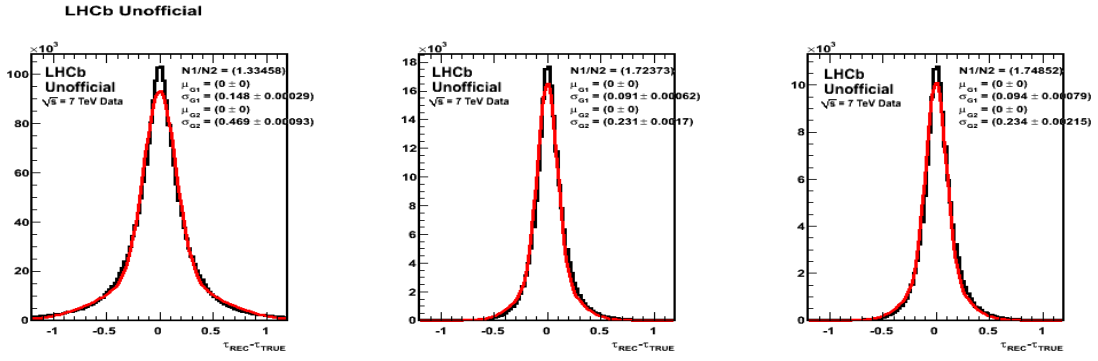


Figure 6.1.28 **MCMATCH** case, Double gaussian fit of the difference  $\tau_{REC} - \tau_{TRUE}$  with reconstructed  $d$  and true  $M$  and  $P$ , a) no offline cuts, b) all offline cuts applied and  $B^0 \Delta Mass < 1000 \text{ MeV}/c^2$ , c) all offline cuts applied and  $B^0 \Delta Mass < 100 \text{ MeV}/c^2$

- 2) Second, the reconstructed  $\tau$  is calculated by considering the *true distance* between the vertices, but using the *reconstructed mass and momentum*. The difference  $\tau_{REC} - \tau_{TRUE}$  is represented in Figure 6.1.29 a), b) and c) also in three cases: a) none of the offline selection cuts are applied, b) all offline cuts are applied and the mass window is  $1000 \text{ MeV}/c^2$ , and c) all offline cuts are applied and the mass window is  $100 \text{ MeV}/c^2$

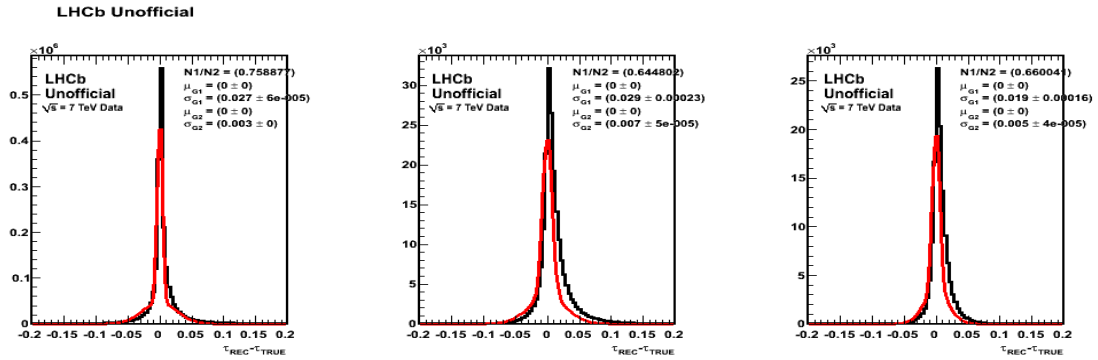


Figure 6.1.29 **MCMATCH** case, Double gaussian fit of the difference  $\tau_{REC} - \tau_{TRUE}$  with reconstructed  $M$  and  $P$  and true  $d$ , a) no offline cuts, b) all offline cuts applied and  $B^0 \Delta Mass < 1000 \text{ MeV}/c^2$ , c) all offline cuts applied and  $B^0 \Delta Mass < 100 \text{ MeV}/c^2$

Next, a similar study is performed for the Stripping case.

## B) Stripping case

$$1) \quad \tau_{REC} = \frac{M_{TRUE} * (d_{REC} \cdot P_{TRUE})}{P_{TRUE}}$$

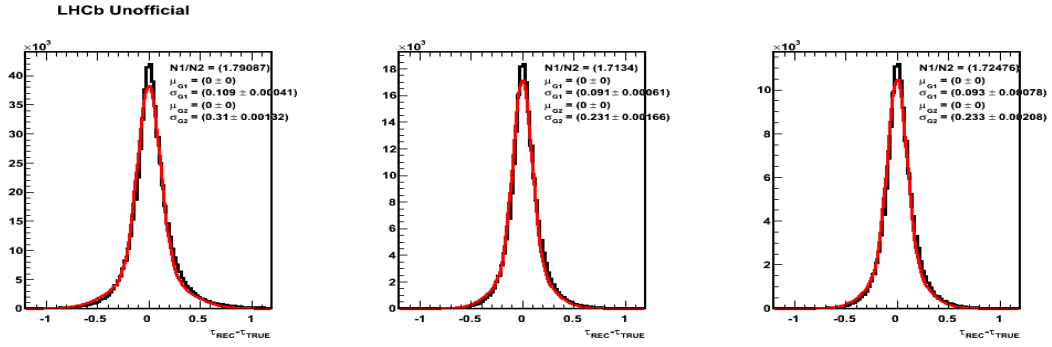


Figure 6.1.30 **Stripping case**, Double gaussian fit on the difference  $\tau_{REC}-\tau_{TRUE}$  with reconstructed  $d$  and true  $M$  and  $P$ , a) no offline cuts, b) all offline cuts are applied and  $B^0 \Delta Mass < 1000 \text{ MeV}/c^2$ , c) all offline cuts are applied and  $B^0 \Delta Mass < 100 \text{ MeV}/c^2$

$$2) \quad \tau_{REC} = \frac{M_{REC} * (\overline{d_{TRUE}} - P_{REC})}{P_{REC}}$$

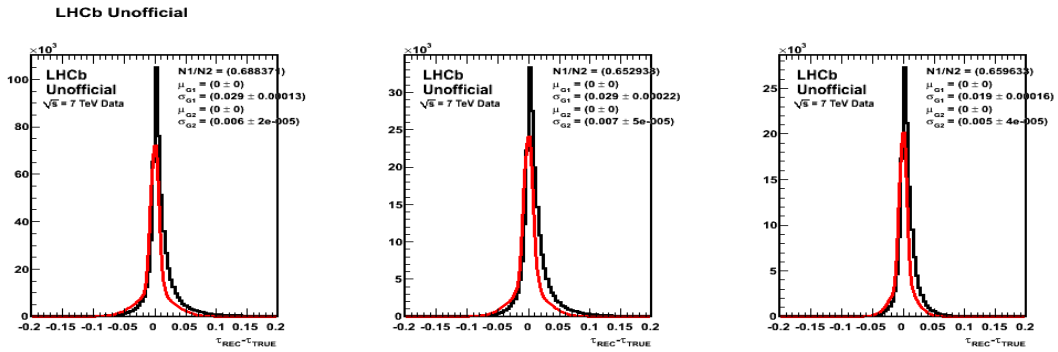


Figure 6.1.31 **Stripping case**, Double gaussian fit on the difference  $\tau_{REC}-\tau_{TRUE}$  with reconstructed  $M$  and  $P$  and true  $d$ , a) no offline cuts, b) all offline cuts are applied and  $B^0 \Delta Mass < 1000 \text{ MeV}/c^2$ , c) all offline cuts are applied and  $B^0 \Delta Mass < 100 \text{ MeV}/c^2$

Figures 6.1.28 and 29 show clearly that the largest bias in the evaluation of the lifetime is introduced by the calculation of the distance between the vertices which relates directly to the precise identification of the primary and secondary vertices. To better illustrate the shift of the distributions towards positive values, the means of the Gaussian functions are fixed parameters with values equal to 0. When using the reconstructed distance (and true  $M$  and  $P$ ), Figure 6.1.28, the difference between the reconstructed and true  $\tau$  is very well fitted by a double Gaussian distribution but the events are widely spread around the mean. Both Gaussians are characterized by large widths, the narrower of the two Gaussians, which is also the dominant one, has a standard deviation  $\sigma \approx 0.1$  ps. This is not the case when using the reconstructed mass and momentum. Although the bias in the distribution of the  $\tau_{REC}-\tau_{TRUE}$  towards positive values is more obvious in Figure 6.1.29, the scale of the shift in this case is

much lower. The dominant Gaussian function has a maximum standard deviation  $\sigma=0.007\pm 5\times 10^{-5}$  ps.

Thus, the largest uncertainty in the lifetime measurement is due to the large uncertainties in the determination of the primary and secondary decay vertices.

Figures 6.1.30 and 6.1.31 indicate that the same situation is found in the Stripping case. The similarity goes even further, the distributions of the  $\tau_{\text{REC}}-\tau_{\text{TRUE}}$  when none of the offline selection cuts are applied are different in the two cases (MCMatch and Stripping), but after the offline selection, with either wide or narrow mass window cut, the fit parameters are identical as far as to the third digit precision.

## 6.2 Conclusions

In this chapter results on the effect of the offline selection cuts corresponding to the  $B^0 \rightarrow K^* \gamma$  decay on the  $B^0$  lifetime distribution and lifetime acceptance function distribution have been presented.

Using simulated data, the lifetime acceptance function and lifetime distribution are studied in the two cases: the case when the pre-selection consists in the stripping selection used for the real data, Table 4.2.2 (right columns), Stripping Case, and second, the case when prior to any offline selection all the reconstructed daughters involved in the decay are matched to the true generated particles,  $K^*$ ,  $\gamma$ ,  $K$ ,  $\pi$ , the MCMatch case.

The lifetime acceptance is defined as the ratio between the reconstructed proper time distribution and the nominal exponential,  $e^{-t/\tau}$ , which ideally would be a flat distribution. It was shown that the  $\tau_{\text{TRUE}}$  acceptance function rises steeply at small lifetimes then reaches a flat plateau, as expected, but the  $\tau_{\text{REC}}$  acceptance function distribution is characterized by a non zero slope.

It is shown that the cut on the photon transverse momentum,  $\gamma P_T$ , and the cut on the difference between the reconstructed and nominal PDG mass of  $B^0$ ,  $B^0 \Delta Mass$ , have the strongest effect of the lifetime acceptance function distribution as these cuts reduce the slope to almost zero.

Other offline selection cuts determine steeper or smoother rising of the acceptance function distribution at small lifetimes, such as the cut on the minimal impact parameter  $\chi^2$  of

K and  $\pi$  and the cut on B direction angle, or even a negative slope in the distribution of the true  $\tau$  acceptance function, the cut on  $B^0 \min IP \chi^2$ .

The evaluation of B lifetime depends on the precise reconstruction of B-meson mass,  $M$ , B-meson flight distance,  $d$ , and B-meson momentum,  $P$ . As such, the effect of the reconstruction of each of these variables on the lifetime measurement is studied.

It is shown that the imprecise determination of the distance between the production and decay vertices introduce the largest bias in the evaluation of the lifetime.

It is also shown that although the difference between the reconstructed and true  $\tau$ ,  $\tau_{\text{REC}} - \tau_{\text{TRUE}}$ , is big before the offline selection, after applying the cuts the lifetime acceptance function distribution is very similar for generated (MCMatch case) and reconstructed (Stripping case) events.

## 7. ILC and CLIC accelerators and detectors

The technological progress of the 21<sup>st</sup> century offers the possibility to explore physics aspects at colossal energy scales. Physics at Terascale is no longer science fiction but a reality. This fact has been proven already by the magnificent performance of the Large Hadron Collider, LHC [23]. Nonetheless, LHC is a discovery machine; its main goal is to prove the existence of the last ingredient of the Standard model of particles, the Higgs boson, and to search for signals which may point to physics Beyond the Standard Model. But the hunger for knowledge pushes us further, if new signals are being discovered, there comes the need to know their properties, their way of interacting and where they come from. For this reason, the scientific community has reached the agreement that an electron-positron collider with center of mass energies between 500 GeV and 3 TeV, coupled with very high luminosities is the next best choice to fulfill the tasks outlined. Such a machine is either the International Linear Collider, ILC [25], or the Compact Linear Collider [26], CLIC. The aim is to bring light over some of the most ardent questions: what are the building blocks of matter and how do they fit together to shape the world? Are there more dimensions? Are all the forces of nature aspects of a single unified theory? Where does matter come from? What is the nature of the dark matter that binds galaxies together? [77]

The two proposed future projects are currently being developed in parallel, although they are at different stages of development. In 2005 the ILC community has completed a baseline design for ILC and based on it a more detailed Reference Design Report, RDR [78][79][80][81], was published in 2007 including more technical aspects and a cost estimate [r]. Presently the ILC is in the engineering design phase preparing to produce a Technical Design Report, TDR, which will be the final step towards the approval and eventual construction of this accelerator. In comparison, the CLIC research community is assiduously working on preparing the Conceptual Design Report, CDR, by the end of 2011.

While two different approaches on the accelerating techniques are envisaged for ILC [80] and CLIC [82], which are detailed in Chapter 7.2, a combined effort is being invested at the moment into the optimization of the experimental detectors proposed to investigate the physics programs at the two linear colliders. Four detector concepts have been initially proposed in the RDR, Volume 4- Detectors, at ILC [81]. Two of the concepts have joint efforts so in the end three detector concepts have submitted a Letter of Intent, LoI to the International Detector Advisory Group (IDAG). Two of them have been validated: the

International Large Detector, ILD [83], and the Silicon Detector, SiD [84]. CLIC community started developing its own detector concepts based on the two concepts proposed for ILC and is now working on adjusting and optimizing these detectors so that they will be able to fit the requirements of a 3 TeV center of mass energy environment.

In this thesis, results on simulation studies regarding two of the sub-detectors of the ILD detector concept are presented, BeamCal, the beam calorimeter, at ILC, one of the components of the Very Forward region placed closest to the beam pipe, and QD0 at CLIC, the last quadrupolar magnet of the Beam Delivery System (BDS) which extends into the Very Forward Region.

## 7.1. Physics at the ILC and CLIC

Many of the scientific opportunities for the ILC and CLIC involve the Higgs particle and related new phenomena at the Terascale energies. A new form of Terascale energy has been hypothesized by the Standard Model to explain the mechanism through which elementary particles acquire mass, called the Higgs field. This field also breaks the fundamental electroweak force into two components, the electromagnetic and weak forces, which are observed by experiments in very different forms. [2]

Until now, the Higgs field or the Higgs particle have not been directly observed and it had been demonstrated that quantum effects of the type already observed in experiments should destabilize the Higgs boson of the Standard Model, preventing its operation at Terascale energies. The corrections for this quantum instability bring forth dramatic phenomena at the Terascale: new forces, a new principle of nature called supersymmetry, or even extra dimensions of space. [2]

Another major opportunity for the ILC and CLIC is to shed light on the dark side of the universe. Astrophysical data show that dark matter dominates over visible matter, and that almost all of this matter cannot be composed of known particles. If Terascale dark matter exists, experiments at the ILC and CLIC should be able to produce such particles in the laboratory and study their properties. [79]

A third matter on which the ILC and CLIC concentrate is Einstein's vision of an ultimate unified theory. It was already suggested that three of the fundamental forces originated from a single “grand” unified force in the first instant of the Big Bang. This idea could be tested at the ILC and look for evidence of a related unified origin of the matter involving supersymmetry. A

theoretical framework called string theory goes beyond grand unification to include gravity, extra space dimensions and new fundamental entities called superstrings. [79]

The detectors at the ILC and CLIC raise some demanding challenges themselves, especially on precision measurements and particle tracking and identification. [81]

Testing and validation of the Higgs mechanism in the Standard Model (SM) or physics models beyond the SM can be accomplished through precision measurements on their parameters, e.g. masses or couplings. For example, the golden channel for the measurement of Higgs production is  $e^+e^- \rightarrow ZH \rightarrow l^+l^-X$ , with the Higgs mass measured by its recoil from the Z boson, which obviously can be explored only at an  $e^+e^-$  machine.[79].

Another challenge is the separation of WW from ZZ production, essential for matching branching fractions to a model, such as identifying strong electroweak symmetry breaking or supersymmetric parameters. For this the detectors must measure jet energy about a factor of two better than the best achieved so far. The low ILC backgrounds permit association of tracks and calorimeter clusters, making possible unprecedented jet energy measurement. Depending on the quark content, jets of high energies deposit roughly 65% of the visible energy in the form of charged particles, 25% in the form of photons and 10% as neutral hadrons.

If evidence of low energy supersymmetry phenomena is indeed observed, one of the most important tasks for the ILC will be to identify SUSY particle spectra and decay chains, and to establish if SUSY particles could be some or all of the dark matter. Since the lightest SUSY particle will not be observable, the detectors must be extremely hermetic, particularly at extreme polar angles. To achieve these goals the effect of beam crossing angle, beamstrahlung and machine backgrounds must be well understood and the development of instrumentation is necessary to measure the luminosity spectrum and beam polarization [79].

## 7.2 General overview on the ILC and CLIC

Both ILC and CLIC are two future projects of accelerators which will collide electrons and positrons. They will be able to complement the physics program of LHC by taking advantage of the cleaner background environment. There is though a theoretical limitation when accelerating leptons: the synchrotron radiation emitted by charged particles following a circular orbit - the higher the trajectory bending, the larger the amount of energy loss. A solution to this problem is to keep as small a curvature as possible, thus the circumference of the accelerator must be increased. In order to reach the energies proposed at ILC and CLIC, it was estimated

that circumferences of hundreds or even thousands of kilometers would be needed. Thus linear accelerators are the best choice when it comes to lepton colliders. [85]

The two accelerators are being developed in parallel until a decision can be elaborated about the scientific and financial benefits of either of them. Meanwhile the combined efforts lead to exploring and testing new technologies which could be useful to both accelerators. [86]

CLIC aims to accelerate electrons and positrons at a center-of-mass energy up to 3 TeV (about 5 times higher than ILC) by using a new accelerating technology, suitable to TeV energy scale, which will allow CLIC to reach the proposed energies over a length comparable to the distance needed for the ILC to accelerate the electrons and positrons up to 0.5-1 TeV. If the same accelerating technology would be used for CLIC as for ILC, a length of 118 km would be required to reach the 3 TeV energy goal. To limit the length of the accelerator, as well as the costs, and to reach the energy of 3 TeV at a nominal luminosity of  $10^{35} \text{ cm}^{-2}\text{s}^{-1}$  a two-beam accelerating technique is under study based on very high accelerating gradients (the accelerating power per one meter of accelerator). High gradients can be obtained with electrical fields which oscillate at very high frequencies. [82]

As compared to the ILC which will operate at 1.3 GHz frequency reaching a gradient of  $\sim 35 \text{ MV/m}$  CLIC aims toward the ambitious frequency of 30 GHz (billion of oscillations per second) generating a gradient of 150 MV/m.

The International Linear Collider, ILC, is a 200-500 GeV center-of-mass high luminosity linear electron-positron collider, with the possibility of upgrade to 1 TeV, based on superconducting radio-frequency accelerating cavities named klystrons. The following technical performances are required at the ILC [80]:

- a continuous center-of mass energy range between 200 GeV and 500 GeV;
- a peak luminosity of  $\sim 2 \times 10^{34} \text{ cm}^{-2}\text{s}^{-1}$ , and an availability (75%) consistent with producing  $500 \text{ fb}^{-1}$  in the first four years of operation;
- $>80\%$  electron polarization at the Interaction Point (IP);
- an energy stability and precision of  $\leq 0.1\%$ ;
- an option for  $\sim 60\%$  positron polarization;
- options for  $e^-e^-$  and  $\gamma\gamma$  collisions.

To achieve a center-of-mass energy of 500 GeV, the current ILC baseline assumes an average accelerating gradient of 31.5 MV/m in the cavities.

Figure 7.2.1 [78] shows a schematic view of the overall layout of the ILC, indicating the location of the major sub-systems:

- a polarized electron source
- an undulator-based positron source, driven by an 150 GeV main electron beam;
- 5 GeV electron and positron damping rings (DR) with a circumference of 6.7 km, housed in a common tunnel at the center of the ILC complex;
- beam transport from the damping rings to the main linacs, followed by a two-stage bunch compressor system at the center of the ILC complex;
- two 11 km long main linacs, utilizing 1.3 GHz SCRF cavities, operating at an average gradient of 31.5 MV/m, with a pulse length of 1.6 ms;
- a 4.5 km long beam delivery system, which brings the two beams into collision with a 14 mrad crossing angle, at a single interaction point which can be shared by two detectors.

The total length is ~31 km. The electron source, the damping rings and the positron auxiliary source are centrally located around the interaction region. The plane of the damping rings is elevated by ~10 m to avoid interference.

The upgrade of the machine, to  $E_{\text{CMS}} = 1$  TeV, will be possible by extending the linacs and the beam transport lines from the damping rings by another ~11 km each. [78]

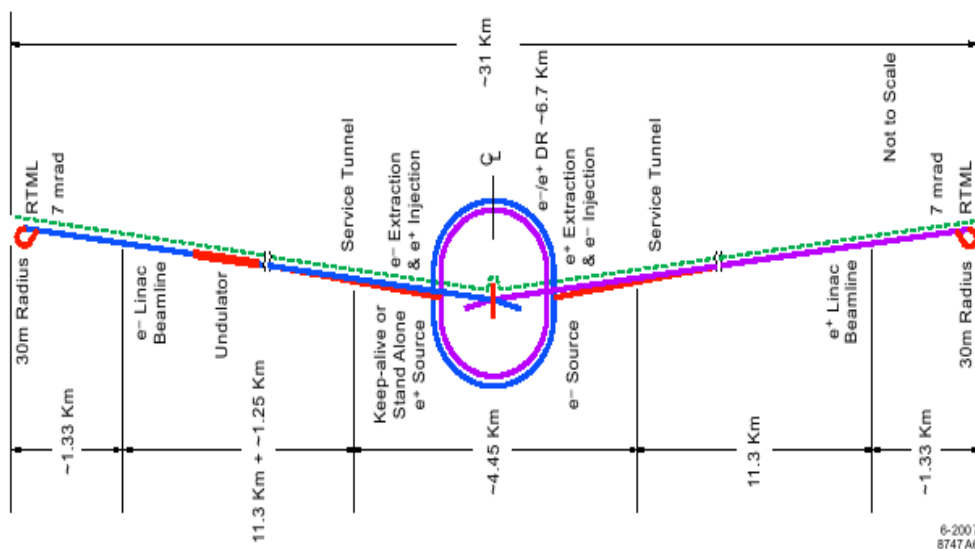


Fig. 7.2.1 ILC baseline design at 500 GeV center of mass energy [78]

The connection between the known accelerator physics and technology challenges throughout the whole accelerator complex is established through a set of parameters. For these simulations, the nominal parameter set has been chosen as it corresponds to the designed luminosity and the targeted  $E_{\text{CMS}}$ . The nominal beam parameter set is given in Table 7.2.1 [78].

Parameter	Unit	
Center-of-mass energy range	GeV	200 - 500
Peak luminosity <sup>a)</sup>	cm <sup>-2</sup> s <sup>-1</sup>	2 × 10 <sup>34</sup>
Average beam current in pulse	mA	9.0
Pulse rate	Hz	5.0
Pulse length (beam)	ms	~ 1
Number of bunches per pulse		1000 - 5400
Charge per bunch	nC	1.6 - 3.2
Accelerating gradient <sup>a)</sup>	MV/m	31.5
RF pulse length	ms	1.6
Beam power (per beam) <sup>a)</sup>	MW	10.8
Typical beam size at IP <sup>a)</sup> ( $h \times v$ )	nm	640 × 5.7
Total AC Power consumption <sup>a)</sup>	MW	230

Table 7.2.1 The nominal set of accelerator parameters at ILC [78]

At a conventional accelerator, the radio-frequency, RF, used for the primary beam acceleration is generated by klystrons which create radio-frequency waves. Power consumption of such devices at CLIC would be way too big thus a “two-beam” accelerating technique was proposed. Parallel to the primary beam, low energy but very high intensity “drive beams” are installed. The RF power is extracted from these beams and transferred in short pulses to the primary beams [82].

The accelerating procedure for the drive beams is far from simple. An electron beam is accelerated to 1.2 GeV through a linac powered by klystron structures. At this stage, the electron bunches are largely spaced with respect to each other. In order to reach the 30 GHz power, a beam compression procedure is engaged; the beams are directed through compressor/combiner rings where parts of the beam are basically interleaved with each other thus reducing the distance between the bunches to the required spacing of 2 cm. This low energy - high intensity beam is then sent to the main tunnel and used to provide RF power to a 625 m segment of the main linac. Then the drive beam is dumped and replaced by the next one. So the RF power needed to produce the accelerating field is intrinsic to the electron beam and it is extracted and transferred to the main beam through special decelerating and transfer structures. The advantage of this approach consists in very small power loss and the fact that the same number of klystrons is used to power either a lower or higher energy accelerator by generating fewer or more drive beams [85].

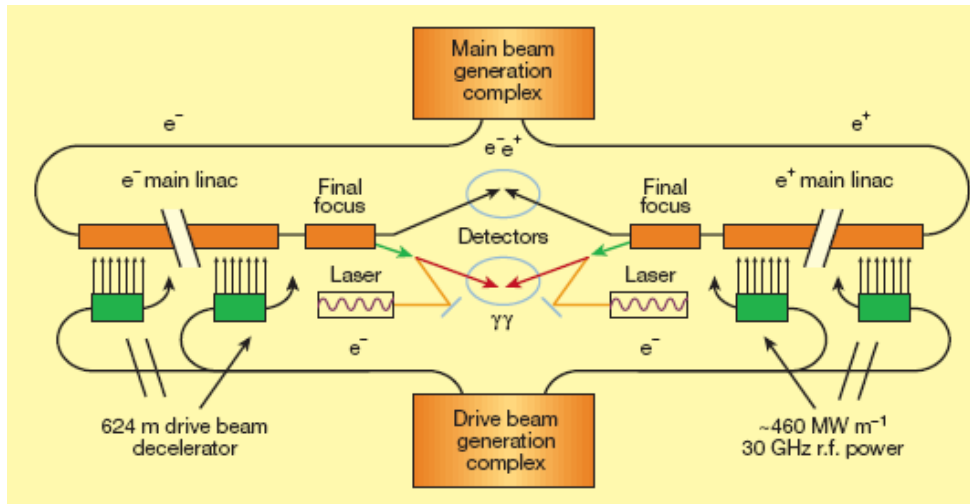


Figure 7.2.2 CLIC baseline design at 3 TeV center of mass energy [85]

## 7.3 Detector concepts at ILC and CLIC

### 7.3.1 Introduction and general overview

The basic outline of the detectors proposed for the two accelerators is common as the CLIC community decided to have as starting point the detectors validated for ILC and then continue adapting and optimizing them for CLIC environment.

The great challenge of the ILC detectors consists in improving measurements on observables determined through a large experimental program designed to explain the mass generation mechanism and electroweak symmetry breaking. For this purposes, new limits on jet energy resolution, momentum and vertex impact parameter have to be reached. Investigations regarding multi-jets and supersymmetry require highly hermetic detectors and large solid angle coverage. Particularly, *the vertex detector and very forward calorimetry must survive in a high background of  $e^+e^-$  pairs produced by the beamstrahlung radiation of the colliding beams. The high level of radiation and fast bunch crossings (once every 300 ns) pose great challenges over the design of the very forward detectors.* [78]

Four detector concepts were proposed in the ILC RDR. The need to extract the maximum information from ILC events dictates a few design characteristics common to all detector concepts. All concepts make use of similar pixellated vertex detectors, for high precision vertex reconstruction and serving as powerful tracking detectors, they all include sophisticated tracking systems, optimized for high track reconstruction efficiency and excellent

momentum resolution. Also, all concepts are designed to accommodate the calorimeters inside the coil, since much of the physics relies on high quality calorimetry. High field solenoids, ranging between 3 and 5 Tesla, have been proposed, to insure excellent momentum resolution and help disperse charged energy in the calorimeters. [81]

Detectors at ILC and CLIC are expected to provide highly efficient tracking, charged particle momentum resolution  $\Delta p/p \approx 5 \times 10^{-5}$ , dijet mass resolution at the 3% level, excellent heavy quark identification capability, and full and hermetic solid angle coverage. Three of the initial concepts used traditional solenoidal magnet designs and adopted the particle flow calorimetry strategy, where highly segmented electromagnetic and hadronic calorimeters allow the discrimination between energies deposited by charged tracks, photons and neutral hadrons. The fourth concept concentrated on obtaining excellent energy resolution while relying less on spatial resolution, and proposed a novel dual readout scheme to allow efficient software compensation [81].

The initial four detector designs were SiD (Silicon Detector), LDC (Large Detector Concept), GLD and the 4'th Concept. LDC and GLD joint efforts and a new combined design emerged, the International Large Detector, ILD. Only ILD and SiD were approved to enter the new development stage and prepare the Detailed Baseline Designs (DBDs).

### **7.3.2 Challenges on detector construction**

A dual readout calorimeter, with a transversely segmentation, can achieve excellent jet energy resolution, a feature which might make the difference between being able to measure the Higgs boson at the ILC/CLIC, or not. Measurements of the mass of the Higgs in the four jet channel,  $e^+e^- \rightarrow ZH \rightarrow qqbb$ , can use momentum-energy constraints and large statistics, and will benefit significantly from improved energy resolution. If the Higgs boson is not discovered, the research will concentrate on studies of WW scattering, thus, improving the jet energy resolution will improve the discrimination of  $WW\nu\nu$ ,  $WZ\nu e$  and  $ZZee$  final states. [79]

The new theoretical concept of “particle flow” requires a highly segmented, both transversely and longitudinally, granular calorimeter. Thus, high granularity becomes much more important than very good energy resolution. Cells about  $1 \times 1 \text{ cm}^2$  have been found suitable for the electromagnetic and possibly even for the hadronic sections, and energy resolutions of  $\sim 15\%$  for the electromagnetic and  $>40\%$  for the hadronic part are under consideration. This represents the principal challenge for the calorimeter system. [81]

Lepton identification requires a lot of specific characteristics for the calorimeters: high granularity, excellent hermeticity, sensitivity to minimum ionizing particles, compact electromagnetic shower development and good electromagnetic energy resolution.

Special attention is placed on tracking. Full solid angle coverage for tracks with energies ranging from the beam energy to very low momenta is required for particle flow calorimetry and missing energy measurements. To preserve lepton identification and high performance calorimetry, a minimal material budget must be used for the tracking system.

Vertex detection is also critical when identifying heavy particle decay vertices and measuring the invariant mass of their charged decay products which tags their flavor. The Higgs branching fractions is measured using this latter feature. Improving the point resolution per measurement, minimizing the beam pipe radius and reducing the thickness of the detector sensors and supports can result in significant enhancements to the flavor tagging efficiency. Also, vertex detection plays an important role in tracking. Multi-layer vertex detectors provide efficient stand-alone pattern recognition and even momentum measurement, which may well be essential in measuring soft tracks. [87]

The design of the vertex detector is affected also by the accelerator background environment. High backgrounds are produced when colliding nanometer sized beams at high luminosity which hit the vertex detector. One of the topics the vertex physics offers is the measurement of the Higgs Branching Fractions, and their dependence on vertex detector resolution. For the relatively low mass Higgs, the dependence of Higgs couplings on mass, which will point to the model which describes best the Higgs behavior, will be possible to study by using precision measurements of the branching fraction. Some studies have been performed in order to improve the spacial resolution and to vary the radius of the innermost layer (and hence the beam pipe radius). They showed that reducing by half the inner radius (from 2.4 cm to 1.2 cm) the errors on branching fractions are reduced by approx. 10% [87].

### **7.3.3 The ILD concept**

The ILD detector [83], depicted in Figure 7.3.1 a), is a complex system of sub-detectors, each with a precise task:

- The vertex detector, VTX, is a multi-layer pixel detector and will record the primary collisions at the interaction point (IP)
- A system of strip and pixel detectors cover the gap between VTX and the TPC

- A tracking system composed of a Time Projection Chamber, TPC, able to provide up to 224 points per track
- A system of Si-strip detectors to improve the track spacial coordinates
- The calorimeter system composed of highly segmented electromagnetic, ECAL, and hadronic, HCAL, calorimeters to identify charged leptons, hadrons and photons
- The very forward region composed of high precision, radiation hard calorimeters to extend the detector acceptance down to about 4 mrad. They provide fast luminosity measurements, fast reading of beam parameters and assist the beam tuning
- The calorimeters are imersed into a superconducting coil which generates an axial magnetic field of 3.5 T
- Iron yoke to return the magnetic flux and play the role of muon detector
- Data acquisition system (DAQ)

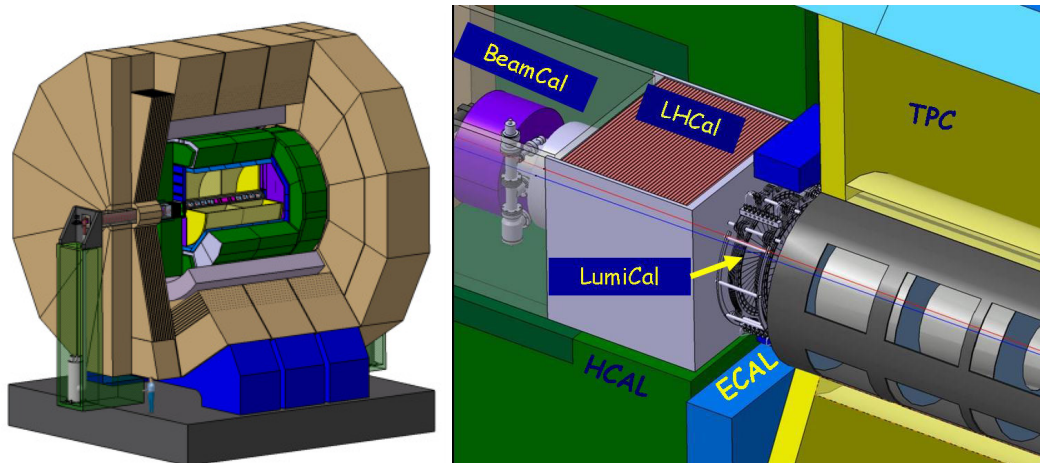


Figure 7.3.1 a) ILD baseline design b) Very forward region design [83]

### 7.3.4 Very forward region

Three calorimeters are planned in the very forward region of a detector concept proposed for ILC and CLIC. BeamCal, adjacent to the beam pipe, LumiCal covering larger polar angles, are electromagnetic calorimeters and GamCal located at 100 m from the interaction point with the role of aiding beam tuning. There is also LHCAL, a hadron calorimeter covering almost the same polar range as LumiCal, which shields the inner detector, and a position monitor placed in front of BeamCal. Also, the last quadrupole magnet, QD0, of the Beam Delivery System (BDS) extends into the very forward region. Its role is to transport and de-magnify the beams in order to bring them into collision and then carry out the spent beams. A schematic view of the Very Forward Region is shown in Figure 7.3.1.1, b) [83]

The calorimeters have several functions. All of them improve the hermeticity of the detector, which is important for new particle searches and jet energy resolution, and they shield the central detectors from backscattered particles. [88]

Due to the large charge and small bunch size, crossing bunches generate beamstrahlung photons which convert to electrons and positrons. They are deflected by the bunch charge and cause large depositions in BeamCal. These depositions allow the use of BeamCal for a fast luminosity determination and a fast tuning of the beam parameters. [89]

LumiCal is the luminometer of the detector. The physics program requires luminosity measurements with accuracies better than  $10^{-3}$ . [90]

All three calorimeters are supported by a tungsten tube. The latter also contains the last quadrupole of the beam delivery system. This structure allows one to move the HCAL and ECAL endcaps backwards in order to dismantle the detector or access the tracking subdetectors. Between LumiCal and ECAL a gap of a few cm is foreseen for readout and power cables of the inner silicon tracker and some readout electronics of the LumiCal. This gap is fully covered by HCAL. The impact of this gap on the electromagnetic shower reconstruction performance is expected to be negligible. The front-face of LumiCal might be covered by a few layers of silicon pixel detectors in order to measure track segments of charged particles just before they enter the calorimeter. The track will be helpful to understand the systematics of the shower position reconstruction. In addition, low energy charged particles will not be lost.

BeamCal is strongly affected by electrons and positrons originating from beamstrahlung photon conversion. These deposits result in a high integrated dose for sensors near the beam pipe. Hence, radiation hard sensors must be used. BeamCal's purpose is to identify high energy electrons at small polar angles in order to veto two photon events which are a serious background in many new particle search channels. [91]

To identify the localised deposits from high-energy electrons on top of a broader spread of energy from beamstrahlung, a fine granulated and compact calorimeter is necessary. Since beamstrahlung remnants cause a very large occupancy per bunch crossing, the signals of all sensors must be readout or stored after each bunch crossing. [92]

The distribution of energy depositions caused by beamstrahlung allows a very precise determination of bunch parameters. To assist the beam tuning within a bunch train, the signals of at least a few sensor planes of the BeamCal must be readout and processed within about a

microsecond. LumiCal will be used to count Bhabha events,  $e+e- \rightarrow e+e-(\gamma)$ , in a predetermined range of polar angles. A precise spatial and energy reconstruction of the electromagnetic showers is essential. Detailed Monte Carlo simulations have shown that very compact diamond-tungsten or silicon-tungsten sandwich calorimeters would have the performance required to match all the above requirements. Sensor layers are interspersed between tungsten disks with a thickness of about one radiation length separated by a gap of approx. 1 mm to accommodate readout circuits [83].

### 7.3.5 BeamCal detector

BeamCal, one of the three detectors of the very forward region of the detectors at the ILC and CLIC, is a compact electromagnetic calorimeter using tungsten as absorber and a radiation hard sensor material as the sensitive layer (Figure 7.3.5.1). Sensors used for BeamCal have to withstand very high levels of total ionizing dose. Artificial diamond, radiation hard silicon, SiC and GaAs sensors are under consideration. [93]

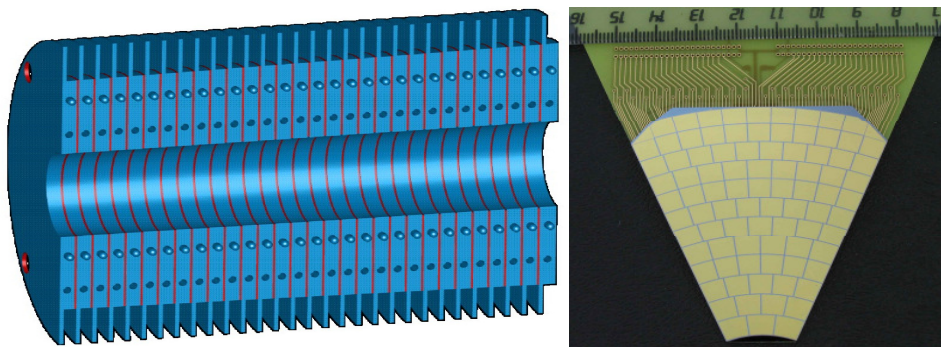


Figure 7.3.5.1 a) The sandwich-like structure of BeamCal calorimeter, the absorber layers, in blue, alternate with diamond sensor layers, in red, b) A sample of one segment of a sensor layer in BeamCal. It is longitudinally segmented into 17 rings and each ring is divided into pads of approx.  $5 \times 5 \text{ mm}^2$

BeamCal is a sandwich electromagnetic calorimeter of 30 alternating absorber (3.5 mm thick) and sensor layers (~0.5 mm thick). The sensor layer includes a segmented sensor and a readout plane which routes the interconnection lines from the segments to the outer radius of the BeamCal, where the readout electronics will be placed. Located at approx. 3500 mm from the IP and with an inner radius of 20 mm and an outer radius of 150 mm it extends the detector acceptance down to 5 mrad and up to 40 mrad. BeamCal will give a fast feedback signal for bunch-by-bunch luminosity measurements and beam parameters tuning.

An important characteristic of BeamCal's sensors is to provide the linearity of the response over at least four orders of magnitude of particle fluences. This arises due to the task

of efficiently veto-ing signals of single high energetic particles (e.g. electrons) in the acceptance region of BeamCal on top of the high amount of background from beamstrahlung pairs. *The energy deposition is strongly dependent on the detector geometry and magnetic field.*[89]

The FCAL (Forward Calorimetry) Collaboration [24] investigates several materials as possible sensors for BeamCal. Requirements are:

- radiation hardness against very high ionizing doses
- a linearity of the response over at least 4 orders of magnitude of particle fluences
- no additional cooling or other support to keep the required compactness of BeamCal.

Chemical Vapor Deposited (CVD) diamond is such a material. It is under investigation since several years and is very radiation hard. The samples are  $\sim 1 \text{ cm}^2$  size and typically 300 - 500  $\mu\text{m}$  thick. It was possible to show, in a high dose irradiation test beam, that after 7 MGy of absorbed total ionizing dose from a 10 MeV electron beam, the sensors were still operational. [94]

Another material taken under consideration is gallium arsenide, GaAs, a semiconducting material with a band gap of about 1.42 eV, which is very radiation hard. Properties of some sensor prototypes with a realistic BeamCal shape, featuring 88 pads of about  $5 \times 5 \text{ mm}^2$  size and a thickness of 500  $\mu\text{m}$  have been studied. The segmentation of the material is done by a metallization in the desired structure, the same procedure as used for diamond sensors. GaAs samples show a significant decrease of their response after about 1 MGy. First tests using radiation hard silicon show that additional measures, like e.g. cooling, have to be considered to operate the sensors in doses of 100 kGy and beyond. [95]

A graphite layer is placed in front of BeamCal, which serves as a low Z absorber to prevent backscattering of charged particles. This absorber is of course missing in the region of the beam pipe for the outgoing beam. Pair particles hitting the inner surface of this hole can scatter back into the tracking region. Low energetic charged particles curl up in the magnetic field and therefore follow the field lines which guide these particles into the innermost layer of the vertex detector producing some azimuthal hit distributions. Careful tuning of the magnetic field might prevent this effect. [95]

# 8. Software details

## 8.1 Introduction

As both accelerators are still at the proposal-phase level, tests are being asiduously conducted in order to establish the best technologies which are going to be pursued, the materials which are going to perform best in the given conditions and, not last, the cost effective choices. Prototypes of sub-detectors or sensitive materials and electronic devices are being tested in beam-test facilities to investigate performances and to develop new technologies, if needed, to withstand the extreme conditions of a powerful future linear collider. Even so, prior to any prototyping, preliminary studies are needed in order to determine the energy scale of the phenomena involved, to better understand the physics phenomena at the tera-scale as well as to establish the conditions in which the detectors are required to perform in order to reach the proposed physics goals.

All these tasks are performed through complex simulation softwares able to describe in great detail the detectors, the primary collisions, interactions of particles with the detector's materials and the response of the detectors. A more detailed description of all the intermediary steps between the simulation of the primary collision and the offline analysis of events is given in Chapter 3 of this thesis. Here, the software framework adopted by both ILC and CLIC communities in what concerns the detector simulation is presented.

## 8.2 Event generator: GuineaPig

The electron-positron interaction is simulated with Guinea-Pig event generator [91].

Under very strong electro-magnetic field together with the high beam energy the synchrotron radiation in the beam-beam field, called beamstrahlung, becomes very energetic. The strong field can even create electron-positron pairs from the beamstrahlung photons. During the collision, the bunches are deformed by the electromagnetic attraction between the electron and positron beams, resulting in luminosity enhancement. Because of the high energy and high beam-beam field, a large amount of energy is expected to be deposited in the form of synchrotron radiation, which, in the case of the beam-beam interaction is called beamstrahlung. Also, it has been recognized that the  $e^+e^-$  pair creation process is a significant source of background for the experiments. [92][93]

Beamsstrahlung can be produced through many physical phenomena; among them Guinea-Pig includes the pinch effect, beamstrahlung, pair creation and the calculation of hadronic backgrounds. The Pinch Effect is the process of two bunches focusing on each other at the interaction point. Because the trajectories of the particles are bent, due to the pinch effect, they emit a radiation called beamstrahlung. This leads to energy losses both in the  $e^+$  and  $e^-$  beams.[91]

### *Electron-Positron Pair Creation*

In a beam-beam interaction, there are two ways of creating pairs: the coherent and incoherent processes. Coherent pair production consists in photon conversions into a virtual electron-positron loop. Incoherent pair production starts from the fact that two colliding real beamstrahlung photons can produce an  $e^+e^-$  pair. This is coupled with the fact that an electron (or positron) is accompanied by a spectrum of virtual photons which can produce pairs with the real or virtual photons of the other beam as well. There are three incoherent processes in total. [91]

Breit-Wheeler process:

$$\gamma\gamma \rightarrow e^+e^- \quad \text{- both photons are real}$$

Bethe-Heitler process:

$$e\gamma \rightarrow ee^+e^- \quad \text{- one is real and one is virtual}$$

Landau-Lifshitz:

$$ee \rightarrow eee^+e^- \quad \text{both photons are virtual}$$

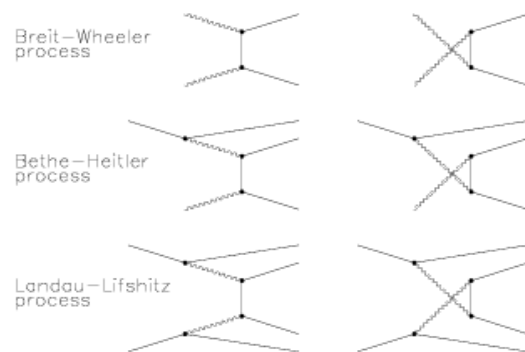


Figure 8.2.1. Incoherent processes which contribute to electron-positron pair creation

### *Coherent pair creation*

The probability per unit length for a photon with energy  $h\omega$  to turn into an  $e^+e^-$  pair in a magnetic field,  $B$ , is given by:  $\frac{d\omega}{dz} = \frac{\alpha^2}{r_c} \frac{B}{B_c} T(\kappa)$ , with  $B_c = m^2 c^2 / (e\hbar)$  and  $\kappa = \frac{\hbar\omega}{mc^2} \frac{B}{B_c}$ .

### *The incoherent pair creation*

The differential cross section for the Breit-Wheeler process [96]:

$$\frac{d\sigma}{dt} = \frac{2\pi\alpha^2 m^2}{s^2} \left[ \left( \frac{t-m^2}{u-m^2} + \frac{u-m^2}{t-m^2} \right) - 4 \left( \frac{m^2}{t-m^2} + \frac{m^2}{u-m^2} \right) - 4 \left( \frac{m^2}{t-m^2} + \frac{m^2}{u-m^2} \right)^2 \right] \quad \text{Eq. 8.1}$$

$s$ ,  $t$  and  $u$  are the Madelstam variables.

The total cross section for the Bethe-Heitler process is approximately given by [96]:

$$\sigma_{BH} = \frac{28\alpha r_e^2}{9} \left( \ln \frac{s}{m^2} - \frac{109}{42} \right) \quad \text{Eq. 8.2}$$

For the Landau-Lifshitz process the total cross section is given by [96]:

$$\sigma_{LL} = \frac{\alpha^2 r_e^2}{\pi} \left( \frac{28}{27} \ln^3 \frac{s}{m^2} - 6.59 \ln^2 \frac{s}{m^2} - 11.8 \ln \frac{s}{m^2} + 104 \right) \quad \text{Eq. 8.3}$$

The simulation of the collision with GUINEA-PIG results in an ASCII file containing the energy of the particle (e+ or e-), the momentum, the position, the process ID (0 - Breit-Wheeler, 1 - Bethe-Heitler and 2 - Landau-Lifshitz) and the particle label. This file can be transformed either into a root file and used as an input file for the fast stand-alone BeamCal simulation, the Geant4 application - BeCaS, or into a HEPEvt file and used as input for the general software framework, Mokka, which is basically a database of detector models for a future linear collider.

## 8.3. Detector simulation: BeCaS and Mokka

### BeCaS

BeCaS [97] is a stand-alone Geant4 application for fast simulation results regarding one of the sub-detectors of the Very Forward Region, BeamCal. It describes in detail the geometry of BeamCal as well as the passing of particles through the detector's material and it is used to obtain a fast estimation of the background levels produced by secondary electron-positron pairs which are a byproduct of the primary interaction. Other components of the Very Forward region are also implemented but only as simple blocks of material, e.g. the beam-pipe, LumiCal, QD0 or the iron support tube for BeamCal.

BeCaS consists in a group of classes which describe the absorber and sensor layers, the detector geometry, the environment surrounding the detector, the materials used for BeamCal or the magnetic field in which BeamCal is placed. Special classes are created to manipulate the information regarding events, tracks or steps. Some of the parameters used in the simulation can be controlled through a steering file, such as the distance from IP to BeamCal center, the

crossing angle (four options available: 0, 2, 14 and 20 mrad), or an option to store the energy of tracks or the magnetic field type and value can also be set. [97]

BeCaS takes as input a ROOT tree containing the kinematic parameters of pre-generated particles. The format of the tree must contain the following information: the energy of the particle, the direction, given by the momentum of the particle on X, Y and Z axes and the position of the particle, also on X, Y and Z, in this exact order. The output generated by BeCaS is also a ROOT file which is interpreted through the ROOT framework for offline analysis. [97]

## **Mokka**

Mokka [98] is a Geant4-based [99] application which is intended to be the general software framework used at a future linear collider for the simulation of detector geometries and detector response. Being a geometry data driven software, the user can build its own detector model based on an existing model, add to an existing model or use the available geometry database. [100]

There are four basic constituents for creating a new geometry model:

- **Drivers:** pieces of C++ code through which sub-detector components are described. Dimensions, relative positions and sensitive volumes are defined through the driver
- **Databases:** MySQL geometry database located on the central (or local) MySQL server
- **Subdetectors:** it is a combination between drivers and databases: a certain driver is invoked and told to connect to a certain database.
- **Models:** a set of subdetectors. All of them form a detector geometry.

There is also the notion of “**superdrivers**” needed to make the transition from static libraries to scalable geometries (one of the great advantages of Mokka framework). A superdriver reads the relevant global geometry parameters and creates a “temporary” faked database, similar to the usual static database, then invokes its subdriver and passes to it the name of the temporary database. [101]

The implementation of new sub-detectors is realized by adding a new Mokka driver to a chosen model. Run control and run conditions can be changed at run time through a steering file, interactive dialogue or macro files. Being a Geant4 application it can interpret the commonly used HEPEvt (High Energy Physics Events) input files. As output it generates either ASCII files or the widely accepted LCIO (Linear Collider Input/Output) with the aim of establishing a standard European format for simulation applications. An agreement has been reached between scientific communities working independently on developing software applications for future linear

accelerators that a common framework should be used to facilitate information exchange, data persistency or trustworthy comparison of models and results. [101]

### **Marlin and ROOT**

Events generated by Mokka software are interpreted by a C++ application framework, Marlin (Modular Analysis and Reconstruction for the LINear collider) [102] through plug-in modules named processors. Each processing command is implemented as a processor or plug-in module which analyzes the LCIO files and creates output collections for each event. These events can then be stored into a ROOT file. The definition of processors and the order in which they are executed is done through a steering file. [102]

Another package, MarlinReco [102], performs the event reconstruction making use of its modules for digitisation, flavour tagging, track finding and fitting or particle flow reconstruction. Track finding and fitting is accomplished through Kalman Filter techniques, first developed for the experiments at LEP. The list can continue, as there are cases when simulation softwares performing the same task are being developed in parallel, or software frameworks performing more specific tasks and cases where fast stand-alone softwares codes are required to fulfill the user's needs.

The offline analysis is accomplished through the ROOT analysis framework. [103]

# 9. BeamCal studies

## 9.1 Introduction

Due to the very small beam sizes and high beam intensity at the ILC and CLIC crossing bunches generate beamstrahlung, photon emission from the beams under the electrical influence of the opposing beam. Beamstrahlung photons are emitted under a very low angle, less than one mrad, but a fraction of the photons can convert into electron-positron pairs which can be deflected by the bunch charge and cause large depositions in BeamCal. These depositions allow the use of BeamCal for a fast luminosity but they result in a high integrated dose for sensors near the beam pipe. Consequently, sensors used for BeamCal must be designed to withstand very high levels of ionizing dose.

In this environment, BeamCal must shield the Inner Detector against backscattering from beamstrahlung pairs while efficiently detecting single high energetic particles at lowest polar angles. The identification of high energy electrons at small polar angles is necessary to veto two photon events. The latter are a serious background in many new particle search channels.

The distribution of the depositions from beamstrahlung potentially allows a very precise determination of bunch parameters. To assist the beam tuning within a bunch train the signals of at least a few sensor planes of the BeamCal must be readout and processed within about a  $\mu\text{s}$ .

In the following chapters the electromagnetic shower shape has been investigated and the background levels have been estimated down to the sensor cell level for one year of operation of the ILC accelerator as well as bunch-by-bunch fluctuations of energy depositions.

Another issue which needs to be addressed is related to neutron fluxes. High energetic interactions will also give birth to neutrons which will damage the detector and the electronic devices. For this purpose, the geometry of the detector described in the stand-alone simulation of BeamCal, BeCaS, has been updated so that it includes the front-end electronics and the iron support tube around BeamCal.

And then, there is also the case of magnetic field configuration. When the ILC beam enters the field of the 3.5 T solenoid of the ILD detector, under a 20 mrad crossing angle, it encounters a vertical orbit change which results in the emittance of synchrotron radiation and with that in a significant deterioration of the vertical beam emittance. Recently a correction

for this effect has been suggested which relies on a local correction scheme, using antisolenoids and a special dipole coil arrangement incorporated into the detector solenoid (Detector Integrated Dipole, DID). The DID adds a horizontal component to the field of the detector solenoid. The DID is designed for the integrated field seen by the incoming beam to be parallel to the beam direction. One alternative in the ILC baseline design is an intermediate crossing angle of  $\sim 14$  mrad. In that case the DID might not be needed or could even be used in reverse polarity (Anti-DID). In that case the integral magnetic field is not parallel to the incoming but to the outgoing beam. [83]

The DID and Anti-DID magnetic field configurations have a twofold influence on the tracking detectors: background levels and magnetic field homogeneity. For this reason, the possibility of finding a solution which would not include additional magnetic fields is somewhat favored. In this context, using the Mokka software framework, background levels in BeamCal have been estimated [104] [110] for different magnetic field configurations.

In summary, the following chapters include studies on the electromagnetic and neutron background levels in BeamCal at the ILC which are estimated [95][105][106][107][108] using either a stand-alone simulation of BeamCal, BeCaS, or the general simulation of the ILD detector concept, Mokka [109]. The impact of different magnetic fields on BeamCal is also presented [110].

## **9.2 BeamCal results in Becas and Mokka**

### ***9.2.1 Electromagnetic shower***

BeamCal geometry simulation and the detector's response have been performed using two different Geant4 applications, BeCaS and Mokka. The electron positron interaction and e+e- background generation is done with Guinea-Pig event generator used with the nominal set of ILC accelerator parameters presented in Table 7.2.1 [79] at an energy of 250 GeV/beam and a 14 mrad crossing angle geometry configuration. The electromagnetic and neutron background levels have been investigated using both configurations and a comparison of the results is performed.

BeCaS has been designed for the geometry proposed for the LDC [111][112] detector concept where BeamCal is positioned at 3650 mm from the interaction point, IP, while Mokka geometry describes the ILD detector concept where BeamCal is moved closer to the IP at 3535

mm. For the consistency of the comparison, BeamCal has been relocated in Mokka configuration to the original position, the new scenario is referred to as Mokka BC (Becas Configuration).

Mokka studies have been performed using a new BeamCal driver [113], BeamCal01, which was included into the ILD\_00fwp01 Mokka model. A Marlin processor has been written in order to convert lcio to root files and create the event collections. Many of the geometry parameters can be modified through a steering file; the complete list is given below:

<b>-- Parameter name</b>	<b>Description</b>	<b>, Default value</b>
('BCal_TubeIncomingRadius'	, 'Radius of the incoming beampipe in mm'	, '15') ,
('BCal_rInner'	, 'Inner Radius (outgoing Beampipe) in mm'	, '20') ,
('BCal_rOuter'	, 'Outer Radius in mm'	, '150') ,
('BCal_nLayers'	, 'Number of Layers'	, '30') ,
('BCal_PairMonitor'	, 'Turn PairMonitor On(1) or Off(0)'	, '1') ,
('BCal_dAbsorber'	, 'Absorber Thickness in mm'	, '3.5') ,
('BCal_dGraphite'	, 'Graphite thickness in mm'	, '100') ,
('BCal_SpanningPhi'	, 'Spanning Angle of Full BeamCal in degrees'	, '320') ,
('BCal_rSegmentation'	, 'Size of Radial Segmentation'	, '8') ,
('BCal_nWafers'	, 'Number of wafers'	, '8') ,
('LHcal_BCal_clearance'	, 'Distance between LHcal_zend and BeamCal start'	, '390');

The distribution of the electromagnetic shower shape is presented in Figure 9.2.2 a) and b) for BeCaS and Mokka BC configurations, respectively. The  $e^+e^-$  energy deposition per bunch-crossing, BX, along the calorimeter depth (layer number) shows approximately 1.5 times higher background levels in BeCaS and a shift of the maximum of the shower deeper into the detector which can be the effect of the more detailed description of the components located between the interaction point and BeamCal in the Mokka framework as well as the fact that the magnetic field in BeCaS configuration is 4 T. The shower shape in Mokka BC geometry is then compared with the ILD Default Configuration, DC, the scenario Mokka DC, represented in Figure 9.2.3 a) and b). The energy deposition is represented as a function of the position of the sensor layer on the z axis, to clearly demonstrate the fact that BeamCal has been moved closer to the IP. The plots are a clear evidence of the fact that moving BeamCal forward on the z axis does not affect the background levels in this calorimeter. The geometry parameters in Mokka BC and Mokka DC configurations are summarized in Table 9.2.1. A schematic representation of BeamCal is given in Figure 9.2.1.

Variable	Mokka Becas Configuration	Mokka Default Configuration
Z position from IP	3650 mm	3535 mm
Graphite layer thickness	50mm	100 mm
Position from LHcal_zend	505 mm	390 mm

Table 9.2.1 Geometry parameters in Mokka BC and Mokka DC configurations

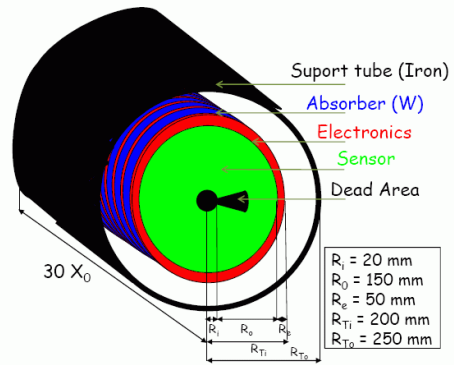


Figure 9.2.1 BeamCal schematic representation

Knowing the energy deposition, the number of bunch crossings per year,  $N_B=3 \times 10^{11} \text{BX/yr}$  and the characteristics of the material (dimensions, composition, mass) the absorbed radiation dose,  $dE/dm$  can be calculated. In Figure 9.2.4 a) and b) each bin of the histograms represents the absorbed dose in one ring of the sensor where the maximum of the shower is located. The highest background is recorded in the rings closest to the beam pipe in both geometry configurations but again the radiation dose is twice as large with Becas in the first rings of the sensor although a decrease of five orders of magnitude in the radial distribution of the electromagnetic dose is recorded in Becas while the dose decreases by only two orders of magnitude from  $r=20 \text{ mm}$  to  $r=150 \text{ mm}$  in Mokka. These simulation studies show that approximately 0.5 MGy/yr is expected in the innermost ring of the calorimeter [95], based on BeCaS studies and approx. 0.2 MGy/yr, based on Mokka simulations [110].

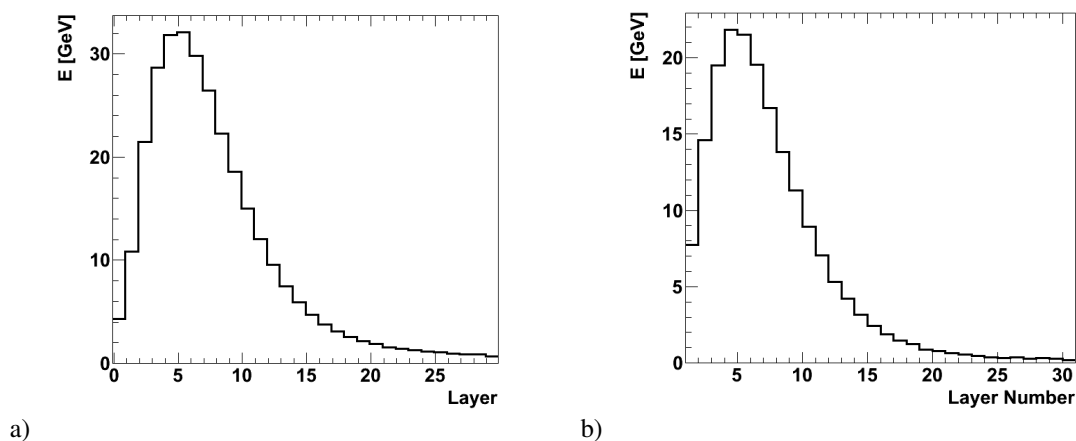
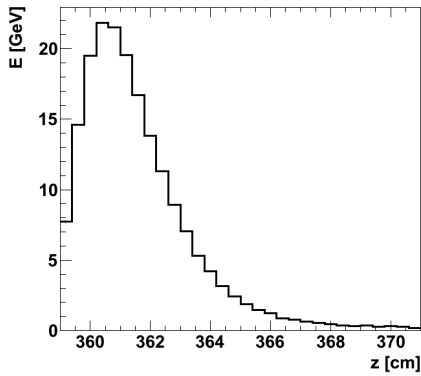
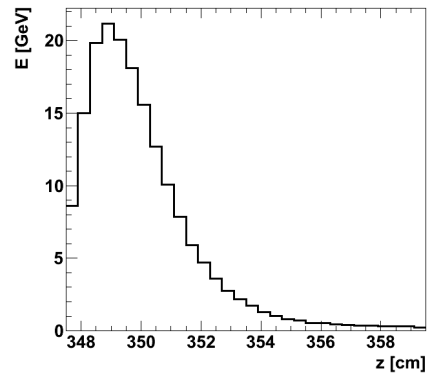


Figure 9.2.2 Energy deposition vs. calorimeter depth a)Becas configuration, b) Mokka BC configuration c)

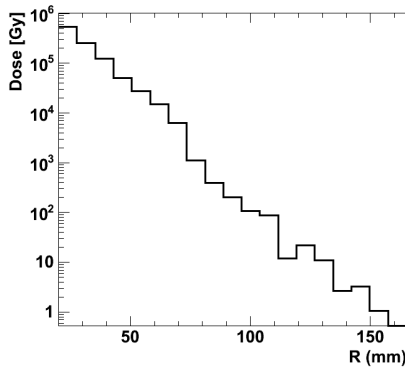


a)

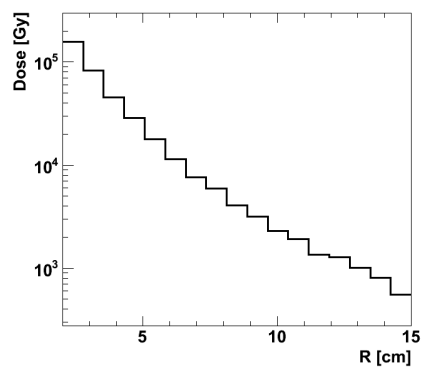


b)

Figure 9.2.3 Energy deposition vs. calorimeter depth a) Mokka BC configuration, b) Mokka DC configuration

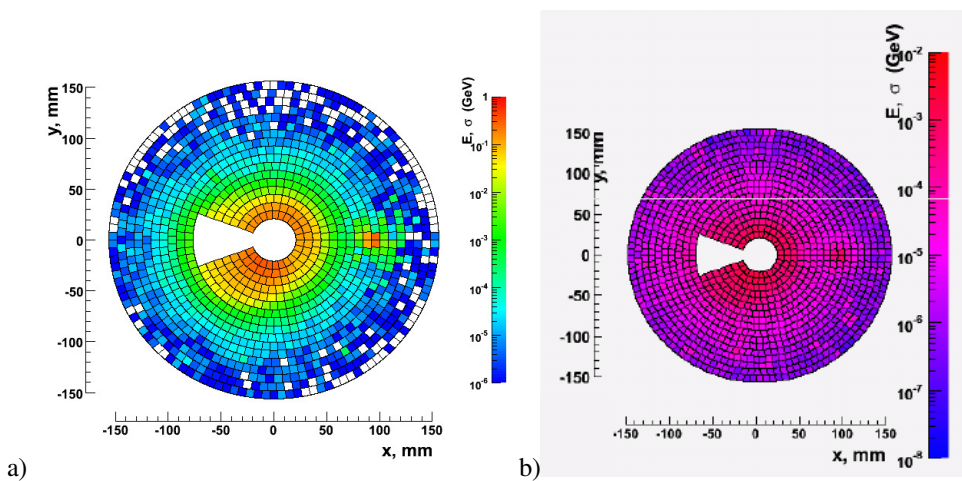


a)



b)

Figure 9.2.4 Radiation dose vs. sensor radius at shower maximum a) BeCaS configuration, layer 5, b) Mokka BC configuration, layer 4



a)

b)

Figure 9.2.5 Front view of a) energy depositions b) bunch-by-bunch energy fluctuations, in BeamCal due to high energetic electron superimposed over the  $e^+e^-$  background, based on BeCaS simulations, integrated over the whole length of BeamCal

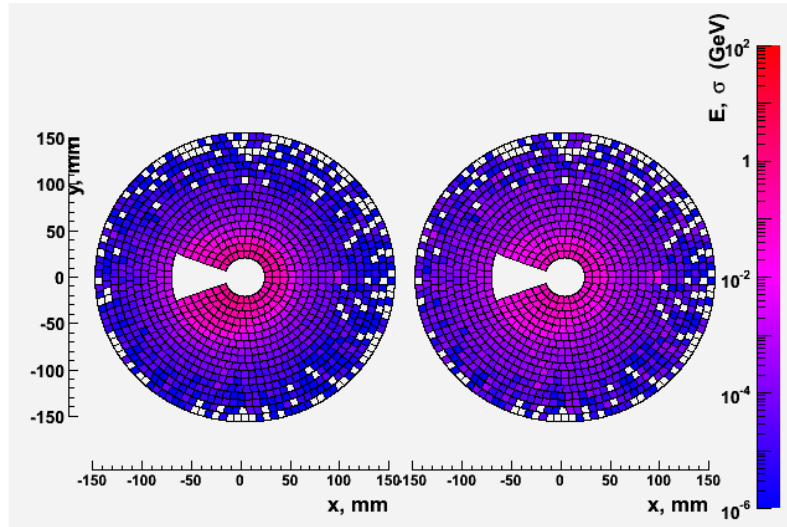


Figure 9.2.6 Front view of energy depositions, left, and bunch-by-bunch energy fluctuations, right, in BeamCal due to high energetic electron superimposed over the  $e^+e^-$  background, based on BeCaS simulations, at the maximum of the shower, layer 5; 40 BX are summed in the energy deposition plot

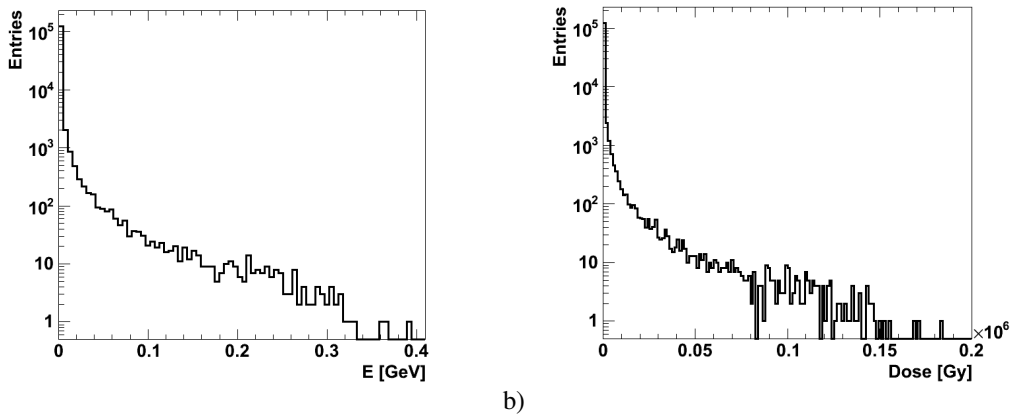


Figure 9.2.7 a) Energy deposition b) the absorbed dose per sensor cell ( $7 \times 7 \text{ mm}^2$ ) in BeamCal, based on Mokka simulation

As each cell of the sensor layer will be independently read, a statistics of the absorbed dose per cell is also required as well as the level of the fluctuations in energy depositions from bunch to bunch readings. For this purpose statistics corresponding to 40 bunch crossings has been generated with Guinea-Pig and the standard deviation has been evaluated as:

$$\sigma = \sqrt{\frac{1}{N} \sum_{i=1}^N E_i^2 - \bar{E}^2} \quad \text{Eq. 9.2.1}$$

where  $N$  is the number of bunch crossings, BX,  $E_i$  is the energy deposited in the  $i$ -th BX and  $\bar{E}$  is the mean energy deposition per BX, averaged over 40 BX

The energy deposition per cell and the bunch-by-bunch fluctuations of the energy depositions are represented in Figure 9.2.5 a) and b) respectively, using BeCaS. The

quantities represented in these figures are integrated over the whole length (sum of all sensor layer depositions) of BeamCal to get an idea of the overall distribution of backgrounds. In parallel, energy distributions and bunch-by-bunch fluctuations have been investigated for each individual sensor layer, Figure 9.2.6 shows the distributions for the 5<sup>th</sup> layer, where the maximum of the shower is located, and it was found that, at the cell level, the energy depositions are below 1 GeV near the beam pipe and go down to few keV in the outer regions of the sensor while the bunch-by-bunch fluctuations are of the order of a few MeV closest to the beam-pipe. This translates into bunch to bunch energy fluctuations of the background levels of approx. 1%.[107]

The distribution of the energy deposition per cell together with the corresponding radiation dose has been estimated also through the Mokka simulation. The energy deposition per cell per *bunch crossing* is represented in Figure 9.2.7 a). Based on this result, the absorbed dose per cell per *year* can be calculated, Figure 9.2.7 b). It is found that the radiation dose is expected to reach up to 0.2 MGy per cell over a period of one year of uninterrupted operation of the ILC accelerator. [109][110]

### **9.2.2 Neutron shower**

Neutrons are created during interactions of energetic  $e^+e^-$  background pairs with the materials of the detector. Neutron interactions at low energies, such as radiative capture, elastic and inelastic scattering and fission, are handled through physics lists. The QGSP\_BERT\_HP [99] physics list is used for the simulation studies presented in this thesis. It makes use of high precision neutron models based on the intranuclear cascade (INC) model developed by Bertini. The target nucleus is modeled as a three-region approximation to the continuously changing density distribution of nuclear matter within nuclei. The cascade begins when the incident particle strikes a nucleon in the target nucleus and produces secondary particles. The secondaries may in turn interact with other nucleons or be absorbed. The cascade ends when all particles, which are kinematically able to do so, escape the nucleus. At that point energy conservation is checked. Relativistic kinematics is applied throughout the cascade. Geant4 includes photonuclear and electronuclear reactions which convert the energy flow of electrons, positrons and photons into the energy flow of mesons, baryons and nuclear fragments. Parton string models for the simulation of high energy final states ( $E_{\text{CMS}} > 0(5 \text{ GeV})$ ) are also considered. Both diffractive string excitation and dual parton model or quark gluon string model are used. String decay is generally modeled using well established fragmentation functions.

Using BeCaS framework the neutron shower development along BeamCal has been investigated as well as neutron distributions in each of BeamCal's sensor layers [95][108]. Figure 9.2.8 a) shows the neutron shower shape with respect to the calorimeter depth. The distribution shows a wide maximum along several sensor layers, 10 to 14, where a neutron fluence of  $\sim 2 \times 10^{15}$  n/yr per layer is recorded. Figure 9.2.9 a) and b) shows the distribution of neutrons over the surface of different sensors. Two representative layers are given here, the sensor layer where the maximum of the electromagnetic shower is located and the sensor where the maximum of the neutron shower is located, respectively. These x-y representations of neutron distributions show that, similarly to the electromagnetic situation, the most affected areas are also those positioned in the close vicinity of the beam pipe. The binning of the histograms has been chosen such that a bin corresponds to an area of  $3 \times 3 \text{ mm}^2$ . Figure 9.2.9 a) and b) shows that a maximum neutron fluence of up to  $0.4 \times 10^{12}$  neutrons per  $\text{mm}^2$  and year is expected near the beam-pipe [95][108].

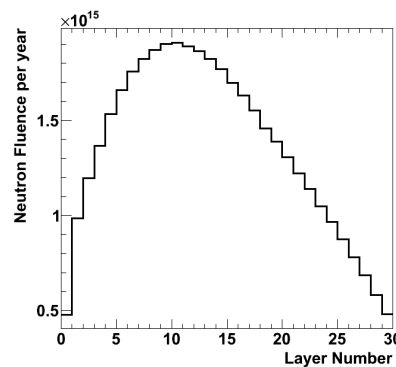


Figure 9.2.8 a) Neutron shower in BeamCal

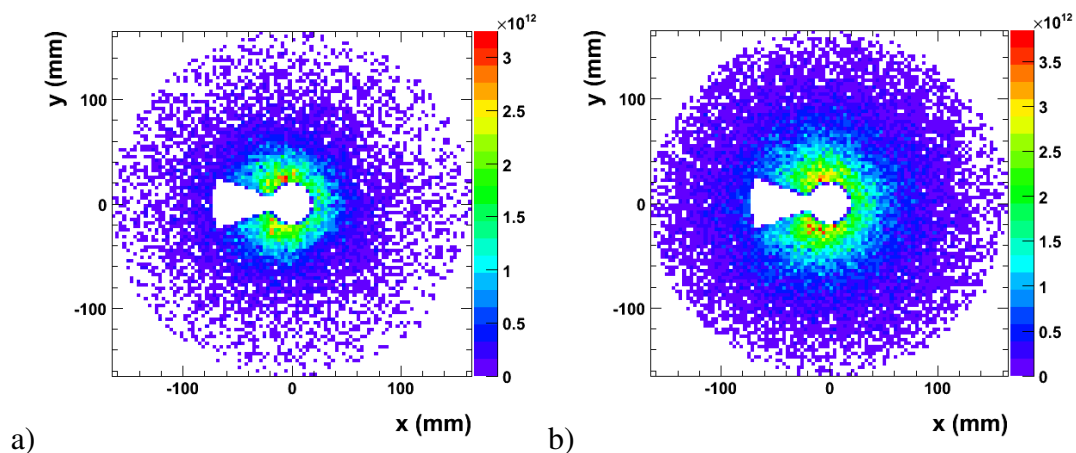


Figure 9.2.9 Neutron distribution over one sensor layer a) 5<sup>th</sup> layer, where the maximum of the electromagnetic shower is located, b) 10<sup>th</sup> layer, where the maximum of the neutron shower is located

### ***9.2.3 The effect of different magnetic fields on backgrounds in BeamCal***

At ILC all detector concepts propose a tracking system placed inside a magnetic field generated by a superconducting solenoid. In the following results regarding the ILD detector concept proposed for ILC are shown [110].

When the beam enters the 3.5 T magnetic field of the ILD detector solenoid, it encounters a vertical orbit change which results in the emittance of synchrotron radiation and with that in a significant deterioration of the vertical beam emittance. Special care must be taken for the design of the Very Forward region where high backgrounds are expected and which must be carried out of the detector while preserving the emittance and minimizing the pair disruption for the exiting beams. A correction for this effect has been suggested relying on a local correction scheme, using antisolenoids and a special dipole coil arrangement incorporated into the detector solenoid: Detector Integrated Dipole (DID or Anti-DID). The DID adds a horizontal component to the field of the detector solenoid and is seen by the incoming beam to be parallel to the beam direction. When an Anti-DID field is applied, the integral magnetic field is not parallel to the incoming but to the outgoing beam.

Backgrounds have been studied in detail for the TESLA detector taking into account all known background sources. It was found that the most important backgrounds stem from pair particles. [114]

In the following, the effect of different configurations of magnetic fields on the electromagnetic doses and neutron fluxes in BeamCal is presented [110], using the general software framework which is being developed for detector concepts at future  $e^+e^-$  linear colliders, Mokka, for the ILD detector concept. The studies presented here have been performed in a 14 mrad crossing angle geometry configuration.

The arguments for the necessity of this study rely on the fact that DID and Anti-DID magnetic field configurations have a twofold influence on the tracking detectors: background levels and magnetic field homogeneity. The reconstruction of particle tracks relies on the excellent knowledge of the magnetic field in the detector, which puts requirements on the precision of the mapping of the magnetic field. As a consequence, it is mandatory to investigate whether such a correction to the solenoid magnetic field results in any significant reduction of the background levels.

Using Mokka language (specific terms have been described in Chapter 8.3), the magnetic field is a special geometry driver detector which can be set or unset when building a detector model and which reads the field map from the given database. For the ILD detector concept the magnetic field is 3.5 T.

Three magnetic field maps have been used for these studies in Mokka framework. Results have been compared with the scenario where no magnetic field is applied. They are described in the Proceedings of the 18<sup>th</sup> FCAL Collaboration Workshop [110]. A comparison with similar results obtained with a stand-alone version of BeamCal simulation software, Becas, has also been performed; the results were published in [95] and [105].

The three magnetic field maps used for these studies are SField01, FieldX02 and FieldX03.

SField01 is a super field depending on the coil and yoke parameters with a field nominal value of 3.5 T. SField01 relies on the *field00* subdriver and belongs to a class of magnetic field maps simulated for the Tesla TDR. Field00 is characterized by a global magnetic field factor of 1.0, thus no scaling is applied to SField01.

The second magnetic field map is FieldX02. It belongs to the class of magnetic field maps designed for the LDC background studies. The novelty it introduces is that it can be used with detector geometries where crossing angles are present. As the LDC detector concept has been proposed with a solenoid field of 4 T, a global magnetic field factor of 0.875 is applied into the field tables.

FieldX03 is the third magnetic field option. This is a new driver for a magnetic field using a 2D field map for the solenoid field and a flat anti-DID as the correction field scaled such that low energetic particles drift from the IP into the outgoing beam pipe. FieldX03 is based on B field simulations for ILD. It also has a nominal value of 3.5 T and it is configured for crossing angle geometries, in this case for the ILC main crossing angle of 14 mrad. FieldX03 value at (0, 0, 0) position coordinates (at the origin) are (0, 9.55058e-07, 3.5) T.[100] [101]

The development of the electromagnetic shower along the calorimeter is shown in Figure 9.2.10 a) for the SField01 (red line), FieldX02 (green line) and FieldX03 (blue line) magnetic field configurations compared with the case when no field (black line) is applied. SField01 results in the highest background levels while the lowest background levels are obtained in the FieldX03 configuration. The ratio between background energy depositions induced by SField01 and FieldX03 indicate a factor 1.5 between simple solenoid field (SField) and 2D solenoid field

map with anti-DID (FieldX03) for most of the sensor layers of BeamCal and up to factor two at the backend of BeamCal, Figure 9.2.10 b).

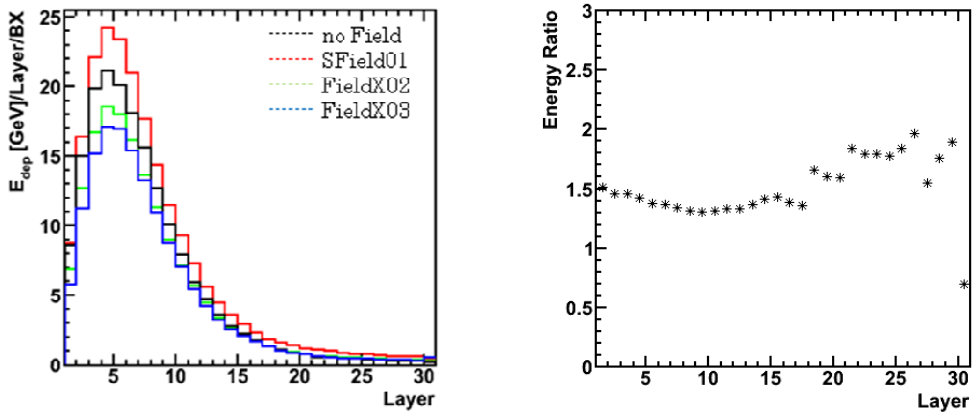


Figure 9.2.10 a) Energy deposition along BeamCal depth in different magnetic field configurations, b) Ratio between energy depositions induced by SField01 and FieldX03

Based on the evaluation of the energy deposition in each individual sensor cell, and knowing the volume of the cells, the electromagnetic dose can be calculated. The distribution of the absorbed dose is represented in Figure 9.2.11. The radiation dose absorbed in each cell is two times higher when using the simple solenoid field map as compared to the solenoid with anti-DID magnetic field. Knowing the number of bunch crossings (BX) per year,  $3 \times 10^{11}$  BX/yr, the maximum dose per cell can be estimated. We find  $\sim 0.21$  MGy/cell/yr for FieldX03 and  $\sim 0.42$  MGy/cell/yr for SField, in the extreme hypothesis that at every BX, the same cell will be loaded with the maximum dose. As previously shown, studies performed in the stand-alone Geant4 simulation software of BeamCal, BeCaS, have indicated that in the *innermost ring* (an array of  $\sim 20$  cells) of the calorimeter a dose of about 0.5 MGy/yr is expected [95] in a 4 T magnetic field.

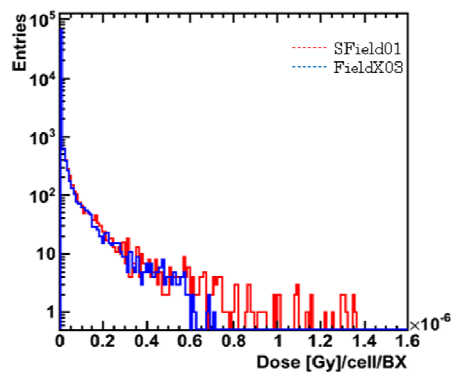


Figure 9.2.11 Dose per cell per BX, in different magnetic fields

The  $e^+e^-$  background pairs, as well as the bremsstrahlung photons, interact with the material of the calorimeter and produce another type of dangerous background: neutrons, which can damage the sensitive components of BeamCal. The neutron shower shape has been investigated for all magnetic field configurations, depicted in Figure 9.2.12 a) for a period of one year of accelerator operation. A factor 1.7 more neutrons are produced in the SField01 configuration compared to the FieldX03 field map, which is understandable with the  $e^+e^-$  pairs being the main source of neutron background. A deeper and not as flat neutron shower maximum is observed for FieldX02. Compared to BeCaS results, although the neutron fluences per layer are comparable, a strong shift of the neutron maximum shower is observed. BeCaS studies have indicated a maximum located deeper into the calorimeter, along several sensor layers (layers 10 to 14) in the conditions of a 4 T magnetic field, while Mokka studies, using a 3.5 T magnetic field, show that the shower maximum reaches the maximum after only 5 radiation lengths (the fifth sensor layer) but in this case also the maximum is scattered across several layers.

The neutron fluence per cell per year is represented in Figure 9.2.12 b). Knowing the number of bunch crossings per year and the surface of the cells a maximum of  $\sim 4.6 \times 10^{11}$  n/mm<sup>2</sup>/yr is being generated in a simple solenoid field and  $\sim 2.6 \times 10^{11}$  n/mm<sup>2</sup>/yr in a solenoid corrected with an anti-DID magnetic field. As a comparison, a neutron fluence of  $0.4 \times 10^{12}$  neutrons per mm<sup>2</sup> and year is estimated near the beam-pipe when using BeCaS [95].

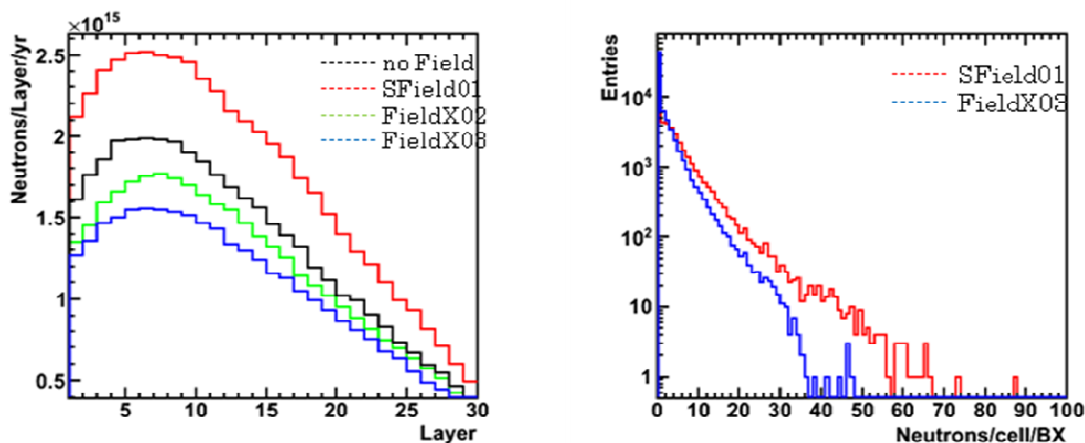


Figure 9.2.12 a) Neutrons per layer per year, in different magnetic fields b) Neutrons per cell per BX, in different magnetic fields

## 9.3 Conclusions

Electromagnetic and neutron showers have been investigated for one of the detector components placed in the Very Forward Region of the ILD detector concept proposed for ILC. The electromagnetic radiation dose and neutron fluxes have been estimated using two different simulation algorithms, a stand alone simulation of BeamCal, BeCaS, and the second one, the simulation of BeamCal in the context of the whole ILD detector concept, Mokka. It was found that the results given by the two detector simulation algorithms are comparable. With BeCaS, a radiation dose of  $\sim 0.5$  MGy/yr is found in the ring of cells placed right around the beam pipe ( $\sim 20$  individual cells) and a maximum dose of  $\sim 0.2 \cdot 10^6$  Gy/yr is estimated by Mokka for a single individual cell.

Electromagnetic energy deposition in BeamCal has been investigated and the radiation dose has been evaluated using also different configurations of magnetic fields. A factor 1.5-2 between energy depositions in simple solenoid magnetic field and 2D solenoid field map with anti-DID has been observed. We find a radiation dose of  $\sim 0.21$  MGy/cell/yr for a 2D solenoid field map with anti-DID and  $\sim 0.42$  MGy/cell/yr in simple solenoid magnetic field.

Almost 2 times more neutrons are produced in the simple solenoid magnetic field than in the solenoid corrected with the anti-DID and a neutron fluence of  $\sim 2.6 \cdot 10^{11}$  n/mm<sup>2</sup>/yr (FieldX03) and  $\sim 4.6 \cdot 10^{11}$  n/mm<sup>2</sup>/yr (SField01) is estimated. The results are in good agreement with the results obtained previously using the stand-alone simulation algorithm for BeamCal [105].

Results presented in this chapter are published in two ISI journals, *JINST* 5 P12002 [95], 2010 and *Rom. J. Phys*, vol. 55, no. 7-8, (2010)687-707 [105] and in extenso in the Proceedings of the 18<sup>th</sup> FCAL Collaboration Workshop, 2011, ISBN: 978-973-0-11117-0, pag 70-74.[110] and presented in many collaboration meetings and international workshops.[106-110]

# 10. QD0 at CLIC

## 10.1 Introduction

Background levels expected at CLIC represent one of the main issues to be considered for the design of the detectors proposed at this future linear collider. There are two main background sources, one due to interactions occurring in the beam (parallel muons produced in the beam halo or neutrons from the spent beam) and another due to beam-beam interactions such as  $e^+e^-$  pair production and hadron production in gamma-gamma processes. Beam dynamics near the interaction point also puts constraints on the detector design while the strength of the interaction between the beams and the solenoidal magnetic field of the detector limits the intensity of the magnetic field which can be used.

In this context, the simulation software of a detector model adapted for CLIC has been updated. A new component of the Very Forward Region, the final focus quadrupole magnet, QD0, has been implemented in the Geant4-based simulation software Mokka and the electromagnetic and neutron dose onto the QD0 in the CLIC interaction region have been estimated.

## 10.2 Very Forward Region at CLIC\_ILD

The very forward region of the CLIC\_ILD detector concept (see Figure 10.2.1) consists of components very close to the beam-pipe, most importantly the LumiCal and BeamCal calorimeters and the last quadrupole magnet QD0.

Compared to the ILC\_ILD detector concept, the detectors placed in the Very Forward Region of the CLIC\_ILD are mainly longer and brought closer to the Interaction Point. LumiCal is a sandwich calorimeter composed of 40 alternating layers of silicon and tungsten (there are 30 layers for LumiCal@ILC), centered on the outgoing beam axis and with an inner radius of 10 cm. BeamCal is also a 40 layer sandwich calorimeter centered on the outgoing beam pipe, at 2.8-m from the Interaction Point (IP). Designed with an inner radius of 3.2 cm (11 mrad) and an outer radius of 15 cm, BeamCal provides an angular coverage from 11 to 47 mrad. [86]

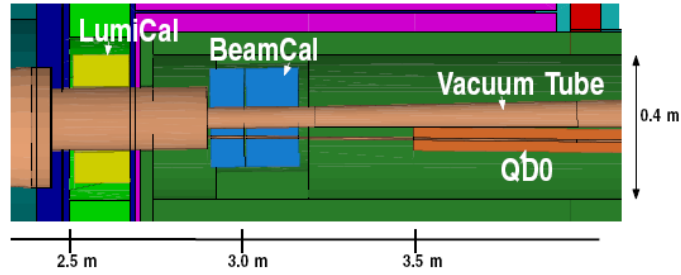


Figure 10.2.1 Very Forward Region layout at CLIC, as implemented for this study. For the quadrupole only the central cylinder is shown

The final focusing quadrupole magnet QD0 is one of the components of the Beam Delivery System, BDS, which extends into the very forward region. BDS, one of the main components of the accelerating system, starts about 3 km before the interaction point and extends through the interaction region to the beam dump. It transports and de-magnifies the beams in order to bring them into collision, and finally disposes of the spent beams. [82]

The QD0 magnet is centered on the incoming beam. It has to provide a gradient of 575 T/m, with an inner radius of 4.125 mm and a total length of 2.73 m [115]. The design has to allow for the outgoing beam-pipe (spent beam), i.e. for a cone with 10 mrad opening [116]. The distance from the QD0 exit to the IP, called  $L^*$ , is 4.6 m. A hybrid magnet, built from permanent magnet pieces combined with a "warm" electro-magnet, is preferred over a pure permanent magnet [117]. In such a design, the coils extend somewhat beyond the actual magnet length. A cross-section of the proposed QD0 design is shown in Figure 10.2.2 a). The QD0 consists of a central permanent magnet, re-enforced by permendur (a mix of equal amounts of iron and copper) elements, and an electro-magnet powered by water-cooled copper coils sustained by low-carbon steel yokes [117][118][122].

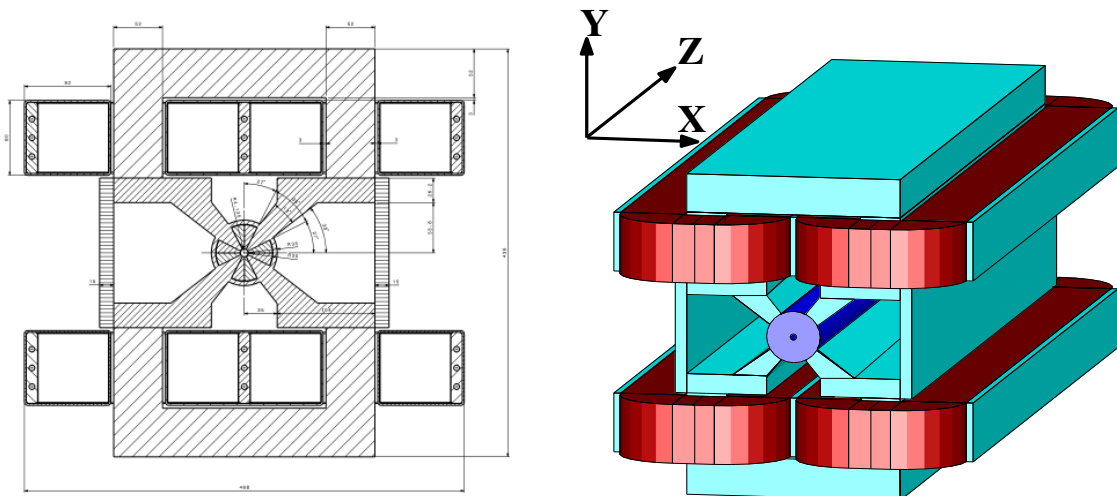


Figure 10.2.2 a) QD0 technical drawing, b) QD0 simulation implemented in Mokka

## 10.3 Motivation for study and simulation details

Usually, synchrotron radiation emitted by charged particles when passing through magnetic fields, is scattered in the two final quadrupolar magnets. Consequently, the collimation depth of these magnets is chosen such that the synchrotron photons would not hit the quadrupolar magnets. Other sources of background are also taken into consideration for the design of the detector, e.g.,  $e^+e^-$  coherent interactions result in a large number of particles, with energies much lower than that of the beam particles, which will scatter at larger angles. Thus coherent pair production puts a constraint on the opening angle of the beam pipe in order to avoid the loss of even the smallest fraction of these particles into the detector. Simulation studies have shown that a 10 mrad crossing angle is sufficient to avoid energy depositions from coherent pairs into the very forward region. Taking into account the space needed for the accommodation of the final focus quadrupole into this region, it has been concluded that 20 mrad would be the reasonable choice for the crossing angle to satisfy all constraints. [82]

On the other hand, a large number of incoherent secondary  $e^+e^-$  pairs are created during the primary collision. Significant contributions come from  $e^+e^- \rightarrow ee^+e^-$ ,  $e^- \gamma \rightarrow ee^+e^-$ ,  $\gamma\gamma \rightarrow e^+e^-$  processes. These pairs carry around 1 % of the beam energy and are deflected first by the electromagnetic fields of the beams, then by the magnetic field of the detector. As a result they deposit large amounts of energy in the equipment closest to the beam-pipe. This energy deposition can become problematic, i.e. equipment is heated and its lifetime could be severely limited due to radiation damage.

The purpose of this study is to estimate the electromagnetic and neutron doses induced by the incoherent pair production to the final focus quadrupole QD0 at nominal CLIC operating conditions [119]. The QD0 geometry was implemented in the Geant4-based [99] simulation software Mokka [98]. The detector model used in this simulation is derived from the ILC\_ILD concept [83] modified for CLIC. The magnetic field is a 4 T solenoid field. A recently modified cross-section of BeamCal is used [113], which provides improved protection for the QD0, and a crossing angle geometry of 20 mrad.

The official CLIC QD0 base-line parameters could not be respected in all cases for the present simulations. The QD0 in this implementation has a length of only 1.0 m, and the  $L^*$  is 3.5 m, the maximum external width of the QD0 is 468 mm and the height 436 mm. The coils extend beyond the core of the QD0 by 83 mm on either side.

The incoherent  $e^+e^-$  background pairs are simulated using GuineaPig [91]. The physics processes induced by particles in the detector components and the QD0 are described by the Geant4 physics list QGSP\_BERT\_HP. The output of the simulation is the deposited energy per cell, which is translated to radiation dose via the mass for any given cell.

The simplified model of QD0, as implemented in Mokka, is presented in Figure 10.2.2 b) and can be compared to the technical drawing, Figure 10.2.2 a). In the simulations, the QD0 model has been divided into three independent components with approximated material choices: an iron central cylinder (inner radius 4.125 mm, outer radius 35 mm) which corresponds to the permanent magnet core, represented in dark blue in Figure 10.2.2 b), a surrounding iron yoke, light blue, representing the permendur and low-carbon steel elements, and the copper coils, the red components. The water-cooling of the copper coils was taken into account by lowering the copper density in the simulation to two-thirds of the nominal density.

In order to be able to estimate the radiation doses and neutron fluxes in the QD0, all the components of the QD0 were defined in the simulation as sensitive elements able to register energy depositions, although the quadrupole is not a sensitive detector [121]. All elements were divided into smaller cells to identify the regions with the highest absorbed energy. Hit distribution in the two geometrical volumes of forward and backward quadrupoles is represented in Figure 10.3.1 which shows that both magnets register hits. These hits are symmetrically distributed with respect to the interaction point placed in the origin of the coordinates system at  $(x,y,z)=(0,0,0)$ , thus there are no forward-backward asymmetries among the generated background events.

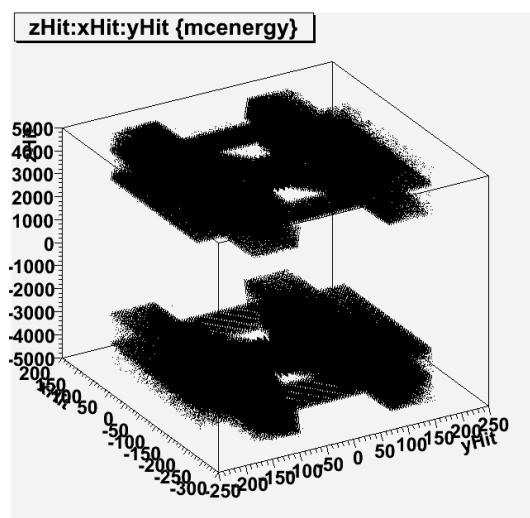


Figure 10.3.1 Hit distribution in x-y-z coordinates

## 10.4 Electromagnetic Dose on QD0 from Incoherent Pairs

There are different processes that produce  $e^+e^-$  pairs during a collision at a high energy  $e^+e^-$  collider [91]. These are incoherent processes, in which single electrons and/or photons interact, and coherent processes, where either a real photon interacts with the coherent field of the bunches, or an electron interacts via a virtual photon with the coherent field (Trident cascade [120]). Because of the opening cone of the beam-pipe with a half-opening angle of 10 mrad only particles above this angle will hit material in the detector region.

We study the effect for the  $e^+e^-$  incoherent pairs produced during one bunch crossing, at nominal CLIC 2008 parameters and 20 mrad crossing angle.

Figure 10.4.1 a) shows a two-dimensional representation of the electromagnetic dose in the central cylinder. The cylinder is segmented into 30 radial and 60 azimuthal sections (1 mm high and 6 degree wide segments). The cylinder is centered on the incoming beam-pipe. The increase in the dose visible on the right hand side of the picture is due to the close proximity of the QD0 cylinder to the outgoing beam-pipe: Because the QD0 is shielded by BeamCal, this is the only area where incoherent pairs can directly hit the QD0 cylinder.

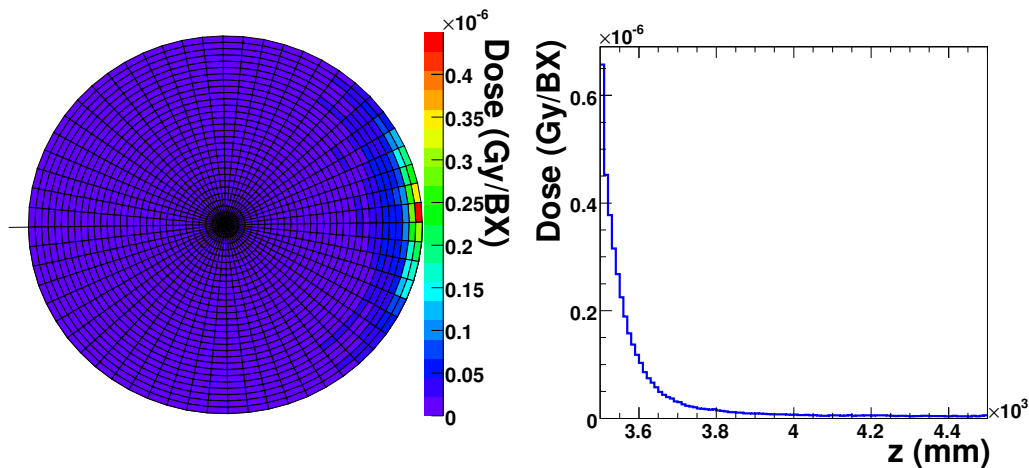


Figure 10.4.1 Electromagnetic dose in the central cylinder of QD0 a) integrated over the full length, b) integrated over the full cross-section

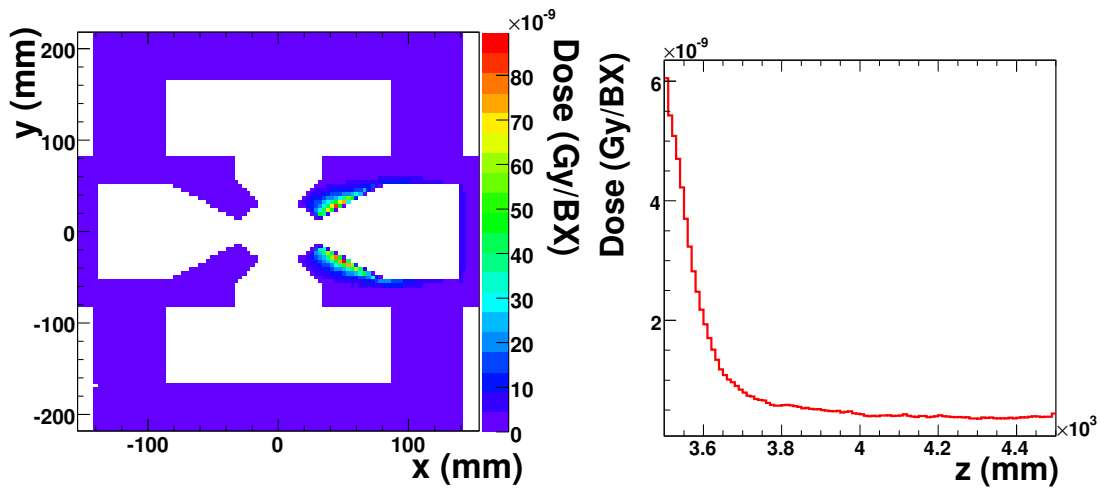


Figure 10.4.2 Electromagnetic dose in the QD0 yoke a) integrated over the full length, b) integrated over the full cross-section

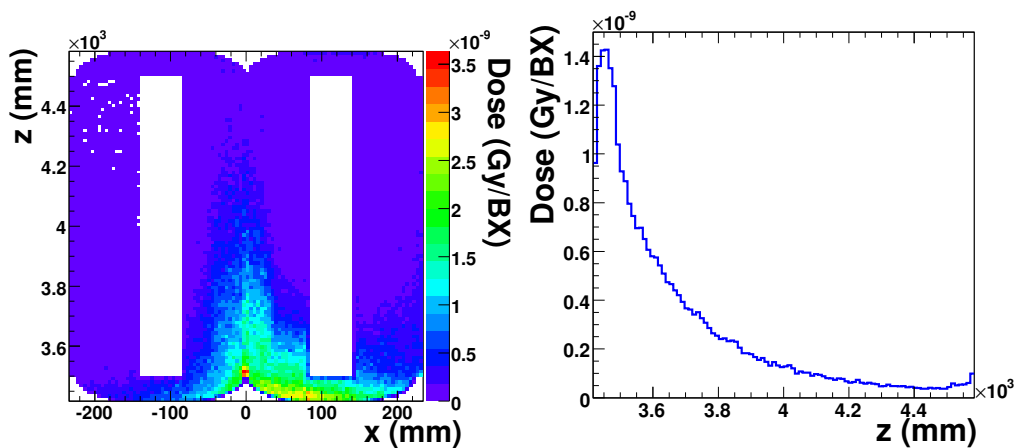


Figure 10.4.3 Electromagnetic dose in the copper coils a) integrated over the full height of both coils, b) integrated over the full cross-section (sum of both sets of coils)

In this region the dose rises up to a value of  $0.5 \times 10^{-6}$  Gy per bunch crossing (BX), corresponding to  $1.35 \times 10^5$  Gy/yr, otherwise being uniformly distributed over the surface of QD0 with values lower than  $0.05 \times 10^{-6}$  Gy/BX [123][124]. Here, a nominal year of CLIC operation is assumed to last 200 days, with 100 % accelerator efficiency.

Figures 10.4.2 a) and 10.4.3 a) show the same two dimensional representation of the electromagnetic dose in the yoke and coils, respectively. (Note that the origin of the X-Y plane is placed in the center of the cylinder, i.e. on the beam axis.) These QD0 model components also have a fine segmentation along all the three Cartesian axes. Both the yoke

and the coils are divided into 100 layers along the X-, Y- and Z-axes leading to segments of approximately  $4.5 \times 4.5 \text{ mm}^2$  in the X-Y plane and approx.  $4.5 \times 10 \text{ mm}^2$  in the X-Z plane.

On average, the electromagnetic dose is much smaller in the yoke than in the cylinder, approximately  $1 \times 10^{-8} \text{ Gy/BX}$  ( $2.7 \times 10^3 \text{ Gy/yr}$ ). It also shows the same increase around the outgoing beam-pipe, on the right side of the plot in Figures 10.4.2 a), where it reaches values up to  $8 \times 10^{-8} \text{ Gy/BX}$  ( $21.5 \times 10^3 \text{ Gy/yr}$ ). Somewhat lower values are found for the coils (Figure 10.4.3 a)). [123][124]

Figures 10.4.1 b), 10.4.2 b) and 10.4.3 b) show the distribution of the electromagnetic dose along the depth (in beam direction, away from the IP) of the cylinder, yoke and coils, respectively. We observe a rapid drop in the electromagnetic dose for the cylinder and yoke, after the first quarter of their length the dose is very close to 0. For the coils, the distribution drops more slowly and it becomes negligible only after the first half of the length. Figure 10.4.4 gives complementary information on the electromagnetic dose: The distribution of the dose per cell in the mesh of the QD0 central cylinder is shown and it is demonstrated that only very few cells are exposed to the highest dose.

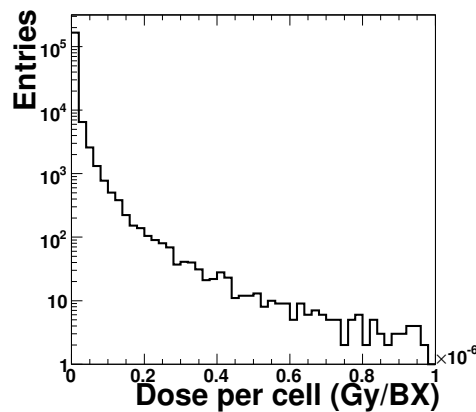


Figure 10.4.4 Distribution of electromagnetic dose per cell in the central cylinder of QD0 from incoherent pairs.

## 10.5 Neutrons from Incoherent Pairs

Interactions of the  $e^+e^-$  background pairs with the material of the detector components can result in neutrons. Figure 10.5.1 a) shows the distribution of neutrons along the depth of the permanent magnet. A maximum of 200 neutrons per layer per bunch crossing is found, where the 1 m long QD0 is segmented into 100 layers along the z axis.

Knowing the surface of each layer and considering a whole year of nominal CLIC operation, the flux of neutrons hitting the central cylinder of the quadrupole is about  $5 \times 10^{12}$  neutrons/mm<sup>2</sup>/yr}. The distribution of the neutron flux passing through each z-layer is represented in Figure 10.5.1 b).

The energy deposition of the neutrons passing through the permanent magnet during one bunch crossing is represented in Figure 10.5.2. We can see that only one neutron, of all neutrons flying through the magnet, deposits any energy in the magnet and it amounts to approximately  $8 \times 10^{-5}$  GeV/cell. This value is equivalent to an absorbed dose of approximately 0.5 Gy/yr. Considering a factor 10 for the deposited energy fluctuations and another factor 10 in neutron number fluctuations from bunch to bunch, we can estimate an upper limit for the neutron dose at about 50 Gy/yr. Compared to the electromagnetic dose (270 kGy/yr), the neutron dose is negligible. [123][124]

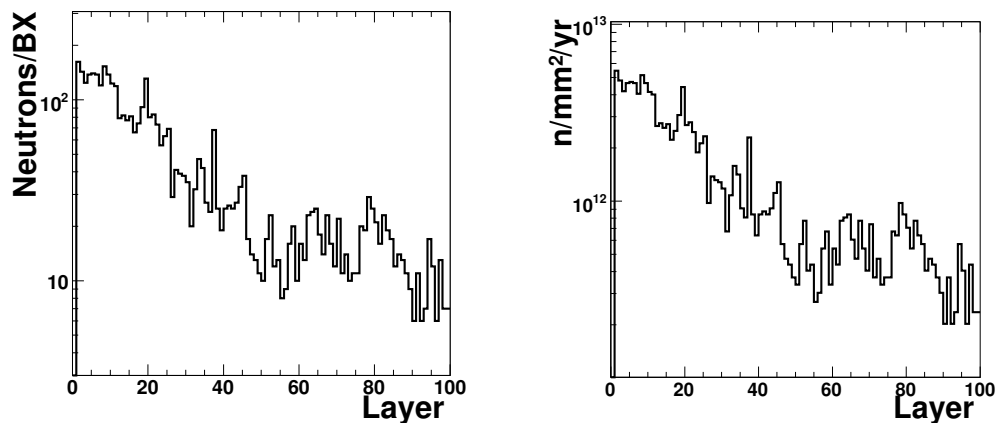


Figure 10.5.1 a) Number of neutrons in the central cylinder of QD0 from incoherent pairs, b) Flux of neutrons in the central cylinder of QD0 from incoherent pairs

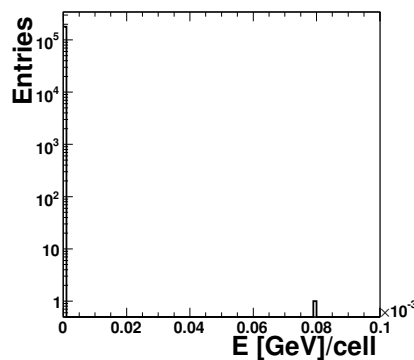


Figure 10.5.2 Neutron dose in the central cylinder of QD0 from incoherent pairs

## 10.6 Conclusions

A detailed model of the final focus quadrupole magnet (QD0) of the Beam Delivery System was implemented in a simulation algorithm for one of the detector concepts proposed for CLIC. The electromagnetic and neutron dose in different components of the QD0 were estimated based on this model.

It was found that the dose decreases rapidly in beam direction (i.e. away from the IP). The electromagnetic dose is highest in a part of the permanent magnet which is located closest to the outgoing beam-pipe, and it is found to be less than 270 kGy/yr for the incoherent pairs. The dose induced by neutrons in the same region is less than 50 Gy/yr and the neutron flux is found to be up to  $5 \times 10^{12}$  neutrons/mm<sup>2</sup>/yr.

The electromagnetic dose in the yoke and the copper coils of QD0 is much smaller. The highest dose in the yoke is 20 kGy/yr in the parts closest to the outgoing beam-pipe, and much less further away from it. In the coil the maximum dose is about 3 kGy/yr.

The results presented in this chapter are included in the CERN-LCD Note, LCD-2010-013: “*Radiation Dose to the QD0 Quadrupole in the CLIC Interaction Region*” [124] and presented at FCAL collaboration meetings, workshops or CERN summer school [109][121][122][123]

# 11 Summary and Conclusions

The main subjects of this thesis involve studies on rare radiative decays using data collected with the LHCb detector at LHC and performance studies on detector components at one of the detector concepts proposed for a future  $e^+e^-$  linear collider.

The first part of the thesis presents results regarding the LHCb experiment. It has been demonstrated that with the  $88 \text{ pb}^{-1}$  of data collected during the 2010 run and partially in 2011 radiative decays are visible at LHCb. The selection strategy proposed for two representative radiative decays,  $B_d \rightarrow K^* \gamma$  and  $B_s \rightarrow \phi \gamma$ , has been described and distributions of the variables on which selection cuts are applied on real data were compared to the distributions of the same variables in simulated data. It is shown that, overall, there is a good agreement between data and simulation, the differences coming from the fact that while in simulation only signal events were included, in real data some background is also present.

Then, the ratio between the signal yields in the two radiative channels has been checked and it has been proved that this ratio is stable within errors with respect to the selection criteria applied. Also, a cut on the transverse momentum of B meson is found to be very efficient in reducing the background level as well as the peaking structures observed in the left and right mass sideband.

The dependence of signal and background yields on each of the selection cuts was studied in two cases, when a cut on  $B_{PT}$  is not applied and when  $B_{PT} > 2 \text{ GeV}$ . This study further confirmed the importance of the  $B_{PT}$  cut and it allowed the calculation of  $\xi = \frac{S}{\sqrt{S+B}}$  which is a measure of how well the signal is discriminated from the background. The goal is to find the cut values which maximize this variable. Based on  $\xi$  distribution as a function of each variable on which a cut is applied, a new set of selection criteria has been optimized to select with increased efficiency the two radiative decays  $B_d \rightarrow K^* \gamma$  and  $B_s \rightarrow \phi \gamma$ .

Then, a study is performed in order to determine possible sources of background which can complicate the analysis of the  $B_d \rightarrow K^* \gamma$  radiative decay.

It has been shown that possible background sources which can affect the offline analysis of the  $B_d \rightarrow K^* \gamma$  decay are the mis-identification of the charged daughters or charged daughters coming from the primary vertex, the erroneous reconstruction of the vector meson,  $K^*$ , the

combination of the  $K^*$  with a random photon coming from a  $\pi^0$  or another B-decay or completely random K,  $\pi$  and  $\gamma$ , coming from different decays, being combined to form the  $B_d$  candidate.

Different sets of offline selection criteria corresponding to  $B_d \rightarrow K^* \gamma$  have been described and tested on several Monte Carlo signal samples identified as potential background for this radiative decay and it has been proved that the new set of offline cuts tuned on the real data collected with the LHCb detector is up to a factor 10 more efficient in reducing background coming from random combinations of particles than the official LHCb selection.

Other specific types of background can be controlled by narrowing the mass window for the vector meson,  $K^*$ , or by tightening the constraints on both charged and neutral particle identification criteria, or on the vector meson vertex isolation, so that the charged daughters do not point towards the interaction region. Also, a cut on the  $B_d$  transverse momentum is efficient in removing low momentum background.

The effect of the offline selection cuts corresponding to the  $B^0 \rightarrow K^* \gamma$  decay on the  $B^0$  lifetime distribution and  $B^0$  lifetime acceptance function distribution has been studied using Monte Carlo simulated data.

The lifetime acceptance is defined as the ratio between the reconstructed proper time distribution and the nominal exponential,  $e^{-t/\tau}$ , which ideally would be a flat distribution. A non zero slope is observed in the distribution of the reconstructed lifetime acceptance function. It was demonstrated that the offline selection cuts specific to the  $B^0 \rightarrow K^* \gamma$  decay reduce this slope to a flat distribution but affect more or less the acceptance function distribution at small lifetimes.

It is also shown that the largest bias in the evaluation of the lifetime is due to the imprecise determination of the flight distance of the B meson.

Results regarding studies at LHCb have been presented inside the Rare Decays Group meetings at the LHCb collaboration and helped at the preparation of the conference note “*Measurement of the ratio of branching fractions  $\mathcal{B}(B^0 \rightarrow K^{*0} \gamma) / \mathcal{B}(B_s^0 \rightarrow \phi \gamma)$  with the LHCb experiment at  $\sqrt{s} = 7 \text{ TeV}$ ” [69]. Two posters have been prepared (one presented) by the author of this thesis, on behalf of the LHCb collaboration, regarding the two radiative channels investigated in this thesis ( $B^0 \rightarrow K^{*0} \gamma$ ,  $B_s^0 \rightarrow \phi \gamma$ ), at two International conferences: 6<sup>th</sup> edition of Physics at LHC conference, Perugia, Italy, 2011 [64], and 5<sup>th</sup> High-Energy Physics Conference, Madagascar 2011 [65].*

The second part of the thesis presents simulation studies on detector components placed in the Very Forward Region of the ILD detector concept proposed for a future  $e^+e^-$  linear collider: BeamCal at ILC and QD0 at CLIC.

BeamCal must shield the Inner Detector against backscattering from beamstrahlung pairs while efficiently detecting single high energetic particles at lowest polar angles. The identification of high energy electrons at small polar angles is necessary to veto two photon events. The latter are a serious background in many new particle search channels and produce very high levels of ionizing dose in which the sensors used for BeamCal have to survive. On the other hand, the distribution of energy depositions coming from background allows for a fast determination of bunch parameters.

Consequently, the background electromagnetic shower shape has been investigated and the radiation levels have been estimated for one year of operation at ILC accelerator as well as bunch-by-bunch fluctuations of energy depositions.

The electromagnetic radiation dose and neutron fluxes have been estimated using two different simulation algorithms, a stand alone simulation of BeamCal, BeCaS, and the general software framework which describes the whole ILD detector concept, Mokka. It was found that the results given by the two detector simulation algorithms are comparable. With BeCaS, a radiation dose of  $\sim 0.5$  MGy/yr is found in the ring of cells placed right around the beam pipe ( $\sim 20$  individual cells) and a maximum dose of  $\sim 0.2 \times 10^6$  Gy/yr is estimated with Mokka for a single individual cell.

Also, radiation doses and neutron fluxes in BeamCal have been evaluated using different configurations of magnetic fields e.g. a simple 3.5 T solenoid field, a detailed 2D combination of solenoid and local dipole correction, anti-DID, etc. A factor 1.5 to 2 between energy depositions in simple solenoid magnetic field and 2D solenoid field map with anti-DID has been observed. A radiation dose of  $\sim 0.21$  MGy/cell/yr for a 2D solenoid field map with anti-DID and  $\sim 0.42$  MGy/cell/yr in simple solenoid magnetic field is determined.

In what concerns neutrons, almost 2 times more neutrons are produced in the simple solenoid magnetic field than in the solenoid corrected with the anti-DID and a neutron fluence of  $\sim 2.6 \times 10^{11}$  n/mm<sup>2</sup>/yr (FieldX03) and  $\sim 4.6 \times 10^{11}$  n/mm<sup>2</sup>/yr (SField01) is estimated. The results are in good agreement with the results obtained previously using the stand-alone BeCaS simulation algorithm for BeamCal. [105]

Results related to BeamCal simulation studies are published in two ISI journals, *JINST* 5 P12002 [95], 2010 and *Rom. J. Phys.*, vol. 55, no. 7-8, (2010)687-707 [105], in the Proceedings of the 18<sup>th</sup> FCAL Collaboration Workshop, 2011, ISBN: 978-973-0-11117-0, pag 70-74 [110] and presented in many collaboration meetings and international workshops.[106-110]

Background levels expected at CLIC represent one of the main issues to be considered for the design of the detectors proposed at this future linear collider. There are two main background sources, one due to interactions occurring in the beam (parallel muons produced in the beam halo or neutrons from the spent beam) and another due to beam-beam interactions such as  $e^+e^-$  pair production and hadron production in gamma-gamma processes. Beam dynamics near the interaction point also puts constraints on the detector design while the strength of the interaction between the beams and the solenoidal magnetic field of the detector limits the intensity of the magnetic field which can be used.

A detailed but simplified model of the final focus quadrupole magnet (QD0) was implemented in a Geant4 application, Mokka. With this model the electromagnetic and neutron doses in different components of QD0 were estimated.

It was found that the dose decreases rapidly in beam direction (away from the IP). The electromagnetic dose is highest in a part of the permanent magnet assembly, and is found to be less than 270 kGy/yr for the incoherent pairs. The dose induced by neutrons in the same region is less than 50 Gy/yr and the neutron flux is found to be up to  $5 \times 10^{12}$  neutrons/mm<sup>2</sup>/yr.

The electromagnetic dose in the yoke and copper coils of QD0 is much smaller. The highest dose in the yoke is 20 kGy/yr in the parts closest to the outgoing beam-pipe, and much less further away from it. In the coil the maximum dose is about 3 kGy/yr.

The results related to QD0 studies are included in the CERN-LCD Note, LCD-2010-013: “*Radiation Dose to the QD0 Quadrupole in the CLIC Interaction Region*” [124] and presented at FCAL collaboration meetings, workshops or CERN summer school [109][121][122][123]

# References

- [1] René Decartes, *Discourse on the Method*, The Harvard Classics. 1909–14 (1637)
- [2] M. Herrero, *The Standard Model*, hep-ph/9812242v1 (1998)
- [3] M. Peskin, D. Schroeder, *An Introduction to Quantum Field Theory*, Basic Books. p. 18. ISBN 0201503972 (1995)
- [4] S. M. Bilenky, CP-Violation and Unitarity Triangle Test of the Standard Model, *Physics of Particles and Nuclei*, Volume 39, Number 5, 641-673, DOI: 10.1134/S1063779608050018
- [5] I. Bigi and A. Sanda, *CP violation*, Cambridge University Press, ISBN 0-521-44349-0 (1999)
- [6] E. Noether, *Invariant Variation Problems*, arXiv:physics/0503066v1 [physics.hist-ph] (2005)
- [7] D. Griffiths, *Introduction to Elementary Particles.*, John Wiley & Sons ISBN 0-471-60386-4 (1987)
- [8] G. Raven, *CP violation: The difference between matter and antimatter*, (talk), NIKEF 2008
- [9] M. Gell-Mann, A. Pais, *Behavior of Neutral Particles under Charge Conjugation*, *Phys. Rev.* 97, 1387 - 1389 (1955)
- [10] N. Cabibbo, *Unitary Symmetry and Leptonic Decays*, *Phys. Rev. Lett.* 10, 531 - 533 (1963)
- [11] S. L. Glashow, J. Iliopoulos, and L. Maiani, *Weak Interactions with Lepton-Hadron Symmetry*, *Phys. Rev. D* 2, 1285 - 1292 (1970)
- [12] M. Kobayashi, T. Maskawa, *CP-Violation in the Renormalizable Theory of Weak Interaction*, *Progress of Theoretical Physics*, Vol. 49, No. 2 (1973)
- [13] L. Wolfenstein, *Parametrization of the Kobayashi-Maskawa Matrix*, *Phys. Rev. Lett.* 51, 1945 - 1947 (1983)
- [14] M. H. Schune, *Flavour physics and CP violation*, talk at TES09
- [15] Sergey Barsuk, Achille Stocchi, *CKM/CP and B physics*, talk at TES08
- [16] A. Buras, *Testing the CKM Picture of Flavour and CP Violation in rare K and B Decays and Particle Anti-Particle Mixing*, arXiv:0904.4917v1, (2009)
- [17] The CKMfitter Group, *CP violation and the CKM matrix: assessing the impact of the asymmetric B factories*, *Eur.Phys.J.C*41:1-131 (2005)
- [18] A. Ceccuci, Z. Ligeti, Y Sakai, *The quark-mixing matrix*, in W. M. Yao et al (Particle Data Group), *J. Phys. G* 33 (2006) 1.
- [19] CDF collaboration homepage <http://www-cdf.fnal.gov/>
- [20] D0 collaboration homepage <http://www-d0.fnal.gov/>

- [21] U. Nierste, *Theoretical status of  $\epsilon'/\epsilon^*$* , arXiv:hep-ph/9910257v1 (1999)
- [22] LHCb collaboration homepage <http://lhcb.web.cern.ch/lhcb/>
- [23] LHC accelerator homepage <http://lhcb.web.cern.ch/lhc/>
- [24] FCAL Collaboration homepage <http://fcal.desy.de/>
- [25] ILC accelerator homepage <http://www.linearcollider.org/>
- [26] CLIC accelerator homepage <http://clic-study.org/>
- [27] Mark Thomson, *Detectors for a Multi-TeV Collider: “what can be learnt from the ILC”*, talk at ALCPG Meeting, Albuquerque, (2009)
- [28] ATLAS collaboration homepage <http://atlas.ch/>
- [29] ALICE collaboration homepage <http://aliceinfo.cern.ch/Public/Welcome.html>
- [30] P. W. Higgs, *Spontaneous symmetry breakdown without massless bosons*, Phys. Rev., 145(4):1156–1163, 1966
- [31] Gordon Kane & Aaron Pierce (editors), *Perspectives on LHC Physics*, World Scientific Publishing Co. Pte. Ltd.
- [32] LEP accelerator homepage [http://sl-div.web.cern.ch/sl-div/history/lep\\_doc.html](http://sl-div.web.cern.ch/sl-div/history/lep_doc.html)
- [33] Tevatron collider homepage [www.fnal.gov/pub/science/accelerator/](http://www.fnal.gov/pub/science/accelerator/)
- [34] CERN press releases homepage <http://press.web.cern.ch/press/PressReleases/List.html>
- [35] LHC Design Report <http://lhcb.web.cern.ch/lhc/LHC-DesignReport.html>
- [36] CERN Communication Group, *CERN FAQ — LHC: the guide*, Geneva CERN, pp. 44, January 2008
- [37] The LHCb Collaboration, B. Adeva et al, *Roadmap for selected key measurements of LHCb*, LHCb-PUB-2009-029, arXiv:0912.4179v1 [hep-ex]
- [38] G. Balbi, *B mesons proper time measurement with the LHCb experiment: impact on physics parameters and calibration methods*, CERN-THESIS-2007-067
- [39] LHCb Collaboration, S. Amato et al., *Technical Proposal*, CERN–LHCC/98–4
- [40] LHCb Collaboration, P.R. Barbosa Marinho et al., *Vertex Locator Technical Design Report*, CERN–LHCC/2001–11
- [41] LHCb Collaboration, S. Amato et al., *Magnet Technical Design Report*, CERN–LHCC/2000–7
- [42] LHCb Collaboration, S. Amato et al., *RICH Technical Design Report*, CERN–LHCC/2000–37
- [43] LHCb Collaboration, A. Franca Barbosa et al., *Inner Tracker Technical Design Report*, CERN–LHCC/2002–29
- [44] LHCb Outer tracker, LHCb Collaboration, P.R. Barbosa Marinho et al., *Outer Tracker Technical Design Report*, CERN–LHCC/2001–24
- [45] LHCb Collaboration, S. Amato et al., *Calorimeter System Technical Design Report*, CERN–LHCC/2000–36
- [46] LHCb Collaboration, P.R. Barbosa Marinho et al., *Muon System Technical Design Report*, CERN–LHCC/2001–10

- [47] LHCb Collaboration, R. Antunes Nobrega *et al.*, *Trigger Technical Design Report*, CERN– LHCC/2003–31
- [48] T. Sjostrand *et al.*, *High-Energy-Physics Event Generation with PYTHIA 6.1*, Computer Physics Commun.**135** (2001) 238
- [49] LHCb Collaboration, S. Amato *et al.*, *Technical Design Report, Reoptimized Detector Design and Performance*, CERN/LHCC 2003-030
- [50] *GEANT detector description and simulation tool*, CERN Program Library long writeup W5013 (1994)
- [51] Landau, L. D.; Lifshitz, E. M.; Pitaevskii, L. P. (1984). *Electrodynamics of Continuous Media*. New York: Pergamon Press, ISBN 0080302750
- [52] G. Welch, G. Bishop, *An Introduction to the Kalman Filter*, SIGGRAPH 2001 Course (2001)
- [53] A. Ali, B. D. Pecjak and C. Greub,  *$B \rightarrow V\gamma$  Decays at NNLO in SCET*, Eur. Phys. J. C 55 (2008) 577
- [54] G. Buchalla, A. J. Buras, M. E. Lautenbacher , *Weak Decays beyond leading logarithms*, Rev. Mod. Phys. 68, 1125–1244 (1996)
- [55] CLEO collaboration homepage, <http://www.lepp.cornell.edu/Research/EPP/CLEO/>
- [56] BaBar collaboration homepage <http://www.slac.stanford.edu/BF/>
- [57] Belle collaboration homepage <http://belle.kek.jp/>
- [58] . M. Neubert, *Standard candles of flavour physics*, Phys. Rev. D 49, 3392 (1994) arXiv:hep-ph/0212360
- [59] O. Deschamps *et al.*, *Photon and neutral pion reconstruction*, CERN-LHCb-2003-091.371
- [60] A. Aref'ev *et al.*, *Design, construction, quality control and performance study with cosmic rays of modules for the LHCb electromagnetic calorimeter*", CERN-LHCb-2007-148.
- [61] K. Voronchev and I. Belyaev, *Energy flow calibration of LHCb ECAL*, CERNLHCb-2006-051
- [62] O. Deschamps, *LHCb Calorimeters: Commissioning and Performance*, talk at IPRD10, Sienna, Italy
- [63] K Senderowska, M Witek, and A Zuranski, *HLT1 Electromagnetic Alley*, LHCb-PUB-2009-001, 2010
- [64] **E. Teodorescu** on behalf of LHCb collaboration, *Rare Decays at LHCb*, LHCb-Poster-2011-181
- [65] [prepared by] **E. Teodorescu** on behalf of LHCb collaboration, *Radiative Decays at LHCb*, LHCb-Poster-2011-189
- [66] P. Pakhlova and I. Belyaev, *Radiative B decays at LHCb*, CERN-LHCb-2003-090
- [67] L. Shchutska, A. Golutvin and I. Belyaev, *Study of radiative penguin decays  $B_d \rightarrow K^* \gamma$  and  $B_s \rightarrow \phi \gamma$  at LHCb*, CERN-LHCb-2007-030
- [68] I. Belyaev, *Rare decays at LHCb*, LHCb-2005-001

- [69] LHCb Collaboration, *Measurement of the ratio of branching fractions  $\mathcal{B}(B^0 \rightarrow K^{*0} \gamma) / \mathcal{B}(B_s^0 \rightarrow \phi \gamma)$  with the LHCb experiment at  $\sqrt{s} = 7 \text{ TeV}$*  LHCb-CONF-2011-055
- [70] K. Nakamura *et al.* (Particle Data Group), *J. Phys. G* **37**, 075021 (2010) and 2011 partial update for the 2012 edition
- [71] J. Ellis, M.K. Gaillard, D.V. Nanopoulos and S. Rudaz, *Comparison of High- $p_T$  Events Produced by Pions and Protons*, *Nucl. Phys. B* 131, 285 (1977)
- [72] J. A. N. van Tilburg, *Track simulation and reconstruction in LHCb*, CERN-THESIS-2005-040
- [73] F. Soomro, I. Belyaev, *HLT2 exclusive selections for  $B_s \rightarrow \phi \gamma$  and  $B_d \rightarrow K^* \gamma$* , LHCb-PUB-2010-007
- [74] The LHCb Collaboration, *Reoptimized detector design and performance, Technical Design Report*, CERN/LHCC-2003-030
- [75] <https://twiki.cern.ch/twiki/bin/view/LHCb/LHCbComputing>
- [76] W. Verkerke, D. Kirkby, *RooFit Users Manual v2.07*
- [77] ILC Collaboration. *Gateway to the Quantum Universe report*
- [78] Brau, James, Okada, Yasuhiro, Walker, Nicholas, *ILC Reference Design Report Volume 1 - Executive Summary*, eprint 2007arXiv0712.1950B
- [79] A. Djouadi, J. Lykken, K. Mönig, Y. Okada, M. Oreglia, S. Yamashita, et al, *ILC Reference Design Report Volume 2: PHYSICS AT THE ILC*, arXiv:0709.1893v1
- [80] N. Phinney, N. Toge, N. Walker, et al, *ILC Reference Design Report Volume 3 – Accelerator*, arXiv:0712.2361v1
- [81] Behnke, Ties; Damerell, Chris; Jaros, John; Myamoto, Akya, *ILC Reference Design Report Volume 4 – Detectors*, eprint 2007arXiv:0712.2356B
- [82] Report of the CLIC Physics Working Group, editors M. Battaglia, A. De Roeck, J. Ellis, D. Schulte, *PHYSICS AT THE CLIC MULTI-TeV LINEAR COLLIDER*, arXiv:hep-ph/0412251 v1 17 Dec 2004
- [83] The ILD Concept Group, *The International Large Detector: Letter of Intent*, arXiv:1006.3396
- [84] H. Aihara, P. Burrows, M. Oreglia (editors), *SiD Letter of Intent*, arXiv:0911.0006v1
- [85] J. Ellis, I. Wilson, *New physics with the Compact Linear Collider*, NATURE, VOL 409, 18 JANUARY 2001
- [86] E. Clements, *CLIC The compact Linear Collider*, Symmetry, volume 02, issue 06, august 05
- [87] Jean-Eudes Augustin, *Detector concepts for a linear collider*, Science Direct, Volume 535, Issues 1-2, 11 Dec. 2004, 36-47
- [88] D. Scultze, *Study of the Electromagnetic and Hadronic Background in the Interaction Region of Tesla*, TESLA 97-08, 1996
- [89] P. Bambade, V. Drugakov, W. Lohmann, *The Impact of BeamCal Performance at Different ILC Beam Parameters and Crossing Angles on  $\tilde{\tau}$  searches*, arXiv:physics/0610145v1, 19 Oct. 2006

- [90] I. Bozovic-Jelisavcic, W. Lohmann, H. Nowak, *Simulation of Physics Background for Luminosity Measurement at the ILC*, talk, <http://www.slac.stanford.edu/econf/C050318/papers/1024.PDF>
- [91] D. Scultze, *Study of the Electromagnetic and Hadronic Background in the Interaction Region of Tesla*, TESLA 97-08, 1996
- [92] C. Grah, *Radiation Hard Sensors for the BeamCal at the ILC*, [villaolmo.mib.infn.it/ICATPP10th\\_2007/Radiation%20Damage/Grah.pdf](http://villaolmo.mib.infn.it/ICATPP10th_2007/Radiation%20Damage/Grah.pdf)
- [93] A. Vogel, *Beam-Induced Backgrounds in the LDC Detector - Dirty Business at Low Angles*, talk given at the ECFA ILC Workshop, València, 2006-11-09
- [94] C. Grah et al., *Polycrystalline CVD Diamond Sensors for the Beam Calorimeter of the ILC*, IEEE Trans.Nucl.Sci., Vol 56 462 – 467, ISSN: 0018-9499
- [95] FCAL collaboration, **E. Teodorescu** et al., *R&D for Very Forward Calorimeters for ILC Detectors*, JINST 5 P12002, 2010
- [96] V. N. Baier, V. S. Fadin, V. A. Khoze and E. A. Kuraev, *Inelastic processes in high energy quantum electrodynamics*, Phys. Rep., 78 (1981) 293
- [97] **E. Teodorescu**, Master thesis, “*Simulations of electromagnetic and hadronic backgrounds in BeamCal at the ILC*”, June 2008
- [98] P. Mora de Freitas and H. Videau. *Detector Simulation with Mokka/Geant4 : Present and Future*, (LCWS 2002). JeJu Island, Korea, 2002
- [99] S. Agostinelli et al. *Geant4 – A Simulation Toolkit*, Nucl. Instrum. Methods Phys. Res., Sect. A, vol. 506(3) pp. 250–303, 2003
- [100] Mokka homepage <http://polzope.in2p3.fr:8081/MOKKA/>
- [101] Mokka release-notes <http://polzope.in2p3.fr:8081/MOKKA/mokka-07-06>
- [102] ILC software homepage [http://www-zeuthen.desy.de/linear\\_collider/](http://www-zeuthen.desy.de/linear_collider/)
- [103] ROOT homepage, <http://root.cern.ch/drupal/>
- [104] C. Coca, M. Orlandea, L. Dumitru, **E. Teodorescu**, *High-Performance Computing System for High Energy Physics*, Rom.J. Phys., vol 56, no. 3-4, (2011)359-365
- [105] C. Coca, W. Lohmann, M. Orlandea, A. Saproinov, **E. Teodorescu**, *Expected electromagnetic and neutron doses for the BeamCal at ILC*, Rom. J. Phys, vol 55, nos 7-8, (2010)687-707
- [106] **E. Teodorescu**, *Energy spectra and particle distributions in BeamCal at ILC*, FCAL Collaboration Meeting, May 6-7, 2008, Krakow, Poland, <http://www-zeuthen.desy.de/ILC/fcal/>
- [107] **E. Teodorescu**, *BeamCal simulations with BeCas - Doses and bunch by bunch fluctuations in BeamCal at the ILC*, FCAL Collaboration Meeting, Berlin-Zeuthen, Germany, 29-30 June 2009, <http://www-zeuthen.desy.de/ILC/fcal/>
- [108] **E. Teodorescu**, *Background Simulations in BeamCal at the ILC*, Proceedings: Trans-European School of High Energy Physics, Zakopane, Poland, July 7-15, 2009, <http://events.lal.in2p3.fr/TESchool09/TESchool09-proceedings.pdf>
- [109] **E. Teodorescu**, *Mokka simulation studies on the Very Forward Detector components at CLIC and ILC*, Workshop: “High Precision measurements of luminosity at future

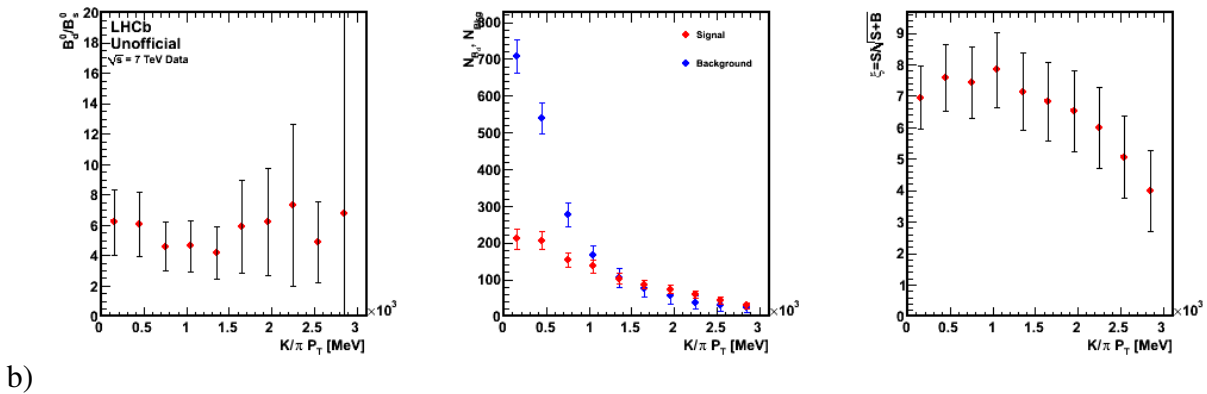
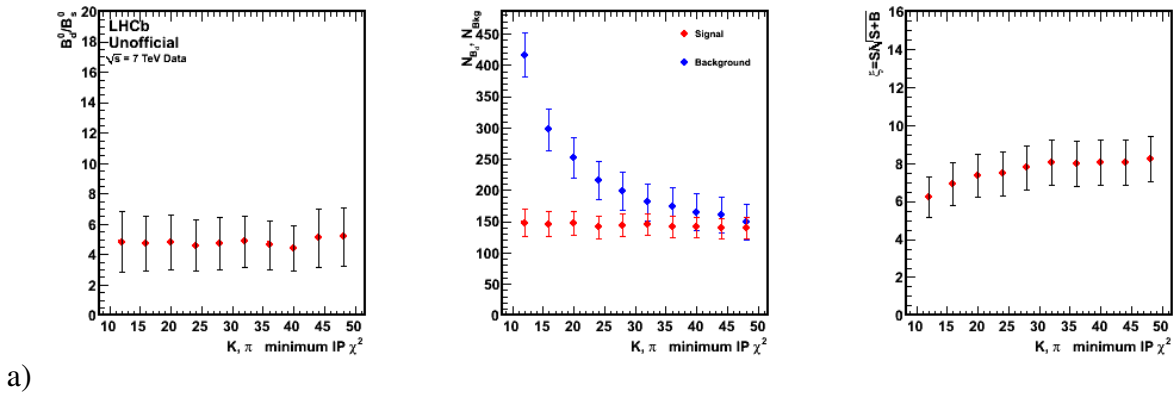
linear colliders and polarization of lepton beams workshop, 3-5 October 2010, Tel Aviv, Israel, <http://www-zeuthen.desy.de/ILC/fcal/>

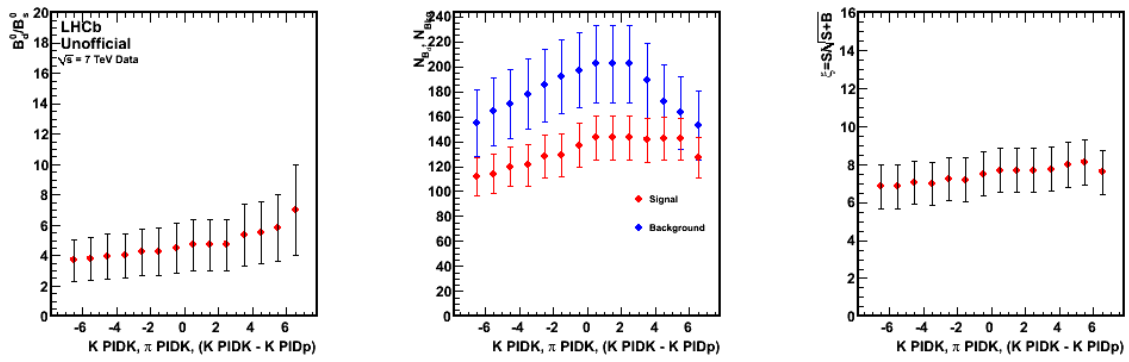
- [110] **E. Teodorescu**, *A look into the effect of supplementary magnetic fields on background levels in BeamCal at ILC*, Proceedings of the 18<sup>th</sup> FCAL Collaboration Workshop May 30 – June 1, 2011, Predeal, Romania, ISBN: 978-973-0-11117-0, pag 70-74 [http://www.nipne.ro/fcal\\_2011/docs/Proceedings\\_FCAL\\_RO\\_2011.pdf](http://www.nipne.ro/fcal_2011/docs/Proceedings_FCAL_RO_2011.pdf)
- [111] LDC Group, *Detector Outline Document* – prepared for the Reference Design Report of the ILC
- [112] The LDC concept group, *Sketch for a Large Detector Concept LDC*, [www.ilcldc.org/documents/LDC\\_introduction.pdf](http://www.ilcldc.org/documents/LDC_introduction.pdf)
- [113] A. P. Sailer, *An updated BeamCal-Driver for Mokka*, talk
- [114] A. Vogel, *Update on the Beam-Related Backgrounds in the LDC Detector*, LC Note LC-DET-2007-008, 2007-09-11
- [115] R. Tomas, *Technical specifications of the CLIC Final Doublet quadrupoles*, 2008. Internal Note
- [116] D. Schulte. *High energy beam-beam effects in CLIC*, IEEE Particle Accelerator Conference (PAC 99). 1999
- [117] M. Modena, *Final Focus Magnets*, <http://indico.cern.ch/contributionDisplay.py?contribId=1&confId=66527>, 2010. Presentation at the CLIC MDI Working Group
- [118] M. Modena, *The QD0 magnet*, <http://indico.cern.ch/contributionDisplay.py?contribId=1&confId=89765>, 2010. Presentation at the CLIC MDI Working Group
- [119] H. Braun, et al. *Clic 2008 parameters*, CLIC-NOTE-764, 2008
- [120] J. Esberg. *Cascade Trident Pair Production*, <http://ilcagenda.linearcollider.org/contributionDisplay.py?contribId=87&sessionId=53&confId=4507>, 2010. Presentation at the IWLC2010
- [121] **E. Teodorescu**, A. Sailer, K. Elsener, C. Coca, *QD0@CLIC: Implementation of QD0 in Mokka*, Student Poster Session at European School of High Energy Physics, Raseborg, Finland, June 30-July 3 2010, <http://physicschool.web.cern.ch/PhysicSchool/ESHEP/ESHEP2010/default.html>
- [122] **E. Teodorescu**, *QD0@CLIC: Implementation of QD0 in Mokka*, FCAL Collaboration Meeting, Cracow, April 2010, <http://www-zeuthen.desy.de/ILC/fcal/>
- [123] **E. Teodorescu**, *Radiation Dose to the QD0 Quadrupole in the CLIC Interaction Region*, CLIC Machine Detector Interface WG, November 5<sup>th</sup> 2010, (<http://indico.cern.ch/conferenceDisplay.py?confId=109217>)
- [124] A.Sailer, **E. Teodorescu**, *Radiation Dose to the QD0 Quadrupole in the CLIC Interaction Region*, CERN-LCD Note, LCD-2010-013

# Appendix 1

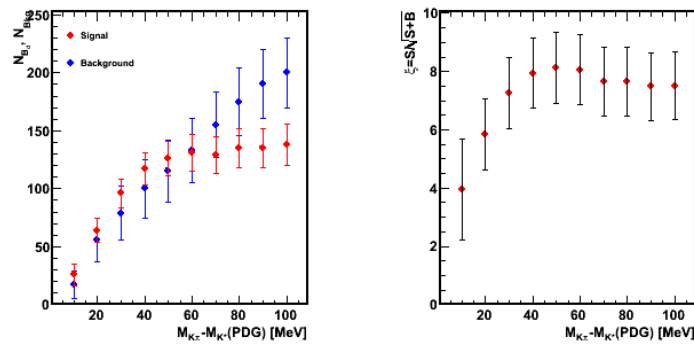
The results on the removal of “Best Tracks” cut are presented.

The ratio of number of signal events in and mass peaks is represented in Figure A.1.1 a) to i), left. Middle plots of the same figure show the number of signal and background events for the  $B_d \rightarrow K^* \gamma$  channel and the right plots show the calculation  $\xi = \frac{S}{\sqrt{S+B}}$ . The results presented here have been obtained using the data recorded with the LHCb detector at the LHC during the 2010 accelerator run. Compared to Figure 5.2.4 a) to i) where all offline cuts are applied, it can be easily seen that the selection of only the best tracks also reduces the background.

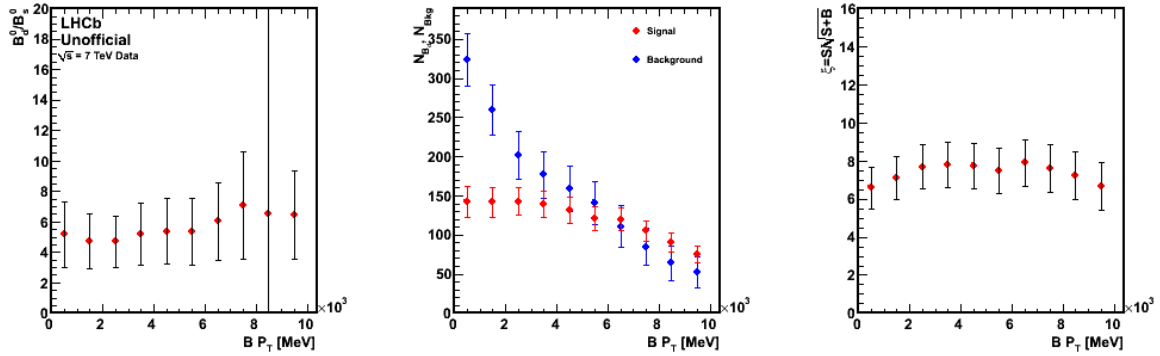




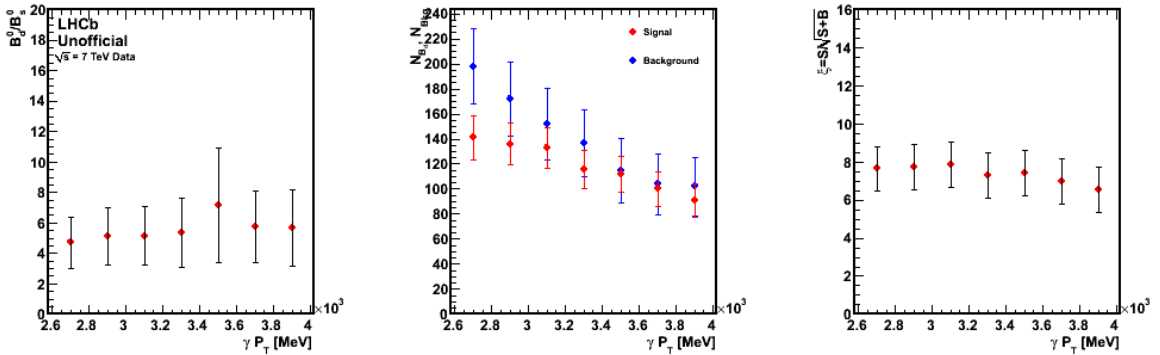
c)



d)

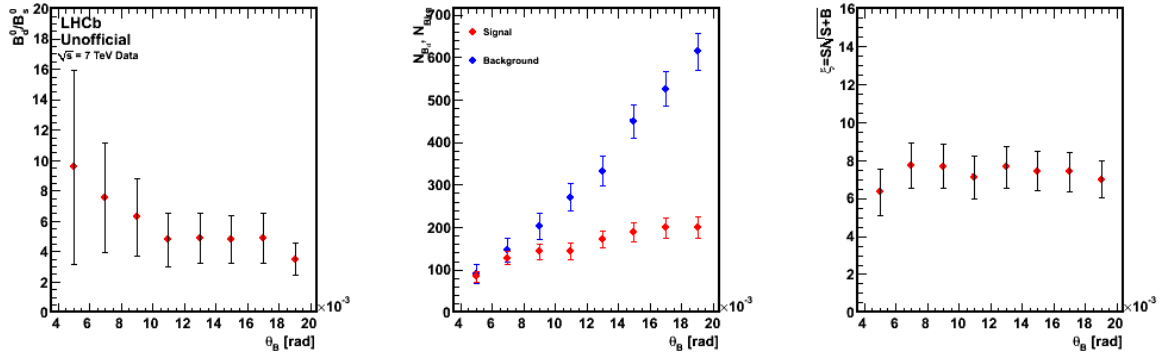


e)

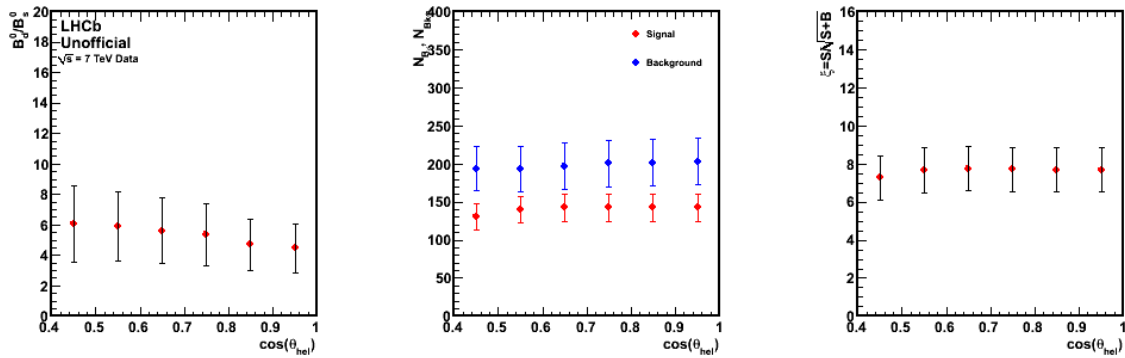


f)

g)



h)



i)

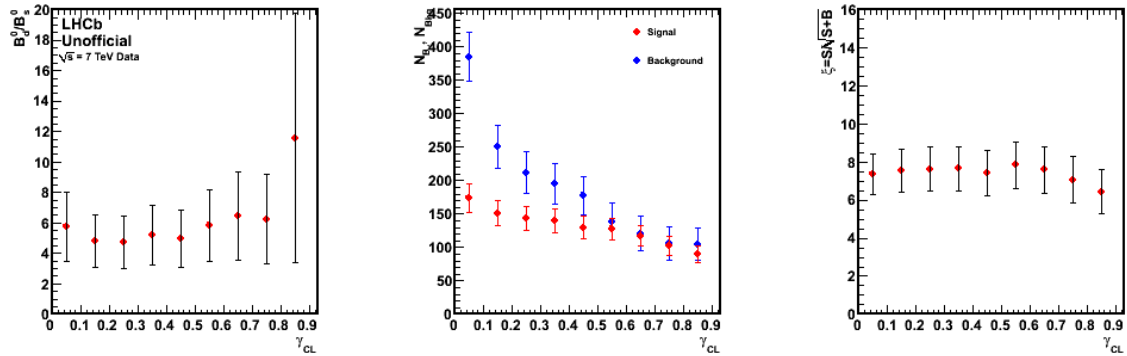
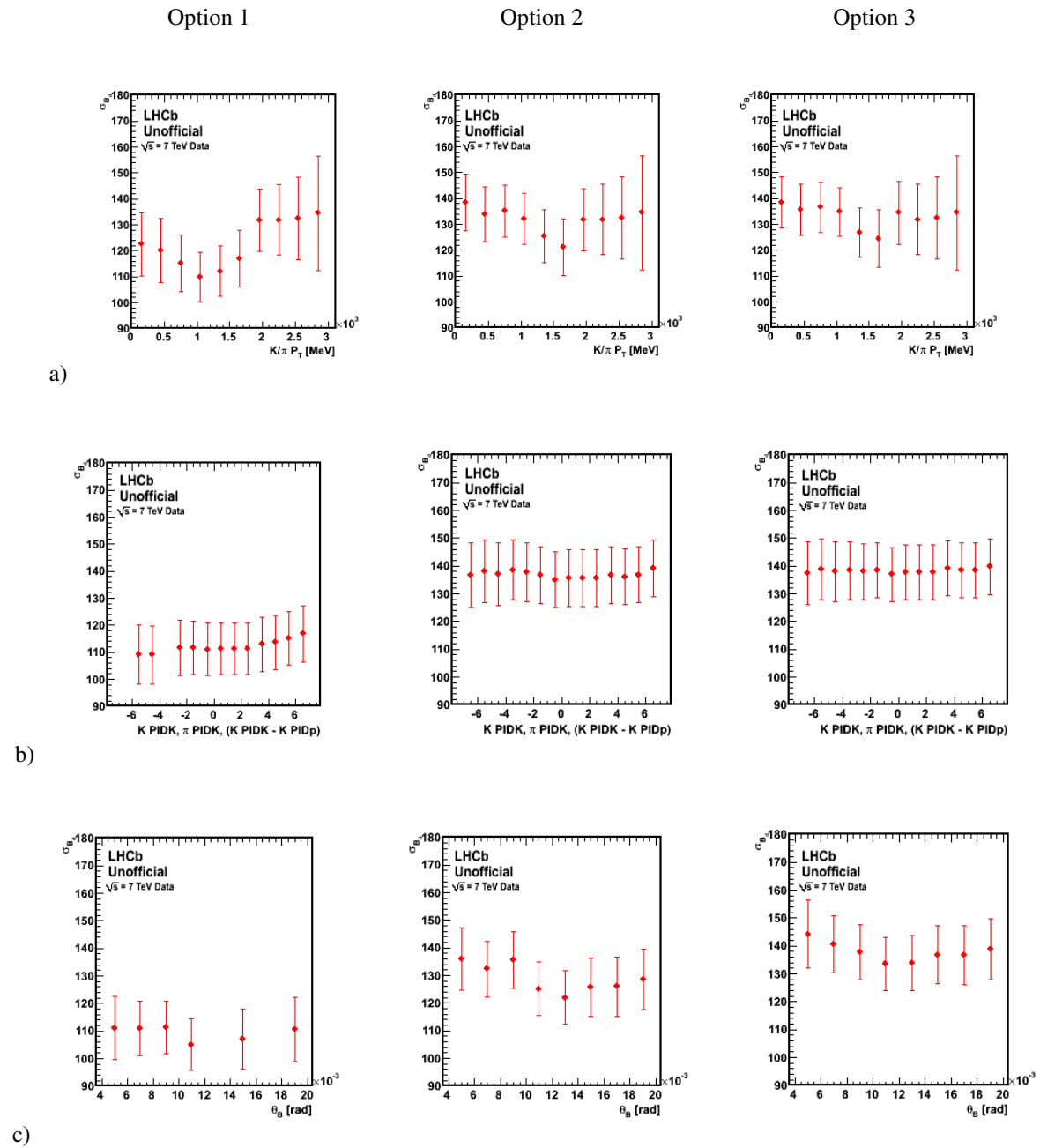
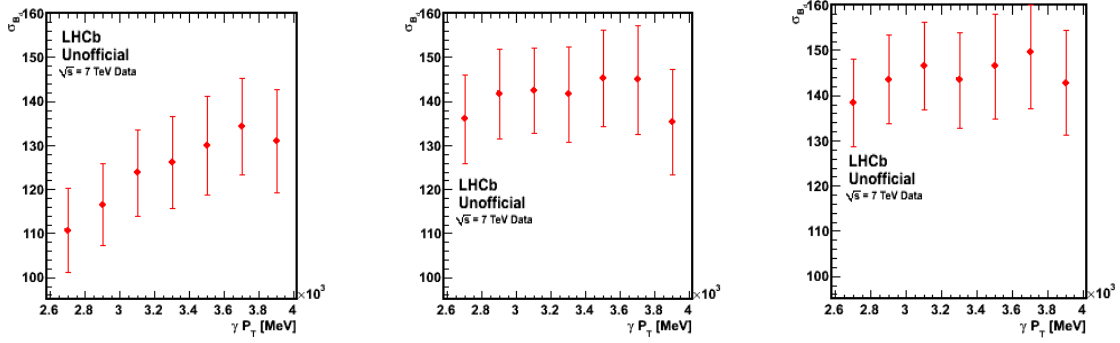


Figure A.1.1 Stability check of the ratio  $\mathcal{R} = \mathcal{N}(B_d \rightarrow K^* \gamma) / \mathcal{N}(B_s \rightarrow \phi \gamma)$  for 2010 data (left-hand plots), the number of signal and background events for the  $B_d \rightarrow K^* \gamma$  channel (middle plots) and the calculation of  $\xi = \frac{S}{\sqrt{S+B}}$  (right-hand plots) at the variance of the following cuts a)  $K, \pi$  minimal IP  $\chi^2$  b)  $K, \pi$  transverse momentum, c)  $K \text{ PIDK}, \pi \text{ PIDK}, (K \text{ PIDK} - K \text{ PIDp})$ , d)  $K^*$  mass window, e) photon transverse momentum, f)  $B_d$  transverse momentum, g) direction angle,  $\theta_B$ , h) helicity angle and i) photon confidence level, when all the other offline cuts are applied at their nominal values presented in Table 5.2.2 but the cut on Best Tracks is removed

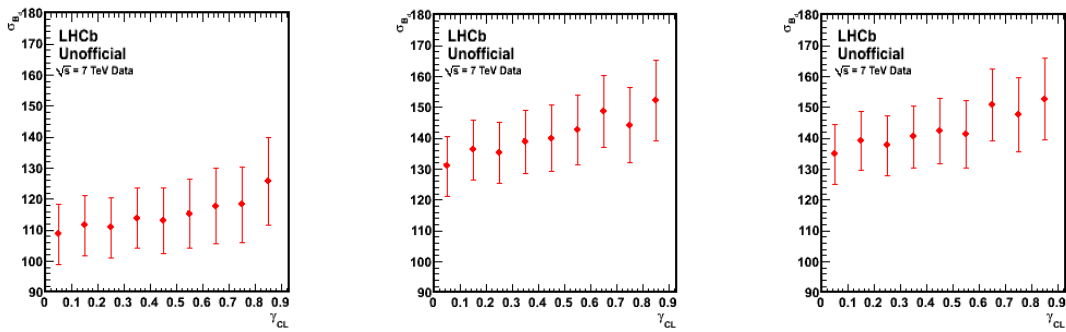
The hypothesis of the standard deviation as a free parameter of the fit has been considered. The official selection criteria have been applied on the 2010+2011 data, while varying one of the cuts. The impact of the removal of the  $B_P P_T$  cut on the  $\sigma$  distribution has

been studied. Three options have been pursued, Option I, the  $B_{PT}$  cut is removed from the selection, Option II,  $B_{PT} > 2$  GeV, and Option III,  $B_{PT} > 3.5$  GeV. The results are shown in Figure A.1.2 a) to e) for the standard deviation of the  $B_d \rightarrow K^* \gamma$  mass peak when K and  $\pi$  transverse momentum, K,  $\pi$  PIDK and (K PIDK - K PIDp), the direction angle of  $B_d$ , the photon transverse momentum and the confidence level of the photon. Simultaneously, the standard deviation of the  $B_s \rightarrow \phi \gamma$  mass peak has been plotted but the limited statistics of the  $B_s \rightarrow \phi \gamma$  sample gives rise to large uncertainties; a few examples are presented in Figure A.1.3.





d)



e)

Figure A.1.2 The distribution of the standard deviation of  $B_d \rightarrow K^* \gamma$  the mass peak, in three different scenarios: Option I, the  $B_{PT}$  cut is removed from the selection, Option II,  $B_{PT} > 2$  GeV, and Option III,  $B_{PT} > 3.5$  GeV, when different selection cuts are varied a) K and  $\pi$  transverse momentum, b) K,  $\pi$  PIDK and (K PIDK - K PIDp), c) the direction angle of  $B_d$ , d) the photon transverse momentum and e) the confidence level of the photon

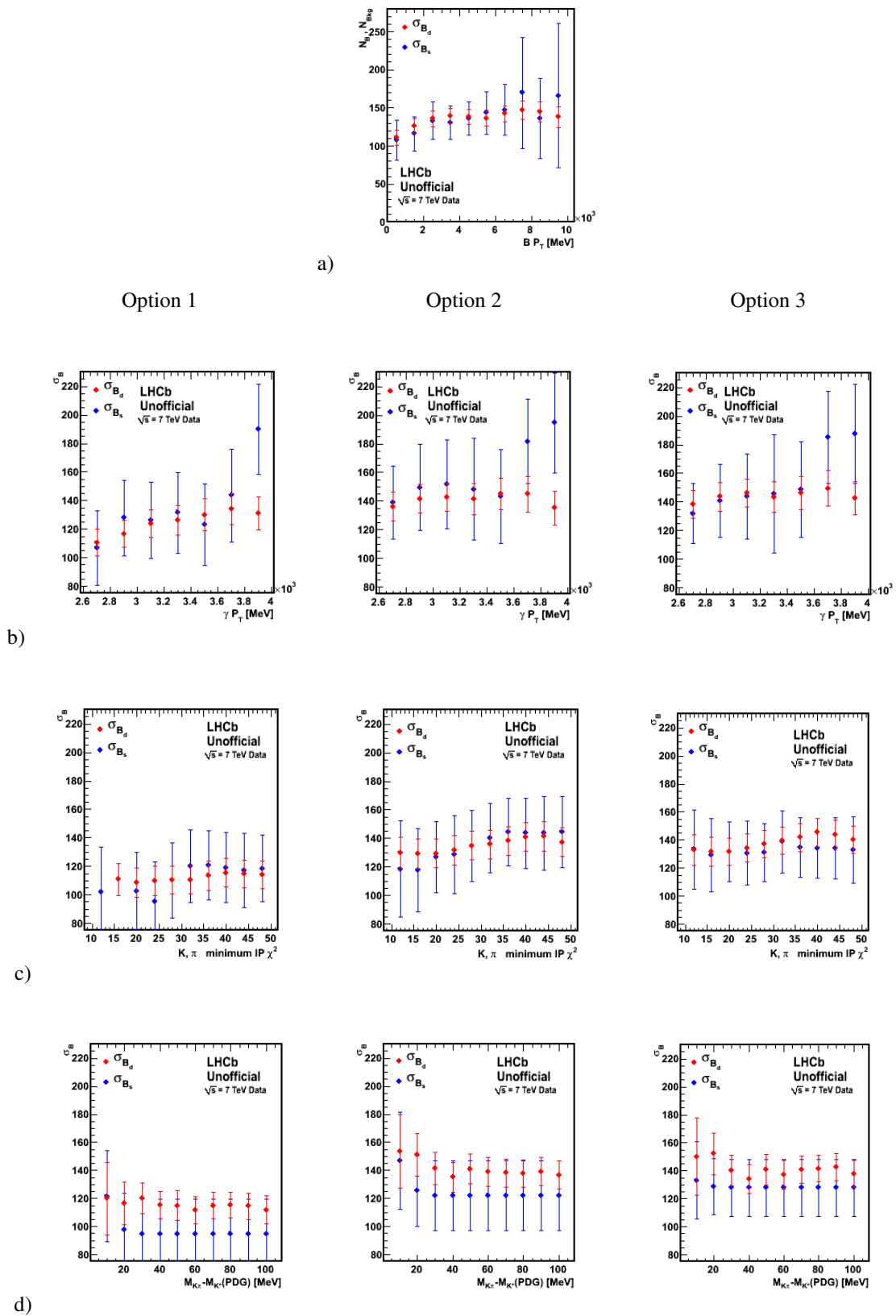


Figure A.1.3 The distribution of the standard deviation of  $B_d \rightarrow K^* \gamma$  the mass peak when different selection cuts are varied a)  $B_{P_T}$ , b)  $K, \pi$  minimal  $IP \chi^2$ , c)  $K^*$  mass window, d)  $\gamma_{P_T}$ , in three different scenarios: Option I, the  $B_{P_T}$  cut is removed from the selection, Option II,  $B_{P_T} > 2$  GeV, and Option III,  $B_{P_T} > 3.5$  GeV

# Appendix 2

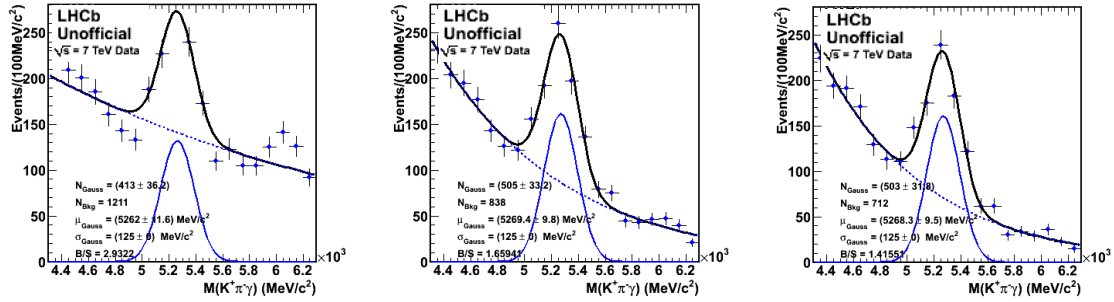
Along with the background removal, the cut on  $B_{PT}$  also significantly reduces the structures present in the distribution of the background. To support this affirmation, the invariant mass distribution of  $B_d \rightarrow K^* \gamma$  has been investigated for different cut values of  $B_{PT}$ . Three cases are presented in Figure A.2.1 a) to g):  $B_{PT} > 0$ , left,  $B_{PT} > 2000$  MeV, middle, (official value) and  $B_{PT} > 3500$  MeV, right, (optimal value extracted from the present study) in the hypothesis where all offline cuts are applied except for the cut on  $\gamma_{PT}$  which is being increased from 2600 MeV (the stripping cut) to 4000 MeV.

$$B_{PT} > 0$$

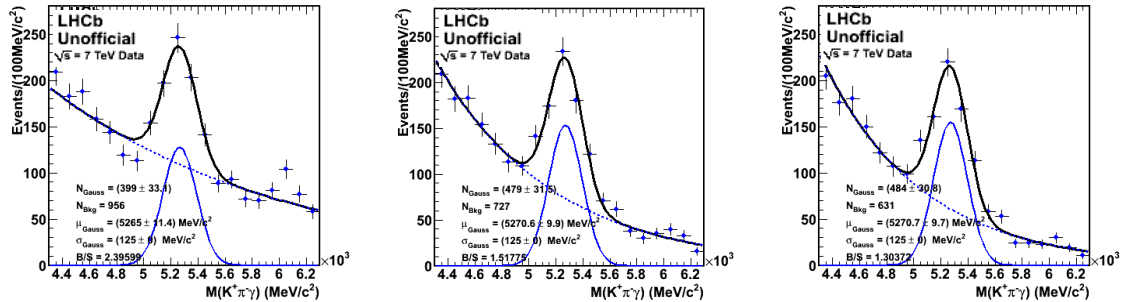
$$B_{PT} > 2000 \text{ MeV}$$

$$B_{PT} > 3500 \text{ MeV}$$

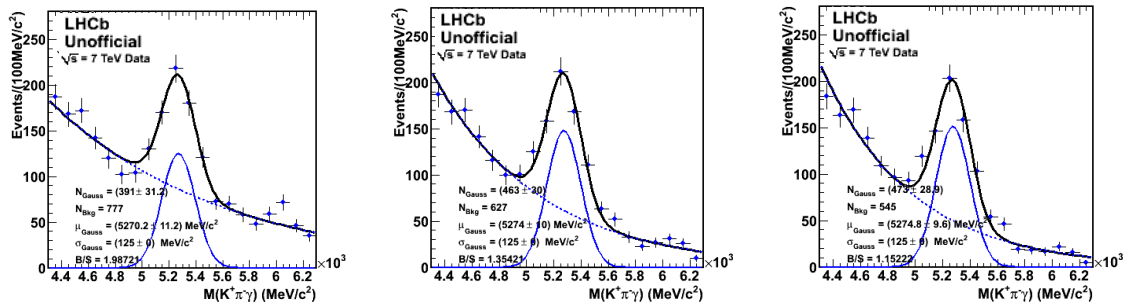
a)  $\gamma_{PT} > 2600$  MeV



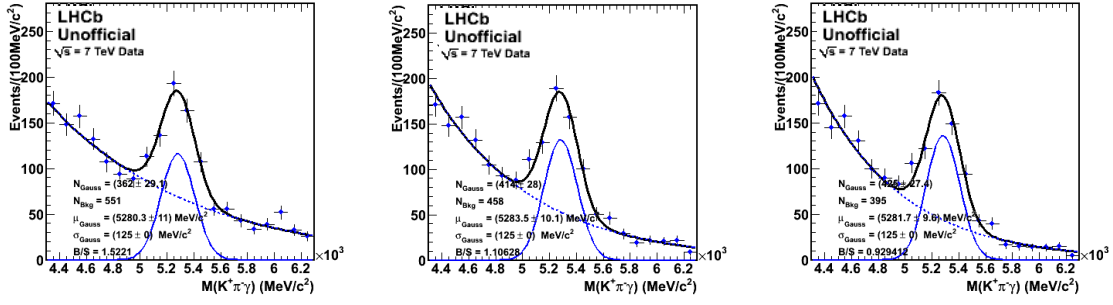
b)  $\gamma_{PT} > 2800$  MeV



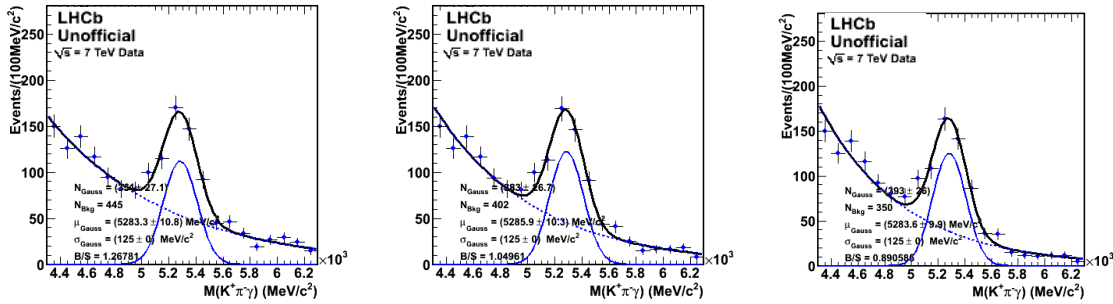
c)  $\gamma_{PT} > 3000$  MeV



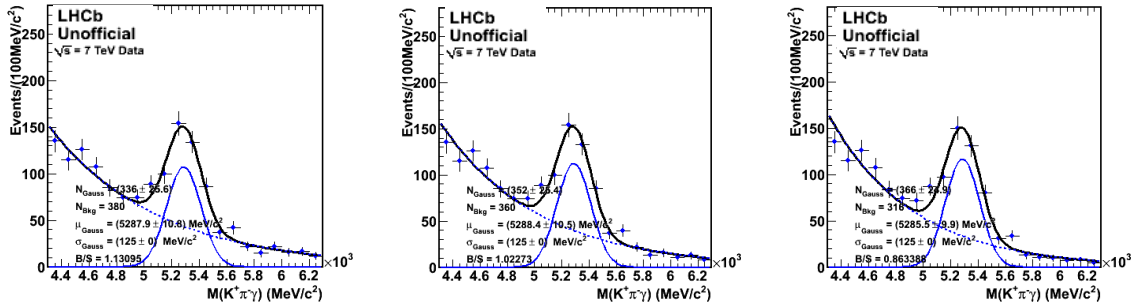
d)  $\gamma_{P_T} > 3200$  MeV



e)  $\gamma_{P_T} > 3400$  MeV



f)  $\gamma_{P_T} > 3600$  MeV



g)  $\gamma_{P_T} > 3800$  MeV

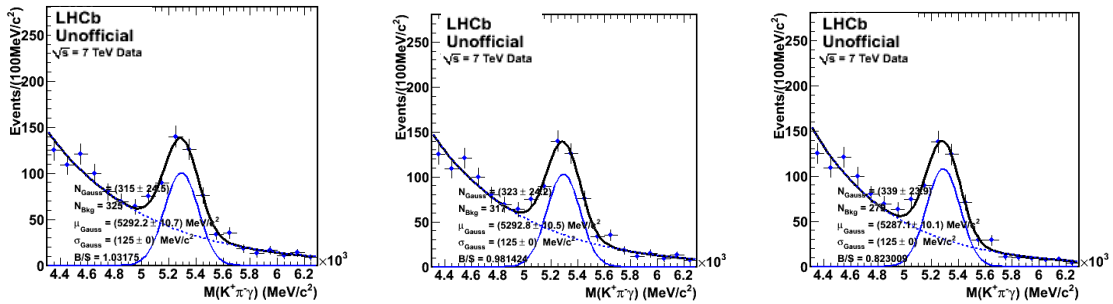
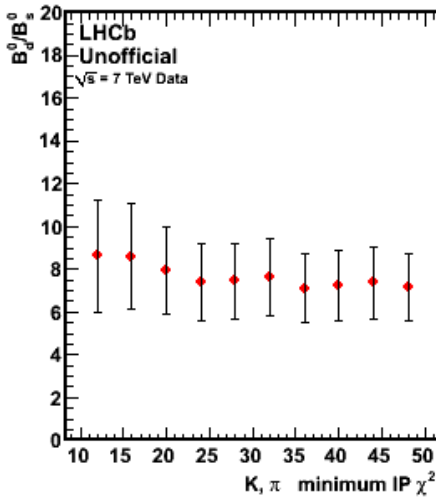


Figure A.2.1 The invariant mass distribution of  $B_d \rightarrow K^* \gamma$  for different cut values of  $B_{P_T}$ ,  $B_{P_T} > 0$  - left,  $B_{P_T} > 2000$  - middle,  $B_{P_T} > 3500$  - right, and  $\gamma_{P_T}$  a)  $\gamma_{P_T} > 2600$ , b)  $\gamma_{P_T} > 2800$ , c)  $\gamma_{P_T} > 3000$ , d)  $\gamma_{P_T} > 3200$ , e)  $\gamma_{P_T} > 3400$ , f)  $\gamma_{P_T} > 3600$ , g)  $\gamma_{P_T} > 3800$

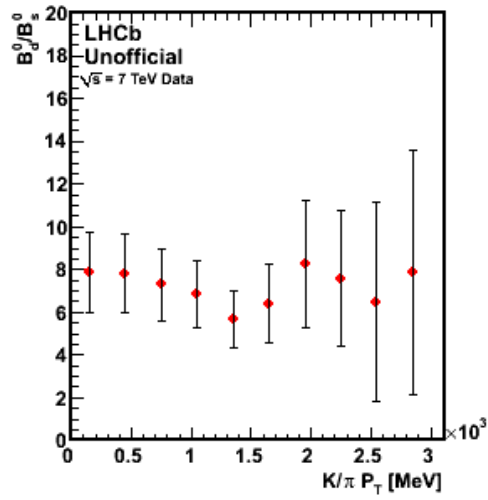
# Appendix 3

Before applying the optimized cuts on the 2010 and 2011 collected data, a check on the stability of the ratio of number of signal events in mass peaks has been performed for the total amount of data. The results show that the ratio is stable within errors for the 2010+2011 as well. The plots are shown in Figure A.3.1.

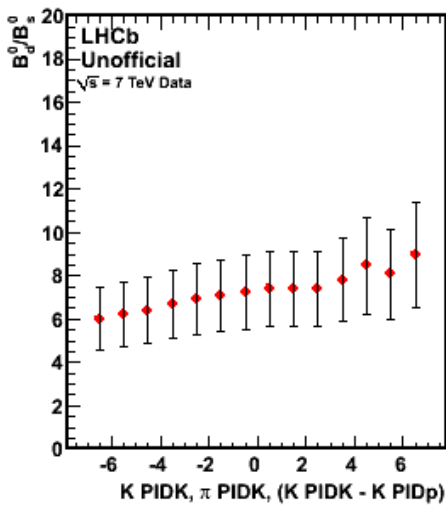
a)  $K, \pi$  minimum IP  $\chi^2$



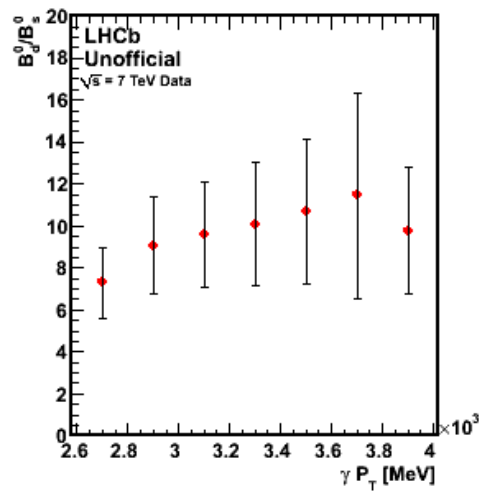
b)  $K \pi P_T$



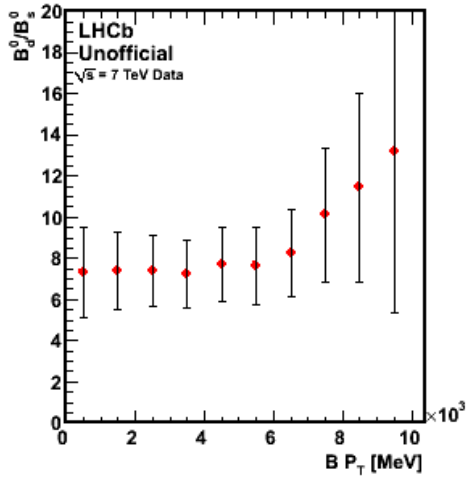
c)  $K$  PIDK,  $\pi$  PIDK,  $K$  PIDK-  $K$  PIDp



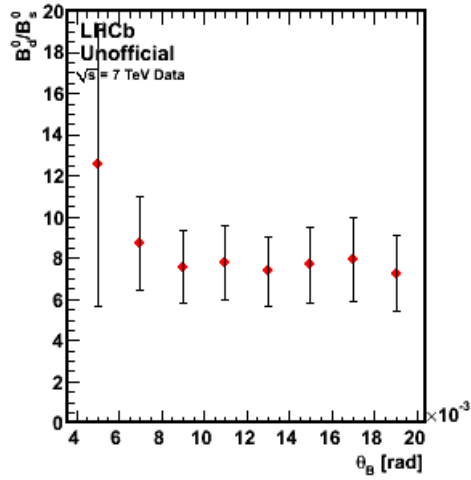
d)  $\gamma P_T$



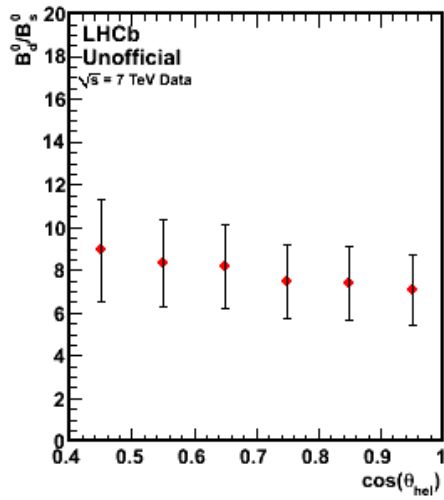
e)  $B P_T$



f) B direction angle,  $\theta_B$



g) Helicity angle,  $\theta_H$



h)  $\gamma$  CL

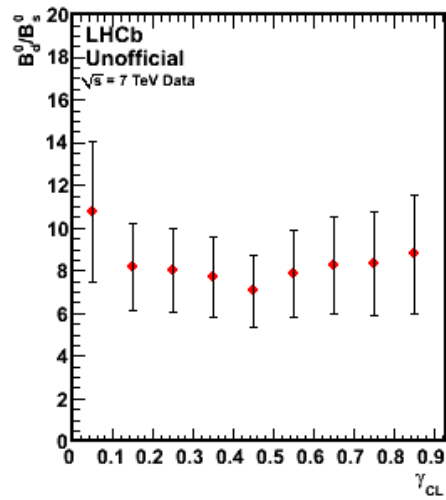


Figure A.3.1 Stability check of the ratio  $\mathcal{R} = \mathcal{N}(B_d \rightarrow K^* \gamma) / \mathcal{N}(B_s \rightarrow \phi \gamma)$  for 2011 data at the variance of the following cuts a)  $K, \pi$  minimal IP  $\chi^2$  b)  $K, \pi$  transverse momentum, c)  $K$   $P_{IDK}$ ,  $\pi$   $P_{IDK}$ , ( $K$   $P_{IDK}$ -  $K$   $P_{IDp}$ ), d) photon transverse momentum, e)  $B_d$  transverse momentum, f) direction angle,  $\theta_B$ , g) helicity angle and h) photon confidence level, when all the other offline cuts are applied at their nominal values presented in Table 5.2.2